Trinity College Dublin
Coláiste na Tríonóide, Baile Átha Cliath
The University of Dublin

Density Optimisation & In-Situ Microstructure Decomposition of As-Built Selective Laser Melted Ti-6Al-4V

HARRY SHIPLEY

Supervisor: Dr Daniel Trimble

Department of Mechanical & Manufacturing Engineering
Trinity College Dublin
Ireland

2022

A thesis submitted to the University of Dublin in partial fulfilment of the requirements for the degree of Doctor of Philosophy

Declaration

I declare that this thesis has not been submitted as an exercise for a degree at this or any other university and it is entirely my own work.

I agree to deposit this thesis in the University's open access institutional repository or allow the Library to do so on my behalf, subject to Irish Copyright Legislation and Trinity College Library conditions of use and acknowledgement.

I consent to the examiner retaining a copy of the thesis beyond the examining period, should they so wish (EU GDPR May 2018).

Funding Acknowledgement

This work was developed with the financial support of Science Foundation Ireland (SFI) under grant number 12/RC/2278 and 17/SP/4721. This research is co-funded by the European Regional Development Fund and SFI under Ireland's European Structural and Investment Fund. This research has been co-funded by Johnson & Johnson 3D Printing Innovation & Customer Solutions, Johnson & Johnson Services Inc.

Dedication

This thesis is dedicated to my dad, Dr David Shipley – who passed away during the course of this research. Without your inspiration, guidance and support over the years this work would not have been possible, and I would not be the person I am today.

Summary

Research into additive manufacturing has grown at an exponential rate since the early 2000's. Much of this has focused on metal additive manufacturing and specifically the process of selective laser melting. The most prominent adopters of selective laser melting have been the aerospace, biomedical and automotive industries. In particular these three industries have focused on selective laser melting of the titanium alloy Ti-6Al-4V. Consequently, a large percentage of selective laser melting research revolves around this alloy. Despite the numerous advantageous afforded by additive manufacturing techniques, post-processing in the form of annealing or thermomechanical treatments are considered necessary due to the sub-optimal microstructure and density conditions of as-built samples.

This work examines the effect of process parameters on the density and microstructure of as-built selective laser melted Ti6Al4V components and relates their conditions to mechanical properties. The hypothesis of this work is that optimisation of density and microstructure simultaneously in as-built samples will remove the need for post process treatments.

An exploration into the available literature revealed techniques reported to increase the density of samples in the as built conditions as well as methods to achieve preferential microstructures without post-processing. However, a significant gap in the field was identified whereby published literature focuses on optimising either density or microstructure but fails to report the effect of their methods on the other. Furthermore, a number of independent methods have been proposed to achieve preferred microstructures during processing, but no combination of these methods exists in the open literature and thus this work represents the first attempt at this.

The first task in this work was to produce fully dense parts using a Realizer SLM50 system. To achieve this, the processing environment was characterised and its effect on the density of parts was established. Following which a systematic statistical design of experiments was conducted to establish the optimal set of laser parameters. A parameter set capable of repeatedly producing parts with a nominal density of 100% was developed and the effect of density on mechanical properties was established.

To examine the as-built microstructure, the laser power and scanning velocity values which were the primary drivers of achieving fully dense parts were retained from the density optimisation study. Then the effects of varying laser spot size, layer thickness, pre-heating temperature and hatch distance on the as-built microstructure and density levels were examined. In order to examine high pre-heating temperatures, a customised heater was developed capable of printing samples at 450 °C. Through microscopy and x-ray diffraction, three different microstructures were identified and quantitatively described.

Finally, the effect of the aforementioned process parameters on the mechanical properties was presented. A number of variables namely, residual stress, density, microstructure, and oxidation were identified as significant with regards to tensile performance. The optimal set of parameters developed within this work facilitated tensile properties akin to those observed following some post-process heat treatments. However, the hypothesis that optimisation of as-built samples could remove the need for post-processing was rejected. Though, suggestions for future work are proposed which would address some of the limitations identified within this work and could validate the hypothesis.

Acknowledgements

First and foremost I would like to thank my supervisor Dr Daniel Trimble for his time, expertise, advice, and resources which were necessary to complete this work. Daniel's door is always open and there were many occasions where small – or sometimes large – interventions sparked a whole new list of ideas when they were needed most. Without his guidance this work would not have been possible.

I would also like to express my gratitude to Dr Garret E. O'Donnell and Dr Rocco Lupoi for their insights throughout the course of this work. To the wider Johnson & Johnson and DePuy Synthes team, thank you for your support and various inputs throughout this research, your level of expertise has been a valuable asset. My sincerest thanks to the technical staff. Specifically, Mick Reilly, Alex Kearns, JJ Ryan, Rob Dunbar, Brendan Caffrey and Peter O'Reilly. Your technical expertise throughout this research has been invaluable and without it the research simply would not have been possible.

My thanks to Luke Dowling, Bobby Gillham, Dr Richard Jenkins, Dr Dominik Seiller, Dr Darren O'Donnell, Tom McKenna, Daniel Tobin, Alex Conway and Conor O'Keefe for your help and friendship throughout the course of this research. I'll miss the Watts office. Specific thanks to Dr Mark Culleton whose impact on this research cannot be over-emphasised. Your patience, expertise, advice, and friendship have been massively appreciated.

I would like to specially thank my family; Mum, Anna, Diego and the Cryan family who collectively have provided uninterrupted support and encouragement over the last number of years. To Ben, Lexi and Willow, thanks for getting me out the door.

Finally, my deepest gratitude goes to Katie, whose level of support knows no bounds. Thanks for always believing in me.

Table of Contents

List of Figures

List of Tables

Nomenclature

Al	Aluminium
AM	Additive Manufacturing
ANOVA	Analysis of Variance Statistical Test
BCC	Body Centred Cubic Crystallographic Structure
CAD	Computer Aided Design
CFD	Computer Fluid Dynamics
CP	Commercially Pure
DLP	Direct Light Projection
DOE	Design of Experiments
EBM	Electron Beam Melting
EC	Critical Input Energy
ED	Volumetric Energy Density
ELI	Extra Low Interstitial
EV	Energy Density
FDM	Fused Deposition Modelling
FOD	Focal Offset Distance
FWHM	Full-Width Half Maximum
HCP	Hexagonally Close Packed Crystallographic Structure
HIP	Hot Isostatic Pressing
MJM	Multi Jet Modelling
OFAT	One Factor at A Time
OM	Optical Microscopy

PBF	Powder Bed Fusion
RP	Rapid Prototyping
SEM	Scanning Electron Microscopy
SLA	Stereolithography
SLM	Selective Laser Melting
SLS	Selective Laser Sintering
Ti	Titanium
Ti64	Ti-6Al-4V Alloy
UTS	Ultimate Tensile Strength
V	Vanadium
W-H	Willamson-Hall Method
XRD	X-Ray Diffraction
YS	Yield Strength

Chapter 1 Introduction

Additive manufacturing (AM) is defined as the process of joining materials to make objects from 3D model data, usually layer upon layer, as opposed to subtractive manufacturing methodologies [1]. AM as a field has grown considerably since its inception whereby parts are now manufactured from metals, ceramics, bio-inks, conductive inks, and polymers amongst others. This has been made possible through process development to the point where many completely separate process techniques including, powder bed fusion (PBF), extrusion, aerosol jetting, lamination and direct deposition amongst others now exist.

In comparison to traditional manufacturing techniques, AM is still in its infancy and accounted for a mere 0.1% of total manufacturing output in 2017. Despite this, AM is widely expected to create a wave of disruptive economic change in the manufacturing field in the coming years, with annual sales of AM products and services expected to hit $27.3 billion by 2023 [2]. Unlike previous noteworthy advances in manufacturing, such as the just-in-time manufacturing process or mass production injection moulding, AM is not expected to completely replace existing mass manufacturing techniques. Rather, AM has created entirely new geometrical opportunities for designers and manufacturers that were previously unobtainable via traditional manufacturing methods [3].

1.1 Additive Manufacturing

1.1.1 AM Process Characterisation

Rapid prototyping (RP) is a term used widely to describe technologies that create physical prototypes directly from model data. The emphasis is on creating a prototype quickly from which further models and eventually a final product will be derived. As this field has progressed and the output from RP machines has improved, many parts are now directly manufactured using these machines. Thus these parts are no longer prototypes. Furthermore the term prototyping overlooks the basic principle in that all RP technologies fabricate parts using an additive approach [4]. Accordingly, the BS ISO/ASTM 52900:2015 standard was developed to provide clear definitions for terms and nomenclature associated with AM [5].

The definition of AM broadly outlines the principles by which parts are fabricated i.e. in an additive manner. However during the development of AM a number of technologies which employ different techniques to process a vast array of materials from polymers to ceramics have been established. Thus AM technologies have been categorised in a number of different ways. Traditionally, AM technologies were classified according to their raw material input or baseline technology e.g. laser or extrusion [6]–[8]. However in some cases these methods of classification led to unusual combinations of processes being grouped whilst others that appear to give similar results were left separated. More recently, a classification system, first proposed by Stucker and Janaki Ram [9], which separates technologies into groups where processes which use a common type of machine architecture and similar materials transformation physics are grouped together. This system has contributed significantly to the standardisation of terminology by the ASTM and ISO respectively. Using this classification system within the BS ISO/ASTM 52900:2015 standard, Table 1.1 outlines some of the most common AM processes [5].

Table 1.1: Common additive manufacturing techniques

Technology Group & Processes	**Applicable Materials**	**Raw Material Form**	**Manufacturing Technique**
Vat Polymerisation • SLA • DLP	UV curable resin	Liquid resin stored in a vat	Light activated polymerisation in the form of a UV or laser
Powder Bed Fusion • SLM • SLS • EBM	Thermoplastics Metals Ceramics	Powder Bed	Full or partial melting of the powder bed through thermal input in the form of a laser or electron beam
Material Extrusion • FDM	Thermoplastics Composites	Filament within a nozzle	Solidification through cooling following extrusion from a heated nozzle
Material Jetting • MJM	Photopolymers	Droplets	Light activated polymerisation through exposure to UV light
Binder Jetting	Metals Ceramics	Powder	Binding of powder bed followed by removal of binding agent and sintering of metal/ceramic material
Direct Energy Deposition	Metals	Powder	Powder is directed into a focused region and melted using a laser source

1.1.2 Advantages of AM

Perhaps the greatest advantage of AM is the ease with which complex parts can be produced. This characteristic of AM over subtractive manufacturing methodologies provides advantages in a number of ways. Parts that could not feasibly be manufactured by subtractive techniques such as graded lattice structures are now possible [10]. Internal features which increase the functionality of parts such as air ducts, internal pathways for acoustic damping devices or cooling channels can now be produced [11]. Finally, the increased freedom of design in AM makes it possible to combine an assembly into one part and therefore reduce the required assembly work and associated costs [12]. Furthermore this added complexity comes for free which contrasts the direct relationship between complexity and cost observed for traditional manufacturing techniques [13].

The relationship between complexity and AM has been the primary driver to determining its position within the broader manufacturing landscape. Pinkerton [14] presented the figure shown in Figure 1.1 where the unit cost of AM produced parts do not change with volume or customisation. In contrast, traditional subtractive methodologies can take advantage of economies of scale whereby tooling developed for production is a fixed cost and thus the cost per part reduces with increasing volume. In contrast, an increase in complexity of parts exponentially increases the cost of traditional manufacturing techniques due to increased labour and tooling costs. Hence, AM has found a niche position within the broader manufacturing field producing low to medium volume of complex parts.

AM also enables manufacturing on demand where for example dental implants have been manufactured using SLM in laboratories within dental practices [15] or where crew aboard ships have used FDM to create tools and fixtures when required [16]. This trait along with the ability that AM provides to decentralise manufacturing hubs leads to supply chain optimisation which significantly reduces lead times and associated shipping costs [17]. Further cost saving measures are possible due to less material waste as parts are built in the net shape whilst the removal of tooling lowers capital investment [3].

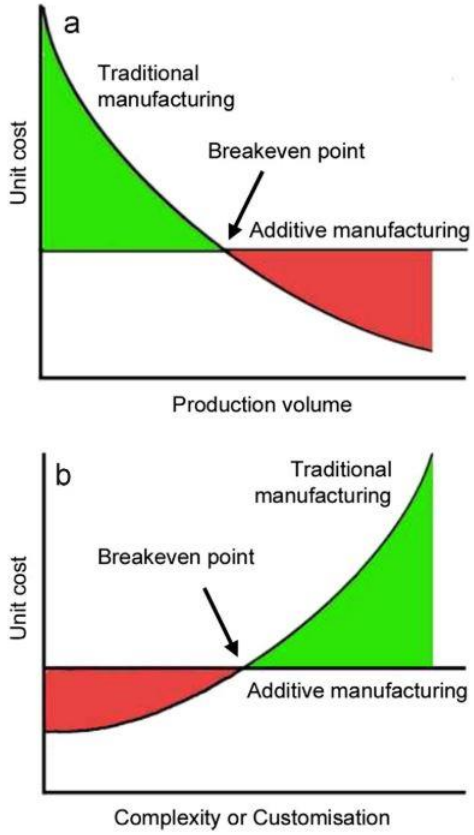

Figure 1.1: Breakeven point between volume and complexity for additive and subtractive manufacturing methodologies

1.1.3 Disadvantages of AM

Despite its advantages, forecasts suggest that long term AM will account for only 5-10% of total manufacturing. One reason for this – as outlined in Figure 1.1 – is that AM does not benefit from economies of scale which limits the applications for which it is economically viable [14]. Raw material cost also represents a challenge within the AM field. Although less material is required per part than for traditional manufacturing, the raw material input for AM processes is frequently multiple times greater than that of traditional processing. As such, material accounts for 30% of the cost of the completed item in comparison to 3% in conventionally processed items [3].

Another issue is production time. In comparison to traditional mass production techniques AM is relatively slow [17]. For example the fastest deposition rate for metal AM currents sits at 200 cm^3/min whilst the record for milling sits multiple orders of magnitude above that [18]. Though many AM techniques are increasing their production rates through

addition of more than one printing head. For example in SLM where commercial machines are now fitted with up to four lasers to increase the production rate. Furtermore, the size of parts that can be processed by AM is inhibited by the size of the printer though this constraint should be considered for each technology. For example some SLM systems have build volumes of less than 200 cm^3 whilst Launcher produces rocket engines using a direct energy deposition technique [19].

Finally, some technological challenges are still present within AM such as producing parts with hanging features, thin walls or slots [11]. Furthermore, as will be discussed throughout this thesis process optimisation has proven challenging within the wider AM field. Porosity, thermal gradients and poor surface finishes are examples of issues which continue to face the AM field. Incorrect choice of process parameters can exacerbate any of these effects such that parts can fail during prints. Given the batch nature of AM, one part failure can impact the rest of the parts in the build which can lead to failure of an entire production run. Thus process parameters are frequently set to ensure build success rather than maximising part performance. This has resulted in the need for post processes such as heat treatments which add considerably to the total cost per part and further limits the window in which AM is economically viable over subtractive techniques.

1.1.4 Applications of AM

Three of the biggest adopters of AM have been the aerospace, biomedical and automotive industries. The ease of customisation through AM of parts sits at the heart of this in two differing ways. In the aerospace and increasingly – with the advancement of electric vehicles – the automotive industries, weight matters. As such the concept of lightweighting has become more and more important as each kilogram increases the fuel required for flight or reduces the range of an electric vehicle.

The opportunities afforded by AM with regard to customisation has enabled the production of parts that are optimised for purpose without the need for excess material. For example, the Airbus Group, EADS Innovations conducted a life cycle study of a bracket used in the Airbus A320, contrasting an AM produced titanium (Ti) bracket to its traditionally manufactured steel alternative. They discovered a weight saving of 10 kg per aircraft which translated into a 40% reduction of CO_2 emissions over the life of the part.

AM has gained traction in the biomedical field in three main capacities; (1) anatomical models, (2) surgical instruments and (3) implants and prostheses [20], [21]. Anatomical models have been used for education and training as well as preoperative planning. Regarding education, 3D printed models have been used extensively in the orthopaedic and cardiovascular fields enabling surgeons to improve on skills, understand deformities and practice procedures before operating on high risk patients [22]–[24]. Neurosurgeons have utilised 3D models to familiarise themselves with delicate nerves, vessels, cerebral structures and bone for which an appreciation can be difficult to achieve through two dimensional imaging alone whilst Condino et al. [25] recreated an entire abdominal cavity based upon patient specific anatomy [26]. Using these patient specific models preoperatively allows the surgeons to better focus on individual surgeries and has the potential benefits of reducing actual operating time and trauma to the patient [20].

The use of AM surgical instruments in an intraoperative environment is increasing. Jigs which constrain operative placement to a specific area have been extensively used in mandibular reconstructive surgery. These jigs have enabled bone movements to be defined accurately and can be tailored to patient anatomy whilst operations using these jigs have reduced operating times [27], [28]. Similarly, Jaffry et al. [29] printed patient specific instruments for use in unicompartmental knee replacements. When compared to conventional instruments, surgeries using the patient specific instruments lead to better positioned implants, which could lead to the implants lasting longer and patients experiencing less side effects.

As well as tools and models, implants which are suitable for implantation can be produced by AM. Popovich et al. [30] and Wang et al. [31] used SLM processing of Ti64 to produce a patient specific hip and pelvic implant respectively with positive postoperative outcomes in both cases. Using AM resulted in a number of advantages including, reduction of intraoperative time, reduced infection ingress due to custom fit and reduced surgical wounds. Looking forward, AM is gaining interest amongst researchers in the area of macroporous structured implants [32]–[34]. These implants have been suggested as a solution to the stress shielding phenomenon, which has been accredited with causing bone resorption and eventual implant loosening and occurs due to the mechanical mismatch between natural bone and metallic biomaterials. These complex shaped porous implants

cannot be manufactured through conventional methods whilst AM methods such as SLM provide the freeform capabilities necessary [32].

Overall, these industries have decided that the advantages of AM outweigh the aforementioned disadvantages. The automotive, aerospace and biomedical industries combined extensively use the Ti alloy Ti-6Al-4V (Ti64) due to its good stability at high operating temperatures, high specific strength and good corrosion resistance properties. The most common AM processing technique of Ti64 is the PBF technique of Selective Laser Melting (SLM) which forms the focus of this thesis.

1.2 Selective Laser Melting Ti6Al4V

SLM is a PBF process, which is a class of AM processes that use thermal energy to selectively fuse regions of a powder bed. Figure 1.2 presents the SLM process illustrating the application of a laser, usually of 1064nm wavelength, to a powder bed using a set of optical mirrors. Deposition systems, generally in the form of a scraper or roller are used to spread the powder material. Initially, a solid build platform is used to counteract warping of the material due to build-up of thermal stresses as the part is built. Upon irradiation the powder material is heated and melts to form a liquid pool, known as the meltpool, which cools rapidly and solidifies. After the cross section of the part is scanned, the previously scanned layers are lowered by a pre-defined layer thickness and a new layer of powder is deposited on top. The un-sintered powder from the previous layers remains in the build chamber and serves to act as support for the succeeding layers. Following conclusion of the process, this un-sintered powder can be collected, sieved and re-used. Finally, the process is conducted under an inert argon atmosphere to avoid contamination of the meltpool or oxidation of the solidified material [35], [36].

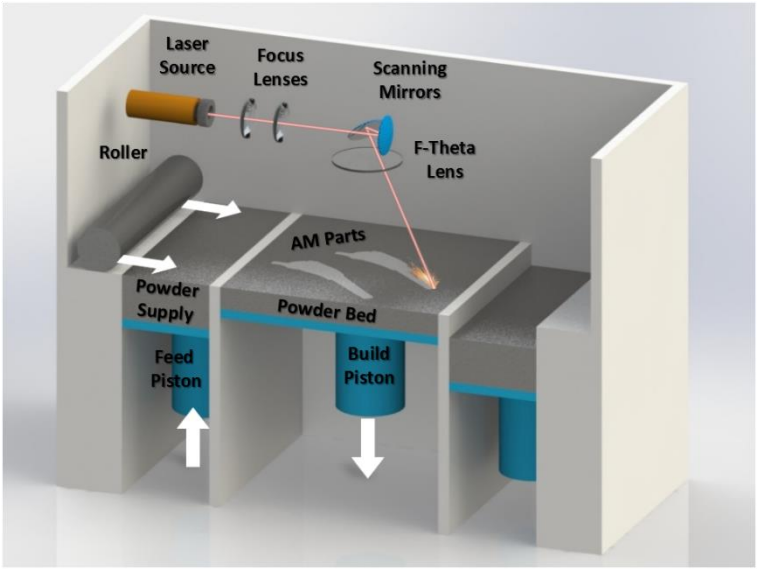

Figure 1.2: Schematic of SLM process

SLM processing of Ti64 enjoys all of the advantages outlined in section 1.1.2 and is an excellent choice for producing Ti64 parts for high-performance applications. However, SLM processing of Ti64 has some inherent problems. Firstly, the production of fully dense parts has proven difficult and process parameters must be optimised for each machine independently. Secondly due to the high energy input from the laser, the cooling rates during the process are extremely high. This in turn causes two issues; (1) the microstructure of as-built parts displays a martensitic structure which causes brittle behaviour and (2) large residual stresses are formed in the part which encourage crack formation and thus premature failure under tensile loading. As a result post processing in the form of annealing or hot isostatic pressing (HIP) is considered essential for SLM produced Ti64 parts. These post processing steps can add significantly to the cost per part and have been estimated to account for at least 6% of the total cost of processing [37].

1.3 Research Focus

The goal of this research is to explore the effect of the density and microstructure on mechanical properties of as-built SLM processed Ti64 components. The hypothesis of this research is that optimisation of density and microstructure simultaneously in as-built samples will remove the need for post process HIP/annealing treatments.

The research objectives are:

(1) **Produce fully dense samples using the Realizer SLM50 printer**. The key to achieving this objective is examining the process environment in combination with the laser parameters utilised during processing. The impact of part density on tensile properties will be established.

(2) **Achieve in-situ decomposition of the brittle martensitic microstructure characteristic of SLM processed Ti64**. Operating conditions developed during density optimisation will be further developed by examining more processing parameters. Their effect on the density and microstructure of the as-built components will be characterised.

(3) **Examine the effect of density and microstructure on the mechanical properties.** The impact of density and microstructure on the mechanical properties of as-built SLM processed Ti64 components will be discussed.

1.4 Thesis Outline

Chapter 2: Literature Review

This chapter provides an insight into the available literature most relevant to this thesis. These include examining the Ti64 alloy, SLM density optimisation efforts and techniques for altering the microstructure in Ti alloys.

Chapter 3: Experimental Methods

This chapter provides an outline for all the processing and analysis techniques used during the course of this research.

Chapter 4: Density Optimisation

The first primary research objective which was to produce fully dense samples with the Realzier SLM50 is addressed in this chapter. Initially, the process environment in the form of the argon gas flow is examined to determine whether this acts as a deterministic variable of part density. Following which a systematic density optimisation investigation

is presented and the optimal laser parameters for maximising density are determined. Finally, mechanical properties are presented to illustrate the importance of density maximisation in the SLM processing of Ti64.

Chapter 5: As-Built Microstructures

Chapter 5 examines the second of the research goals which was to Achieve in-situ decomposition of the brittle martensitic microstructure characteristic of SLM processed Ti64. Firstly, the experimental design is outlined which takes the laser power and scanning velocity optimised from Chapter 4 and adds hatch distance, layer thickness, pre-heating temperature and laser spot size to examine their effect on as-built microstructures. The custom designed high-temperature heating apparatus is then introduced. Following which the effect of the outlined parameters on the density and as-built microstructure is examined through quantitative analysis.

Chapter 6: Mechanical Properties

The final research goal is addressed in this chapter. The combined effect of the process parameters and the influence they have on density, microstructure, residual stress and chemical composition of as-built SLM processed Ti64 parts is examined with reference to microhardness and tensile properties.

Chapter 7: Conclusions and Future Work

Conclusions from the aforementioned chapters are presented and the hypothesis of this research is addressed. Commentary on future work that could be carried out to advance this topic of research further is provided.

Chapter 2 Literature Review

2.1 Introduction

This research focuses on the SLM processing of Ti64. Hence the aim of this chapter is to inform the reader of the relevant literature regarding SLM of Ti64 with a focus on density maximisation, microstructure decomposition and mechanical properties. The chapter is concluded by summarising the main findings within the literature whilst the research into literature culminated in the journal article below.

- H. Shipley, D. McDonnell, M. Culleton, R. Lupoi, G. O'Donnell, and D. Trimble, "Optimisation of process parameters to address fundamental challenges during selective laser melting of Ti-6Al-4V: A review," Int. J. Mach. Tools Manuf., vol. 128, no. January, pp. 1–20, 2018

2.2 Titanium and Ti-6Al-4V

Titanium is an allotropic element whereby it exists in more than one crystallographic form. At room temperature Ti has a hexagonally close packed (HCP) crystallographic structure referred to as the α phase. This transforms to a body cubic centred (BCC) crystallographic structure known as the β phase at the β transus temperature. The β transus temperature is defined as the lowest equilibrium temperature at which the material is 100% β. For commercially pure (CP) Ti this occurs at 882 °C but changes when alloying elements are added. Titanium alloys are generally classified into three categories according to their volume fraction of α and β phases. α and near α alloys are those which have less than 10% stable β volume fraction at room temperature. (α+β) alloys have stable β volume fraction between 10 and 50% whilst β alloys have a high volume fraction of β phase at room temperature [38]–[40].

Alloying elements are classified as either α or β stabilizers depending on whether they decrease or increase the CP β transus temperature of 882 °C. The substitutional element aluminium (Al) and the interstitial elements oxygen, nitrogen and carbon are all strong α stabilisers and serve to increase the β transus temperature as seen in Figure 2.1. Of these, Al is the most commonly used as it is the only α stabiliser which has large solubilities in both the α and β phases.

Regarding the interstitial elements, oxygen is the most commonly used as a stabiliser in Ti alloys as the oxygen content can be used to obtain a desired strength level. However, performance of Ti alloys either at or following exposure to high temperatures can be limited due to gradual oxidation and subsequent degradation of the material [41]. Yan et al. [42] determined that SLM processed Ti64 specimens are particularly sensitive to increases in the oxygen content. They reported that increasing oxygen content beyond 0.15 wt-% leads to a significant decrease in fracture strain whilst total brittleness is observed at 0.22 – 0.25 wt-%. Furthermore, during periods of exposure to high temperatures, the increase in oxygen promotes a layer of oxygen enriched α phase near the surface which is known as α-case. The formation of this α-case has been reported to cause cracks on the surface on Ti parts due to compressive stresses [41].

β stabilising elements are divided into β eutectoid and β isomorphous elements depending on the resulting phase diagram, as illustrated in Figure 2.1. The most commonly used β stabilizers all belong to the isomorphous group and include vanadium (V) and molybdenum as they result in stability of the β phase at lower temperatures. Ti64 is characterised by alloying Ti with 6 (5.5 – 6.5) wt.% Al and 4 (3.5 – 4.5) wt.% V thus leaving it in the (α+β) category [38], [43].

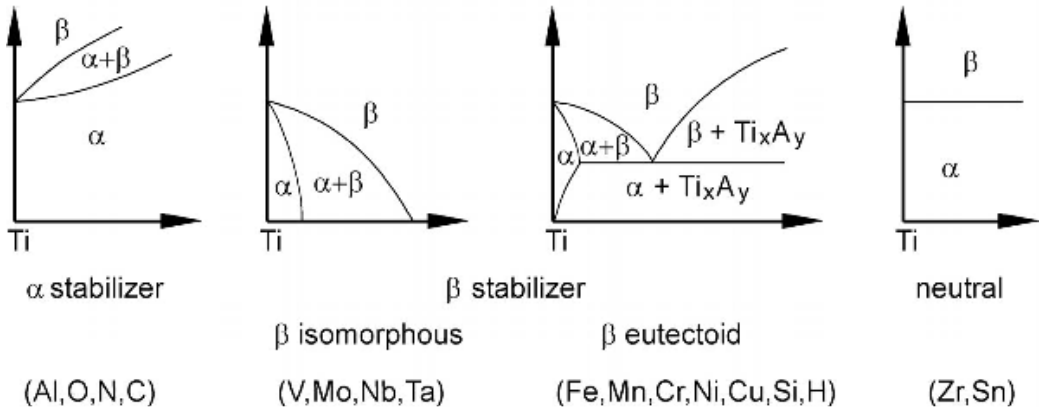

Figure 2.1: Phase diagrams illustrating the effect of alloying elements on Ti alloys (note: temperature and alloy percentage on the x and y axis respectively)

Ti64 is the most widely used titanium alloy, accounting for more than 50% of all titanium usage worldwide [44]. This is due to its good stability at high operating temperatures, high specific strength and good corrosion resistance properties. Conventionally, Ti64 components have been manufactured through processes such as powder metallurgy, forging and casting which cannot easily produce complex shapes and frequently result in components with poor mechanical properties [44], [45]. However, the disadvantage with Ti alloys has always been cost in comparison to its alternatives. Furthermore, Ti64 has been classified as a difficult to machine metal, thus the cost of extraction is only a small fraction of the total cost of a component when fabricated using conventional manufacturing methods [46], [47].

In contrast, AM techniques do not have the same extent of design constraints that limit conventional processes [48]. AM allows a far greater degree of geometrical freedom and material flexibility enabling mass customisation of parts. Moreover, remaining unprocessed powder can be reused which, along with savings in time, energy and other costs can reduce the cost per part substantially [49], [50]. Of the various AM techniques

available, SLM is perhaps the most versatile with regards to the range of materials that can be processed. Accordingly, SLM machines have become popular in industrial settings which has led to extensive research regarding the use of SLM for Ti64 processing, particularly for use in the aerospace, automotive and biomedical fields [51]–[54].

2.3 SLM Optimisation

During SLM processing, parameters are generally optimised in order to maximise density. As a result, annealing steps are commonly considered to be required so that residual stresses can be removed and to achieve a microstructure conducive to improving mechanical properties, typically fracture strain. Given the difference between SLM systems available on the market, there are approximately 130 – 160 controllable process parameters on any given SLM system [55], [56]. For the purpose of this thesis, these can be categorised as; pre-process, inter-process and post-process parameters, examples of which are given in Table 2.1.

Of these, inter-process parameters, some of which are illustrated in Figure 2.2 are the most heavily investigated aspect of the process chain with regards to process optimisation. The most conventional method of optimising mechanical properties is through optimisation of laser parameters, namely, laser power, scanning velocity, layer thickness and hatch distance which is defined as the distance between the centre point of two successive laser scans as illustrated in Figure 2.2.

Considerable research has been conducted on the influence of these parameters to optimise the microstructure, process defects or residual stresses for a variety of materials [36], [57]–[73]. Much of this research utilises a metric known as the volumetric energy density (ED) (Equation 2.1) which attempts to describe the average applied energy per volume of material. It is the most frequently used combination of these parameters by authors relating process parameters to part properties.

$$ED = \frac{P}{v \cdot h \cdot t} \ [J/mm^3] \qquad \text{Equation 2.1}$$

Where; P is the laser power, v is the scanning velocity, t is the powder layer thickness and h is the hatch distance.

Table 2.1: Example of process parameters as categorised for this thesis

Pre-Process	Tool operator, process preparation, CAD & file preparation, part orientation, powder properties etc.
Inter-Process	Beam diameter, scanning speed, laser power, hatch distance, focal offset distance, argon flow, build platform temperature, oxygen percentage etc.
Post-Process	Thermomechanical treatment employed, annealing duration, method of cooling, machining, support removal etc.

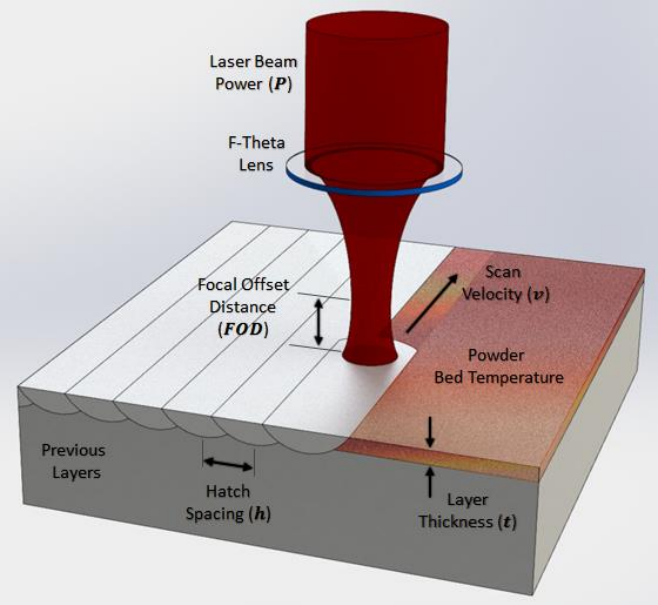

Figure 2.2: Examples of inter-process parameters for SLM processing

Some authors have studied the effects of alternative parameters such as powder bed temperature, focal offset distance (FOD), laser spot size, scanning strategies and inter-layer time to optimise mechanical performance of parts in the as-built condition [64], [74]–[76]. However, these have primarily been with the goal of decomposing the

martensitic microstructure or reducing residual stresses with many studies neglecting possible effects on the density of the parts.

As the research completed in this work focuses on using inter-process parameters to explore the mechanical properties of as-built Ti64, they form the primary focus of the literature reviewed. However, some pre and particularly post processes have been reviewed to provide context of what density levels and microstructure composition are required for mechanical property maximisation.

2.3.1 Density

Many studies have shown that incorrect choice of inter-process parameters leads to porosity and defects such as balling [57], [69], [77], [78]. The balling phenomenon is a common defect observed during SLM and causes the deposition of the following layer to be impeded which in turn leads to bad layer deposition, cracking or even process failure (Figure 2.3). This transpires when molten material does not wet the underlying substrate well due to high surface tension differences generated as a result of variations in thermal properties across the melt pool [79]–[81].

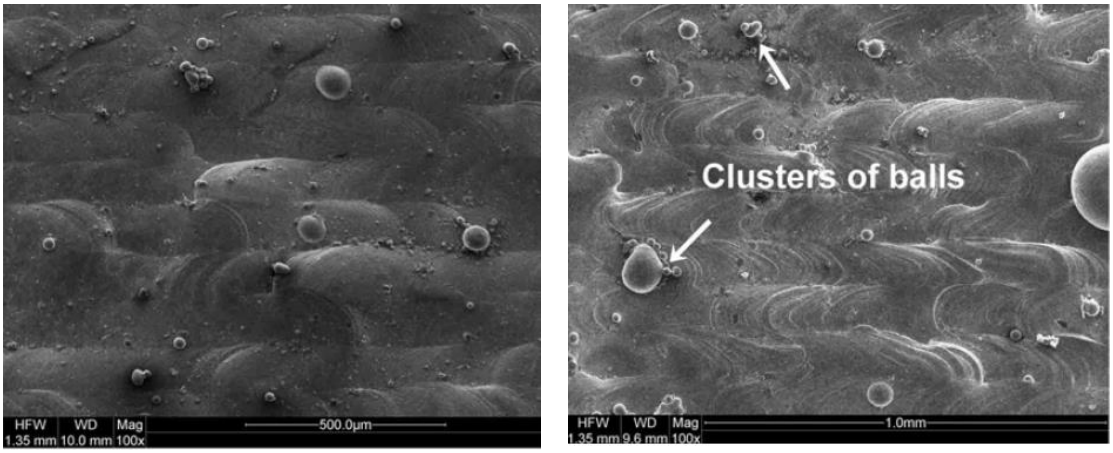

(a) (b)

Figure 2.3: SEM images of balling observed during SLM processing of CP Ti at high (a) and low (b) energy densities [57]

Even more common than balling, is the presence of spherical and/or sharp crack-like pores in the volume of SLM fabricated components (Figure 2.4). It is the minimisation of these pores which forms the main focus of the inter-process parameter selection reported

in literature. Reports on the mechanism of pore formation are limited with some researchers focusing on the quality of the feedstock but most relying on assumptions concerning the detailed mechanisms that occur during melting and solidification in SLM [82], [83].

The lack of fusion defects have been ascribed to insufficient energy input, otherwise referred to as under-melting. Processing with a low energy input – frequently characterised by low ED values – leads to a shallower melt pool. Due to the inhomogeneous nature of the size of powder particles and distribution across each layer, some powder particles may become partially melted rather than achieving full melting. Pal et al. [84] outlined the mechanism displayed in Figure 2.5 where they referred to a change in the powder height as a mounded place. This caused the meltpool to shift upwards which created a void between two successive meltpools and prevented the melting region from reaching the bottom of the layer. This results in only partial melting of the powder particles in this region and causes the sharp crack-like pores observed in Figure 2.4.

The spherical pores observed in Figure 2.4 (b) can be attributed to the keyholing mechanism which occurs as a result of excessive energy input into the powder bed [58], [70], [85]–[91]. Figure 2.6 illustrates the mechanism of keyhole porosity formation. Over melting causes increased evaporation of the metal powder which results in a deep keyhole depression. In such circumstances, the surface tension of the meltpool is low whilst the recoil pressure will be higher than normal [84]. Combined this causes the keyhole depression to become unstable and collapse which traps the inert shielding gas to become trapped thus resulting in a spherical pore [92].

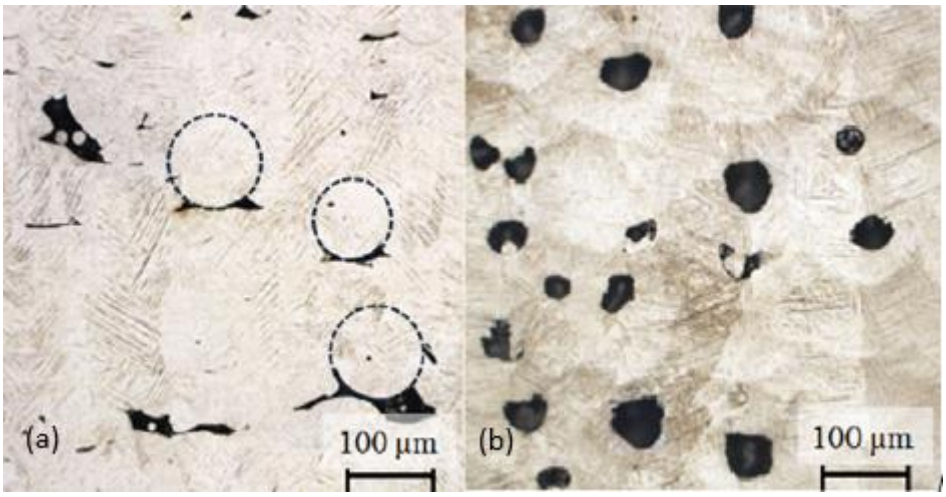

Figure 2.4: (a) Sharp-crack like and (b) spherical pores commonly observed post SLM processing [85]

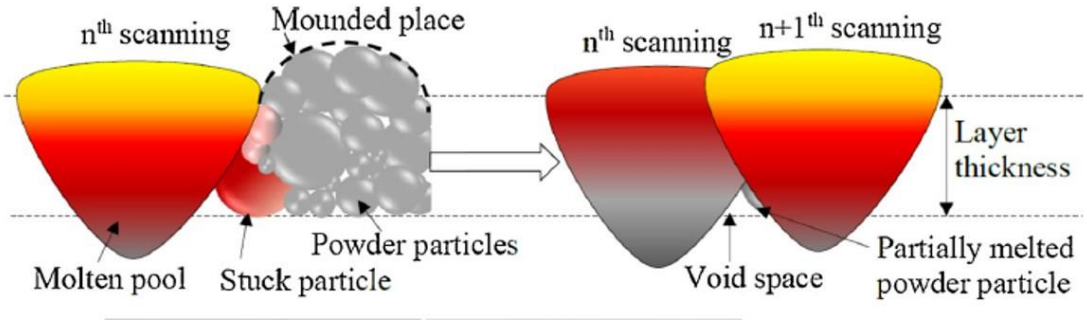

Figure 2.5: Pore formation due to insufficient energy input as illustrated in [84]

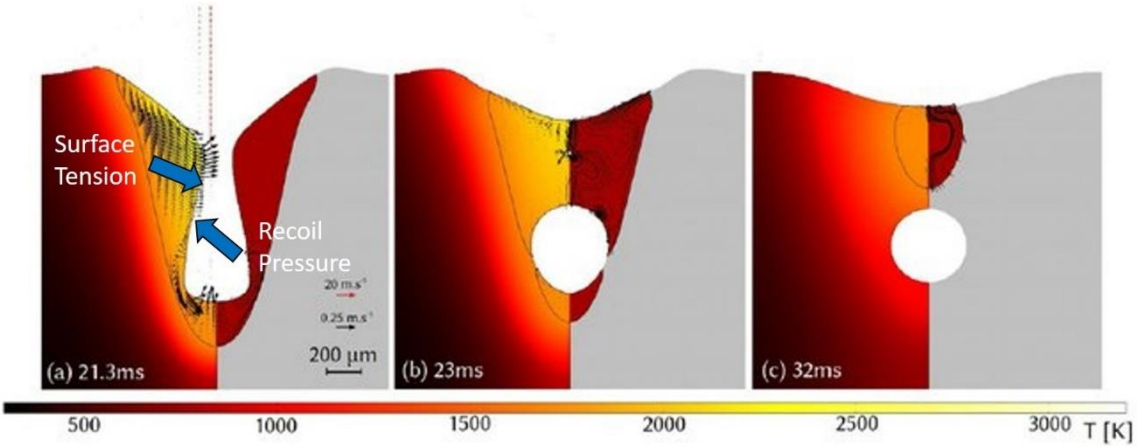

Figure 2.6: Keyhole porosity formation adapted from [89]

Porosity is critical for SLM processed Ti64 parts. It has detrimental effects on fracture properties and exerts the largest influence on fatigue performance as cracks initiate from internal pores and propagate radially outwards [69], [93]. Gong et al. [94] observed a direct relationship between fracture strain and density of Ti64 samples. However, literature has most commonly related defects to dynamic mechanical properties and in particular fatigue. Leuders et al. [78] examined the fatigue behaviour of SLM processed Ti64 in the as-built, heat treated and HIP conditions. Employing HIP treatment reduced the pore size below the detection limit thus the samples had a theoretical relative density of 100% whilst the mean density of as built and annealed samples was 99.77%. This difference was reflected in the mean fatigue life of the samples which ranged from 27,000 to 290,000 cycles for the as built and heat treated samples whilst none of the HIP samples failed before being interrupted at $2x10^6$ cycles.

Similarly Kasperovich et al. [95] examined the fatigue resistance of SLM processed Ti64 in as-built, annealed and HIP treated conditions. They noted that the sites with the highest stress concentrations served as crack initiation sites and the most critical of these were crack like pores induced by lack of fusion during processing. Their results were similar to those obtained by Leuders et al. [78] whereby their results demonstrated a fatigue life of $2.3x10^3$ – $5.6x10^3$ cycles for samples in the as-built condition. Annealing samples at 700 °C and 900 °C did not lead to any significant change in porosity, thus no significant improvement in fatigue life was observed. In contrast, samples which were HIP treated exhibited significant improvement with fatigue lives ranging from $1.5x10^5$ – $3x10^5$ cycles which was comparable to the fatigue life obtained in a reference sample of wrought Ti64.

2.3.1.1 Inter-Process Parameters

Due to the aforementioned effect on mechanical properties the primary consideration when choosing inter-process parameters is overwhelmingly the need to minimise these defects and produce fully dense parts. To achieve this, individual process parameters such as laser power, scanning speed, powder layer thickness, hatch distance, and focal offset distance have been examined. Of these, hatch distance is determined to have the least impact. In their studies on SLM processed Ti64 Kasperovich et al. [85] and Han et al. [96] observed a variation in porosity of less than 1% for a 450% and 42% increase in hatch distance respectively while all other process parameters remained constant.

Layer thickness remains relatively unexplored with regards to process optimisation. Xu et al. [74] managed to produce samples with a density greater than 99.5% for layer thicknesses from 30 – 90 µm. Qiu et al. [82] concluded that the overall porosity and the size of pores increase continuously with increased layer thickness. As shown in Figure 2.7 there is little effect on porosity for layer thicknesses from 20 – 40 µm. In contrast, the top surface displayed open pores thus increasing porosity considerably for layer thicknesses greater than 60 µm.

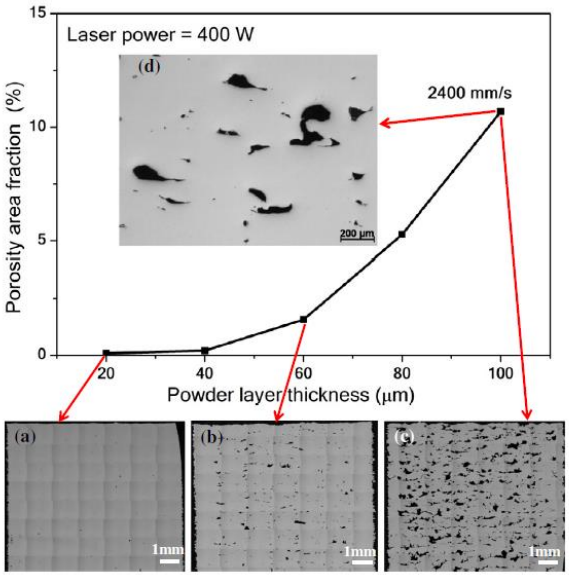

Figure 2.7: Influence of powder layer thickness on porosity as adapted from [82]

It is well accepted that the stability, dimensions and behaviour of the melt pool determine the extent of porosity. Thus, it can be inferred that laser power and scanning velocity which have the greatest effect on the melt pool, will therefore have the maximum influence on porosity [85], [90].

Scanning velocities from 100 to 4250 mm/s and laser powers from 40 – 400W have been examined and their impact on porosity of Ti64 components assessed [57], [72], [82], [85], [86], [90]. Han et al. [96] achieved components with density greater than 99% for scan velocities of between 400 and 1100 mm/s. Gong et al. [72] reported less than 1% porosity for velocities from 600 – 1600 mm/s whilst Qiu et al. [82] reported 99.9% density for scanning velocities up to 2600 mm/s. The spread in these values suggests that scanning velocity alone is not a determinitsic variable, thus it is incorrect to consider these parameters independently. The window with which fully dense parts can be manufactured

is a function of – amongst other things – the relationship between scanning velocity and laser power rather then a result of each individually.

Gong et al. [72], [86] composed a process window based on this relationship, from which porosity classifications can be made (Figure 2.8 (a)). They concluded that Zone I parameters would produce fully dense components. Zone OH parameters should be avoided as the heat produced cannot be conducted away immediately. Zone II and III parameters, which are referred to as *"marginal parameters"*, can be used to fabricate Ti64 samples with varying levels of porosity. Similarly Song et al. [97] used scanning speed and laser power to define a process window for SLM processed Ti64 (Figure 2.8 (b)). They determined that the high energy input in Zone I would yield cracks, Zone II would produce fully dense components whilst Zone III would result in balling due to melt pool instability. Whilst similar conclusions are reported by both sets of authors, the parameters that define their zones are substantially different (Figure 2.8 & Figure 2.11).

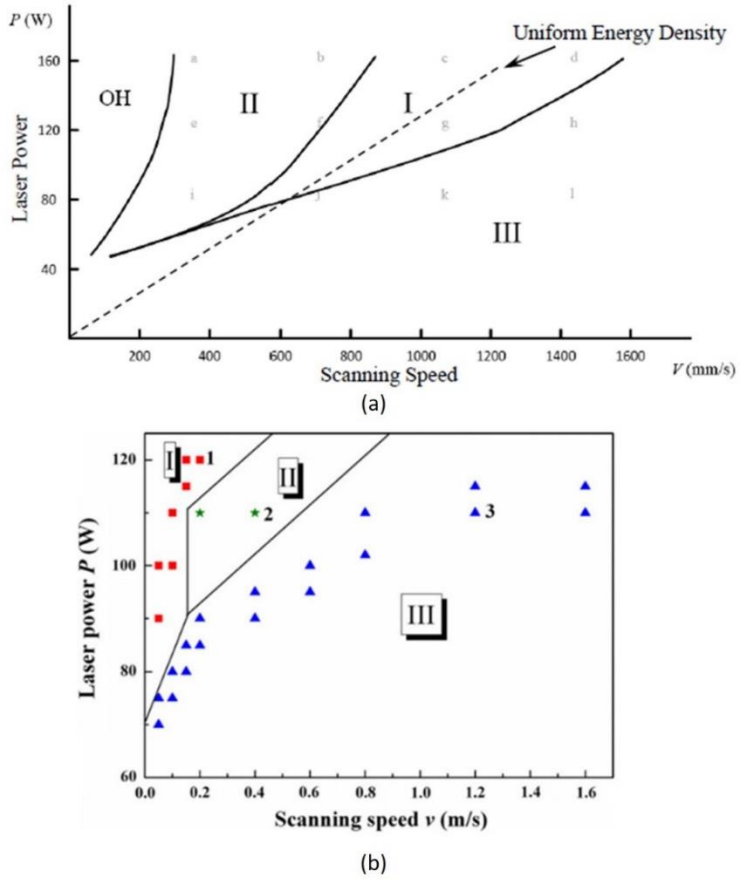

Figure 2.8: Process windows relating scanning speed and laser power to porosity as defined by (a) Gong et al. [72], [86] and (b) Song et al. [97]

2.3.1.2 Energy Density

Another common method to optimise density has been through use of the ED variable (Equation 2.1). Kasperovich et al. [85], Han et al. [96] and Cunningham et al. [98] used the ED to characterise the presence of pores through the development of process windows. Han et al. [96] and Kasperovich et al. [85] defined process windows of 120 – 202 J/mm^3 and 83 – 120 J/mm^3 respectively to produce Ti64 components with a density greater than 99.9% (Figure 2.9). Moreover, Kasperovich et al. [85] stated an energy density of 117 J/mm^3 should be used to produce fully dense components and this value closely correlated with that of 120 J/mm^3 reported by Attar et al. [36], [58]. In contrast, Cunningham et al. [98] reported a far wider process window, observing parts with densities greater than 99.9% for energy densities ranging from 48.61 – 194.44 J/mm^3 whilst Gong et al. [94] fabricated fully dense parts with a density of only 33.33 J/mm^3.

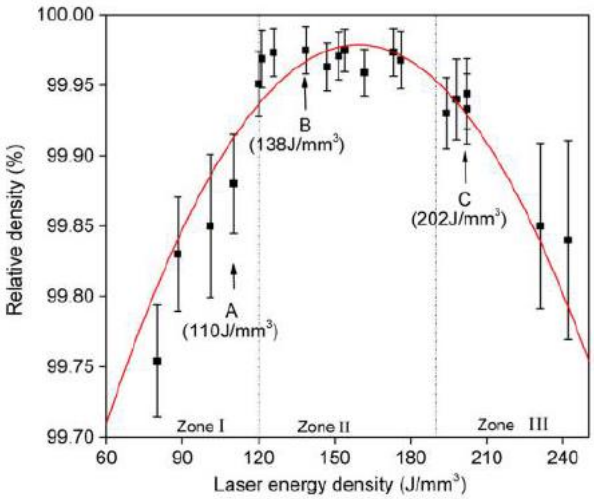

Figure 2.9: Process window defined by Han et al. [96] relating relative part density and energy density

Though some agreements can be observed between authors, a closer examination of the literature reveals variability in part density obtained given the same energy densities. For example Figure 2.10 demonstrates that for SLM processed Ti64, different levels of porosity can be obtained given the same energy density [90], [94]–[96], [98]–[100]. Accordingly, the validity of using the energy density variable as a means of process characterisation has recently been questioned by Prashanth et al. [101] and Bertoli [102].

In their study Bertoli et al. [102] examined the limitations of the energy density as a means of process characterisation in 316L stainless steel. They noted that the same energy density value can be obtained using significantly different process parameters. Prashanth et al. [101] investigated if the energy density equation was a reliable metric during SLM of Al-12Si. Variations in mechanical properties led the authors to question whether the energy density variable properly represents the effective energy transferred to the powder bed noting that important process parameters such as laser spot size, hatch style and others are disregarded. These process parameters have varying influence on porosity, thus a comparison by energy density alone can be misleading and insufficient.

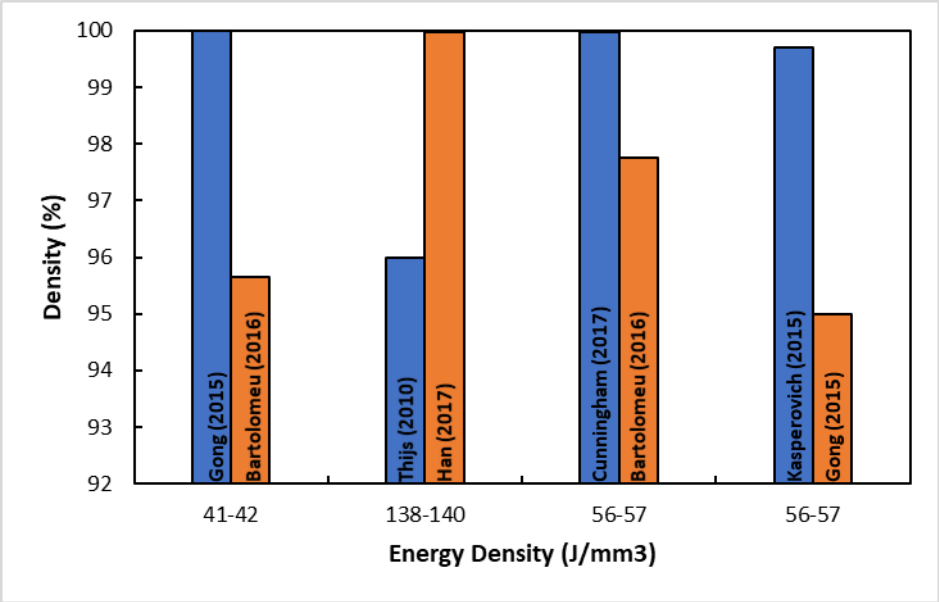

Figure 2.10: Comparison of density of SLM Ti64 parts built at identical energy densities from literature [90], [94]–[96], [98]–[100]

Examining the process windows defined using scanning speed and laser power also leads to questions regarding their applicability. Figure 2.11 illustrates data that has been collated from across the literature where authors have reported the processing parameters and porosity achieved in Ti64 components overlaid with the process zones reported by Song et al. [97] and Gong et al. [72], [86]. It is evident that processing with low laser power values at all scanning speeds results in parts with poor density. Scanning velocities under 200 mm/s appear to be sparsely studied but show discouraging signs from the available literature. Thus, it is between these limits that the uncertainty appears.

The fully dense zone reported by Song et al. [97] sits inside the over-heating zone and *"marginal parameter"* zone reported by Gong et al. [72], [86]. Furthermore, comparing it to the wider literature, parts with varying levels of porosity including some with <99% density are present. Examining the fully dense zone reported by Gong et al. [72], [86] it appears to be better correlated with the additional literature. Apart from one outlying data point, the minimum density reported for components processed in that zone is 99.5% although the vast majority of the points in that region have a density of less than 99.9%. What neither study accounted for, but what shows very encouraging results is processing at higher laser powers. Of the data available, the average density of components processed under 190 W is 97.63% whilst those processed at or above 190 W is 99.83%. Currently, no process zone has been defined at these higher laser powers and more studies are required to fully understand the density of parts processed in this range.

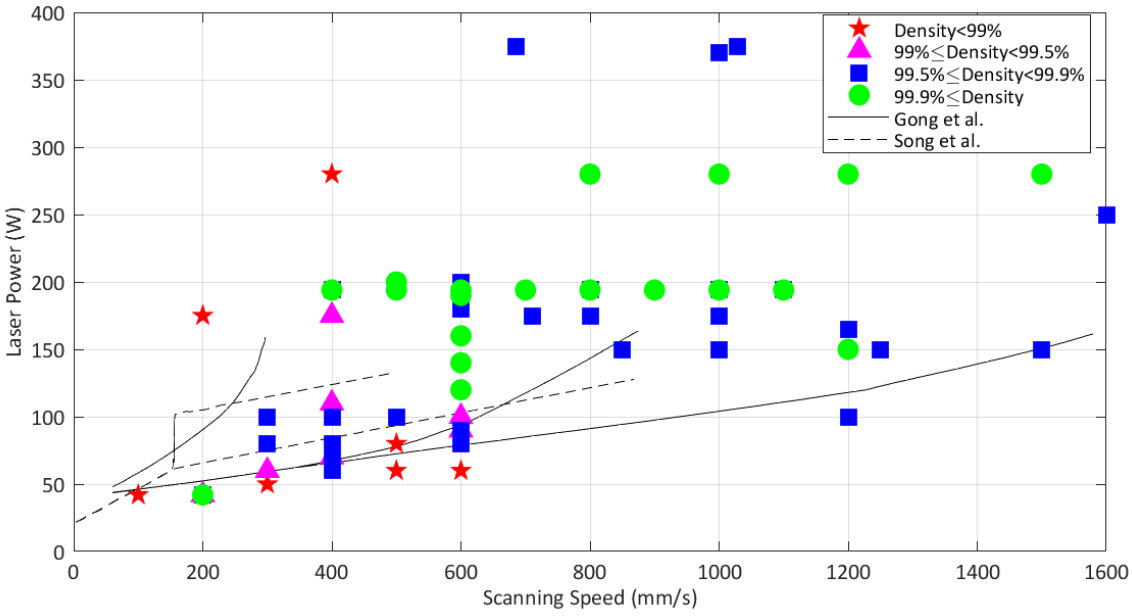

Figure 2.11: A meta-analysis assessing the relationship between scanning velocity and laser power as reported in the literature [64], [72], [74], [85], [86], [88], [90], [95], [98], [100], [103], [104]. The data discovered in the literature is compared to the process windows as reported by Gong et al. [72], [86] and Song et al. [97]

2.3.1.3 Gas Flow

Although sparsely studied in comparison to the laser parameters, there is evidence to suggest that the gas flow during processing will affect the level and/or reproducibility of

density in as-built parts. Though the primary role of the gas flow within the chamber is to provide an inert atmosphere and thus prevent chemical reactions such as oxidation, it also has an important secondary role of removing process by-products from the path of the laser. These by-products may include condensate, spatter or ejected powder (Figure 2.12); all of which are capable of shifting the focal point through scattering or even absorbing incident laser energy when present in the laser path [105].

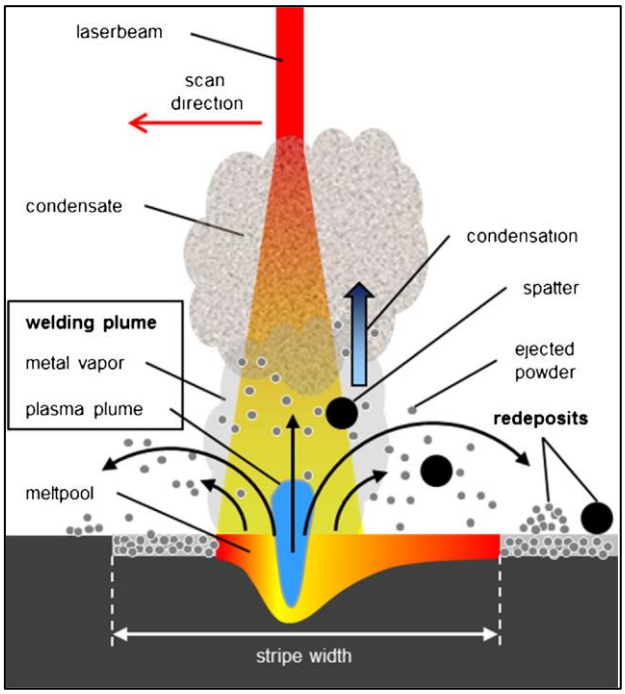

Figure 2.12: Schematic representation of by-products observed during SLM processing [105]

Spatter formation which is linked to instability in the melt pool causes particles that are noticeably bigger in size than the powder [106]. Along with ejected powder, these larger spatter particles may be deposited on surfaces which are exposed to the laser beam afterwards, thus causing an increase in the local layer thickness. This can be detrimental to the density of parts produced as a critical layer thickness exists for any given input energy such that the molten material can be properly connected to the previous layer. If the local layer thickness exceeds this critical value, a lack of fusion defect can be formed. Therefore, it is considered critical that the spatter and ejected powder particles are removed from the build plate with a sufficient gas flow.

Shceglov et al. [107] and Greses et al. [108] reported a maximum attenuation of the laser of up to 40% for fiber lasers used in SLM. Attenuation of the power at this scale is

certainly sufficient to cause lack of fusion defects. Similarly, Grünberger and Domröse [109] investigated shifting the focal position which can occur as a result of by-products in the laser path. They purposely provoked a disturbed unstable process which they named the “splashy process” and determined that it can have a negative effect on the process. Given this “splashy process” usually happens due to interaction with the welding plume, the authors indicated that the probability of its occurrence is linked to the gas flow rate during processing.

Acknowledging the effect of gas flow within the process, several researchers have conducted comprehensive studies on gas flow uniformity across the build plate [105], [110], [111]. Kong et al. [110] examined two different baffles and discovered that regardless of energy input, large pores were observed when using the standard baffle whilst their insert resulted in significantly smaller pores. They attributed this to a greater velocity across the build envelope for the modified baffle when compared to the standard. Similarly Ferrar et al. [111] examined a number of nozzles through computer fluid dynamic (CFD) models and empirical investigations. They determined that the standard nozzle in their SLM setup was delivering a flow which was not running parallel from inlet to exhaust and instead was causing circulation within the chamber. This resulted in poor removal of condensate and consequential variability in part properties.

In their study they highlighted the importance of uniformity across the build plate stating that the uniformity of gas flow was shown to significantly affect the strength of the parts across the build plate. Through an iterative process of changing the nozzle; they were able to increase the density of their samples as a result of an increased melt pool which was caused by better flow conditions.

2.3.2 Microstructure

Resulting from thermomechanical processing Ti alloys can attain an equiaxed, lamellar or bimodal microstructure, each of which possess different mechanical characteristics. Optimising inter-process and post-process parameters enables tuning of the microstructure in SLM processed Ti alloys. The desired microstructure and mechanical properties are dependent on the application of the part. For parts requiring high strength properties such as some aerospace components, a martensitic microstructure may be ideal

whilst applications such as biomedical implants or other aerospace components may require increased fatigue or strain performance thus necessitating an equilibrium or coarser lamellar structure.

Mechanical properties of microstructures produced during SLM processing are dependent on the β grain size, α lamellae thickness, α lamellae size and α colony size which are greatly affected by cooling rate [112]. Due to the full melting mechanism inherent to the SLM process along with the process parameters selected to maximise density, the cooling rate during SLM processing of Ti64 has been identified from $10^3 – 10^8$ K/s. A lath-type martensite is observed throughout this range with finer acicular martensite α' morphology present for cooling rates above 10^5 K/s and hence is observed in as-built Ti64 [113]. Thus, controlling the cooling rate during solidification is the most commonly used method of microstructure control [114].

As illustrated in Figure 2.13, α' martensitic microstructure produced during SLM processing of Ti alloys is contained within elongated prior β grains which grow epitaxially through successive layer depositions [57], [70], [74], [90], [115]. These α' structures consist of closely spaced interfaces, separating neighbouring laths along with a high density of dislocations which results in a more effective barrier against dislocation movement during deformation when compared to α structures. Thus these α' structures produce components with strength and microhardness properties which are frequently greater than those observed in cast or wrought Ti64 [36], [96].

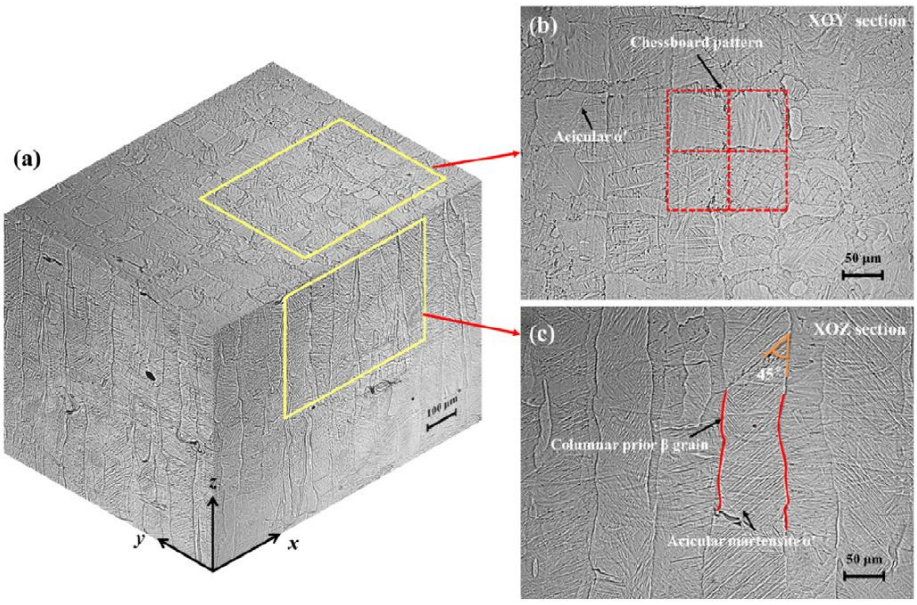

Figure 2.13: (a) Three-dimensional OM composite of as-built SLM Ti64 with magnified views of perpendicular (b) and parallel (c) to the build direction showing the α' martensitic structure. Illustrated by Yang et al. [116].

As inter-process parameters are almost exclusively designed to produce fully dense parts, post-process steps have been considered essential to decompose the α' microstructure into an (α+β) structure which facilitates greater engineering strain. Annealing and HIP processes have been heavily studied with respect to their effect on martensitic decomposition [70], [78], [91], [95], [117]. Several authors have demonstrated that the microstructural transformation that occurs as a result of annealing is comparable to that obtained by HIP treatment. Kasperovich et al. [95], Qiu et al. [91] and Leuders et al. [78] reported both processes transform the as-built α' martensite into (α+β) structures.

With regards to these treatments, three primary considerations; temperature, residence time and cooling rate have been heavily investigated. Heat treatment of Ti64 can be divided into sub-transus heating in the (α+β) field and super-transus heating in the β field as illustrated in Figure 2.14. Vrancken et al. [117] studied the effect of heat treatment on SLM processed Ti64 ELI and observed an increase in the β fraction with an increase in temperature. Following sub transus heat treatment prior β grains were easily observed, however after heat treatment above the β transus the prior β grains were no longer present indicating extensive grain growth. Similar results were obtained by Sercombe et al. [118],

Gil et al. [119], Sallica-Leva et al. [120] and Vilaro et al. [70] in their studies of SLM processed Ti alloys.

According to Sallica-Leva et al. [120] the degree of martensite decomposition will determine the balance between mechanical strength and ductility in heat treated components. Theoretically, as the martensite is decomposed into an (α+β) structure and the grain size increases as the temperature is increased, ductility should improve whilst yield strength and UTS values will decline. Experimental results published by Vrancken et al. [117] and Sallica-Leva et al. [120] concurred with this theory as they observed sharp increases in ductility values as the temperature was increased.

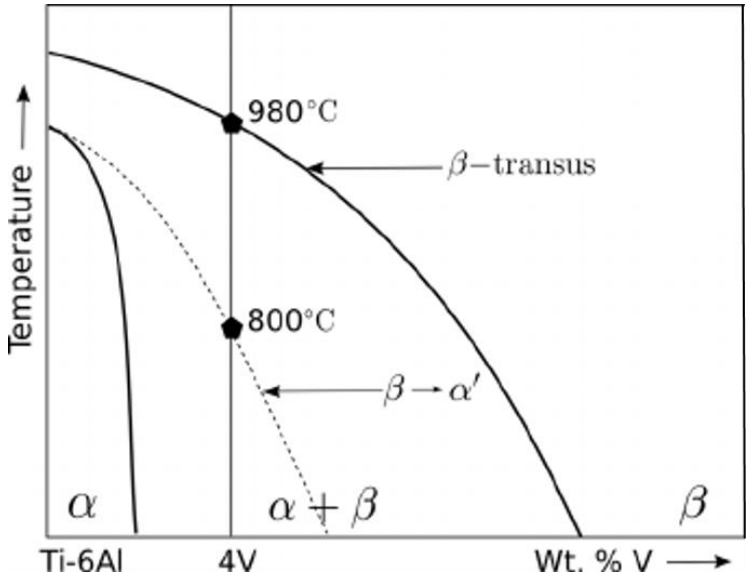

Figure 2.14: Phase diagram for Ti64 showing the sub-transus (α+β) and super-transus β fields

Residence times are intrinsically linked to the maximum temperature achieved during heat treatment. For sub-transus treatments, a limited difference in grain size and consequently mechanical properties has been observed for a wide variety of residence times [117]. In contrast, residence time has a greater influence on microstructural evolution when samples are treated above the β transus, with larger grain sizes possible which are beneficial to mechanical properties.

Also relevant to this research is the studies conducted regarding cooling rate during heat treatment cycles. For high cooling rates such as those in water quenching (≈ 1500 K/sec) both Vrancken et al. [117] and Vilaro et al. [70] observed a new form of α' martensitic microstructure following heat treatment above the β transus, as would be experienced

during SLM processing. They observed a shearing mechanism followed by nonthermal nucleation which resulted in equiaxed β grains in contrast to the columnar β grains observed at lower treatment temperatures (Figure 2.15). This corresponds to the findings of Ahmed and Rack [121] in their study of phase transformations during cooling in (α+β) Ti alloys. They observed a comparable transformation in a conventionally processed Ti64 bar whereby the β phase was transformed into an α' martensite structure after water quenching due to the high cooling rates.

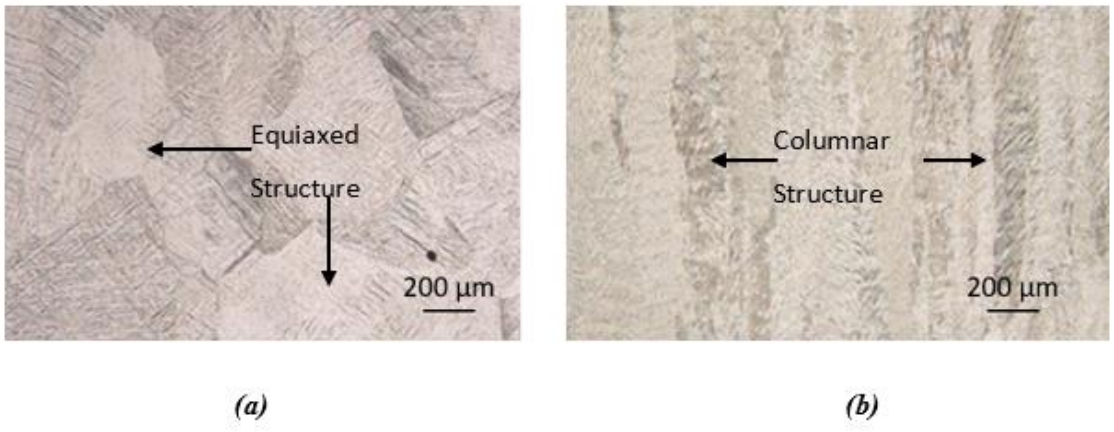

Figure 2.15: α morphology exhibited in SLM processed Ti64 after water quenching from heat treatment in the (α+β) region (a) and β region (b) respectively [70].

Regarding slower cooling techniques, furnace cooling produces a lamellar (α+β) structure following heat treatment in both the (α+β) and the β fields. In contrast, the influence of air cooling appears to be heavily dependent on the maximum temperature. Vilaro et al. [70] observed a gradual decomposition of the α' martensite into an (α+β) structure as the temperature increased in the (α+β) field. However, for annealing temperatures around the β transus, α' needles originating from the β phase are present resulting in a so called α-Widmanstätten structure. Thus, for an adequate transformation from the α' martensitic structure to an (α+β) structure, a slow cooling rate is required.

More recently, a number of researchers have been trying to achieve this slow cooling rate during the SLM process. In-situ or in-process martensite decomposition is an alternative to heat treatment which focuses on reducing the cooling rates formed during SLM processing with the aim of decomposing the α' martensitic structure and thus improving

mechanical properties in the as-built state. In-situ decomposition forms a major focus of this research and so is detailed further in sections 2.4 – 2.8 of this work.

2.3.3 Residual Stress

Residual stress can be defined as stresses that remain inside a body that is stationary and at equilibrium with its surroundings [122]. As early as 1993, residual stresses were recognised as one of the major flaws in metal AM [123]. This holds true for laser-based processes which are known to introduce large amounts of residual stress due to large thermal gradients inherently present in the process. Unmanaged, these stresses result in deformation, reduced resistance to crack formation, reduced fatigue performance and anisotropic mechanical behaviour [40], [57], [65], [104], [124].

Mercelis & Kruth [124] outlined the method by which residual stresses occur during SLM. They proposed a two-stage mechanism including; the temperature gradient mechanism and the cool down phase (Figure 2.16). The temperature gradient mechanism induces residual stress into the material by way of steep temperature gradients which are formed due to the rapid heating of the upper surface by the laser beam, followed by the relatively slow heat conduction through the material. As the expansion of the heated top layer is restricted by the underlying material, elastic compressive strains are introduced whilst simultaneously the material strength is reduced due to the temperature rise. During the cool down phase; the top layers shrink as a result of thermal contraction. This deformation is restricted by the underlying material thus tensile stresses are introduced on the outer layers and are balanced by compressive stresses below [40], [124].

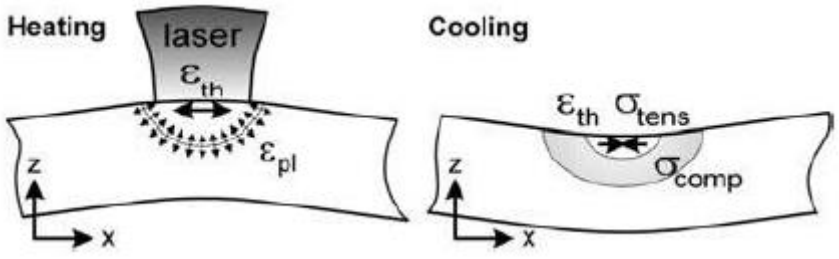

Figure 2.16: Two stage mechanism by which residual stresses occur proposed in [124]

Predicting residual stresses in as-built components has proven difficult due to highly localised temperatures and rapid temperature cycles resulting from fluctuating laser

power amongst other factors. Furthermore, similar to the microstructure, residual stress optimisation is hampered by the primary objective that is producing fully dense parts. Thus, stress relieving post processes are considered essential, especially in high cycle fatigue components, to minimise residual stresses.

With regards to inter-process parameters, variations in melt pool size and dimensions that occur due to fluctuating laser power during each scan, melt pool instabilities and dissimilar powder beds mean that correlations between many inter-process process parameters and the residual stresses produced are weak [40]. It is well understood that in SLM, the choice of scan strategy will affect the build-up of residual stresses. Many authors have reported the greatest stress is generated parallel to the scanning vector due to the high thermal gradients generated in comparison to the perpendicular direction [40], [65], [104], [125]–[128]. According to Vrancken [55], the scan vector length has the maximum influence on residual stress compared to other process variables, excluding preheating. Parry et al. [65] determined that increasing the scan area size from 1 to 3 mm^2 increases the maximum stresses generated from 189.3 to 305.2 MPa. Similar results were reported by Gibson et al. [4] who found that increasing the scan vector length leads to increased residual stress. Accordingly, limiting scan vectors will reduce the time that passes between the depositions of two successive tracks. In such circumstances, the heat has not been fully dissipated and so the second track is deposited on to warm material which leads to a reduction in thermal gradient [40].

Finally, it is universally accepted that the use of preheating during SLM reduces residual stress [64], [126], [129]–[132]. Abe et al. [133] and Aggarangasi et al. [131] suggested another laser could be used to locally pre-heat the powder. Vora et al. [134] successfully reduced residual stresses in their study of the aluminium alloy AlSi12 by preheating the powder bed. Similarly Tang et al. [134] discovered that preheating the powder thus re-heating each layer during EBM eliminated cracks in a TiAl alloy. More recently, Ali et al. [64] and Vrancken et al. [135] observed substantial decreases in residual stresses of Ti64 through the use of pre-heating of the powder bed with more detail on this presented in Section 2.5.

2.4 Hatch Distance

As outlined in section 2.3 and illustrated in Figure 2.2 the hatch distance can be defined as the distance between the centre point of two successive laser scans. Therefore, the hatch distance and spot size are intrinsically linked. Figure 2.17 shows the relationship between the spot size and hatch distance. Given a constant hatch distance, changing the laser spot size will significantly impact the percentage of the powder bed that gets re-scanned.

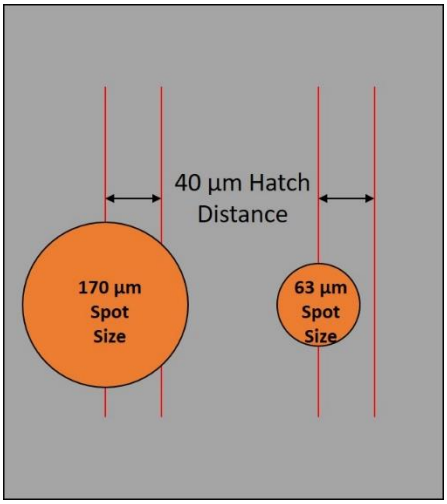

Figure 2.17: Relationship between spot size and hatch distance

2.4.1 Density

As previously mentioned, the optimisation of density is almost exclusively focused on the optimisation of the ED parameters. Of these, the hatch distance and the layer thickness receive considerably less attention in the literature than either laser power or scanning velocity. Despite this, a number of authors have examined the hatch distance in their respective optimisations of process parameters.

Han et al. [96] varied the hatch spacing from 70 – 120 µm in an optimisation of process parameters using a self-developed SLM system with a 100 µm spot size. Their results showed that density was insensitive to a change in hatch distance as they produced samples greater than 99.95% dense for all hatch distances examined. Similarly, Kasperovich et a. [85] examined hatch distances from 40 – 180 µm in their optimisation of process parameters using a SLM-250 Solution system with an unspecified spot size.

They reported an almost constant porosity of approximately 0.1% – 0.15% for all hatch distances examined. They determined that the meltpool was sufficiently large to overlap even when the largest studied hatch distance was employed whilst the remelting caused by the smaller hatch distances did not cause any increase in porosity as reported elsewhere. However, they did notice evidence of pore formation in the boundary regions of the samples processed with small hatch distances and recommended against using hatch distances below 60 μm.

Sun et al. [136] conducted a parametric optimisation of SLM parameters including studying hatch distances from 40 – 70 μm using a DiMetal-280 system with a 70 μm spot size. They observed fluctuating results for the effect of hatch spacing on density whereby the samples produced with small and large hatch distances recorded lower density levels due to over and under melting respectively. However, a statistical analysis of all parameters studied revealed hatch spacing to have an insignificant effect on density.

Despite the above studies using different SLM systems with different spot sizes as well as a wide variety of laser power and scanning velocity combinations, they all determined that density was insensitive to a fluctuation in hatch distance. This indicates that hatch distance may be an appropriate variable for mechanical property optimisation if changes in microstructure and/or residual stresses are observed for different hatch distances.

2.4.2 Microstructure

As aforementioned, the high cooling rates during processing result in the α' martensitic microstructure illustrated in Figure 2.13. This microstructure has been reported by the vast majority of studies, including those examining hatch distance. Sun et al. [136] and Han et al. [96] both observed α' martensite within prior β grains throughout the range of process parameters examined including by changing hatch distance.

Han et al. [96] observed a decrease in the α lath width and corresponding increase in microhardness as the ED value was increased which has shown a tendency to decrease the fracture strain of as-built Ti64 samples [75]. Though relevant, presenting results using the ED metric rather than as a function of either hatch spacing or laser velocity which were the parameters examined fails to answer which of these two parameters are responsible for the microstructure observed.

Barriobero-Vila et al. [137] presented a study in which they proposed using a tight hatch distance of 40 µm in combination with previously optimised laser parameters as a method of decomposing the α' martensite structure in what they described as an intrinsic heat treatment. They proposed that the longer interaction times at high temperatures would facilitate the decomposition of α' martensite into a stable (α+β) phase. Their previously determined parameters along with the tight hatch distance resulted in an ED value of 243 J/mm^3 for which Han et al. [96] reported a fine α' martensite which produced poor engineering strain values.

In contrast, Barriobero-Vila et al. [137] reported that the intrinsic heat treatment provoked the decomposition of α' martensite during SLM into a fine lamellar (α+β) structure, with the exception of an α' martensite region at the top 150 – 250 µm of the samples. They attributed the formation of β to the successive precipitation of β in each layer which is experiencing a sort of heat treatment as the number of layers above continues to increase. This intrinsic heat treatment allows the partitioning of vanadium to β and aluminium to α which causes higher stabilities of each phase upon cooling which reduced the amount of retained α'. As the build progresses the formation of α + (α'+β) microstructures that evolve through each layer successively move towards an (α+β) structure.

The evolution of the microstructure from the α' section observed at the top of the samples to the stable (α+β) structure observed lower into the sample as a result of continued heating cycles throughout the build was illustrated in the microhardness of the samples. Throughout the sample, hardness values of approximately 420 HV are observed which are comparable to values obtained in the literature for fine lamellar (α+β) structures whilst a steep increase in hardness toward 475 HV which is characteristic of a α' structure was observed in the top section of the samples. Although no mechanical properties were investigated in the study, it would be reasonable to assume that desirable yield strength and strain values would be obtained as literature with similar microstructures has demonstrated values of 1100 MPa and 11.4% respectively.

2.4.3 Residual Stress

The effect of hatch distance on residual stress is largely unknown and unreported in the literature. As discussed in Section 2.3.3, a study conducted by Pohl et al. [125] concluded

that increasing the hatch distance from 100 to 300 µm reduced the deflection caused by residual stresses by more than half. They attributed this to an increased thermal gradient caused by more localised heating when a smaller hatch distance is used. However, they failed to account for the number of tracks deposited or the density of the material whilst the values tested are significantly larger than most hatch distances utilised when density is optimised. Hence, the effect of hatch distance on residual stresses in fully dense parts remains unknown.

2.5 Powder Bed Temperature

The concept of pre-heating the base plate is well established in the SLM field. It is industry practice to pre-heat the base plate to between 150 and 200 °C in order to reduce the residual stresses built up within the first few layers and thus reduce the probability of uplift from the base plate.

Vrancken et al. [135] provides perhaps the first example of high temperature pre-heating of the base plate during SLM of Ti64. They examined the effect of pre-heating temperatures ranging from no pre-heating to 400 °C upon density, microstructure, residual stresses and mechanical properties. Their density optimisation program included three laser powers and three scanning velocities as illustrated in Figure 2.18 whilst the layer thickness and hatch distance remained constant at 30 and 70 µm respectively. Their results illustrated that densities above 99% were not possible at the lowest laser power of 50 W or indeed for any laser power that used a lower scanning velocity of 400 mm/sec which they attributed to under and over melting respectively.

With regards to the change in pre-heating temperature, no statistical difference was observed between samples produced at different pre-heating temperatures. However, in theory, pre-heating the base plate should reduce the energy required for producing fully dense parts. This could potentially increase the density of samples produced with lower laser powers whilst those parameter sets already producing high density parts may now form instable meltpools and observe a reduction in density as has been observed in other alloys. Analysis of the residual stresses yielded an expected result whereby the principal stress reduced as the pre-heating temperature increased with a principal stress of 628 MPa reported for no pre-heating in contrast to 313 MPa reported for prehearing of 400 °C.

As the pre-heating temperature increased from no heating to 400 °C a change in the microstructure from an α' martensitic to a lamellar (α+β) microstructure was observed. Given this change in structure a softer material would be expected. However, microhardness tests revealed the opposite effect whereby the hardness of the material increased with increases in pre-heating temperature. Further analysis of the oxygen content in the parts revealed that the increased temperature of the meltpool for higher pre-heating temperatures resulted in an increase in oxygen pickup in the parts, despite the argon atmosphere, and subsequently increased the hardness of the parts produced. Furthermore, this increase in oxygen content resulted in inferior mechanical properties whereby engineering strain reduced from 6.9% when no pre-heating was used to 3.9% for a pre-heating temperature of 400 °C.

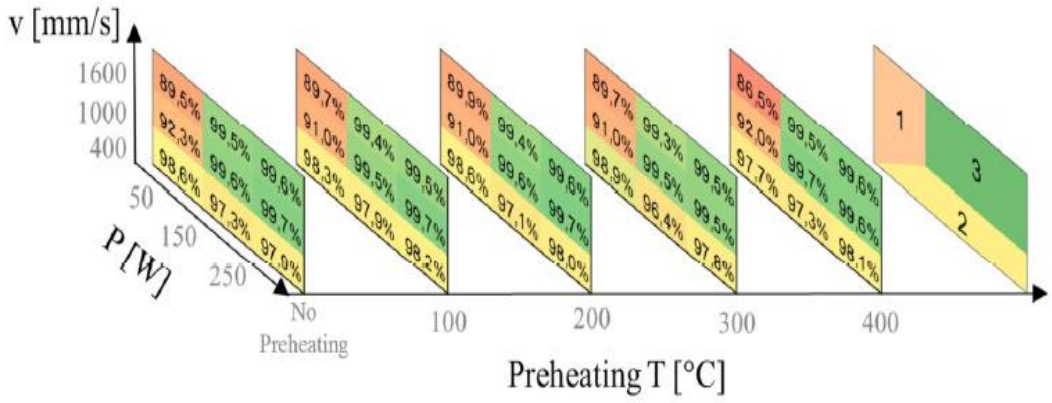

Figure 2.18: Density optimisation program implemented by Vrancken et al. [135] for five powder bed temperatures

One other comprehensive study regarding high temperature pre-heating during SLM processing of Ti64 was conducted by Ali et al. [64]. In their study they examined six pre-heating temperatures ranging from 100 – 770 °C. During density optimisation, they too observed significant defects at either end of the energy spectrum from too much and too little energy inputted into the process. However, in contrast to Vrancken et al. [135], the density optimisation was conducted at one pre-heating temperature and the results were applied for all parts built thereafter.

From examining the microstructures of the highest (770 °C) and lowest (100 °C) temperatures used in the study, they established that prior β grains were present

throughout the entire temperature range. However, within the prior β grains, the initial martensitic microstructure began to decompose as temperature was increased. Although the martensitic decomposition temperature is considered to be above 600 °C for Ti64, complete martensite decomposition was observed at a powder bed temperature of 570 °C whilst the α needle size and β volume continued to increase for temperatures above this [119]. Moreover, from powder bed temperatures of 670 °C α globularisation initiated leading to increased α colony size which according to Lütjering et al. [138] has the largest effect on mechanical properties for Ti64.

With regards to residual stress, as the pre-heating temperature was increased from 100 °C up to 570 °C the average maximum principal stress measured reduced from 214 to 1 MPa. The dramatic reduction in stress can be attributed to the reduction of the thermal gradient as a result of the higher powder bed temperature. Similar results have been observed elsewhere in the literature including by [64], [126], [129]–[132] and it is now universally accepted that the use of pre-heating during SLM reduces the residual stresses.

Examining the mechanical properties for varying powder bed temperatures, they observed high yield and UTS values, characteristic of SLM processed Ti64. These values remained relatively consistent for powder bed temperatures from 100 – 670 °C (Figure 2.19). Above this, no yield strength or ductility measurements were possible due to premature failure which was ascribed to the larger grain sizes generated for higher powder bed temperatures. Regarding fracture strain, a 66.2% increase was observed for a powder bed temperature increase from 100 – 570 °C. However, as temperature was increased to 670 °C a significant decline was observed (Figure 2.19). The cause of the decrease can be extended from an explanation given by Qian et al. [139] in their study regarding DLF processing of Ti64. They determined that α needles grow more rapidly as temperatures approach the β transus. Indeed, as temperatures increased above 570 °C the α needles increased in size whilst some globular α was also observed. The presence of these microstructural features indicate that the slip length had increased which results in lower yield strength and engineering strain as was observed during testing.

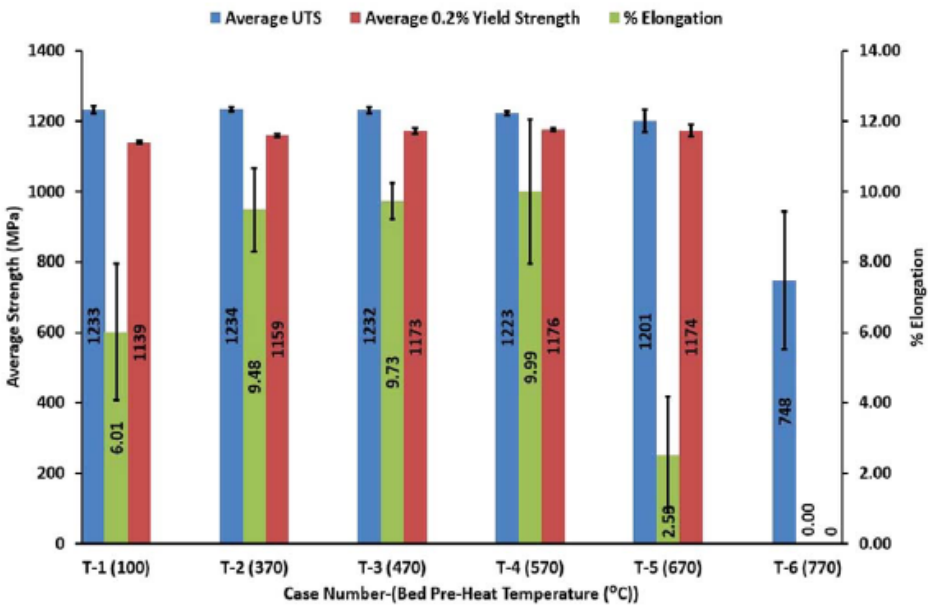

Figure 2.19: Mechanical properties observed as a function of varying powder bed temperature as observed by Ali et al. [64]

2.6 Laser Spot Size

The laser spot size can be characterised by a number of different methods with the most commonly used being full width half-maximum (FWHM), D4σ and $1/e^2$. Figure 2.20 illustrates the different methods of calculating the spot size with arbitrary horizontal and intensity values used. The full width half-maximum is defined as the distance between the two points closest to the gaussian curve that have 50% of the maximum intensity. The $1/e^2$ value emanates from a simplification describing a Gaussian beam's radial distribution. Given Euler's constant can be approximated as 2.71828, the $1/e^2$ value is measured at 13.5% of the maximum intensity of the beam (Figure 2.20). As outlined, both of these methods are calculated as a function of the lasers intensity yet do not consider the overall beam profile. The D4σ method does exactly that and is commonly used due to the recommendation by ISO 11146-1 [140]. The D4σ method can be calculated as four times the standard deviation of the distribution of intensity along both the major and minor axis of the beam thus for a perfect gaussian beam the D4σ and $1/e^2$ are equal [141].

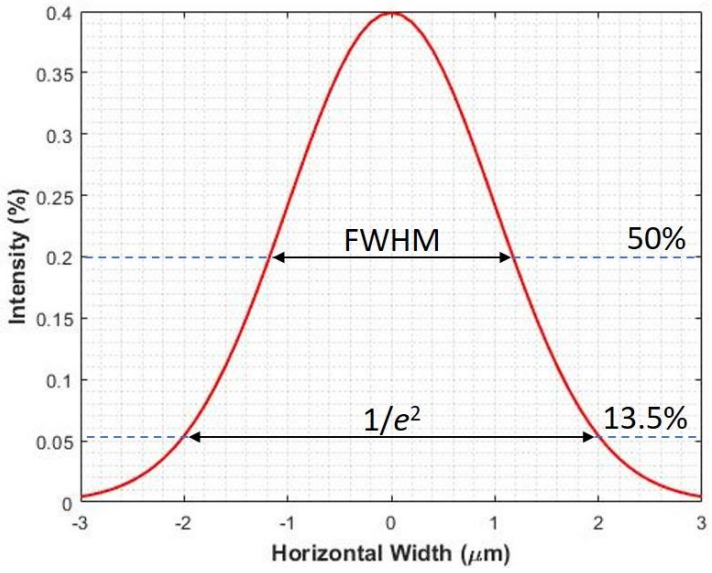

Figure 2.20: Illustration of different spot size measurement methods with arbitrary horizontal width and intensity values

As outlined in section 2.3 SLM processing is most commonly optimised using the ED parameters with a focus on density. Changing these ED variables in essence changes the energy input into the powder bed yet the beam diameter is frequently disregarded. However, the selection of laser spot size determines the area over which the laser is irradiated. Thus, given a constant power input, an increase in the laser spot size will result in a reduction in the energy input into the powder bed. As a result a number of studies have adapted the ED equation to include the spot size as indicated in Equation 2.2 [142], [143].

$$EV = \frac{P}{(v \cdot d \cdot t)} \qquad \text{Equation 2.2}$$

Where; EV is the energy density, P is the laser power, v is the scanning velocity, d is the laser diameter or spot size and t is the layer thickness.

Studies have determined a critical input energy (EC) value for each material to generate a continuous scan path where the melted material bonds well with the previous layer. When the EV value is below that of the EC, the energy input into the process is insufficient to completely melt all the powder thus generating voids within the solidified

part. In contrast, if the EV values exceeds that of the EC, then a very deep meltpool is generated and the keyhole melting mode is observed which results in over melting pores [144], [145]. Furthermore, excessive energy input can also result in a stochastic splashing process where semi-molten powder particles are ejected from the meltpool causing issues with dimensional precision [146]. Therefore, with regards to density the appropriate laser spot size should provide sufficient energy to melt the current powder layer such that it fuses with the previous layer without providing too much energy such that keyhole melting is prevented.

With regards to Ti64, very few publications have examined the influence of the beam diameter directly. Shi et al. [147] examined the effect of beam diameter in thick layer, high powered SLM processing of Ti64. Figure 2.21 shows a figure presented in their study which outlines the effect of changing the beam diameter given all other process parameters remain constant. Figure 2.21 (a) and (c) show the impact they observed when using a smaller spot size whereby an increase in the meltpool depth was observed which resulted in keyhole melting occurring which results in pore formation in the base of the meltpool. In contrast, the larger spot size shown in Figure 2.21 (b) and (d) results in a more homogenous meltpool and heat effected zone which enabled full melting of the powder without an excessive energy input.

The effect of spot size variation on the microstructure of as-built Ti64 remains relatively unexplored. Shi et al. [147] observed a Widmanstätten structure for samples produced using a 200 µm spot size. However, they failed to compare this to the structures formed during processing with a 50 µm spot size which they also used in the study. Furthermore, the layer thickness of 200 µm employed in their study is markedly greater than conventional layer thickness values and will have an effect on the cooling rate during processing.

Laser spot size has also been studied in the guise of the focal offset distance (Figure 2.22). Though expressed differently, the focal offset distance is intrinsically linked to the laser spot size as the diameter of the beam varies along the propagation path of the beam. Xu et al. [74] examined the effect of the focal offset distance during SLM Ti64 concluding that that a complete transformation from a fully acicular α’ martensite to an ultrafine lamellar structure is possible with a reduction in FOD from 4 to 0 mm. However, they

noted that optimisation of a single processing variable i.e. FOD is insufficient for martensite decomposition but rather the proper combination of parameters is required.

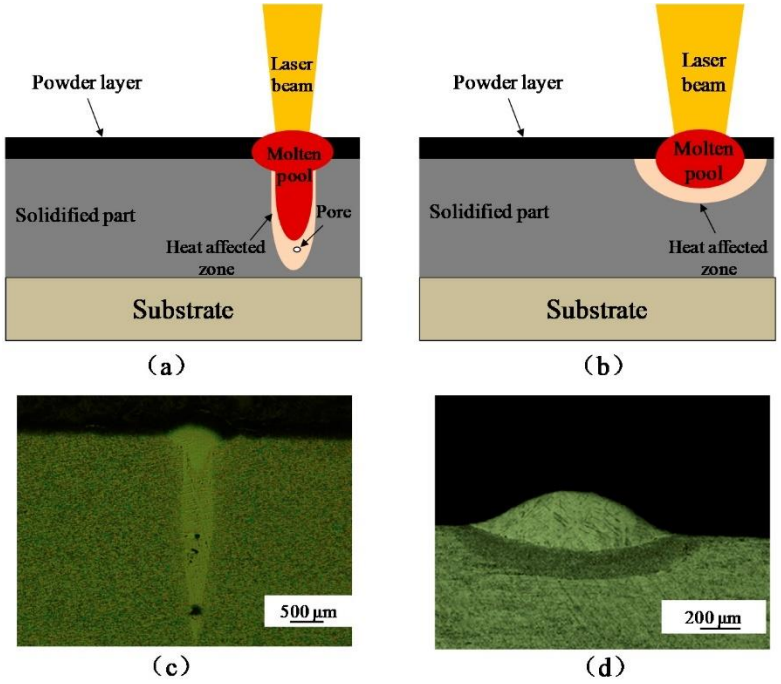

Figure 2.21: Schematic illustration of the effect of changing the laser spot size presented by Shi et al. [147]

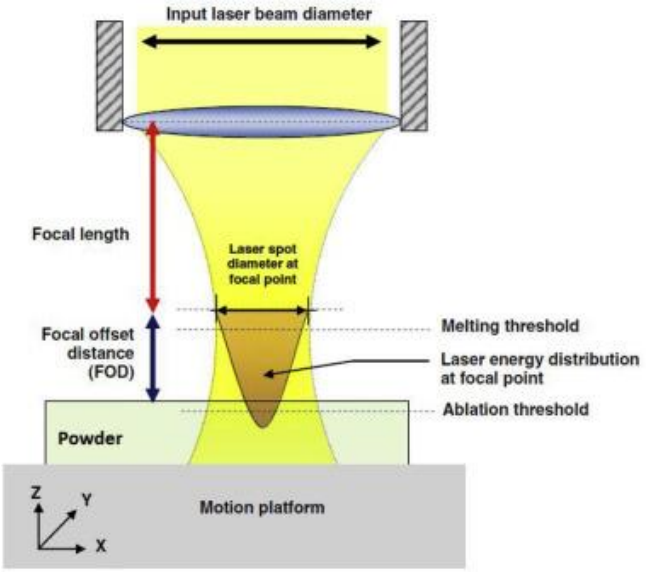

Figure 2.22: Illustration of the focal offset distance as presented by Chow et al. [148]

2.7 Layer Thickness

As discussed in section 2.3 the impact of changing layer thickness remains relatively unexplored despite its inclusion in the ED and EV variables. Section 2.3 highlighted how the influence of layer thickness on density will depend on the energy input. However, given a constant energy input, Qiu et al. [82] observed an increase in porosity as the layer thickness was increased. Xu et al. [74] provide one of the earliest examinations of the impact of layer thickness on the microstructure of as-built SLM processed Ti64. They observed in-situ martensite decomposition for samples processed with a higher layer thickness when combined with an appropriate ED input.

Further studies by the same research group led to mixed findings where one study [75] determined that increasing layer thickness was beneficial to α' decomposition whilst another [149] found no α' decomposition in varying layer thicknesses. Kumar et al. [150] reported similar results whereby a departure from the characteristic prior-β microstructure was observed given an appropriate combination of scan strategy and layer thickness. Yet they neglected to individually examine the effect of layer thickness on the as-built microstructure.

Due to the lack of information in the literature and somewhat conflicting results in studies that have been completed, the effect of layer thickness on as-built microstructures of SLM processed Ti64 remains unknown. Furthermore, none of the aforementioned studies have given detailed examinations of both density and microstructure as a function of layer thickness but instead have focused on one or the other.

2.8 Summary

The three fundamental elements which need to be addressed in order to obtain optimal mechanical properties in SLM processed Ti64 are the density, microstructure and residual stresses. Since the inception of the SLM process, the majority of research has focused on optimising process parameters with the aim of producing fully dense parts. This has led to a dependence on post processes such as annealing and HIP treatments to deal with the undesirable microstructure and residual stresses produced as a result of the large thermal gradients and cooling rates. Through the use of post processing methods in combination

with fully dense parts it has been established that an (α+β) microstructure with minimal residual stresses is required to optimise mechanical properties.

More recently, several authors have examined a number of techniques including focal offset distance (spot size), layer thickness, hatch distance and powder bed pre-heating in an effort to address these fundamental elements and thus remove the need for post processing. Whilst many of these techniques have been successful in achieving their stated goal whether that be α' martensite decomposition or residual stress reduction, few have considered the effect of their efforts in combination with density. To that end, Ali [151] was successful in decomposing the α' microstructure and reducing residual stresses yet failed to consider if density was affected throughout the range of powder bed temperatures utilised. Vrancken et al. [135] provide perhaps the only example where all three of the fundamental elements are considered together. Whilst they were successful in achieving the desired microstructure, density and residual stresses they observed a dramatic increase in oxygen pickup which led to inferior mechanical properties. It is possible that this may have resulted from conducting their tests in a self-developed system which may have an inferior level of oxygen control in the chamber though that cannot be validated and thus it may also be a bigger issue with high temperature heating of Ti64.

Furthermore, though independently these new techniques for optimisation of as-built components have provided reason for optimism, no study in the literature has attempted to examine these techniques together. For example, analysing the influence of hatch distance at elevated powder bed temperatures. This is the void that this research aims to fill. In the following chapters, hatch distance, layer thickness, pre-heating temperature and laser spot size are analysed simultaneously and their impact on the density, microstructure and mechanical properties of as-built SLM processed Ti64 assessed.

Chapter 3 Experimental Methodology

3.1 Introduction

This chapter aims to give the reader an insight into the procedures used throughout the experiments completed in this thesis. The Ti powder, SLM system, mechanical testing processes as well as density and microstructure characterisation techniques have all been outlined. Where possible internationally recognised standards have been employed.

3.2 SLM System

The SLM system used in this work was exclusively the Realizer SLM50 machine shown in Figure 3.1. The machine uses a 100 W Ytterbium fibre laser which is focused using an F-Theta lens and galvanometer scanning mirrors. The processing chamber operates in a positive pressure inert argon environment with oxygen levels controlled to below 0.2% required to help prevent oxidation of Ti during processing.

Figure 3.1: Realizer SLM50 selective laser melting machine

3.3 Ti64 Powder

Argon gas atomised spherical powder particles of extra low interstitial (ELI) Ti64 grade 23 with chemical composition shown in Table 3.1 conforming to ASTM B348-09 [152] was used for experimental testing. The powder had a nominal particle size between 24.5 µm (D10) and 55 µm (D90), with a Gaussian distribution centred on 36.8 µm (D50) as measured by laser diffraction using a Malvern Instruments Mastersizer 2000.

Table 3.1: Chemical composition of Ti64 ELI powder used during this research

Element	N	C	H	Fe	O	Al	V	Ti
Mass Fraction (%)	0.02	0.01	0.003	0.17	0.08	6.4	3.9	Bal

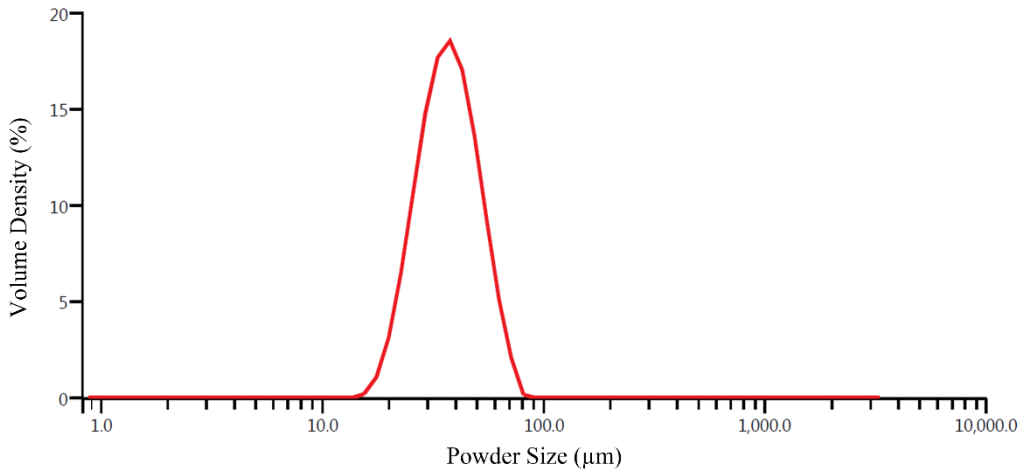

Figure 3.2: Distribution of Ti64 powder measured by laser diffraction

3.4 Image Segmentation and Analysis

Image analysis has been used for a number of characterisation processes namely, density analysis and grain size quantification. Images were taken on optical and scanning electron microscopes with details outlined in section 3.5.2. The images were then processed using Fiji, an open-source image processing package based on ImageJ [153]. Specifically, the Trainable Weka Segmentation plugin was used to segment pores and grains for analysis [154]. Figure 3.3 shows the flowchart used for segmentation of an image, in this case to analyse porosity of a sample. Firstly, the raw image or image stack is loaded into ImageJ and the scale is set. Then the Trainable Weka Segmentation plugin is opened, and the model is trained.

Training takes place by manually defining known regions, such as pores and bulk material. Once these definitions are made, the algorithm classifies the image by combining the manual definitions and the selected classification features. Given that grain

and pore boundaries were the primary usage in this research, edge-detection filters including the Sobel filter, Hessian matrix eigenvalues and the difference of Gaussians were employed [154]. Furthermore, textural features were used to calculate the summary statistics of pixels within a given radius of targeted pixels whilst noise reduction filters including Gaussian blurs reduced imaging artefacts. The classifier is a multi-threaded version of a random forest which is an ensemble learning method for classification that operates by constructing a multitude of decision trees during training with the output determined as the class selected by the most trees [155]. After each iteration of training the classified image was compared to the raw image and the model was retrained.

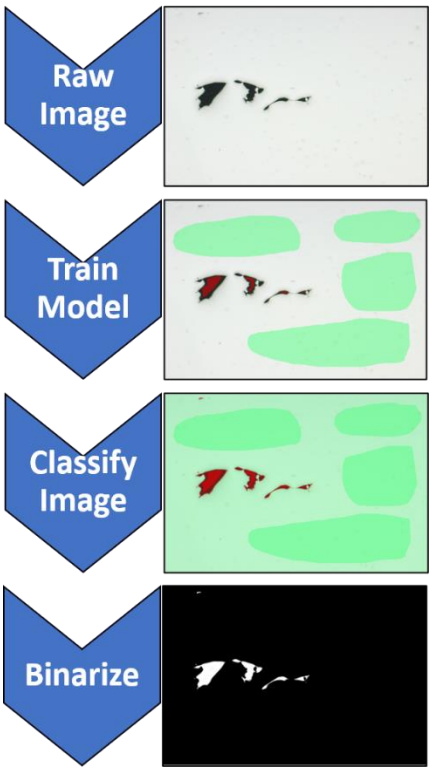

Figure 3.3: Flow chart for image segmentation and analysis

3.5 Microstructure Characterisation

3.5.1 Sample preparation

Samples were removed from the build plate and sectioned for examination using a wire electrical discharge machine. Following which, samples were hot mounted in conductive resin. Grinding consisted of two stages. Firstly, successively finer silicon carbide grinding

paper starting at P320 up to P4000 was used to obtain a planar surface. Following which 6 µm diamond suspension was used to prepare the surface of the sample for polishing. Polishing was conducted using a mixture of 90 ml fumed silica and 10 ml hydrogen peroxide to achieve a mirror finish. In the case where samples were etched, Kroll's reagent with 6% nitric acid and 1% hydrofluoric acid was applied to the surface until the microstructure was revealed.

3.5.2 Microscopy

Following polishing and again after etching, samples were imaged using a Zeiss Axio Vert A.1 optical microscope (OM) for porosity and microstructural analysis respectively. For more detailed imaging of the microstructure, a Zeiss ULTRA plus scanning electron microscope (SEM) was used with a voltage of 5 kV utilising the SE2 detector.

3.5.3 X-Ray Diffraction

Further microstructure evolution analysis was carried out by means of x-ray diffraction (XRD). Measurements were obtained using a Bruker D8 Advance with a step size of 0.2° and a dwell time of 2 seconds with a 2θ range of 33 – 90° as illustrated in Figure 3.4. Raw data was read into MATLAB where it was plotted for crystal plane identification.

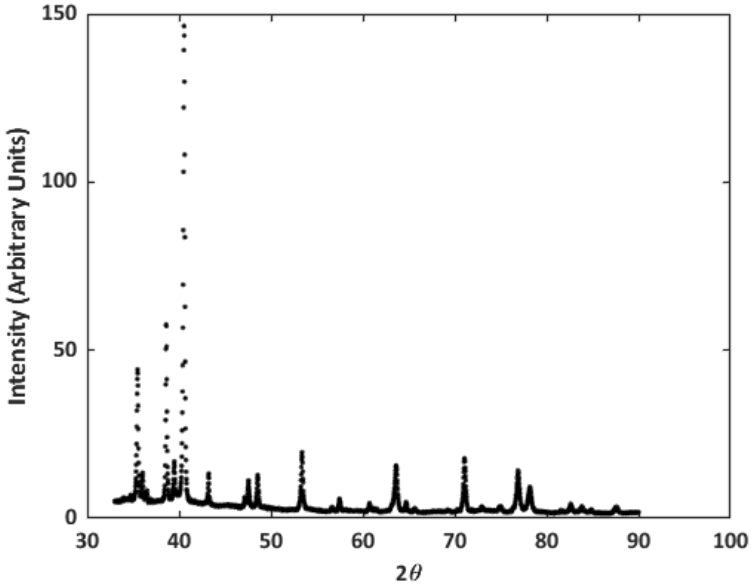

Figure 3.4: Raw XRD data obtained using the Bruker D8 Advance system and plotted with MATLAB

Following plane identification; specific peaks were selected for analysis using the curve fitting toolbox within the MATLAB software [156]. Peaks were selected according to their 2θ position and were fitted using gaussian models in the curve fitting toolbox. Each peak was fitted with eight different gaussian models according to the number of terms in the model. Each fit was plotted to allow the best fit to be chosen as shown in Figure 3.5. Once the best fit was chosen the maximum intensity of the peak and subsequently the peak width at the half maximum position (FWHM) could be obtained from the fitted data.

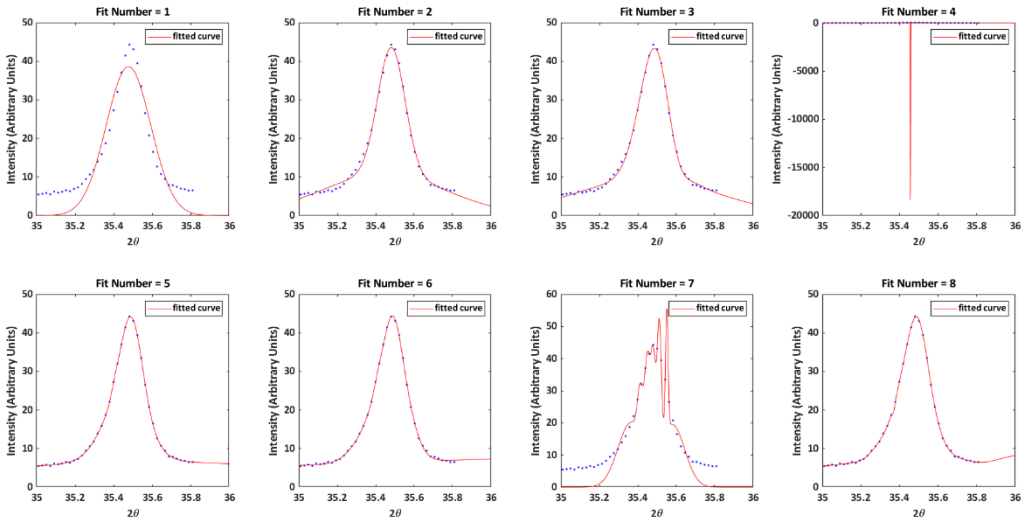

Figure 3.5: Gaussian fits applied to specific peak for FWHM analysis

The value obtained for the FWHM of the peak was then corrected for instrument broadening using Equation 3.1 where the instrument broadening was calculated using Equation 3.2. This was derived by scanning a corundum standard reference material 1976b sample and measuring the resultant FWHM of the peaks obtained.

$$FWHM_{peak} = FWHM_{measured} - FWHM_{instrument} \quad \text{Equation 3.1}$$

$$FWHM_{instrument} = (((2\theta * 0.0005) + 0.0321)/(720)) * 2\pi \quad \text{Equation 3.2}$$

Where the 2θ position of the peak is given in radians.

Once the true FWHM of the peak is calculated, the Williamson-Hall (W-H) method was used to determine the lattice strain and crystallite size [157]. The W-H method is a

simplified integral breadth method where size-induced and strain-induced broadening are deconvoluted by considering the peak width as a function of 2θ. The W-H method assumes that the size and strain broadening are additive components of the total integral breath of a Bragg peak. Using the fact that strain-induced broadening arising from crystal imperfections can be related by Equation 3.3 and the Scherrer equation (Equation 3.4), which relates the crystallite size to the diffraction peak, the W-H method can be expressed in Equation 3.5 and Equation 3.6.

$$\varepsilon \approx {\beta_s}/{tan\theta} \qquad \text{Equation 3.3}$$

Where; β_s is the portion of the FWHM broadening attributable to strain and θ is the peak position

$$D = {k\lambda}/{\beta_D cos\theta} \qquad \text{Equation 3.4}$$

Where; D is the particle size in nanometres, λ is the wavelength of the x-ray source (1.54056 Å for CuK_α radiation), k is a constant equal to 0.94, β_D is the portion of the FWHM broadening attributable to size and θ is the peak position

$$\beta_{hkl} = \beta_S + \beta_D \qquad \text{Equation 3.5}$$

Rearranging gives;

$$\beta_{hkl}\cos\theta = \left(\frac{k\lambda}{D}\right) + 4\varepsilon sin\theta \qquad \text{Equation 3.6}$$

In order to deduce the lattice strain and crystallite size from a sample, the Williamson-Hall plot is produced where the term βcosθ is plotted with respect to 4sinθ for the preferred orientation of peaks as illustrated in Figure 3.6. Accordingly, the slope and y-intersect of the fitted line represent the lattice strain and crystallite size respectively.

Lattice parameters a and c for the HCP α phase as shown in Figure 3.8 were investigated using a Reitveld refinement completed in the MAUD software developed by Lutterotti

[158]. The initial phase information for use in Reitveld refinement was obtained from the Inorganic Crystal Structure Database [159]. During the Reitveld refinement the RWP value – a measure of the goodness of fit of the refinement to the data set – was minimised. A RWP value of 15% and below was accepted as an appropriate fit. Though values of RWP as low as 5% have been accepted in the literature, the resin used to mount the sample rendered this impossible during this study [160]. Figure 3.8 shows the Reitveld refinement for a Ti64 sample as well as that same sample plotted with a scan of just the resin that was used to mount the samples. The image shows that the peak that can be observed at approximately 39.5° 2θ can be attributed to the resin rather than the Ti64 material. Thus, this peak is not accounted for in the database of the α and β phases used in MAUD for Reitveld refinement and thus increases the RWP value as the refinement cannot be fit to the peak [158].

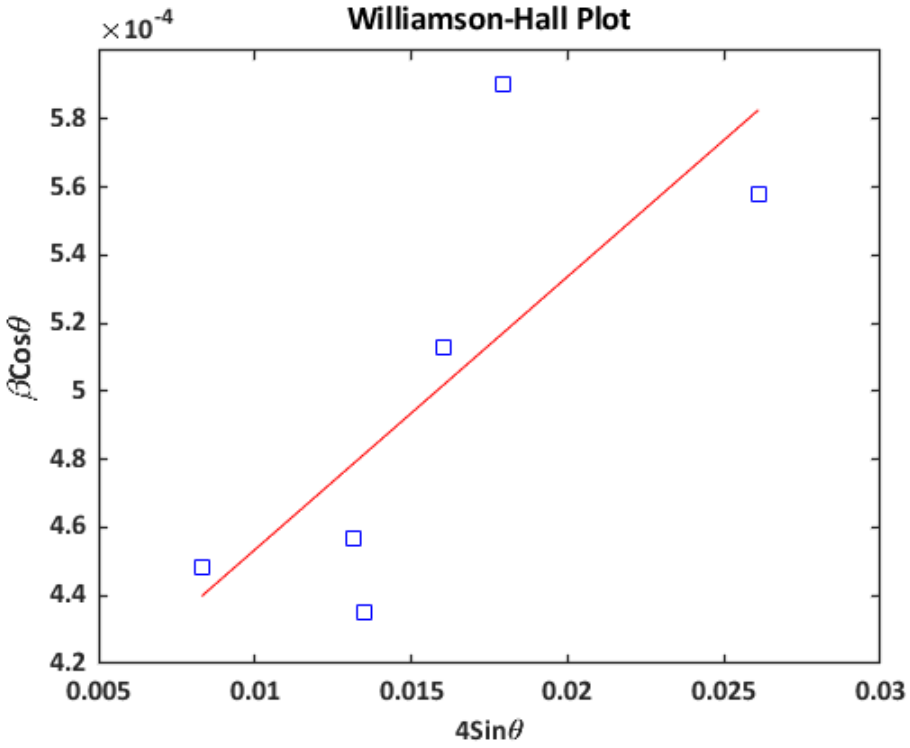

Figure 3.6: Williamson-Hall plot enabling calculation of lattice strain and crystallite size

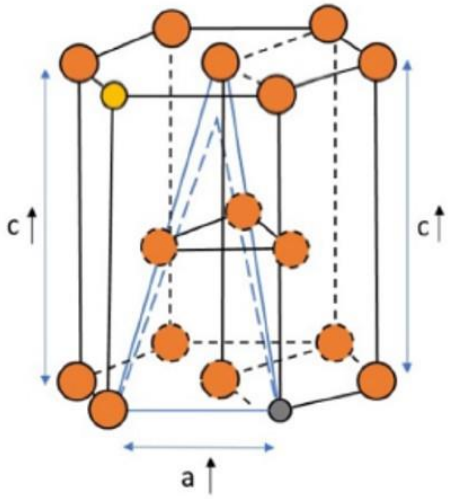

Figure 3.7: HCP unit cell for the α phase as illustrated by [161]

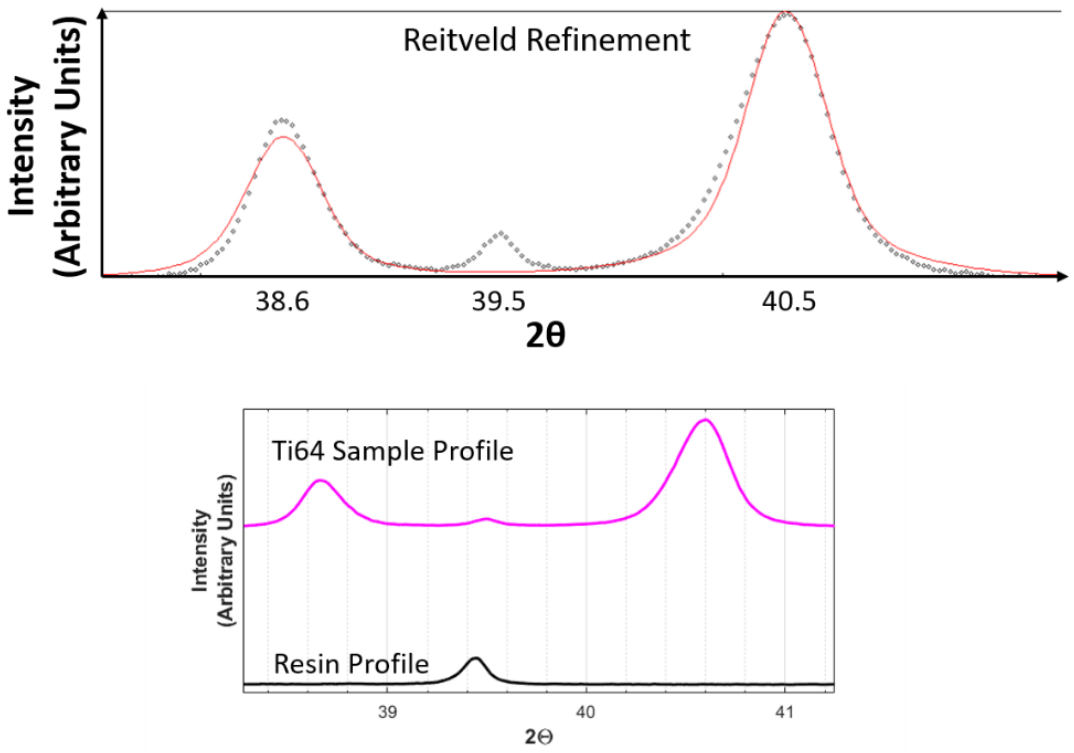

Figure 3.8: Reitveld refinement of Ti64 sample (top) and the same sample plotted with a scan of just the resin used to mount the samples (bottom)

3.5.4 Grain Size Analysis

SEM images of the microstructure were used for quantitative analysis of the primary α laths. The SEM images were first segmented as outlined in section 3.4. Using the Analyse Particles command within Fiji/ImageJ, an elliptical shape was fit to each grain from which the size of the major and minor axis of the grain was determined (Figure 3.9).

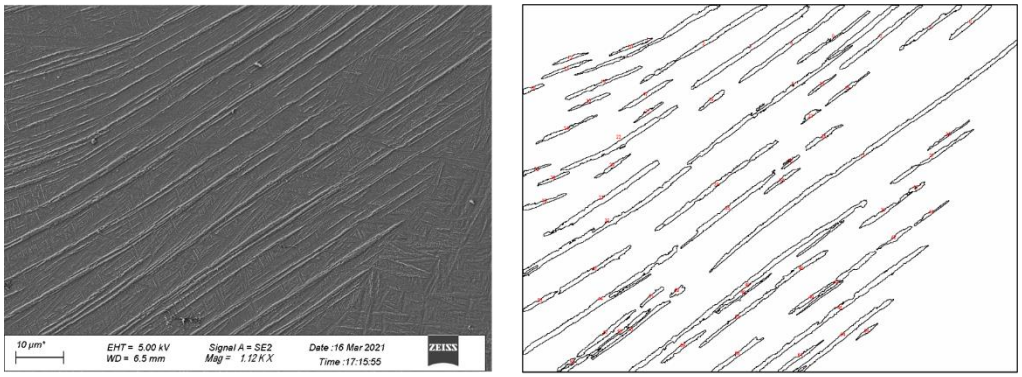

Figure 3.9: (a) SEM image of Ti64 microstructure showing needles and (b) outlines of fitted shapes for quantitative analysis following image segmentation

3.6 Density Characterisation

3.6.1 Archimedes Principle

After removal from the build plate, samples were assessed for density using the Archimedes principle according to ASTM B962 [162]. Initially samples are weighed in air and then again when immersed in water with their mass recorded for each. The density of the sample is then calculated using Equation 3.7 and compared to the theoretical density of Ti64 (4.44 g/cm^3 [163]) to give the sample as a percentage.

$$\rho_{sample} = \frac{m_{air}}{\left(\frac{m_{air} - m_{water}}{\rho_{water}}\right)} \qquad \text{Equation 3.7}$$

Where; m_{air} is the mass of the sample in air, m_{water} is the mass of the sample in water ρ_{sample} is the density of the sample and ρ_{water} is the density of the water.

3.6.2 Optical Microscopy

Another method of measuring the density of samples is through optical microscopy. As stated in section 3.5.2 samples were imaged directly after polishing but prior to etching. The imaged samples were then segmented according to the procedures outlined in section 3.4. Once the image is in binary format the Analyze Particles command within Fiji/ImageJ was used to calculate the percentage of the pixels classified as pores and compared to the total number of pixels as shown in Figure 3.10.

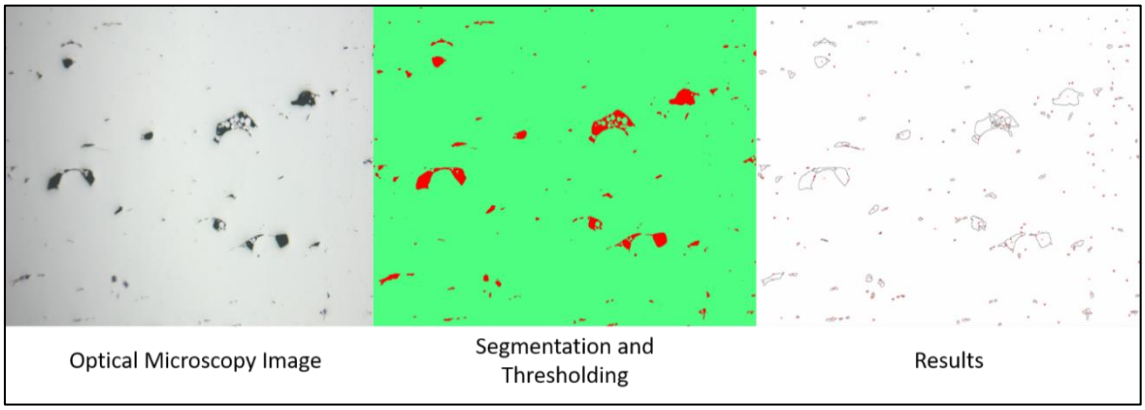

Figure 3.10: Process showing OM determination of part density using Fiji/Image J

3.7 Mechanical Testing

3.7.1 Microhardness

Vickers hardness measurements were performed using a Mitutoyo MVK-H1 hardness testing machine following the method outlined in ASTM E384-17 [158]. In each case 9 samples were taken randomly across the sample with a load of 500g and a loading of 15 sec.

3.7.2 Tensile Testing

Tensile samples were printed according to ASTM E8/E8M figure 8 sample 4 with dimensions shown in Appendix B [164]. Tensile testing was carried out on an Instron 8801 ServoHydraulic testing system with an Epsilon axial extensometer attached to the gauge section of the samples as shown in Figure 3.11. The tests were conducted in strain control with two ramp rates. Initially the ramp rate is set at 2.4 %/min until the strain

reached 6.3% at which point the ramp rate increases to 3.2 %/min until failure. A MATLAB code was developed to calculate the stress values from the applied force and the cross-sectional area of the specimen whilst the strain was read directly from the extensometer. Finally, yield strength and strain were determined using the 0.2% offset method.

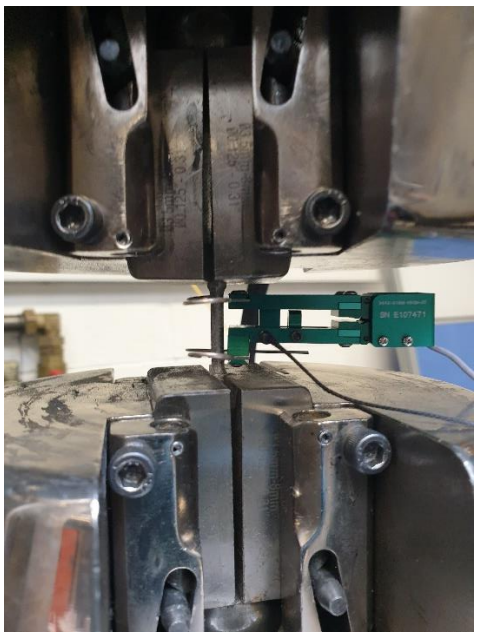

Figure 3.11: Tensile testing using the Instron 8801 and axial extensometer

Chapter 4 Density Optimisation

4.1 Introduction

As identified in literature, the production of fully dense parts is the most fundamental requirement in SLM processing of Ti64. This chapter addresses the first primary goal of this work by examining the feasibility of producing fully dense parts with the Realizer SLM50. Firstly the overall part density and the influence of the position of the part on the build plate is investigated as a function of the gas flow. Then a statistical examination of the laser power, scanning velocity, hatch distance and layer thickness is conducted. The chapter is concluded by examining the effects of density on the mechanical properties.

4.2 Gas Flow Characterisation

As outlined in Chapter 2 the vast majority of literature regarding process characterisation and optimisation of SLM processed Ti64 focuses on the parameters which dictate the energy input into the process, namely, those which constitute the ED variable. Whilst this is justified, before optimising these variables for the Realizer SLM50 it is also prudent to look at the environment in which the processing takes place and specifically the gas flow within the SLM chamber, which remains relatively sparsely studied within the literature.

As highlighted in Chapter 2, the gas flow during SLM serves two functions; primarily it is used to create an inert atmosphere such that no chemical reactions such as oxidation can occur. Secondly, the gas flow is used to remove process by-products from the laser path. These by-products may include condensate, spatter or ejected powder (Figure 4.1). All of which are capable of shifting the focal point through scattering or even absorbing incident laser energy when present in the laser path [1].

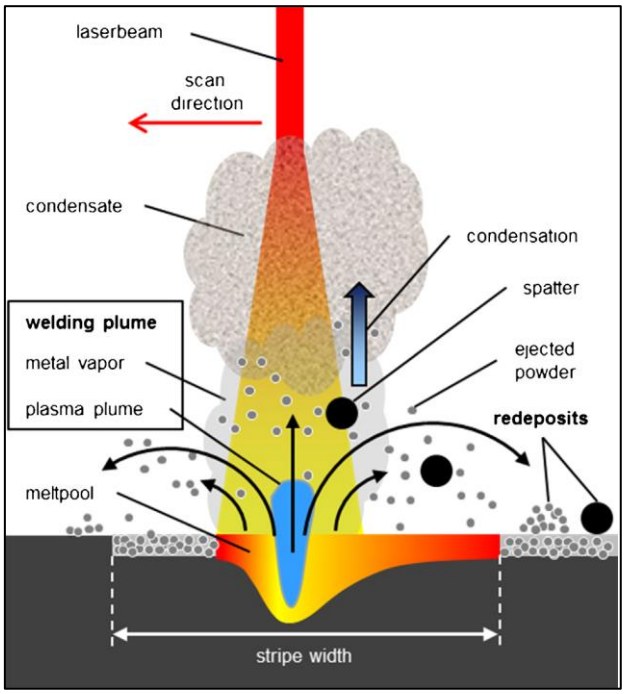

Figure 4.1: Schematic representation of by-products observed during SLM processing [105]

The gas flow circuit of the Realizer SLM50 is shown in Figure 4.2. The system pumps argon through 4 inlet nozzles into the process chamber, across the build plate and out through 2 outlet nozzles before it is filtered and re-circulated. As it is controlled by the

differential pressure between the inlet and outlet flow of argon from the process chamber, the flow rate is independent of the filter saturation level. Typical pump power values range between 1.5 and 3 volts for a volumetric flow rate of 60 L/min depending on the filter saturation level.

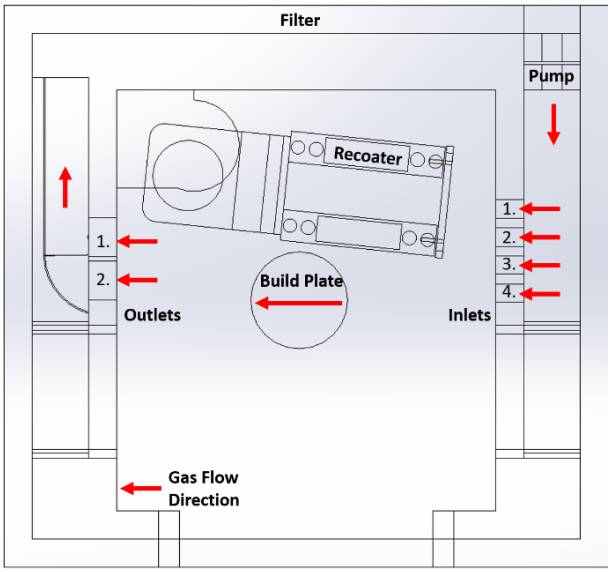

Figure 4.2: Gas flow circuit within the Realizer SLM50

4.2.1 Method

Two elements of gas flow in the Realizer SLM50 have been examined. The flow rate of argon gas into the chamber and the nozzle design were studied with the effect on part density set as the output goal as illustrated in Figure 4.3. This effect has been characterised in two ways, firstly as a function of the flow rate and secondly as a function of position on the build plate. For each input variable two levels are chosen. With regards to the flow rate 60 and 100 L/min are examined whilst the two nozzle designs are the default nozzle configuration within the Realizer SLM50 and a nozzle printed by fused deposition modelling (FDM) which had internal baffles to redirect the initial flow as illustrated in Figure 4.4. The FDM nozzle was examined due to concerns arising from the placement of the inlet nozzles of the default configuration whereby a number of the inlet nozzles appear to aim the gas flow directly into the recoater as shown in Figure 4.2.

Figure 4.3: Flow chart of gas flow experimental design

Figure 4.4: (a) Realizer nozzle configuration utilising four input holes on the right-hand side of the chamber and (b) the FDM printed nozzle inside the Realizer chamber

Figure 4.5 shows the build layouts used for both nozzle configurations whereby the two levels of flow rate were evaluated for each configuration. Firstly, single scan vectors were analysed across the build plate such that the meltpool width could be evaluated. Literature suggests a direct correlation exists between the meltpool width and the density of the parts [105]. To do so, 2 mm high cuboids were built up to replicate a real build environment and the individual scan vectors were scanned on top. Three scan vectors were scanned across nine locations on the built plate such that the position on the build plate could be analysed. Then the scan vectors were imaged using OM and the width of the meltpool analysed using ImageJ. Each vector was imaged and measured separately with a minimum of 300 measurements taken across the plate. Secondly, nine 10 mm^3 cubes were built using the zig-zag scan strategy across the plate with Realizer's default process parameters outlined in Table 4.1. Their density was assessed using the Archimedes principle as outlined in section 3.6.1.

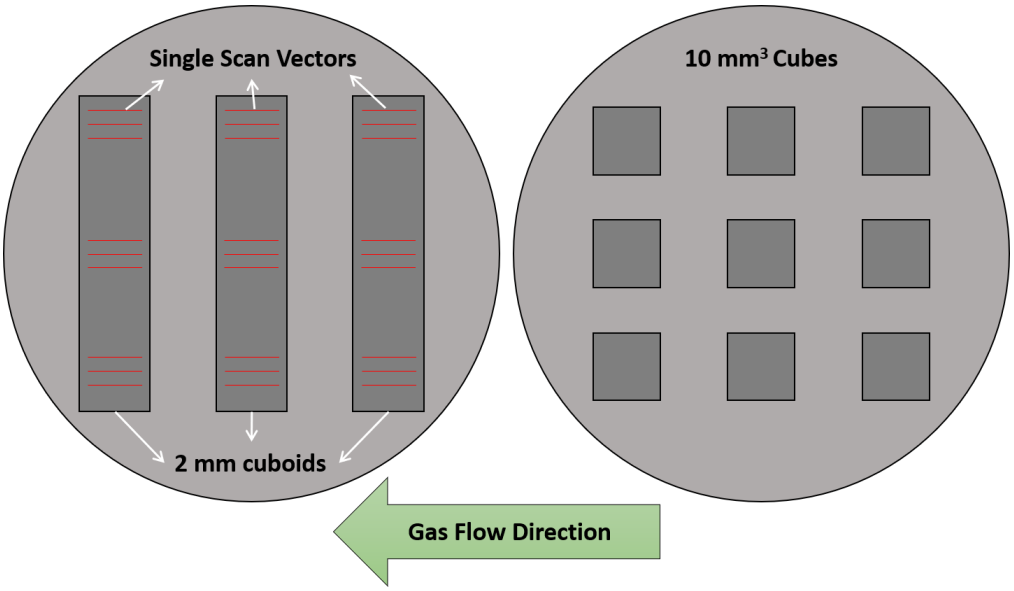

Figure 4.5: Build layouts for gas flow evaluation using single scan vectors and cubes for density analysis

Table 4.1: Realizer default process parameters used during gas flow experiments

Power (W)	Velocity (mm/sec)	Hatch (µm)	Layer Thickness (µm)	Energy Density (J/mm3)
80	300	80	25	133

Finally, a CFD simulation of each gas flow condition with the different combinations of flow rate and nozzle design was completed using Solidworks Flow Simulation. The two nozzle configurations were set up and boundary conditions of 60 and 100 L/min flow rate at the pump, inlets and outlets of the system were assessed. A tetrahedron mesh was employed with the max and min mesh element size of 13 and 0.1 mm, respectively. The fluid medium of the build chamber was argon with a density of 1.784 g/cm^3 (room temperature density) to simulate the flow behaviour post-purge.

4.2.2 Results

4.2.2.1 Build to Build Analysis

Figure 4.6 shows summary statistics of the velocity profile obtained from the CFD simulation, along with the meltpool width and part density recorded for each of the flow rate and nozzle configurations examined. From Figure 4.6 (a) it is evident that the nozzle configuration produces a higher mean velocity than the Realizer configuration for both flow rates examined. Furthermore, the standard deviation is almost six times greater for the Realizer configuration than the Nozzle configuration for each flow rate analysed. These results are not surprising when the gas flow profile of each of the profiles examined. Figure 4.7 shows that the flow profile produced by the nozzle configuration is more consistent across the build plate for each of the flow rates examined.

Considering the effect of these flow conditions on the meltpool width and density of parts produced using these flow conditions shows a clear trend. Comparison of Figure 4.6 (b) and (c) show that an increase in the mean size and standard error of the meltpool results in an increase in the density of the samples produced. However, what differs is the method of obtaining a larger melt pool width which shows an inverse trend between the two nozzle designs. Increasing the flow rate when using the Realizer nozzle layout appears to decrease the size of the meltpool as well as the standard error whilst the opposite trend is observed when using the nozzle configuration. Overall, the highest density was obtained for the Realizer 60 samples which had the largest meltpool width and standard error as well as the lowest mean velocity.

Similar results were obtained by Shi et al. [147] who observed increased density when increasing the meltpool width during SLM of thick layered Ti64. It is reasonable to assume that the lower velocity observed for the Realizer 60 configuration is less effective at removing process by-products which become suspended in the gas flow. These by-products increase the possibility of scattering which in turn reduce the power input into the powder bed. Examining the standard error of the meltpool width in Figure 4.6 (c) would support this theory as the Realizer 60 samples demonstrated the greatest spread in meltpool widths indicating that scattering was occurring. Although the literature suggests that this would be the antithesis of what would produce quality parts, in this case these affects are helping rather than harming.

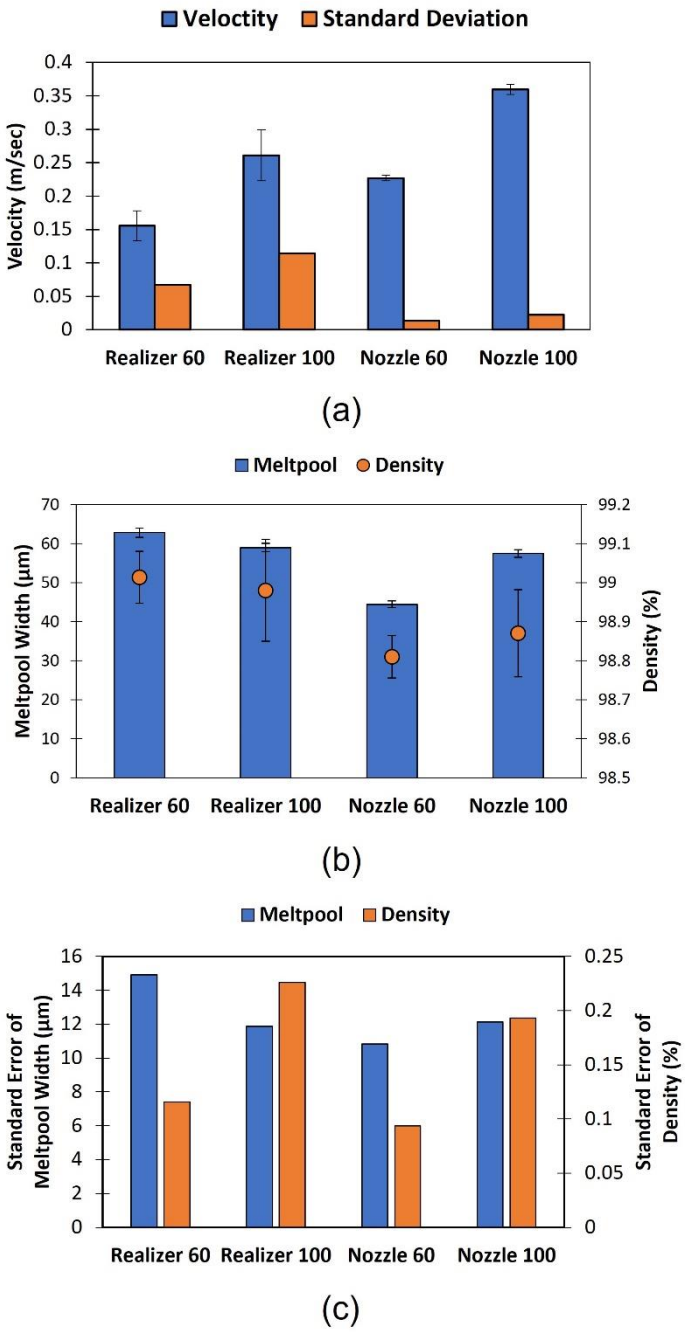

Figure 4.6: (a) Summary statistics of the velocity observed, (b) mean meltpool width and density measured and (c) standard error of the meltpool width and density values. Error bars represent one standard error in each case

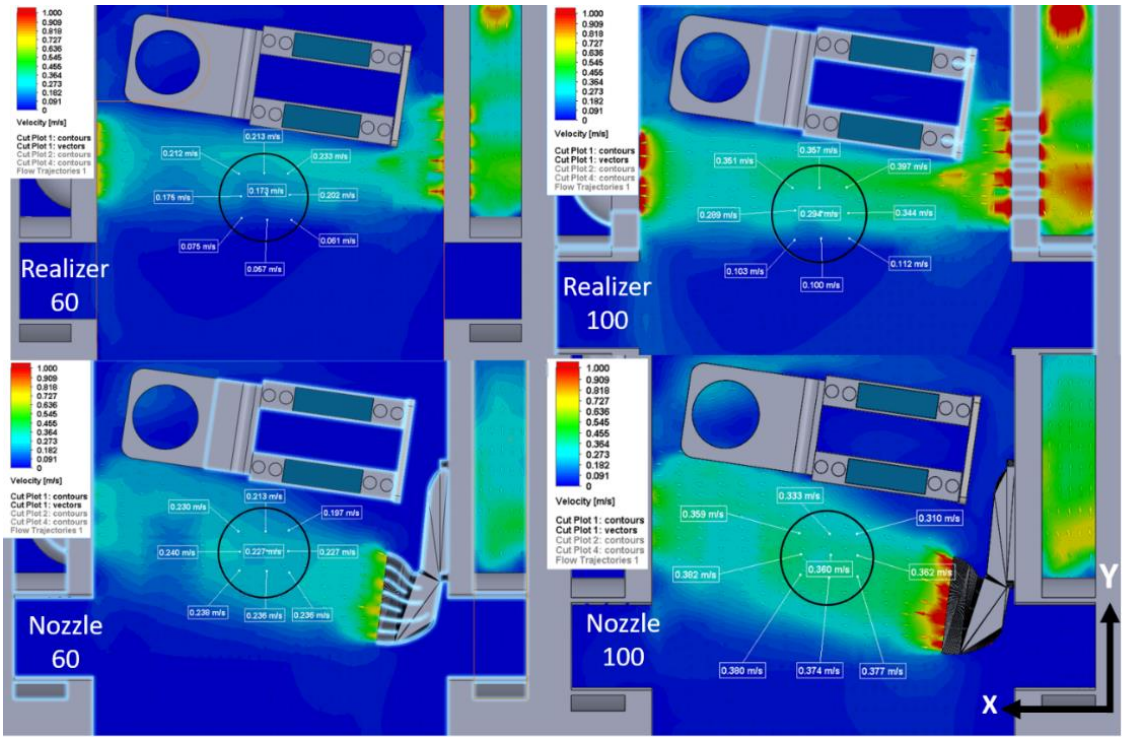

Figure 4.7: Top-down view of the four nozzle and flow rate configurations examined, each centred at the centre point of the respective nozzle outlet.

4.2.2.2 Within Build Analysis

Figure 4.8 shows the velocity recorded in the CFD model of the gas flow across the plate from top to bottom and from left to right as observed in Figure 4.5. Overall, it is evident that significantly greater variation in the velocity is observed for the Realizer configuration than is observed for the nozzle configuration which can also be observed in Figure 4.7. Regarding the Realizer nozzle layout, examining the plate from left to right or outlet to inlet in the gas flow circuit shows no direct correlation as the mean values are similar within each flow rate group whilst the standard error is large. The opposite is true when examining the velocity readings from top to bottom where significantly greater flow rate can be observed at the top of the plate then the bottom for both flow rates. In contrast, the FDM nozzle configuration appears to produce a more evenly distributed flow across the build plate both from inlet to outlet and from top to bottom.

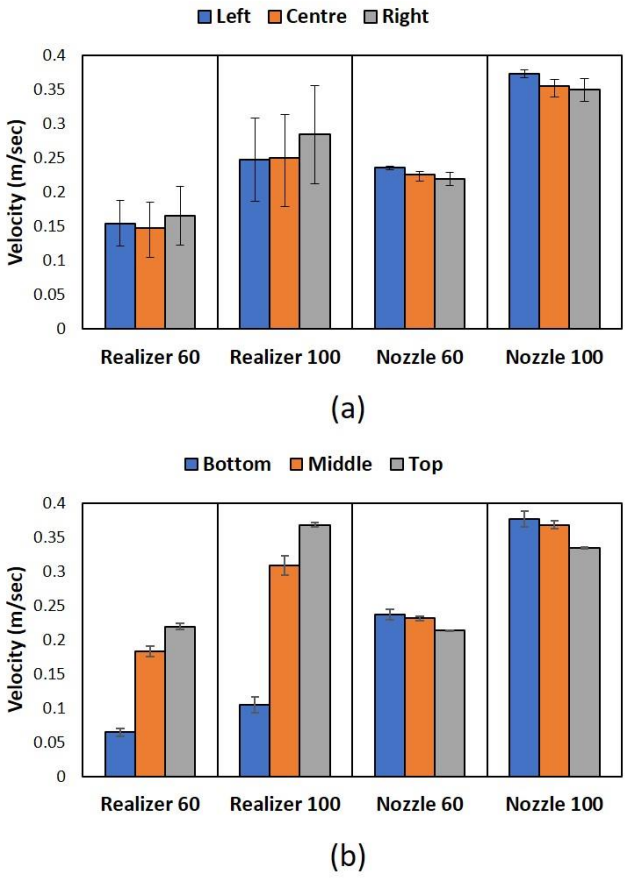

Figure 4.8: Analysis of gas flow velocity across the plate presented from (a) left to right and (b) top to bottom as observed in Figure 4.5. Error bars represent one standard error

The meltpool width and part density are plotted as a function of build plate position in Figure 4.9. The more consistent velocity across the build plate observed for the nozzle configuration has translated into a repeatable meltpool width for both flow rates studied. In contrast, when processing with the Realizer nozzle the meltpool width decreases across the build plate moving from top to bottom. Despite this, the difference observed within each flow rate is not as significant as the differences observed between flow rates. Regarding density, no distinct pattern was observed with reference to position on the build plate despite statistical differences occurring. In general, the bottom of the plate tended to produce samples with higher density though the exact position on the build plate is not a deterministic variable with regards to density of samples.

As previously stated, the Realizer 60 configuration produced the highest density of any flow condition with a considerably lower standard error then the next best layout being

the Realizer 100. Although some differences were observed across the plate using the Realizer 60 layout, the differences were less significant than those observed between other flow rates. Thus, from this point forward the Realizer 60 configuration is adopted for all remaining builds.

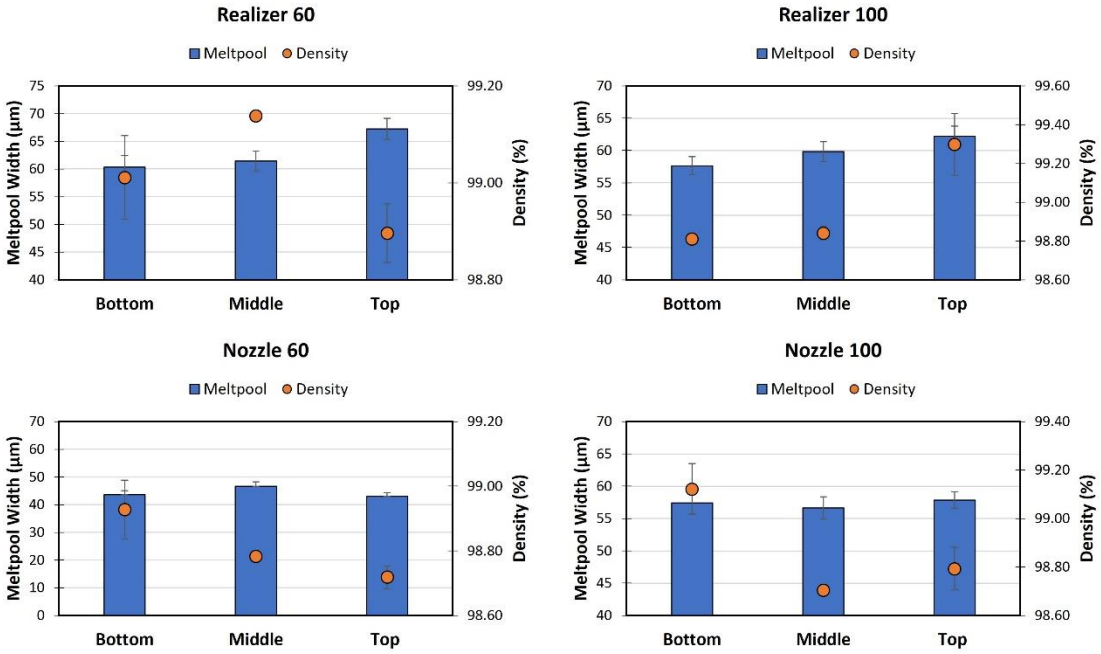

Figure 4.9: The effect of the build plate position on the meltpool width and density of parts. Error bars represent one standard error

4.3 Laser Parameter Optimisation

As outlined in Chapter 2 optimising the density is critical to maximising the mechanical properties. If the part is not fully dense, the effect of residual stresses in the part will be magnified as the stresses will encourage crack growth from the present pores. In such circumstance, fracture will occur at a low engineering strain as a result of crack propagation from the pores and so the state of the microstructure is essentially insignificant. Hence, it is essential that the proper process parameters are chosen to print fully dense parts. As these parameters will change for each SLM system and due to the lack of literature regarding processing of Ti64 using a Realizer SLM50, it was necessary to find the optimal printing parameters.

4.3.1 Experimental Method

The four processing parameters that constitute the ED variable namely layer thickness, laser power, scanning velocity and hatch distance were chosen as inputs into the process whilst the output was part density as illustrated in Figure 4.10. All of the parameters aside from layer thickness could be changed for different parts within one build and so were suitable for a factorial style design of experiments (DOE) whilst the layer thickness needed to be fixed. A factorial experiment is an experimental strategy in which input variables are varied together, instead of one at a time [165]. The advantages of a factorial design include efficiency over one factor at a time (OFAT) experiments as well as providing the ability to examine the effect of the interaction between multiple factors on the output variable.

2^3 factorials whereby laser power, scanning strategy and hatch distance examined at two levels, low and high, were conducted. Further, the centre point between the low and high values of each factor was repeated four times for each factorial design such that the error of the system could be evaluated.

Figure 4.10: Flow diagram showing DOE process for density optimisation

To determine what level to fix the layer thickness at, a screening study was completed by repeating the first factorial experiment for two layer thicknesses (Figure 4.11) such that an appropriate value could be determined. Following the screening study an iterative factorial DOE approach was conducted whereby the output from the first factorial informed the levels of the inputs for the succeeding experiment.

Following optimisation through the factorial approach a new DOE was designed whereby a second output variable of build time (Figure 4.12) was introduced to examine if fully dense parts could be built faster. This was investigated due to hardware restrictions of the

Realizer SLM50 whereby the filter needs to be changed after approximately 20 hours of processing (depending on the geometry of the parts and process parameters being used), hence emphasising the advantage of building parts faster.

Two variables which have a significant effect on build time are hatch distance and scanning velocity. In this case, these were examined using a OFAT approach to try and limit the effect on part density. Furthermore, using a OFAT approach enabled three parts to be printed per parameter set which facilitated reproducibility analysis for each parameter set which was not possible during the factorial designs due to the number of parts on the build plate.

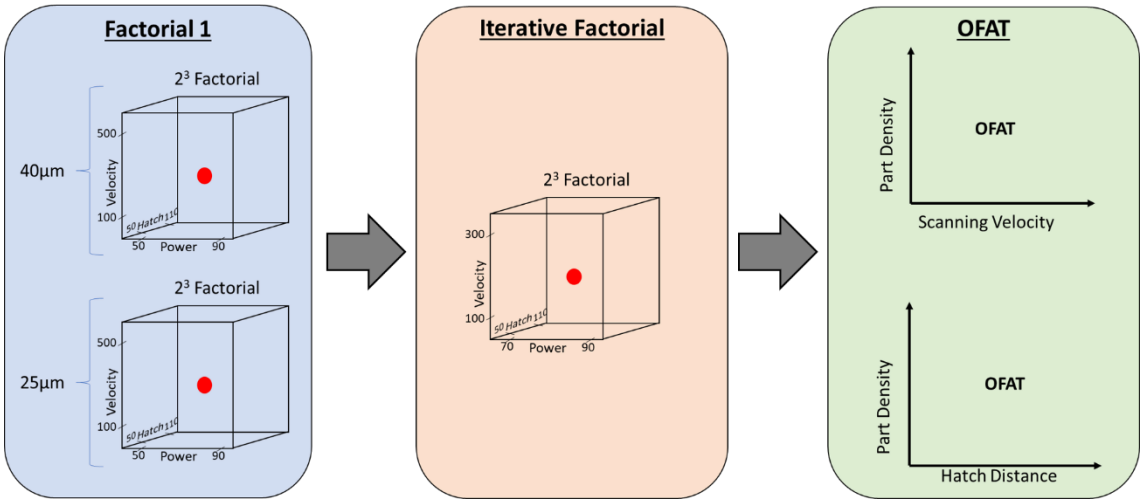

Figure 4.11: Process diagram illustrating the first factorial, iterative factorial and OFAT stages to the experimental design

Figure 4.12: Flow diagram showing DOE process including build time

As outlined in sections 3.2 and 3.3 all experiments were conducted using the Realizer SLM50 system and Ti64 powder with a 32.7 µm (D50) particle size. In each case, 10 mm^3 cubes were built for density analysis using the Archimedes principle as outlined in section 3.6.1. Table 4.2 shows the factorial design used to decide on a layer thickness whilst Table 4.3 outlines the second factorial experiment for optimisation of process parameters. For each parameter, both the actual value used as well as the coded values are given whereby 1 indicates a high value, -1 indicates a low value and 0 indicates the centre point between the two. Table 4.4 shows the process parameters used for the OFAT experiments completed to attempt to reduce the build time whilst facilitating fully dense parts. In both cases, four parameter sets were designed and three cubes built for each with the mean density and subsequent standard deviation reported in each case.

Following optimisation of density, cylindrical bars with a diameter of 8 mm were built in the vertical orientation and machined to tensile bars according to ASTM E8/E8M figure 8 sample 4 [164]. The samples were built with four parameter sets given in Table 4.5 to gain an insight into the role of density in mechanical performance. Before removal from the build plate the samples were heat treated at 900 °C for two hours with a heating ramp rate of 10 °C/min and were left to furnace cool following completion of the residence time. The aim of the heat treatment was to remove the residual stresses and transform the microstructure to a (α+β) structure such that any difference in mechanical performance could be attributed to the difference in density. To confirm the change in microstructure, one specimen from each parameter set was prepared for microstructural evaluation as outlined in section 3.5.1. Following heat treatment the tensile tests were completed according to section 3.7.2 whilst the yield strength and strain were determined using the 0.2% offset method.

Table 4.2: Process parameters and corresponding density values for the factorial experiment focusing on layer thickness

	Power (W)		Velocity (mm/sec)		Hatch Distance (µm)		Part Density (%)	
	Actual	**Level**	**Actual**	**Level**	**Actual**	**Level**	**40µm**	**25µm**
Two Layer Thicknesses	50	-1	100	-1	50	-1	98.43	99.20
	50	-1	500	1	50	-1	94.54	97.09
	50	-1	100	-1	110	1	98.44	98.87
	50	-1	500	1	110	1	94.36	96.09
	90	1	100	-1	50	-1	99.61	99.93
	90	1	500	1	50	-1	98.60	99.34
	90	1	100	-1	110	1	99.25	99.30
	90	1	500	1	110	1	98.07	98.94
	70	0	300	0	80	0	98.68	98.59
	70	0	300	0	80	0	98.30	98.67
	70	0	300	0	80	0	98.19	98.89
	70	0	300	0	80	0	98.43	98.41

Table 4.3: Process parameters and corresponding density values for the iterative factorial experiment

	Power (W)		Velocity (mm/sec)		Hatch Distance (µm)		Part Density (%)
	Actual	**Level**	**Actual**	**Level**	**Actual**	**Level**	
Iterative Factorial	70	-1	100	-1	110	1	99.29
	70	-1	300	1	110	1	98.91
	70	-1	100	-1	50	-1	99.53
	70	-1	300	1	50	-1	98.69
	80	0	200	0	80	0	99.29
	80	0	200	0	80	0	99.03
	80	0	200	0	80	0	99.12
	80	0	200	0	80	0	99.20
	90	1	100	1	50	-1	100
	90	1	100	1	110	1	99.65
	90	1	300	-1	110	1	99.43
	90	1	300	-1	50	-1	99.72

Table 4.4: Process parameters and corresponding observed density for the OFAT experiments completed

		Power (W)	Velocity (mm/sec)	Hatch Distance (µm)	Layer Thickness (µm)	Density (%)	Standard Deviation (%)
OFAT	**Velocity**	90	100	50	25	100	0.047
		90	300	50	25	99.46	0.03
		90	500	50	25	98.99	0.208
		90	700	50	25	98.87	0.16
OFAT	**Hatch**	90	300	40	25	99.96	0.082
		90	300	60	25	99.73	0.076
		90	300	80	25	99.62	0.037

Table 4.5: Parameter sets designed for printing tensile bars

Parameter Set	Power (W)	Velocity (mm/sec)	Hatch Distance (µm)	Layer Thickness (µm)	Energy Density (J/mm^3)
A	90	300	50	25	240
B	50	500	50	25	80
C	80	300	80	25	133
D	70	300	100	25	93

4.3.2 Results

4.3.2.1 First Factorial and Layer Thickness

Figure 4.13 shows the main effects plot for the first factorial experiment which was conducted for two layer thicknesses, 25 µm and 40 µm respectively. It is evident that there is an inverse relationship between the layer thickness and density whereby the mean density value for 40 µm is almost 0.5% lower than that of samples built using a 25 µm layer thickness. This can be attributed to insufficient melting due to the relatively low laser power of the Realizer SLM50 in comparison to other SLM systems which frequently have maximum power values four times that of the Realizer system.

From Table 4.2 it is also evident that the highest density value obtained using a 40 µm layer thickness was 99.61% in comparison to 99.93% for that of the 25 µm layer thickness. In both cases, these values were produced with the settings using the maximum energy input in the parameter set where laser power is at its highest of 90 W and the scanning velocity and hatch distance are at their lowest values of 100 mm/sec and 50 µm respectively. This indicates that it is not possible to produce fully dense parts using a 40 µm layer thickness. No discernible difference between the standard deviation of the replicated centre points was observed with values of 0.18% and 0.17% reported for the 40 and 25 µm layer thicknesses respectively. Hence, due to the superior density values obtained, a 25 µm layer thickness was employed for all following experiments.

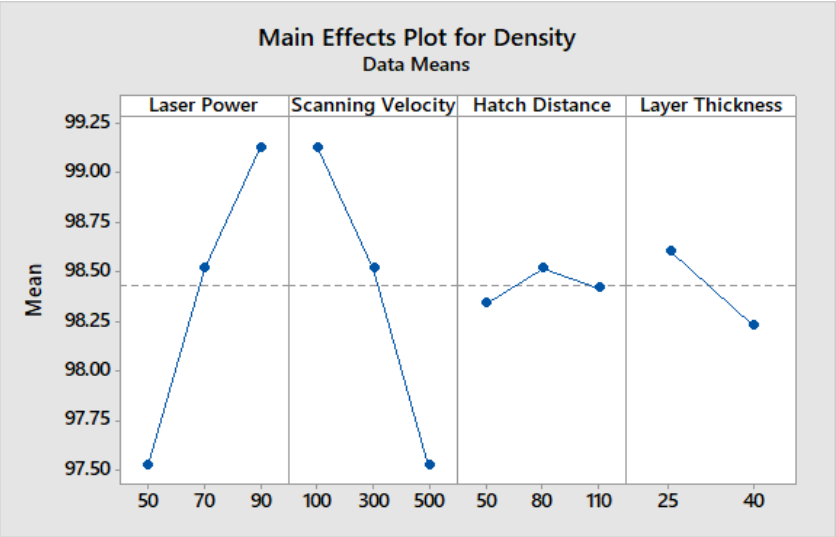

Figure 4.13: Main effects plot for the factorial experiment conducted with two layer thicknesses

Figure 4.14 (a) shows the main effects plot for the 25 µm factorial experiment from the screening study (Figure 4.11) independently so that the levels of the succeeding iterative factorial could be decided. A positive relationship was observed between density and power whilst velocity and hatch distance presented a negative relationship to density. This indicates that a high energy input is required to produce fully dense parts. Hence the parameter levels for the iterative factorial design included increasing the base laser power to 70 W from 50 W and reducing the maximum scanning velocity from 500 to 300 mm/sec. The hatch distance levels remained constant as it was the least responsive variable observed at a 0.05 significance level as outlined in the Pareto chart in Figure 4.14 (b). Furthermore, a larger hatch distance would facilitate lower build times which is desirable given a fully dense part can be produced.

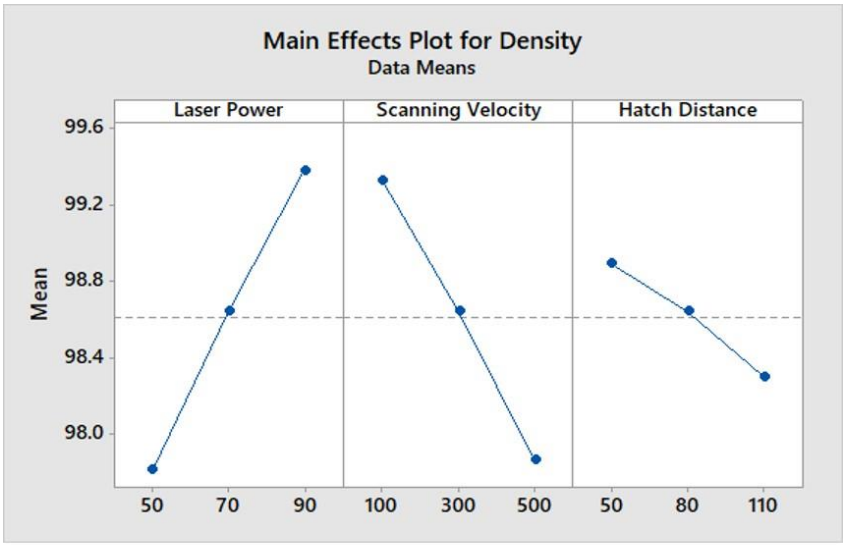

(a)

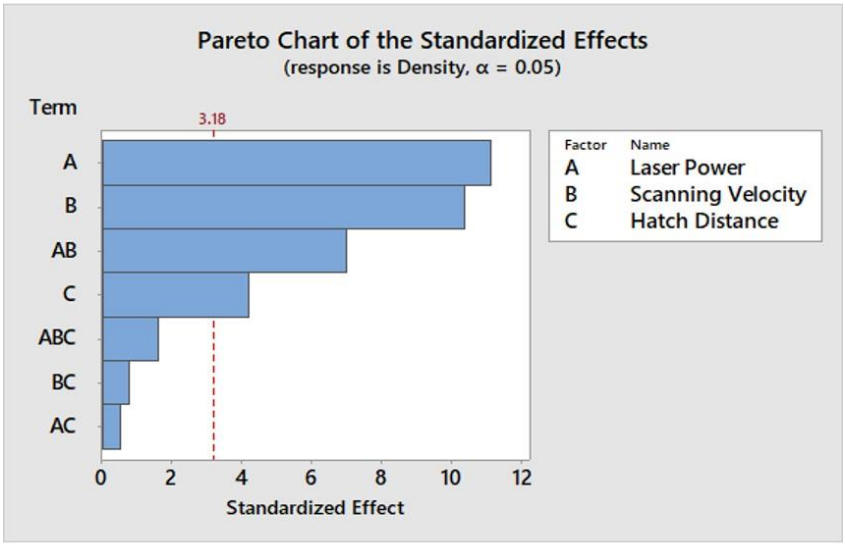

(b)

Figure 4.14: (a) Main effects plot and (b) Pareto chart for first factorial experiment with a 25 µm layer thickness

4.3.2.2 Iterative Factorial

Figure 4.15 presents the Pareto chart where the response is density and the inputs are laser power, scanning velocity and hatch distance. Laser power and scanning velocity have the greatest, and only statistically significant influence at a 0.05 significance level on the density of parts. Examining the interaction plot in Figure 4.16 (a) shows that the density is completely unresponsive to a change in the hatch distance when lower laser powers or higher scanning velocities are used. However, these settings also coincide with lower

density values and do not represent the optimal parameters. In contrast, when higher laser powers and/or lower scanning velocities are used the hatch distance shows an inverse relationship to density. This suggests that at the inferior process settings the energy input into the powder bed is insufficient to produce fully dense parts irrespective of the hatch distance used. Whilst the combination of high power and low scanning speed will impart enough energy into the powder bed to produce fully dense parts given the interaction time is long enough by using a lower hatch distance.

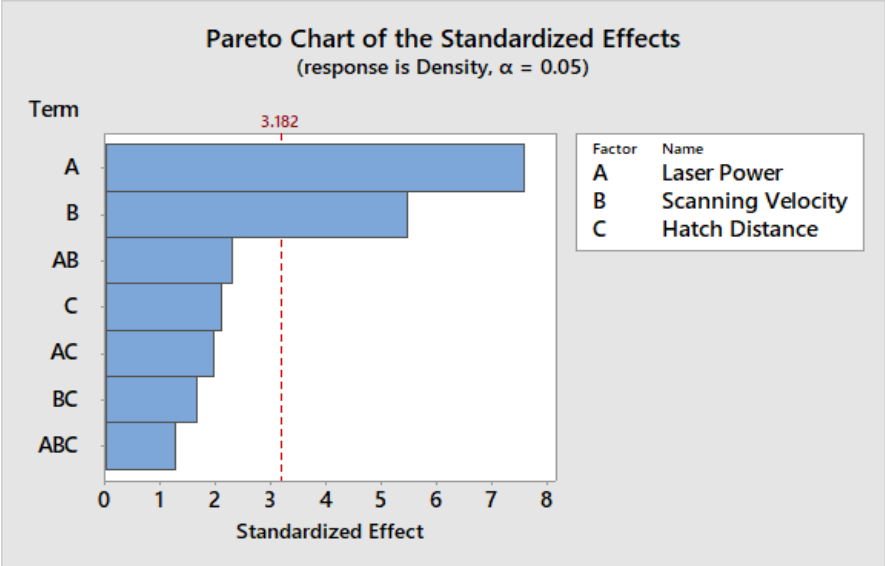

Figure 4.15: Pareto chart analysing the significance of parameters from the iterative factorial experiment

Furthermore, examining Figure 4.16 (b) and (c) which illustrate density plotted as a function of laser power and scanning speed respectively indicates that the higher laser power of 90 W must be selected to maximise density. Both images plot the mean density for the respective sub-group with the error reported as one standard deviation. Figure 4.16 (b) shows that the samples produced with 90 W laser power are statistically superior than those produced at either of the other two power settings, irrespective of the scanning velocity or hatch distance. In contrast, Figure 4.16 (c) indicates that although the maximum density values are obtained for the lowest scanning velocity of 100 mm/sec the result cannot be determined as statistically different from the samples produced using 300 mm/sec. Hence, the results from the iterative factorial experiment demonstrate that a laser

power of 90 W must be used, and hence it was adopted for the OFAT experiments with respect to both velocity and hatch distance.

(a)

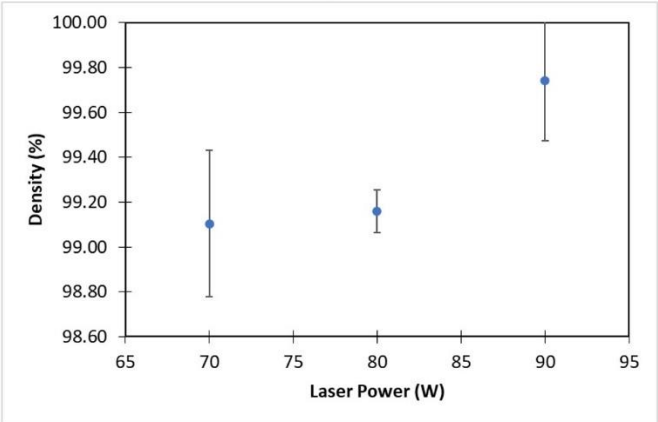

(b)

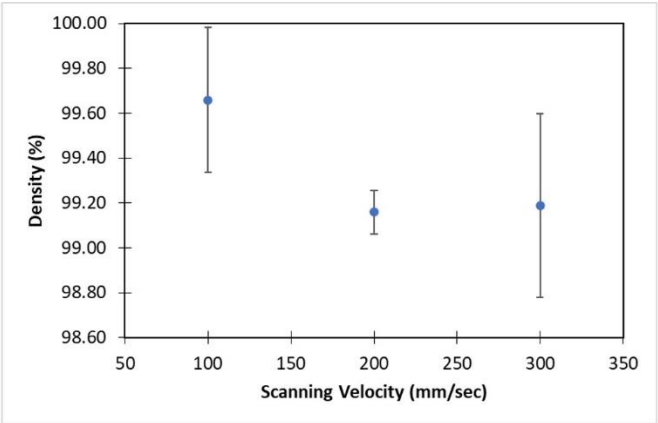

(c)

Figure 4.16: (a) Interaction plot for density illustrating the interactions between the three examined factors. (b) and (c) present the effect of laser power and scanning velocity independently where the error bars represent one standard deviation

4.3.2.3 OFAT Scanning Velocity and Hatch Distance

Table 4.4 shows the parameters utilised in both of the OFAT experiments where four scanning velocities from 100 – 700 mm/sec and three hatch distances from 60 – 100 µm were examined. Figure 4.17 shows the inverse relationship between velocity and density given a fixed laser power, layer thickness and hatch distance with a 1.2% difference in density between samples produced at 100 and 700 mm/sec respectively. Furthermore, the standard deviation of the groups reported in Table 4.4 shows that samples are extremely repeatable at lower scanning velocities of 100 and 300 mm/sec but are considerably more stochastic in nature at higher scanning velocities.

This is a significant result in this overall research as it demonstrates that fully dense parts can be produced using the Realizer SLM50 which is a primary goal of this thesis. Further, it confirms previous postulations that fully dense parts can be produced given a sufficient interaction time between the laser and powder bed. However, the secondary objective of build time has to be sacrificed in order to achieve this. Moreover, building multiple components larger than the sample size of 10 mm^3 using the combination of scanning velocity of 100 mm/sec and hatch distance of 50 µm is not feasible on this SLM system. Such long interaction times lead to significantly more process by-products which when combined with the length of the build time saturate the filter of the system. This is (a) not a safe working environment and (b) potentially damaging for the pump of the SLM system.

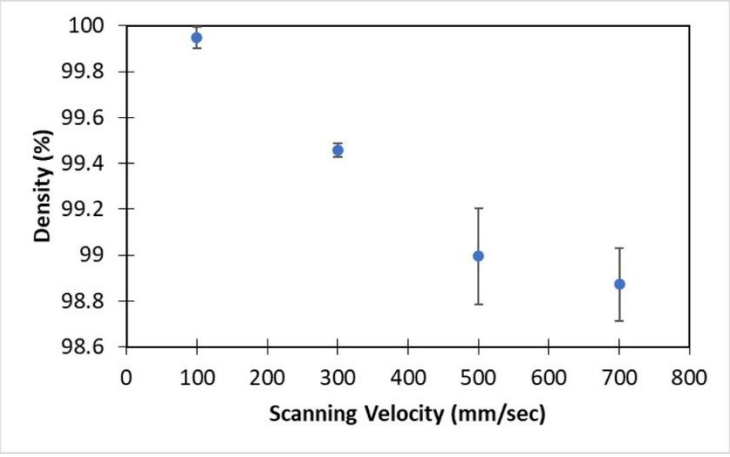

Figure 4.17: Density reported as a function of scanning velocity from the OFAT velocity experiment where the error bars represent one standard deviation

Given the impracticality of the optimal settings discovered, either a faster mechanism of producing fully dense parts is required or else part density must be sacrificed. One method of reducing build time which has shown relative insensitivity to part density was hatch distance and so was examined in the OFAT hatch experiment with parameters outlined in Table 4.4. Similar to scanning velocity, an inverse relationship is evident with hatch distance and density as illustrated in Figure 4.18. However, as was previously observed in the factorial experiments, density is less sensitive to a change in the hatch distance than was observed for velocity with each 20 µm increase in hatch distance correlating to a 0.15% reduction in density. Furthermore, the standard deviation was below 0.1% for all hatch distance groups which indicates that the repeatability of the samples is also influenced more by laser power and scanning velocity than hatch distance.

From these experiments the optimal parameter settings with respect to density optimisation have been established as; 90 W laser power, 100 mm/sec scanning velocity, 50 µm hatch distance and 25 µm layer thickness. However, issues with build time on the Realizer SLM50 at these process settings make them impractical and potentially dangerous to implement for many build jobs where large and/or multiple parts are required on a build plate. In such circumstances, a small adjustment of scanning velocity and/or more significant adjustments in hatch distance could be used to reduce the build time with the density level marginally sacrificed.

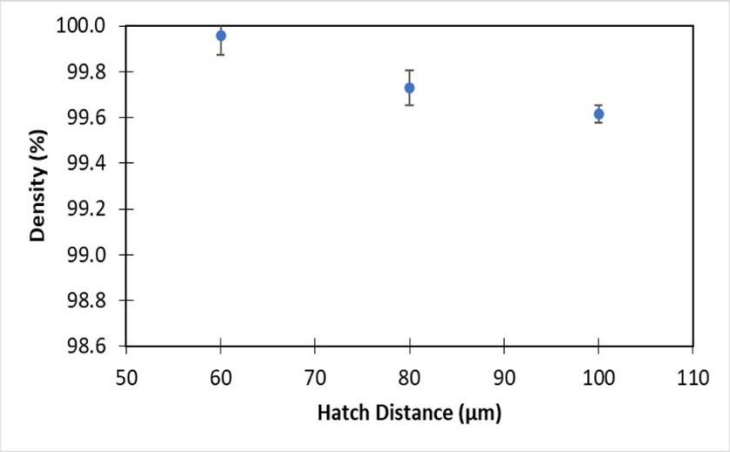

Figure 4.18: Density reported as a function of hatch distance from the OFAT hatch experiment where the error bars represent one standard deviation

4.3.2.4 Mechanical Performance

As previously stated, it was impossible to build tensile bars using the optimal settings found for density due to the build time required. Thus, the closest parameter set to the optimal settings used a scanning speed of 300 mm/sec rather than 100 mm/sec and as such produced the highest density of the tensile samples at 99.4% (Table 4.6) rather than the 100% observed in Figure 4.18. This corresponds to the density value observed for the same parameters in the OFAT velocity experiment shown in Figure 4.17 which indicates that this is repeatable over multiple build jobs and not just within each build.

Table 4.6 shows the density obtained for tensile bars built using the parameters outlined in Table 4.5. Astonishingly groups C and D reported the exact same density despite a significant difference in parameters, with group C having a higher laser power and lower hatch distance than group D. In theory, and according to the optimisation studies this should have produced higher density samples, yet both groups reported 98.6%.

Table 4.6: Mechanical properties and density values observed for the four parameter sets studied

Parameter Set	**Density (%)**	**Yield Stress (MPa)**	**Yield Strain (%)**	**UTS (MPa)**	**Failure Strain (%)**
A	99.4	860.7	2.55	946.8	13.21
B	97.5	724.8	2.35	811.1	4.53
C	98.6	830.1	2.56	906.5	7
D	98.6	844.3	2.45	932.9	6.6

Figure 4.19 reports mechanical properties as a function of the mean density of the three samples for each group, where a clear positive trend between density and failure strain can be observed. For example, at 13.2%, the mean failure strain of samples built with 99.4% density is over three times greater than those built with a mean density of 97.5% whilst the failure strain values obtained for groups C and D are statistically the same. In contrast, the yield strain remains statistically identical for all samples tested irrespective of the density. The differences in performance of the mechanical properties can be attributed entirely to the density of the samples. Figure 4.20 shows SEM analysis for all samples where identical (α+β) microstructures were observed. Hence the brittle

martensitic α' has been decomposed as a result of the heat treatment facilitating increased fracture strain values in samples with increased density.

Examining Figure 4.19, the stress values appear to reveal a minimum threshold in terms of density. All groups which have density values over 98% display UTS values above 900 MPa and yield strength (YS) values above 800 MPa which aligns with values observed in the literature for heat treated specimens [166]. In contrast, the samples produced with 97.5% density repeatedly presented stress values of circa 820 MPa whilst the YS was repeatedly around 730 MPa. Furthermore, both the UTS and YS appear to show a positive relationship with density as the sample with the highest density also had the highest mean UTS and YS values.

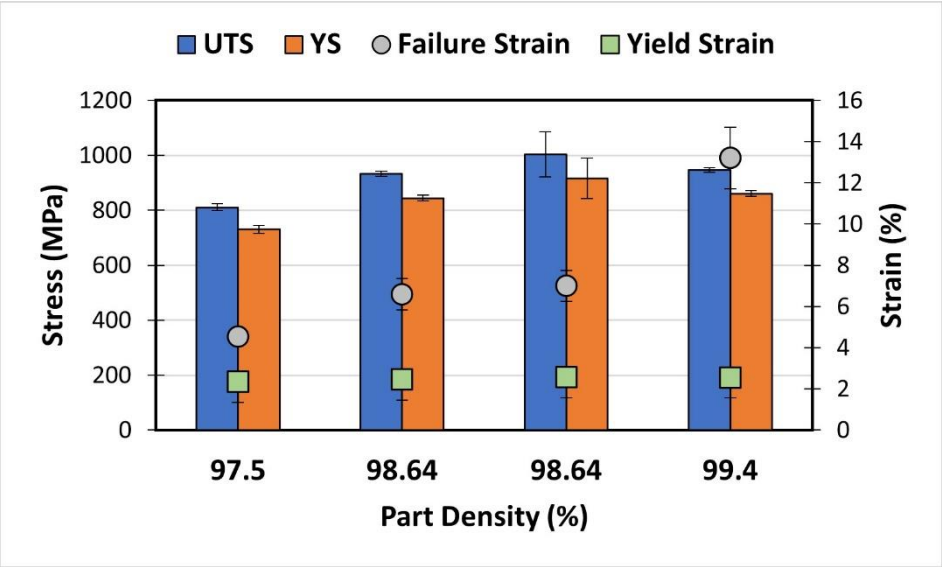

Figure 4.19: Mechanical properties reported as a function of part density and parameter set where error bars represent one standard error

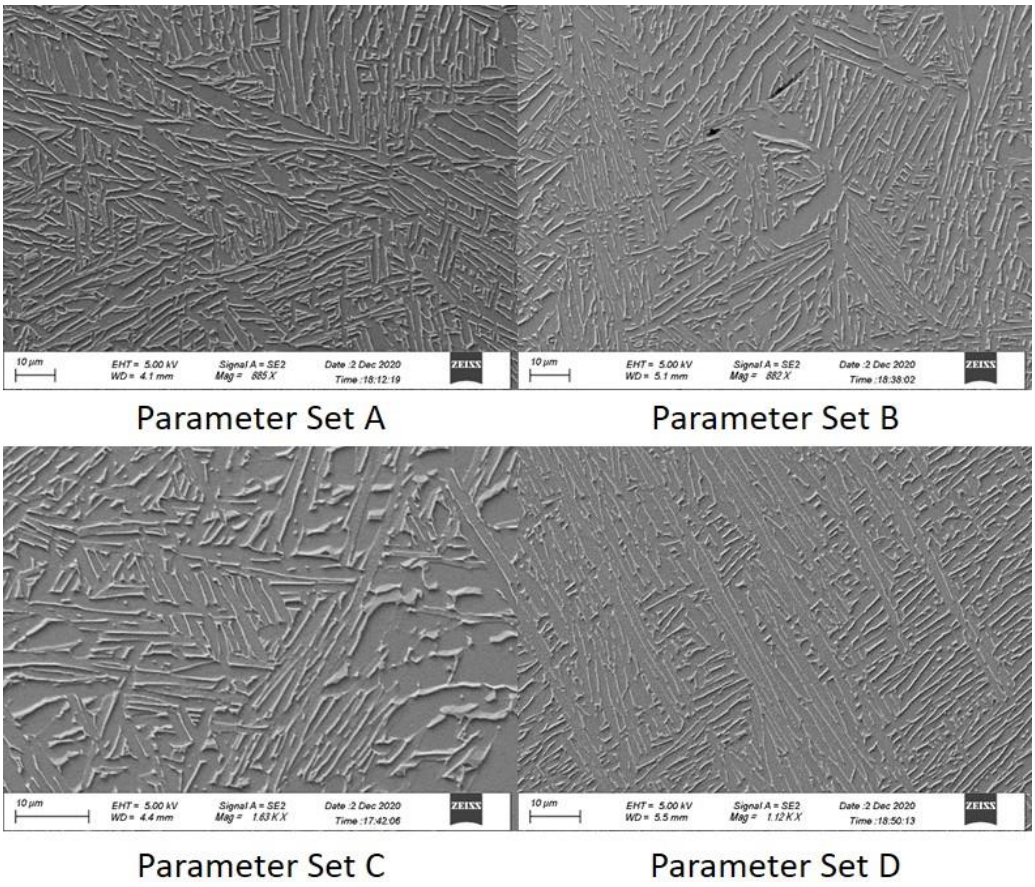

Figure 4.20: SEM images of (α+β) microstructure observed for all parameter sets

4.4 Conclusion

Density optimisation using the Realizer SLM50 has been conducted by examining the process environment in the form of the gas flow along with the laser parameters. The gas flow optimisation considered a total of four flow scenarios in the form of two nozzle layouts namely the default Realizer and an FDM printed nozzle as well as two flow rates 60 and 100 L/min respectively. Results from the CFD model presented lower flow velocity for the Realizer nozzle. This correlated well with an increased meltpool width which was attributed to a reduction in the removal of by-products during the process as a result of a low velocity. The increase in meltpool width led to increased density values. Thus, the Realizer nozzle with a 60 L/min flow rate which presented the lowest velocity and greatest meltpool width also resulted in the highest density. Furthermore, analysis of the effect of gas flow on the position of parts on the build plate revealed that the same

flow scenario was also the most repeatable. Thus the Realizer 60 flow configuration was adopted for the remaining builds.

A statistical examination of the laser parameters took place where laser power, layer thickness, scanning velocity and hatch distance were examined through a number of factorial and OFAT style experiments. Initially, examination of the layer thickness revealed that a 25 µm layer thickness was required to produce samples with a high density. In contrast the 40 µm layer thickness yielded lower density values irrespective of any other process parameters. Further examination of the parameters demonstrated that laser power and scanning velocity had the greatest impact on the density as was observed in literature [85], [90]. Increasing the laser power and decreasing the scanning velocity led to increased density within the as-built parts irrespective of the hatch distance used. Fully dense parts were printed using a laser power of 90 W, scanning velocity of 100 mm/sec and a hatch distance of 50 µm. However, this parameter set is not conducive to printing parts of a any significant size due to hardware restrictions. Hence OFAT experiments were conducted focusing on scanning velocity and hatch distance with the aim of reducing the build time.

Increasing the scanning velocity from 100 – 700 mm/sec led to a reduction in density from 100% to 98.87% whilst a 70% increase in the standard deviation was also observed. Increasing hatch distance had a less significant effect whereby an increase in the hatch distance from 40 – 80 µm only reduced the density from 99.96% to 99.62% with standard deviation reducing as the hatch distance was increased. Hence, using a 90W laser power was considered essential to process high density parts with the Realizer SLM50 whilst scanning velocity or in particular hatch distance can be varied to enable more parts to be built.

Four parameter sets were designed to analyse mechanical properties as a function of density by heat treating as-built samples to remove the effects of microstructure and residual stresses. Increasing density from 97.5% – 99.4% led to an increase in the mean fracture strain from 4.53% – 13.21% whilst two sample groups with the same density presented statistically identical tensile properties. Furthermore, UTS shows an increasing trend with regards to density where a critical threshold was established.

Chapter 5 Microstructures

5.1 Introduction

This chapter addresses the second goal highlighted in section 1.3 which is to achieve in-situ decomposition of the brittle martensitic α’ microstructure. The effects of pre-heating temperature, hatch distance, laser spot size and layer thickness are examined. The DOE, experimental setup and experimental methods are presented to outline the procedures used. Following which the impact of each parameter upon the density of the samples is presented due to the importance of building fully dense specimens. Then, the microstructures of the different parameter sets are presented and discussed through OM, SEM and XRD analysis.

5.2 Design of Experiment

Figure 5.1 outlines the DOE constructed to explore as-built Ti64 microstructures. The inputs of build plate pre-heating, hatch distance, layer thickness and laser spot size are examined with reference to part density and microstructure whilst mechanical performance is discussed in Chapter 6. Literature has demonstrated that the chosen parameters can aid in the decomposition of the martensitic microstructure which is omnipresent within SLM of Ti64. As outlined in section 2.3.3 pre-heating in particular has also been shown to drastically reduce residual stresses formed during processing [64], [74], [137], [149]. However, these parameters have never been examined together and the interactions between them remain unknown. Section 2.3 outlines that laser power and scanning velocity are the most critical for density optimisation. As such, the laser power of 90 W and scanning velocity of 300 mm/sec developed in Chapter 4 have been retained with the aim of maintaining dense samples.

Figure 5.1: Flow diagram showing DOE used to explore as-built Ti64

Similar to the density optimisation study, a factorial approach DOE was deemed appropriate. Figure 5.2 shows the experimental design for exploration of as-built microstructures. The design is centred around a factorial DOE including laser spot size, hatch distance and layer thickness, which is repeated for three pre-heating temperatures of 150, 300 and 450 °C respectively. Table 5.1 outlines the parameters examined for each pre-heating temperature. The limits of each parameter were chosen with the aim of achieving α' decomposition without adversely affecting density. Barriobero et al. [137] observed α' decomposition for when using tight hatch distance of 40 µm whilst Qiu et al. [82] observed porosity for layer thicknesses in excess of 60 µm. With regards to spot size, limited literature exists for guidance so the two values were chosen to represent high and

low power densities calculated according to Equation 5.1. In each case the energy density metric, is calculated using Equation 2.1.

The variation in ED values is attributed to the changes in hatch distance and layer thickness as shown in Figure 5.2. However, the energy input into the powder bed will change significantly given changes in the laser spot size. These effects are not reflected in the ED variable and thus analysis by ED alone can be misleading. Therefore, a second measure of energy input in the form of the power density is presented in Table 5.1. The power density is a representation of the instantaneous energy input into the powder and is calculated according to Equation 5.1. It considers the area over which the laser power is applied and so represents changes to energy input with regards to variations in spot size. Consideration of these two metrics in combination rather than individually leads to a more accurate understanding of the energy input into the powder bed during processing.

$$PD = \frac{P}{CSA_{D4\sigma}} \qquad \text{Equation 5.1}$$

Where PD is the power density, P is the laser power and $CSA_{D4\sigma}$ is the cross-sectional area of the $D4\sigma$ laser spot size.

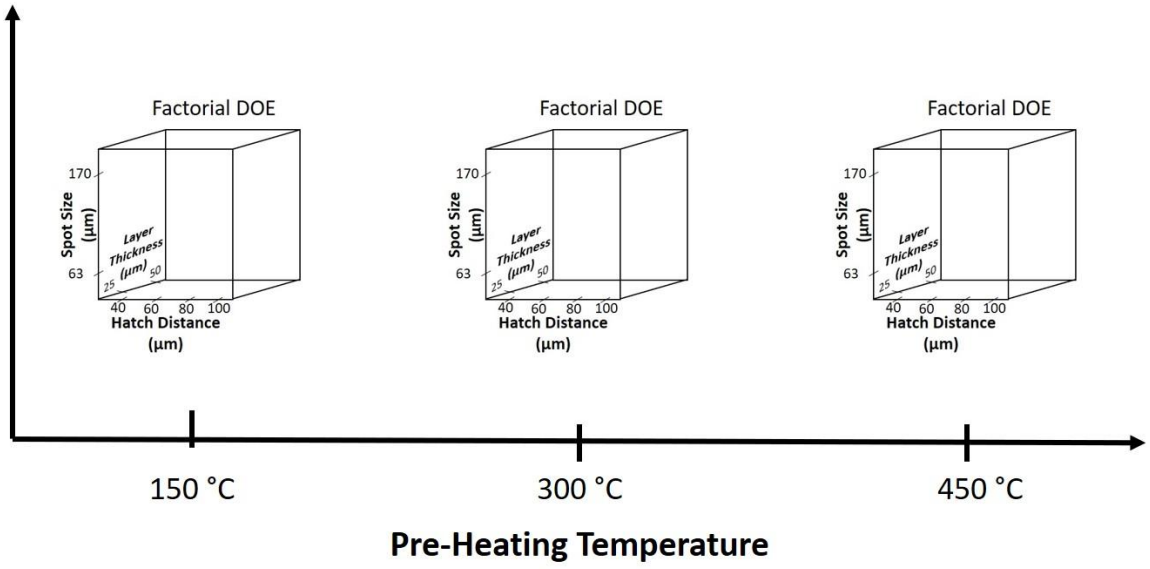

Figure 5.2: Experimental design for as-built exploration

Table 5.1: Factorial parameters examined at three pre-heating temperatures

Layer Thickness (µm)	**Spot Size (µm)**	**Hatch Distance (µm)**	**Laser Power (W)**	**Scanning Velocity (mm/sec)**	**Energy Density (J/mm^3)**	**Power Density (W/mm^2)**
25	63	40	90	300	300	0.029
25	63	60	90	300	200	0.029
25	63	80	90	300	150	0.029
25	63	100	90	300	120	0.029
50	63	40	90	300	150	0.029
50	63	60	90	300	100	0.029
50	63	80	90	300	75	0.029
50	63	100	90	300	60	0.029
25	170	40	90	300	300	0.004
25	170	60	90	300	200	0.004
25	170	80	90	300	150	0.004
25	170	100	90	300	120	0.004
50	170	40	90	300	150	0.004
50	170	60	90	300	100	0.004
50	170	80	90	300	75	0.004
50	170	100	90	300	60	0.004

5.3 Experimental Method

5.3.1 Experimental Setup

Figure 5.3 shows the Realizer SLM50 printer used in this study fitted with a custom designed heating assembly capable of heating the build plate up to 450 °C. Figure 5.3 (d) shows a detailed view of the heater sub-assembly which consists of; the titanium build plate, a resistance heater, a carriage to facilitate movement in the vertical direction and an insulator made from pyrophyllite. The insulator component has a low thermal conductivity of 1.5 W/m.K which protects electrical components located below the build

chamber as well as enabling the maximum heat transfer from the resistance heater into the build plate above. The resistance heater consists of a ceramic heating element made of silicon nitride type OMA which has a maximum operating temperature of 500 °C.

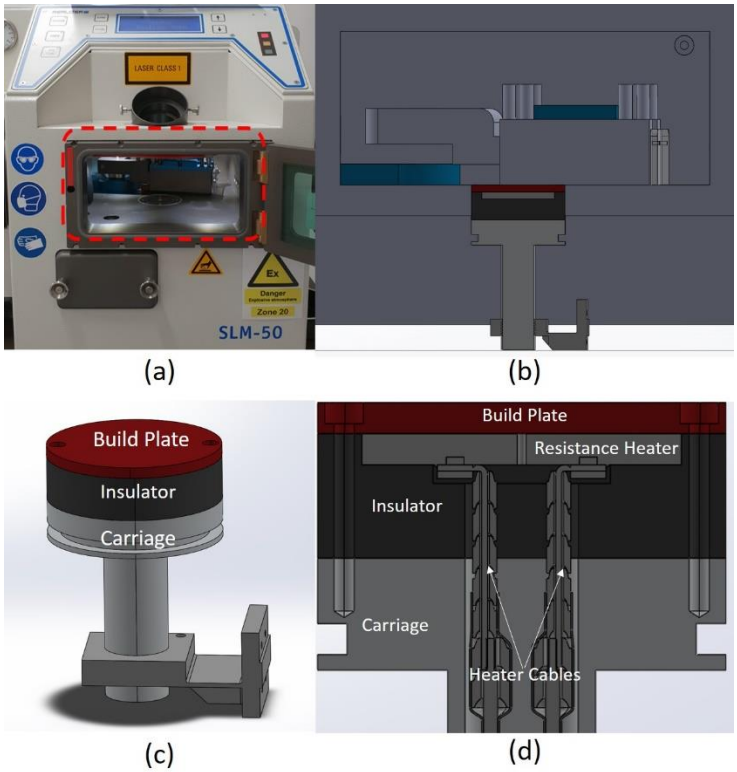

Figure 5.3: (a) Photograph of build chamber of the Realizer SLM50 printer used for this work. (b) cross-section of CAD showing the build chamber and build plate assembly (c) heated build plate sub-assembly and (d) detailed section view of the heater sub-assembly

The temperature of the build plate was monitored using a type k thermocouple which was fed through the heater and embedded into the build plate. The thermocouple was calibrated using an Ametek Model 650SE high temperature thermocouple calibration unit. Eleven measurements were made by reading the thermocouple through a NI9219 universal analogue input module into NI LabView. The data recorded was compared against the temperature set on the calibration unit and plotted in Figure 5.4. The calibration equation is shown in Figure 5.4 and was subsequently used to adjust the temperatures recorded during SLM builds.

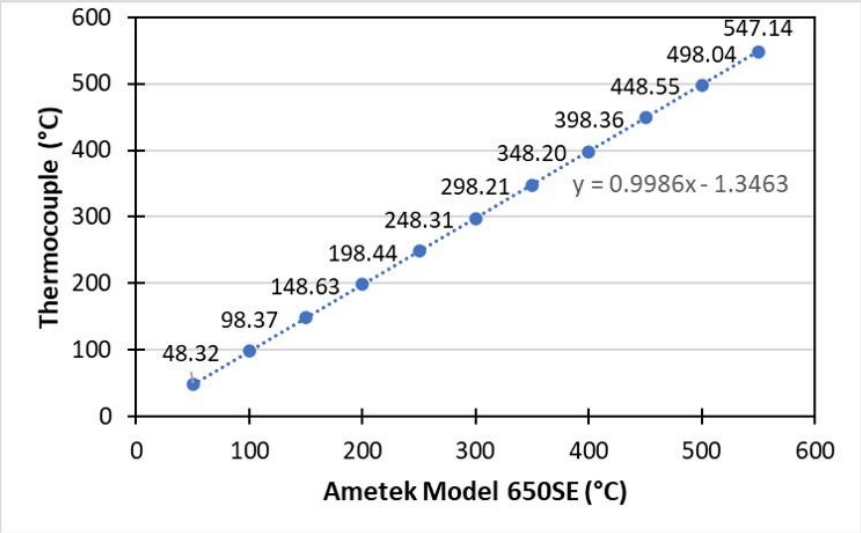

Figure 5.4: Thermocouple calibration chart showing the calibration function

The laser spot size on the Realizer SLM50 can be altered by changing the relative distance between the laser and the focusing lenses. The spot size was measured using an Ophir Photonics SP1203 beam profiling camera at the centre of the build plate. As outlined in section 3.3 all experiments were conducted using the Realizer SLM50 system and Ti64 powder with a 32.7 µm (D50) particle size. For each parameter set, the customised build plate shown in Figure 5.3 (c) and (d) was pre-heated to the target temperature and allowed to settle for five minutes. One 10 mm^3 cube and five tensile specimens were built according to ASTM E8/E8M figure 8 sample 4 using a zig-zag scan strategy [164].

5.3.2 Post-Printing Analysis

Two samples from each cube were prepared for microstructural evaluation as outlined in section 3.5.1. Prior to etching the polished samples were imaged and used for density analysis using the OM technique as outlined in section 3.6.2. Following density analysis, one sample was used for XRD and microhardness analysis whilst the other sample was etched and used for OM and SEM examination as outlined in section 3.5.

5.4 Results and Discussion

Though the primary focus of this chapter was to explore differences in as-built microstructures, the effect of the process parameters on density is presented given its

importance for mechanical properties of Ti64 components. Following which the results for microstructural evolution is presented through OM, SEM and XRD analysis.

5.4.1 Density

5.4.1.1 Overview

Figure 5.5 shows the Pareto and main effects plots for the impact of pre-heating temperature, spot size, layer thickness and hatch distance on part density. The Pareto plot in Figure 5.5 (a) indicates that the laser spot size and the relationship between spot size and layer thickness have a statistically significant effect on density for a 95% confidence interval. Following this is the hatch distance and the relationship between hatch distance and the laser spot size which also show a noteworthy effect on the density of as-built parts.

These findings are reflected in the main effects plot (Figure 5.5(b)) which plots the effects of each parameter individually on the density of as-built samples. The pre-heating temperature appears to have fundamentally no effect on the density of specimens, as was reported by Vrancken et al. [135]. In contrast, the other three studied parameters all have strong correlations to density. Spot size and hatch distance both demonstrate a positive correlation with density whilst the layer thickness shows a reduction in density as the thickness was increased from 25 to 50 μm. The interaction plot presented in Figure 5.6 gives a better insight into the relationship between the factors.

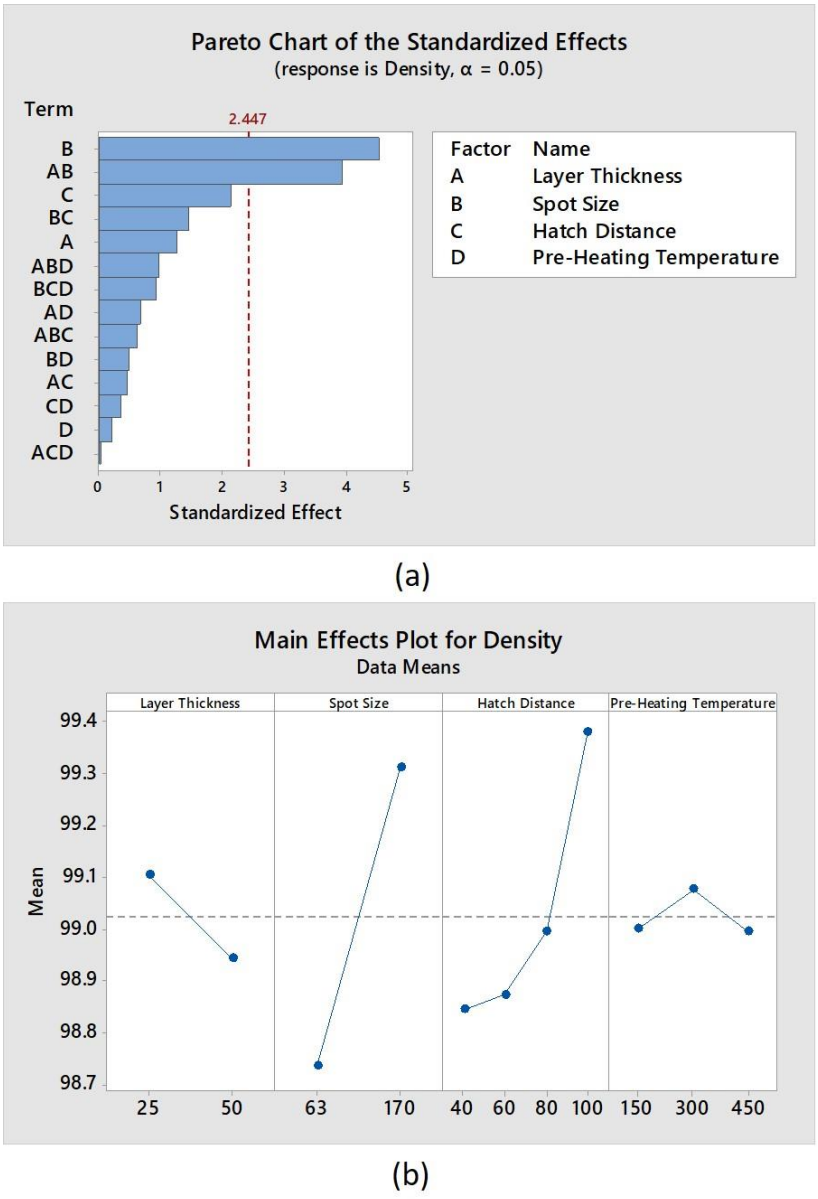

Figure 5.5: (a) Pareto and (b) main effects plots for density as a function of the four process variables examined

Examining the interactions regarding the laser spot size from Figure 5.6 shows no statistically significant difference across the three pre-heating temperatures at each of the spot sizes used. Though the 170 µm spot size was superior for all three pre-heating temperatures which can be ascribed to the fact that the laser parameter optimisation from Chapter 4 took place at the larger setting. With regards to the relationship between hatch distance and spot size, a positive correlation was observed between hatch distance and density for both spot sizes examined. However, processing with the 63 µm spot size

resulted in a lower mean density across all hatch distances as well as a larger spread between the different hatch values.

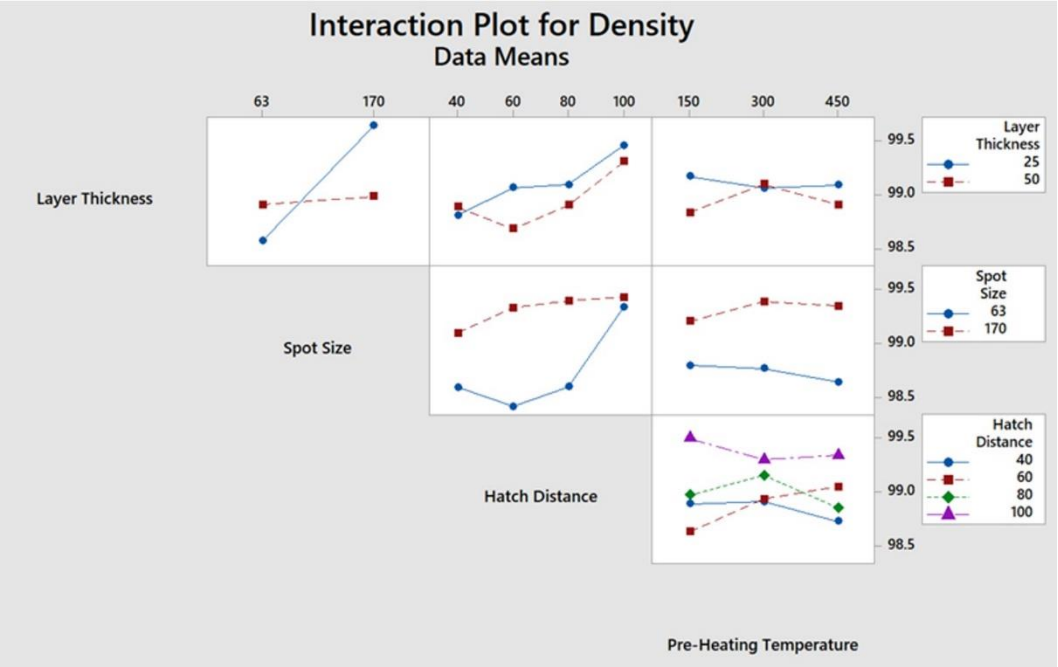

Figure 5.6: Interaction plot showing the relationships between the various process parameters examined during the pre-heating study

The relationship between the laser spot size and layer thickness is critical for the density of as-built parts. With mean values below 99%, using a layer thickness of 50 µm yielded a poor mean density irrespective of the spot size. With regards to samples built with a 50 µm layer thickness, all samples produced using the smaller spot size of 63 µm resulted in over-melting whilst those produced with the larger spot size of 170 µm resulted in under-melting (Figure 5.9). In contrast, the samples produced with a 25 µm layer thickness presented excellent density when combined with a 170 µm spot size whilst significant over-melting was observed when the spot size was reduced to 63 µm.

As aforementioned the build plate temperature shows no significant effect for either of the layer thicknesses examined. Though, at all three pre-heating temperatures the 25 µm thickness is superior to the 50 µm samples. Examining the interaction between the layer thickness and hatch distance shows an increase in density as the hatch distance is increased for both layer thicknesses. Further, samples built with a 25 µm layer thickness produced significantly greater density than those with the 50 µm for all hatch distances

apart from the tightest hatch distance examined which yields approximately the same density value.

The superior performance of the 25µm samples can be attributed to the laser parameter optimisation taking place at that value and with a 170 µm spot size. Yet, the results of interactions from the 50 µm samples where both over and under melting were observed for different laser spot sizes, indicates that the relationship between these two factors and not each individually should be considered during future laser parameter optimisation attempts.

The hatch distance shows a positive relationship with density whereby an increase in hatch distance from 40 to 100 µm resulted in an increase in density irrespective of the other process settings used. This is reflected in the relationship between hatch distance and build plate temperature which shows no significant difference for any given hatch distance across the three build plate pre-heating temperatures. Yet it can be observed that the mean density of each sample group across the three pre-heating temperatures shows the aforementioned positive relationship.

5.4.1.2 Individual Process Settings

In order to fully understand the porosity development during SLM, the individual process settings must be analysed in more detail rather than just examining the data means as is the case in the Pareto and main effects plots. Given that the laser spot size had the greatest effect on the density of the as-built samples as outlined in Figure 5.5 (a), it is logical to examine the other parameter groups with reference to that.

Figure 5.7 shows OM images of samples produced with a 63 µm spot size and 300 °C pre-heating temperature. Samples built at this temperature were chosen for OM imaging but could have been substituted with those built at the other two temperatures given the low impact of pre-heating temperature on part density. Figure 5.8 shows the density values obtained for all samples processed using the 63 µm laser spot size as a function of both pre-heating temperature and hatch distance respectively. Figure 5.8 (a) and (c) confirm the findings that the pre-heating temperature has no effect on density whilst (b) and (d) reveal the positive relationship between hatch distance and density.

Despite the increase in density, the highest mean value using the 63 µm spot size was only 99.61% which was obtained for a 100 µm hatch distance and a 50 µm layer thickness. In fact, samples produced with a 25 µm layer thickness struggled to obtain densities over 99% which is evident from the images in Figure 5.7. Furthermore, the OM images reveal that the porosity evident can all be attributed to over-melting due to the spherical nature of the pores. As outlined in section 2.3.1 excessively high energy inputs such as those created during melting with a small spot size leads to improper closure of the keyhole type meltpool during melting due to entrapped gas and/or material evaporation [147]. Furthermore, literature suggests that processing with smaller spot sizes leads to a deeper melt pool [167]. Regarding which, Ma et al. [168] determined that when processing with deep melt pools, the gas at the bottom of the melt pool cannot escape during the rapid solidification which in turn causes pores in the scan tracks.

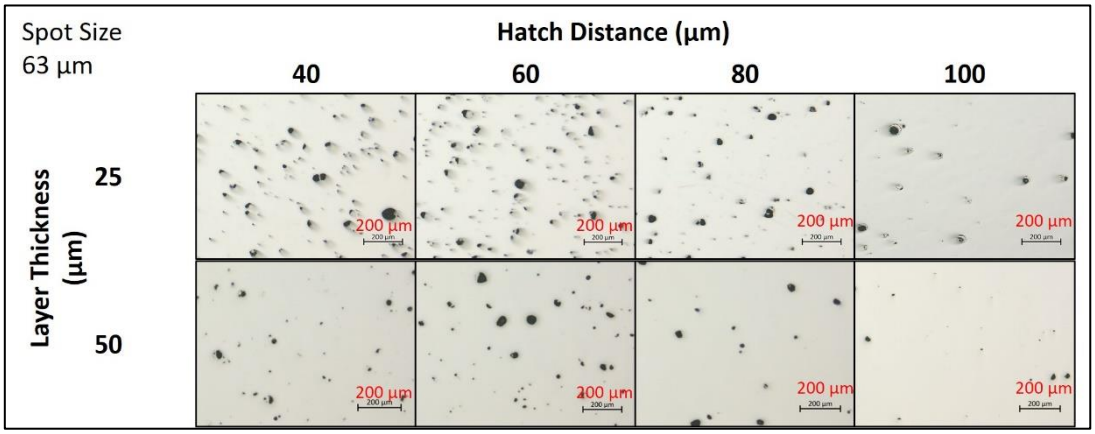

Figure 5.7: OM images of samples produced with a 63 µm laser spot size and various layer thicknesses and hatch distances

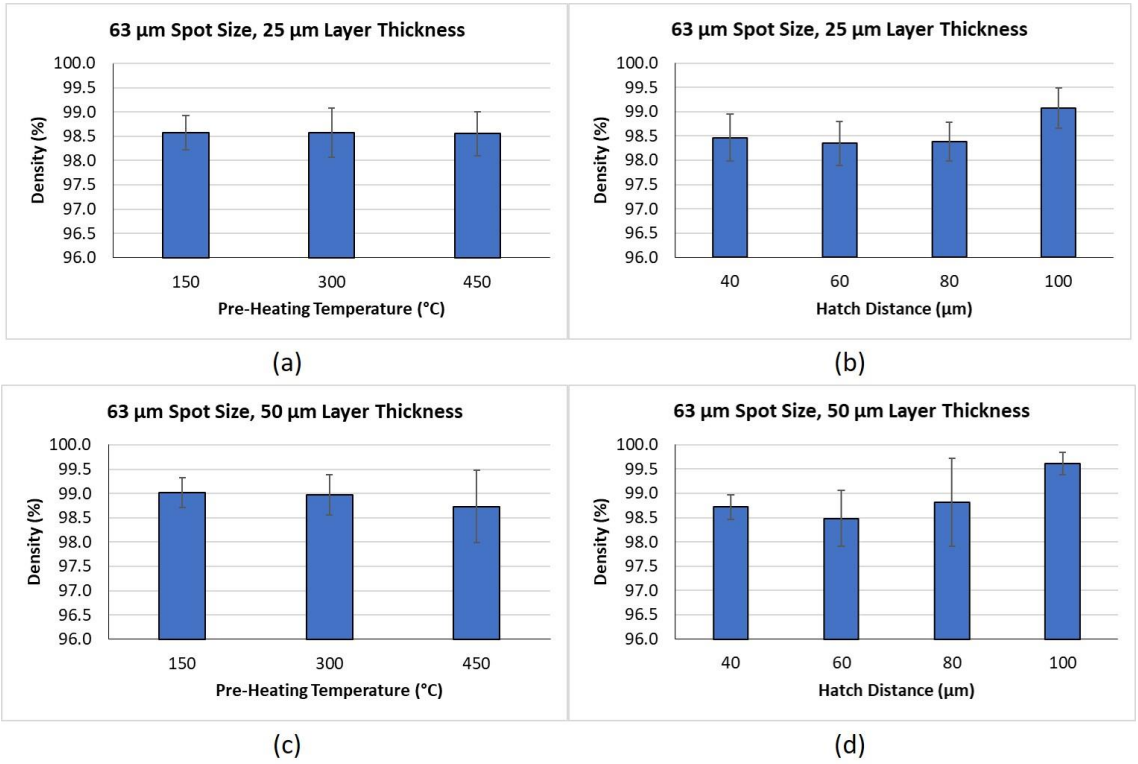

Figure 5.8: Mean densities and standard error obtained for samples produced with a 63 µm laser spot size

Figure 5.9 shows the OM images for samples produced using the larger 170 µm laser spot size. Again, in each case the samples were taken from the 300 °C pre-heating temperature but similar images would be expected from any of the pre-heating temperatures studied. Figure 5.10 shows the density values obtained for all samples produced using a 170 µm laser spot size.

Figure 5.10 (b) reveals that the samples produced with a 25 µm layer thickness show a similar positive relationship to hatch distance as those reported for the 63 µm spot size but with significantly higher density. The highest mean value of 99.84 % was again obtained for the 100 µm hatch distance, yet the mean value of all samples produced with a hatch distance of 60 µm or greater was 99.8 %, a clear increase on any other sample group. These results are also reflected in the OM images in Figure 5.9 for the 25 µm layer thickness which show almost fully dense samples when processing with hatch distances in the range of 60 – 100 µm. The pores evident in the lower section of this range can be attributed to over-melting due to the increased laser-sample interaction time at smaller

hatch distances. However, as hatch distance increases and the laser-interaction time decreases, the number and size of these pores reduce.

Figure 5.10 (c) shows the samples produced with a 50 µm layer thickness as a function of pre-heating temperature. As in other cases, there is no statistical difference between the sample groups and the difference in the mean values can be attributed to stochastic events such as spatter ejection or improper recoating between layers. In contrast to other sample groups, Figure 5.10 (d) shows that the hatch distance has no effect on the mean value of the density with all hatch distances reporting a mean density of 98.8% and above. Figure 5.9 provides some insight where crack-like pores can be observed for all hatch distances within the group. This indicates that irrespective of the difference in interaction times between the laser and sample caused by the change in hatch distance, the energy input was insufficient to achieve full melting. As indicated in literature, the larger spot size of 170 µm leads to a shallower melt pool which provides insufficient energy to fully melt the larger layer thickness of 50 µm [167]. Furthermore, these crack-like pores have been identified as more detrimental to mechanical performance than the spherical pores observed for other sample groups, and hence must be avoided [169].

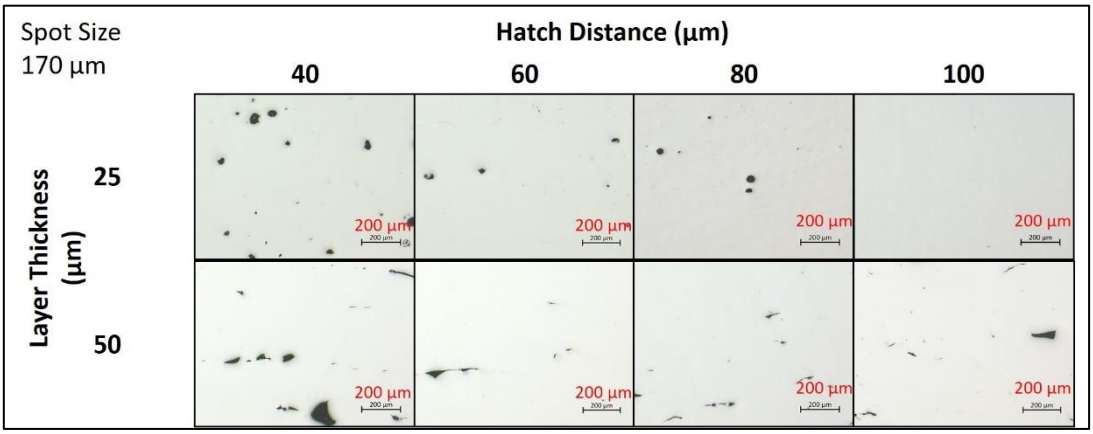

Figure 5.9: OM images of samples produced with a 170 µm laser spot size and various layer thicknesses and hatch distances

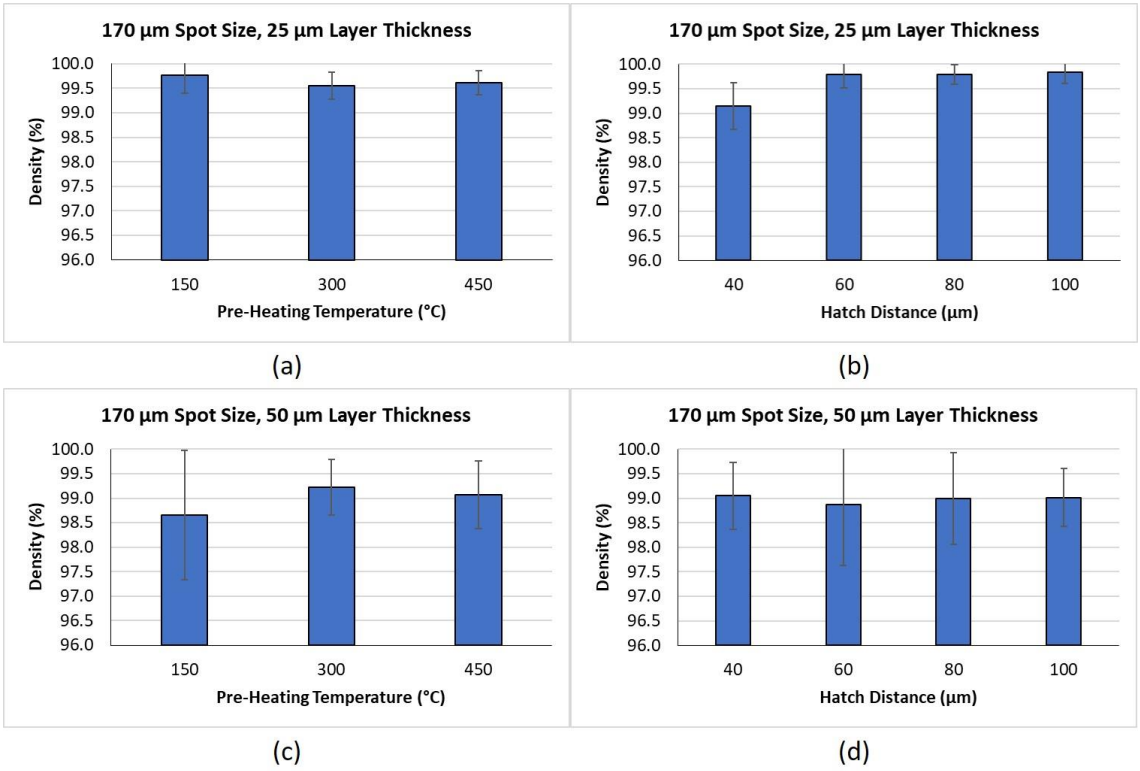

Figure 5.10: Mean densities and standard error obtained for samples produced with a 170 µm laser spot size

5.4.2 Thermal History

The microstructure of SLM processed Ti64 parts is a direct result of the thermal history that the part undergoes. Figure 5.11 presents the critical cooling stages during SLM processing of Ti64 as well as indicative cooling paths of three different microstructures. As a result of scanning by the laser, the Ti64 material is in a molten state at temperatures above the β transus which depend on the processing parameters chosen. Following this, the cooling path can be divided into three critical stages as shown in Figure 5.11;

1. Rapid cooling from the molten state towards the quasi-isothermal temperature of the previously solidified layers
2. Residence time within the quasi-isothermal tempering window until completion of the build
3. Gradual cooling towards room temperature once the build is completed

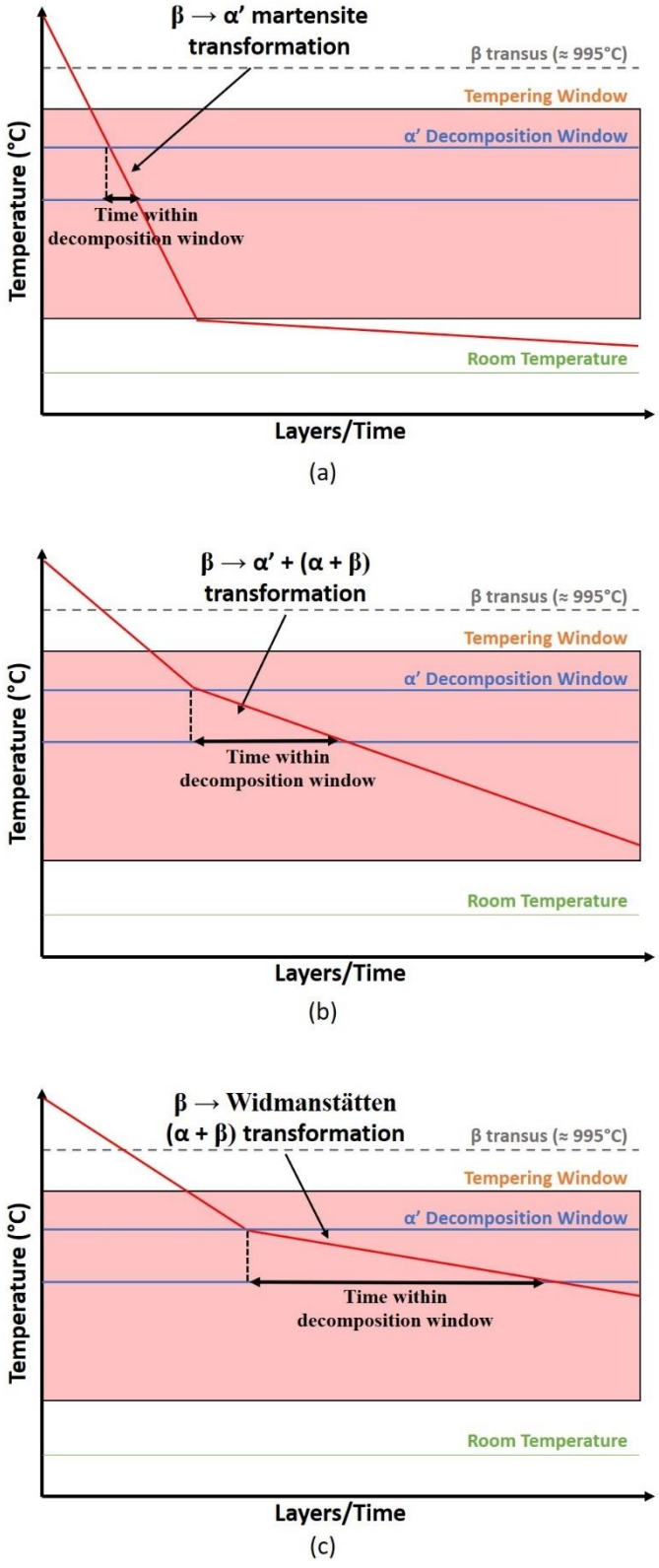

Figure 5.11: Possible cooling paths observed during SLM processing and indication of potential microstructures

The first stage is cooling of the meltpool during solidification towards the quasi-isothermal tempering temperature. The maximum temperature reached and cooling rates during this stage can be regarded as the most critical stage for β grain formation and subsequent transformation to the β phase [170]. The maximum temperature of the meltpool is determined by the process parameters used though the cooling rate in this range remains largely uncontrollable during the first melting of any given layer. During this first melt the β phase will undergo a diffusionless transformation to the α' martensitic phase as the cooling rate – estimated at 10^3 – 10^5 K/sec – is significantly higher than the critical martensitic cooling rate of 410 K/sec [171].

Figure 5.12 shows the thermal profile that each specific point within a part experiences where the process parameters chosen will impact the subsequent re-melting of any given layer. During re-melting the maximum temperature reached is lower than that observed during initial melting and hence over time the cooling rate will be reduced. Hence, by controlling parameters that effect the re-melting of layers during processing, the number of times each layer crosses the β transus temperature and the subsequent cooling rate from that point, can be controlled.

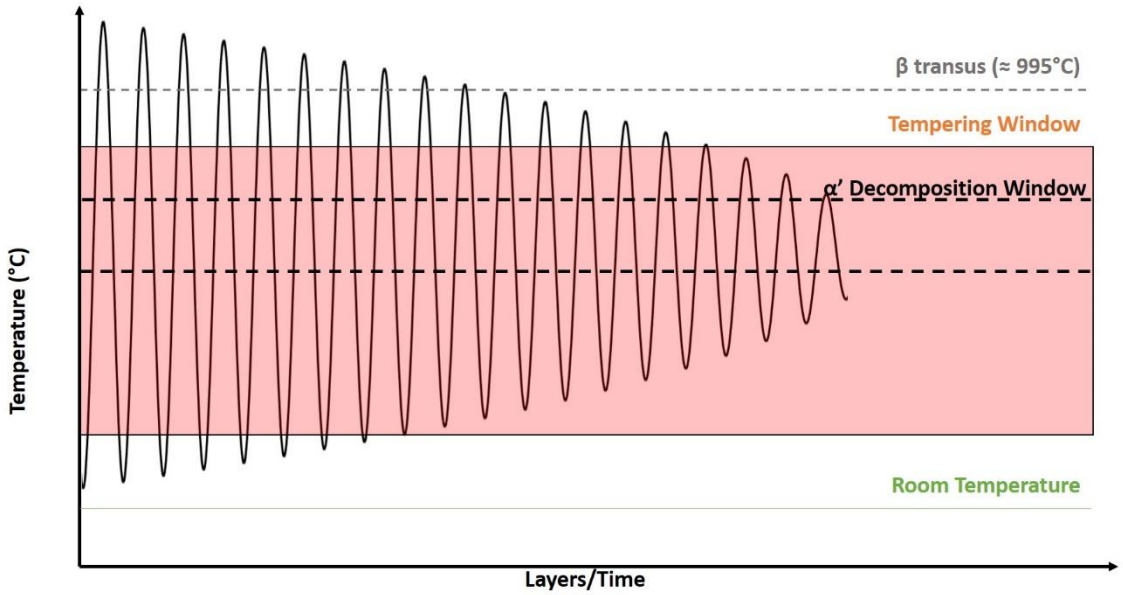

Figure 5.12: Thermal profile in a point of a part which experiences initial melting and subsequent remelting as a function of laser parameters

The second cooling stage consists of a dwell at a quasi-isothermal temperature where the previously melted layers have settled at a quasi-equilibrium temperature. This temperature is dictated by the processing parameters used. For example, increasing pre-heating temperature or interaction time between the laser and material will serve to increase the quasi-equilibrium temperature of the part. For the remainder of this work, this stage will be referred to as the tempering window. Higher temperatures will increase the time spent within the α' decomposition window which has been identified as 600 – 800 °C in previous literature [75], [172]. Increased residence time in the martensitic transformation window has been shown to lead to transformation from the α' martensite phase towards the more stable (α+β) phase as illustrated in Figure 5.11 [149].

The final stage in the cooling regime of SLM processed Ti64 specimens is a gradual cooling to room temperature once the build has completed. With regards to the heated build plate employed in this work, once the build was completed the cooling was controlled to 0.66 °C/min. These three stages outlined broadly represent the cooling regimes experienced by any given point in the build. However, in reality the thermal history is far more complex where various degrees of re-melting or re-heating occur and are dependent on the process parameters. For example, the actual temperature experienced during the tempering window will cycle significantly during the first number of layers after the initial scanning as the subsequent layers are scanned and re-heating and re-melting occurs (Figure 5.12). Over time the sensitivity of any given point to the newly scanned layers diminishes and the quasi-equilibrium is achieved. Controlling these complex interactions during initial scanning and subsequent heating is crucial in controlling the as-built microstructure.

5.4.3 Optical Microscopy

Figure 5.13 shows a graphical representation of the experimental design used to explore microstructural possibilities in the as-built state. Three different microstructures namely, martensitic α', α' + (α+β) and Widmanstätten (α+β) were identified amongst the 36 different parameter sets. The martensitic α' microstructure which is widely reported for SLM processed Ti64 was observed for 26 of the parameter sets examined. Figure 5.14 (a) shows the needle like α' laths within columnar prior-β grains. This structure has been

heavily reported in the literature for as-bult SLM processed Ti64 [57], [70], [74], [90], [113], [115].

The martensitic α' structure was observed for all samples processed at a pre-heating temperature of 150 °C. Further, 66% of samples processed with a pre-heating temperature of 300 °C also presented α' martensite microstructures. Of the 300 °C pre-heating group, only those samples with tight hatch distances and a 63 µm spot size demonstrated any change in the as-built microstructures (Figure 5.13). As noted previously, the α' structure is formed during SLM when the cooling rates during solidification exceed the critical martensitic cooling rate of 410 K/sec [171]. Hence, those samples with a martensitic α' structure were unsuccessful at reducing the cooling rate sufficiently during processing to enable decomposition of the α' structure.

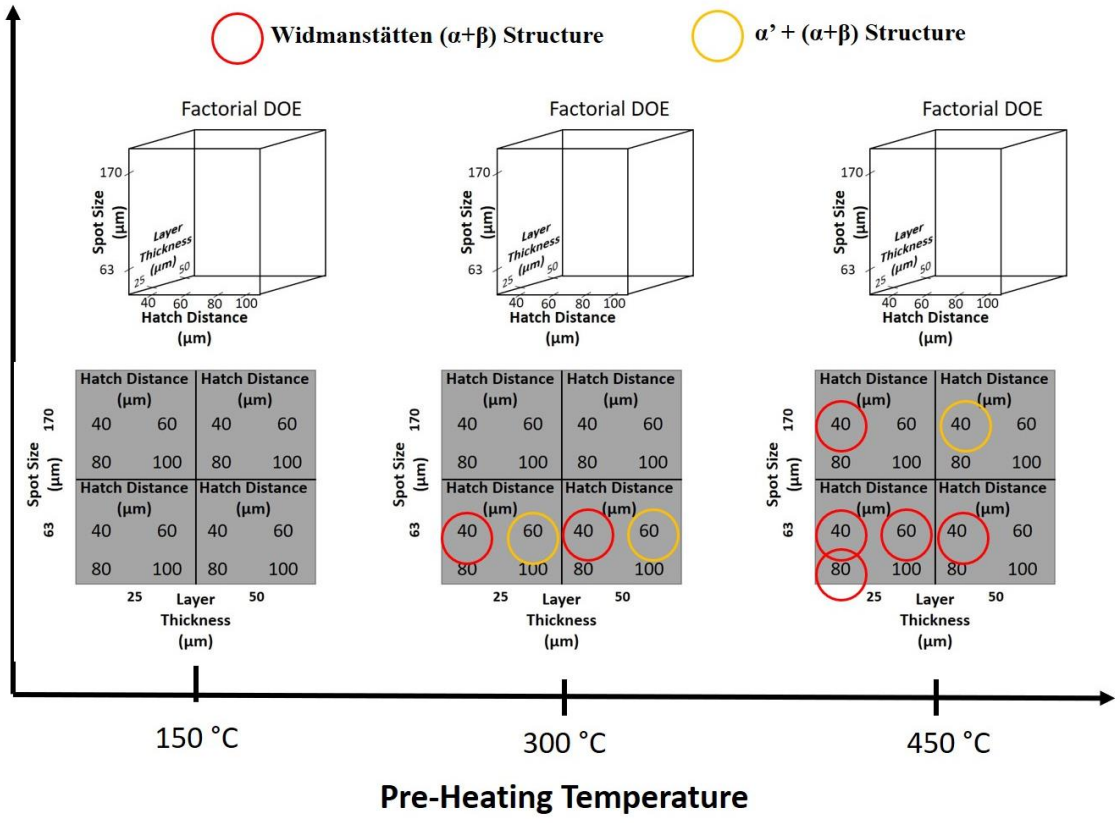

Figure 5.13: Experimental design and indication of subsequent microstructures observed

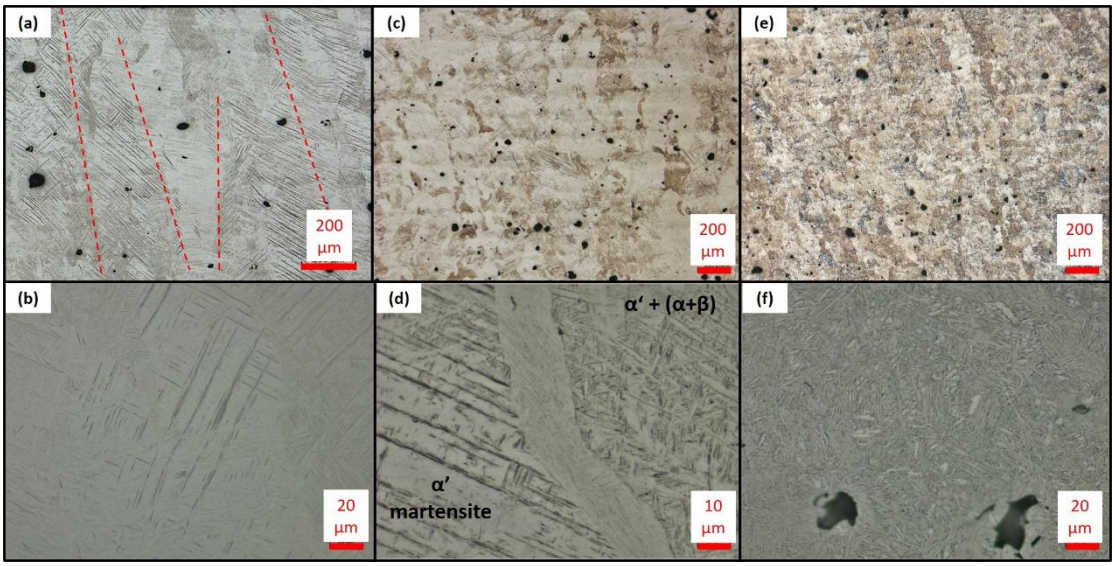

Figure 5.14: Examples of the three different microstructures observed throughout the different parameter combinations. (a)-(b) shows the martensitic α' structure, (c)-(d) shows the partially decomposed α' + (α+β) and (e)-(f) shows the Widmanstätten (α+β) structure

Figure 5.14 (c) – (d) shows the second microstructure observed whereby partial decomposition from the α' martensite structure has taken place. Figure 5.14 (c) shows a low magnification micrograph whereby the typical needle-like structure within columnar prior-β grains is not evident. Instead, small pockets of α' needles sit interspersed amongst larger α grains within a semi-equiaxed β grain structure. Furthermore, under higher magnification as observed in Figure 5.14 (d), some expanded grains can be seen mixed with α' needle-like laths. This structure has been observed for samples within the 300 and 450 °C pre-heating groups. In the case of the 300 °C group, this partial decomposition has been observed where a 63 µm spot size and 60 µm hatch distance has been used for both the 25 and 50 µm layer thicknesses. These tighter hatch distances increase the area of the powder bed that undergoes re-heating which, in combination with the pre-heating of 300 °C, have enabled an increase in the quasi-equilibrium temperature within the tempering window during processing. This in turn facilitates a reduction in the cooling rate such that the residence time within the α' decomposition window is increased sufficiently to enable minor α' decomposition.

Finally, Figure 5.14 (e) – (f) shows the low and high magnification micrographs of the Widmanstätten (α+β) structure which was observed for 7 different parameter sets as observed in Figure 5.13. Figure 5.14 (e) shows that, as was the case with the α' + (α+β)

structure aforementioned, the columnar prior-β grains are no longer present. Rather, the microstructure consists of α colonies inside large semi-equiaxed, previous β grains (Figure 5.14 (c) and (e)). This difference in the β grains is indicative of extensive growth at temperatures above the β transus temperature [117]. Following processing above the β transus the Widmanstätten (α+β) structure will form where intermediate cooling rates of <20 °C/sec are present [173]. The Widmanstätten (α+β) structure is formed due to the preferential growth of the α phase parallel to the (110) crystallographic plane of the β phase according to the Burgers relationship given in Equation 5.2 [173]–[175]. Due to the fast growth possible along these crystallographic planes, the α phase is formed as flat plates or fine lamellae as can be seen in Figure 5.15 (a).

$$(1\ 1\ 0)_{\beta} \leftrightarrow (0\ 0\ 0\ 1)_{\alpha} \qquad \text{Equation 5.2}$$

$$\langle 1\ \bar{1}\ 1\rangle_{\beta} \leftrightarrow (0\ 0\ 0\ 1)_{\alpha}$$

Gil et al. [173] examined the formation of the Widmanstätten structure as a function of cooling rate for the Ti64 alloy. Figure 5.15 (b) shows the comparative microstructure they observed when cooling Ti64 samples from 1100 °C at a rate of 0.81 °C/sec. Increases in the pre-heating temperature serves to reduce the cooling rate during solidification which is reflected in the observed microstructures. As illustrated in Figure 5.13, a number of samples processed with a 300 °C pre-heating temperature presented a Widmanstätten (α+β) structure. However this represented only 2 of the 12 parameter sets, whilst an increase in the pre-heating temperature to 450 °C resulted in 5 of the 12 parameter sets processed displaying a Widmanstätten (α+β) structure.

Examination of Figure 5.13 reveals that decreasing layer thickness, hatch distance and laser spot size all had a positive influence on the decomposition from α' martensitic to Widmanstätten (α+β) microstructures. Table 5.1 shows that a reduction in these parameters all serve to increase energy input into the process by measure of the ED and power density variables. Further, the reduction in the hatch distance serves to increase the percentage of the powder bed that undergoes re-melting which gives greater opportunity for β grain growth. Combined these effects all serve to increase the quasi-isothermal

temperature of the tempering window. Furthermore, reducing layer thickness from 50 to 25 µm serves to approximately double the build time. This means that whilst each new layer is subsequently being scanned, the bulk that has already been solidified is being tempered for a longer duration.

The combination of these three parameters and their subsequent effect in increasing the tempering window temperature can be compared to heat treatment below the β transus temperature. Heat treatment studies of Ti64 have shown that an increase in residence time below the β transus temperature results in increased α and β grain size [169]. Plaza et al. [166] determined that heat treating Ti64 in the (α+β) field results in a microstructure that consists of α grains, whose size depends on the temperature and duration of the treatment. Furthermore, Vrancken et al. [117] observed a greater influence of residence time for treatments above the β transus temperature. At the elevated temperatures, the β grain size significantly increases which enables the α colony size to increase. Reduction in the hatch distance increases the time spent above the β transus during processing which facilitated transformation of the prior-β grains into the semi-equiaxed structure that was observed for the α' + (α+β) and Widmanstätten (α+β) structures illustrated in Figure 5.14 (c) – (f).

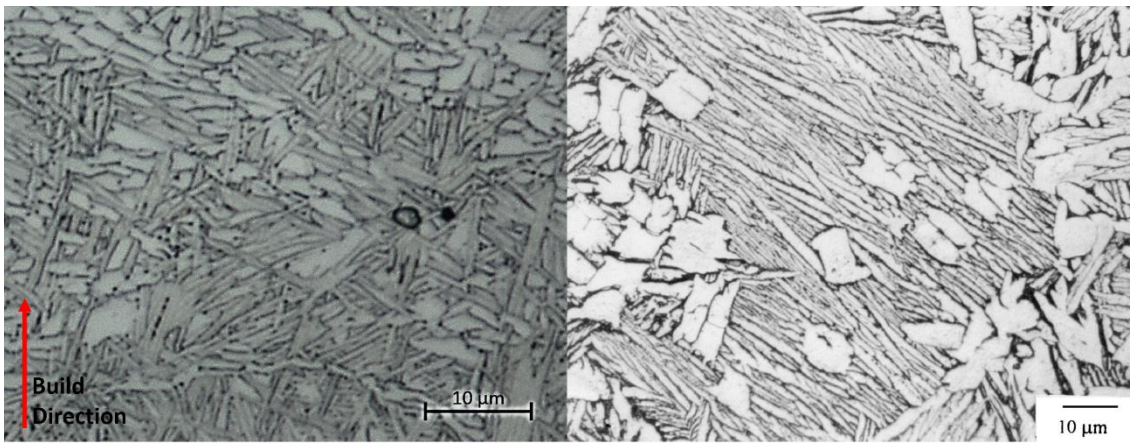

Figure 5.15: (a) Higher magnification image of Widmanstätten microstructure observed for sample built with 40 µm hatch distance at a pre-heating temperature of 450 °C (b) Widmanstätten structure observed by Gil et al. [173].

5.4.4 SEM

Figure 5.16 shows high magnification SEM micrographs for the three microstructures observed through OM imaging. Figure 5.16 (a) illustrates the α' martensitic structure obtained for the vast majority of the samples. Figure 5.16 (b) provides high magnification images of the α' + (α+β) observed initially in Figure 5.14 (d). This structure shows the α' laths interspersed amongst regions of α' + (α+β) where some of the martensite has decomposed towards a (α+β) structure. Finally Figure 5.16 (c) shows the high magnification image of the Widmanstätten (α+β) structure observed in Figure 5.15 (a). White dot and rod β phase is observed along and between the enlarged α phase grains indicating the increased volume fraction of β phase in the sample in comparison to the other two microstructures observed. Xu et al. [149] reported a similar microstructure for a SLM processed Ti64 sample heat treated at 800 °C for four hours.

Figure 5.17 shows the Pareto chart where the response is the primary α lath thickness, and the variables are the parameters highlighted in the DOE (section 5.2). Chapter 2 outlines how an increase in the α lath thickness is correlated with an increase in fracture strain. The results indicate that pre-heating temperature is the only statistically significant variable acting on the primary α lath thickness at a 0.05 significance level. However, notable effects are also observed for the laser spot size, as well as the relationship between the laser spot size and the layer thickness.

Figure 5.18 (a) shows the main effects for the relationships between the process parameters studied and the primary α lath thickness. Independently, primary α lath thickness appears to be insensitive to a change in the layer thickness. Reducing the hatch distance from 100 to 40 µm serves to increase the mean primary α lath thickness from 0.7 to 0.77 µm whilst hatch distances between these are open to variations. Spot size shows a negative relationship to the primary α lath thickness with a difference of 0.1 µm observed between the means of samples produced using 63 and 170 µm respectively. The trend observed for pre-heating temperature is positive where increases in the pre-heating temperature from 150 – 450 °C led to an increase in the mean primary α lath thickness from 0.66 to 0.85 µm.

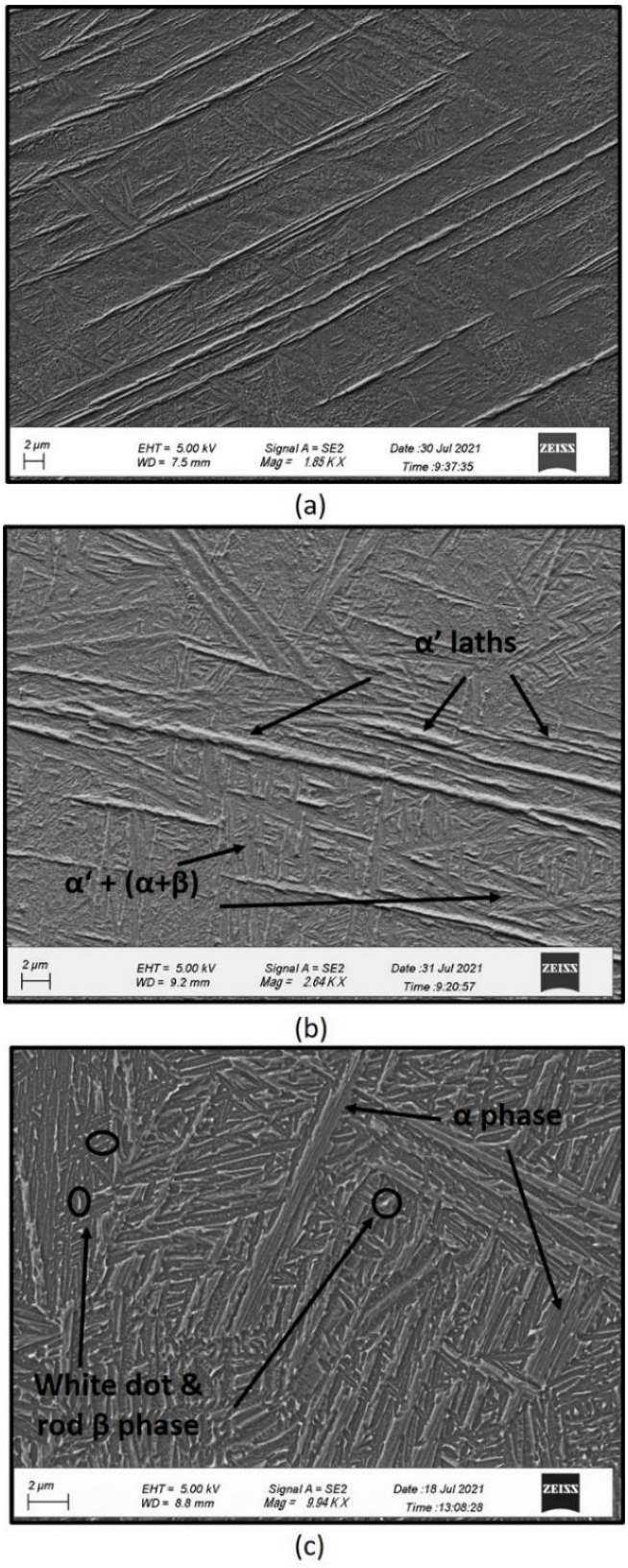

Figure 5.16: SEM micrographs showing the microstructures of (a) α' martensite (b) α' + (α+β) and (c) Widmanstätten (α+β)

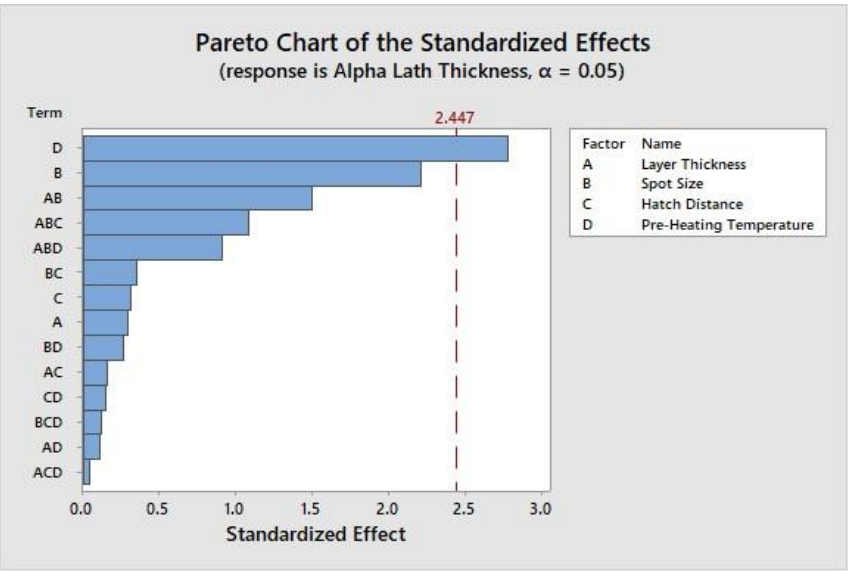

Figure 5.17: Pareto chart showing the effects of the studied parameters on the primary α lath thickness

Figure 5.19 shows the primary α lath thickness presented as a function of pre-heating temperature divided and sub-divided by layer thickness and spot size respectively. This, along with the interaction plot (Figure 5.18 (b)) enables evaluation of the effect of the pre-heating temperature as well as the relationship between spot size and layer thickness as identified in the Pareto chart (Figure 5.17). Figure 5.19 shows that the primary α lath thickness is insensitive to an increase in pre-heating temperature from 150 – 300 °C for most sample groups. The one exception to this is the samples produced using a 63 µm spot size and 50 µm layer thickness for which positive linear relationship between pre-heating temperature and primary α lath thickness can be observed.

Figure 5.19 (a) shows that the primary α lath thickness is less sensitive to a change in spot size for samples produced with a 25 µm layer thickness where the mean primary α lath thickness value drops by only 0.04 µm given an increase from 63 to 170 µm in the laser spot size. Furthermore, examining the 25 µm layer thickness group yields no statistical difference for samples produced with varying spot sizes for pre-heating temperatures of 150 and 300 °C respectively. In comparison, at the highest pre-heating temperature of 450 °C a substantial increase of 0.15 µm was observed for the 63 µm spot size.

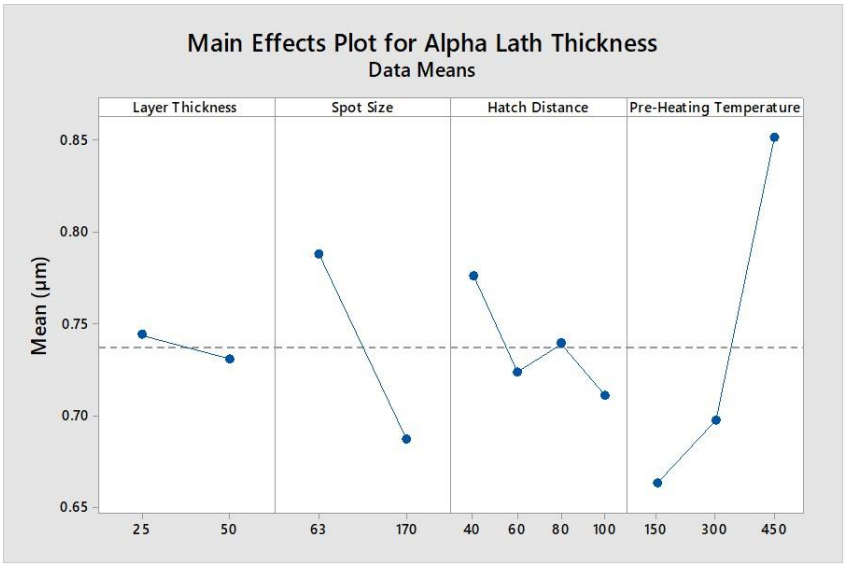

(a)

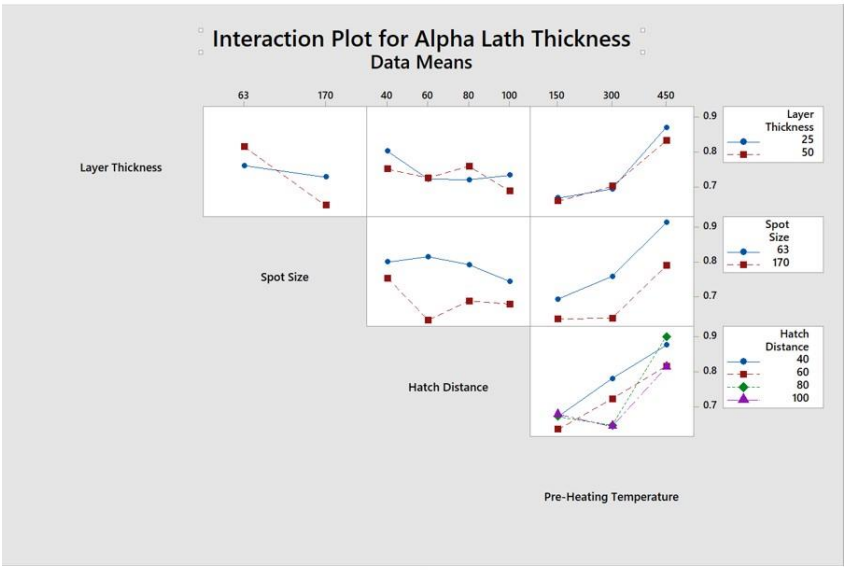

(b)

Figure 5.18: (a) Main effects and (b) interaction plots for the effect of each studied parameter on primary α lath thickness

The interaction plot in Figure 5.18 (b) confirms that the spot size has a more significant impact on primary α lath thickness when processing with a 50 µm layer thickness whereby a mean difference of 0.17 µm was observed between the two spot sizes. Figure 5.19 (b) shows that this holds for all pre-heating temperatures whereby a statistically significant difference can be observed between the 63 and 170 µm spot sizes for all pre-heating temperatures examined. Furthermore, samples produced with a 63 µm spot size

and 50 µm layer thickness demonstrated the greatest mean primary α lath width of any other group analysed. However, the single parameter setting that produced the greatest primary α lath thickness used a 25 µm layer thickness, 63 µm spot size and 450 °C pre-heating temperature.

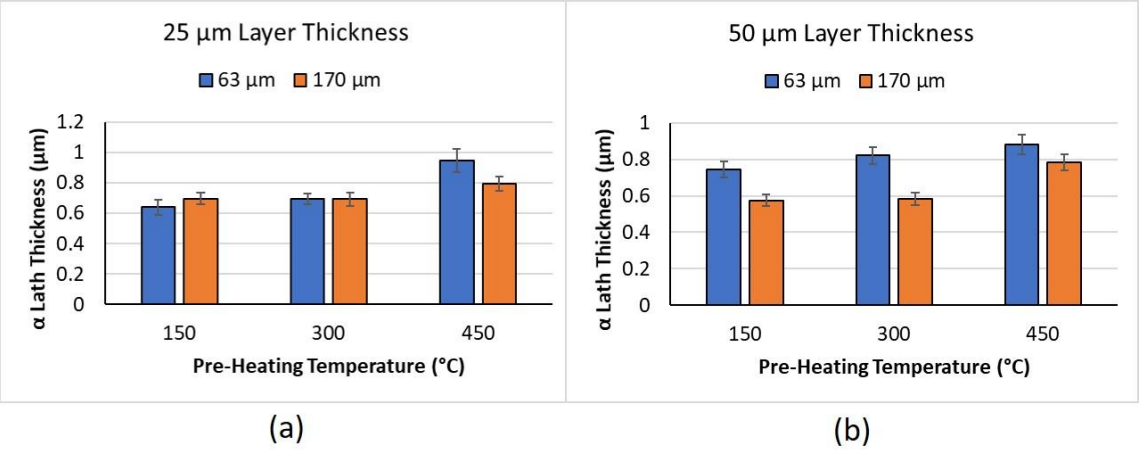

Figure 5.19: Primary α lath thickness and standard error presented as a function of pre-heating temperature for (a) 25 µm and (b) 50 µm layer thicknesses respectively

Results reported above indicate that increasing the pre-heating temperature to 450 °C and decreasing the laser spot size from 170 to 63 µm facilitate increased primary α lath thickness. The increase in pre-heating temperature serves to increase the quasi-equilibrium temperature of the part following scanning which leads to reduced cooling rates hence giving increased time for expansion of the α grains. Decreasing the laser spot size to 63 µm serves to increase the power density as reported in Table 5.1. This in turn increases the total energy absorbed into the powder bed which leads to an increase in the meltpool temperature. This increase in meltpool temperatures enables primary α lath expansion in two ways. Firstly, the increase in temperature above the β transus temperature leads to increased β grain expansion which is the limiting factor for the α grain size. Thus increased β grain expansion leads to larger α grain size. Secondly, the increase in meltpool temperature also increases the quasi-isothermal conditions within the part. Hence the subsequent layers are subjected to lower cooling rates.

The same benefit of lowering the spot size is not realised within the 25 µm layer thickness sample group. This can be attributed to the increased cooling rates observed when processing with lower layer thicknesses [74]. In fact, at the lower pre-heating

temperatures, reducing the spot size appears to be detrimental to the primary α lath thickness. This results from the combined effects discussed above whereby the reduction in laser spot size leads to an increase in the meltpool temperature however, the reduction in layer thickness increases the cooling rates. In such circumstances finer grains would be expected as can be observed for samples processed with the 150 °C pre-heating temperature. Increasing the pre-heating temperature to 450 °C appears to reduce the cooling rates sufficiently such that the increase in meltpool temperature becomes beneficial due to advantages of the increase in temperature above the β transus as previously discussed.

Analysing the 50 µm layer thickness samples appears to confirm this. The increased layer thickness facilitates a lower cooling rate which results in greater α lath thicknesses for samples produced with the 63 µm spot size. Finer grains are observed for the 170 µm spot size as the lower power density (Table 5.1) reduces the overall energy input which results in a lower temperature meltpool which is not conducive to primary α lath expansion. Hence, primary α lath expansion is determined by two factors. Firstly, increasing the meltpool temperature and secondly controlling the cooling rates sufficiently to prevent fine martensitic grains forming.

5.4.5 X-Ray Diffraction

Phase analysis of the material was conducted using XRD analysis according to processes outlined in section 3.5.3. Figure 5.20 shows a sample of XRD spectra scanned for one specimen over (a) the full range scanned and (b) a reduced range between 33 – 45 2θ. The XRD spectra for each parameter set broken down by pre-heating temperature are available in Appendix A. The spectra observed in Figure 5.20 are characteristic of SLM produced Ti64 whereby HCP α or α' phase peaks can be indexed according to published research with matching XRD patterns [176]–[178]. Generally in as-built SLM processed Ti64 specimens no BCC β peaks are observed. Accordingly the β volume percentage of all samples in this work was below the threshold that could be measured using the MAUD [158] software.

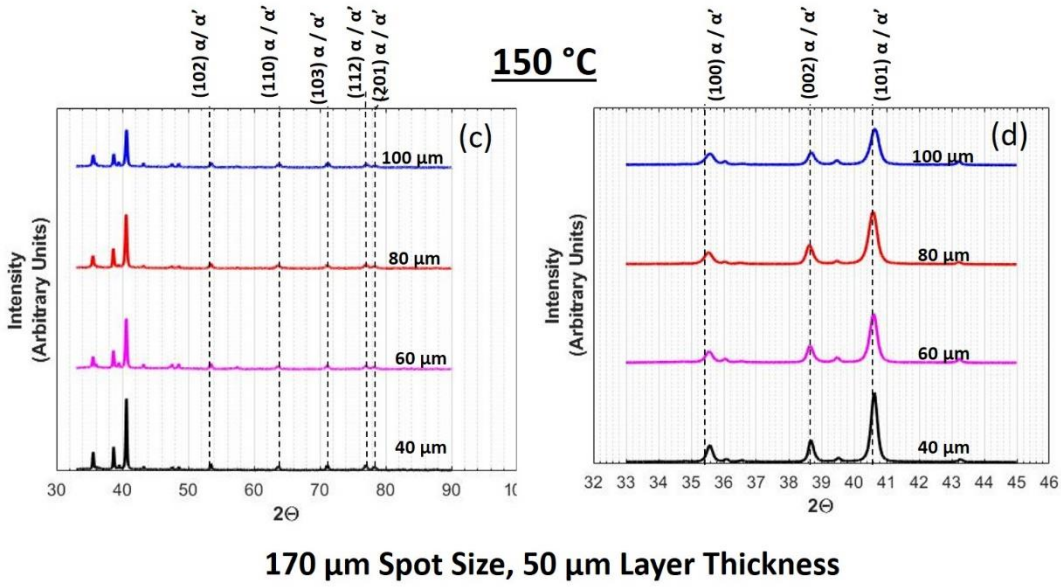

Figure 5.20: Sample XRD spectra indicating the indexed α/α' peaks plotted for (a) the full scanned range and (b) reduced 33 – 45 2θ

Analysis of the XRD spectra through the W-H method as outlined in section 3.5.3 enables evaluation of the HCP lattice as a function of the pre-heating temperature, layer thickness, spot size and hatch distance respectively. The lattice strain of each sample was calculated using the slope of the W-H plot where a positive slope indicates the presence of tensile strain in the material [179]. The α/α' peaks corresponding to the (002) and (101) planes as illustrated in Figure 5.21 were examined to determine the lattice constants a and c through Reitveld refinement. Finally, curve fitting of the XRD spectra was completed according to the process outlined in section 3.5.3 which enables evaluation of the FWHM, peak intensity and peak position respectively.

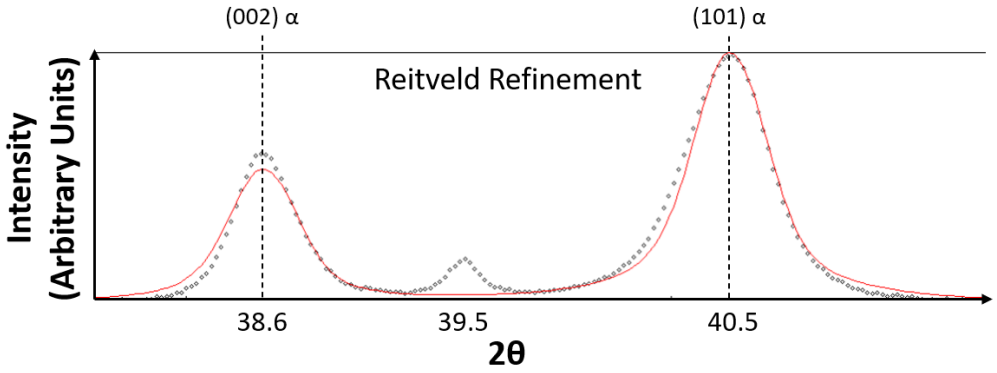

Figure 5.21: Reitveld refinement conducted for the (002) and (101) α planes

Figure 5.22 and Figure 5.23 plot the XRD spectra for two reduced ranges between 37 – 42 and 52 – 58 2θ for all the samples processed subdivided by laser spot size and layer thickness. In contrast to Figure 5.20 which plots the intensity of the spectra on a linear scale, Figure 5.22 and Figure 5.23 plot the peak intensity on the logarithmic scale which enables analysis of subtle changes in peaks.

Figure 5.22 (a) – (b) and Figure 5.23 (a) – (b) respectively show the (002)α/α' and (101)α/α' peaks as previously indexed. Furthermore, a small peak is present close to 39.5 2θ which has been attributed to the resin that is used to hold the sample as outlined in section 3.5.3. However, the 2θ position of the (110) BCC β peak also sits close to 39.5 2θ. Examination of Figure 5.22 (a) – (b) and Figure 5.23 (a) – (b) reveals that a number of peaks in this 2θ position show deviations from the peak generated by the resin and thus can be attributed to the (110)β peak formation.

As indicated by the solitary red arrow in Figure 5.22 (a), evidence of the (110)β peak can only be observed for one sample processed using a 170 µm spot size. Similarly, analysis of the (200)β peak is presented in Figure 5.22 (c) – (d) and Figure 5.23 (c) – (d). Again the use of a 170 µm spot size is not conducive to the formation of β phase in the as-built state with only two samples demonstrating minor indications of the presence of the (200)β peak as shown by the arrows in Figure 5.22 (c). Both the (110)β and (200)β were evident for samples processed with a 40 µm hatch distance and 25 µm layer thickness at a pre-heating temperature of 450 °C. Although some evidence of the (200)β was observed for the same parameters at pre-heating temperatures of only 300 °C which indicates a certain level of β phase in samples processed with these conditions.

The parameters for which the β phase can be observed result in increased re-melting of previous layers and high meltpool temperatures due to the tight hatch distance and small layer thickness. In combination with high pre-heating temperatures, low cooling rates from above the β transus temperature and an increased quasi-isothermal temperature within the tempering window are facilitated. In contrast, the lack of β phase in 50 µm samples as observed in Figure 5.22 (b) and (d) can be attributed to the lower meltpool temperature and reduction in previous layer re-melting during processing which is not conducive to β grain expansion. Thus when processing with a 170 µm spot size, the β

phase is only identifiable when pre-heating temperature, ED and power density values are maximised to enable a high meltpool temperature and low cooling rates.

In contrast to the solitary (110)β peak observed for 170 µm spot size samples, Figure 5.23 (a) – (b) illustrates 6 peaks where the (110)β peak can be observed from the XRD spectra of samples produced with a 63 µm spot size. Similarly, the (200)β peak was identified for 12 samples within the 63 µm spot size group (Figure 5.23 (c) – (d)). Examining the process parameters of samples with β phase identifiable reveals significant overlap between the (110)β and (200)β peaks.

With regards to the (110)β peak, both layer thicknesses enable β phase formation for hatch distances of 40 µm providing the pre-heating temperature is 300 °C or greater. This implies that the decrease in hatch distance is (a) facilitating higher meltpool temperatures where β grains can expand rapidly and (b) reducing the cooling rates such that a $\beta \rightarrow \alpha$ transformation will occur. Furthermore, within the 25 µm layer thickness group (110)β peaks can also be observed for greater hatch distances up to 80 µm providing the pre-heating temperature is 450 °C. Although smaller layer thicknesses have been linked with increased cooling rates the reduction in layer thickness will also facilitate greater re-melting of previous layers [74]. This means that the material is experiencing greater opportunity for β grain growth whilst the higher pre-heating temperature reduces the cooling rate sufficiently to compensate for the higher cooling rates associated with larger hatch distance.

Similar results can be observed for the (200)β peak in Figure 5.23 (d). In fact all samples that indicate presence of the (110)β peak also indicate presence of the (200)β peak. Furthermore, the (200)β was also identified for a greater range of pre-heating temperatures and hatch distances which indicates a certain level of β phase formation within these samples. As previously stated, reducing the spot size and hatch distance both serve to increase the meltpool temperature whilst increasing pre-heating temperature serves to decrease the cooling rate. Hence the β phase has formed in samples which have a high meltpool temperature but sufficiently slow cooling rates such that a $\beta \rightarrow \alpha$ or $\beta \rightarrow \alpha+\alpha'$ transformation can take place. In general, it can be concluded that a small spot size, tight hatch distance, small layer thickness and high pre-heating temperature are conducive to increasing the β volume fraction in the as-built state of SLM processed Ti64 samples.

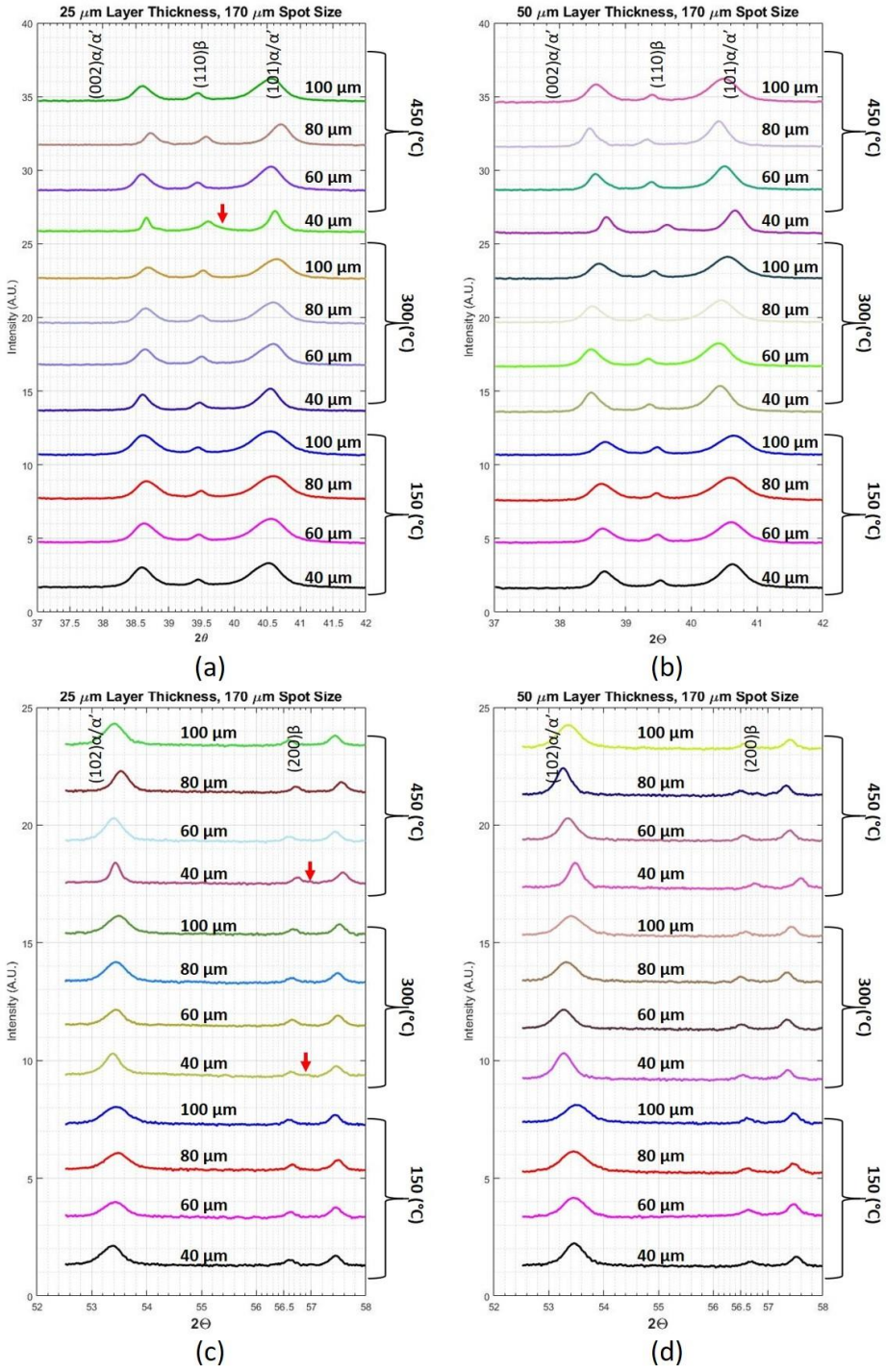

Figure 5.22: XRD spectra plotted for the reduced ranges of 37 – 42 2θ (a) and (b) as well as52 – 58 2θ (c) and (d) for samples processed with a 170 μm spot size and layer thicknesses of 25 and 50 μm respectively. The hatch distance of each sample is labelled, and the pre-heating groups are identified

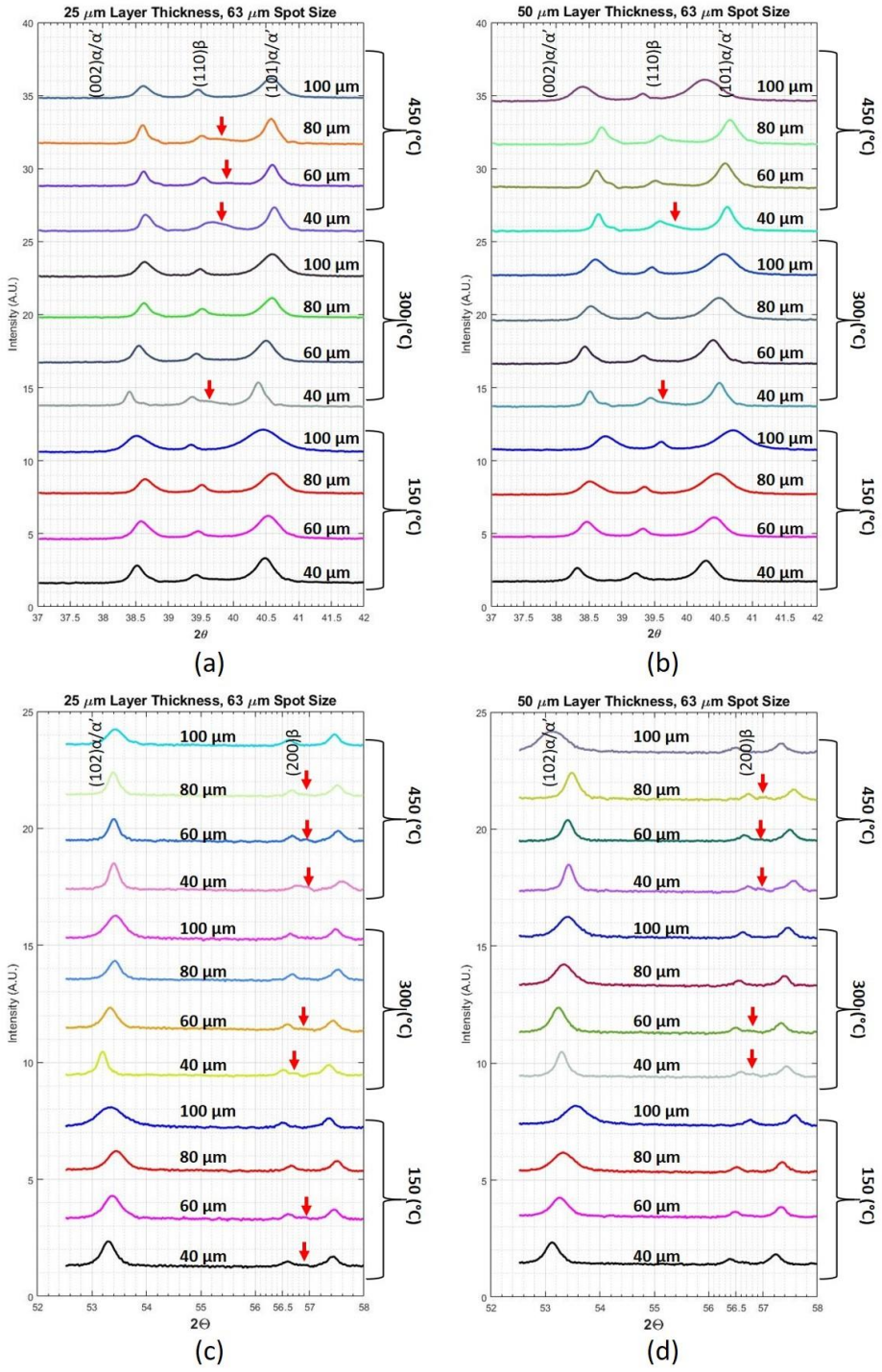

Figure 5.23: XRD spectra plotted for the reduced ranges of 37 – 42 2θ (a) and (b) as well as52 – 58 2θ (c) and (d) for samples processed with a 63 μm spot size and layer thicknesses of 25 and 50 μm respectively. The hatch distance of each sample is labelled, and the pre-heating groups are identified

5.4.5.1 Crystal Lattice Strain

Crystal lattice strain can provide a valuable insight into the phase composition of Ti64. As outlined in section 2.2 the equilibrium α phase has a HCP crystal structure which has theoretical lattice parameters of a = 2.935 Å and c = 4.685 Å. However, the α' martensitic phase also presents a HCP structure but is compressed in comparison to the equilibrium α phase with lattice parameters of a = 2.933 Å and c = 4.655 Å respectively [45]. Thus, increases in tensile lattice strain are indicative of decomposition of the α' structure whereby the compressed martensite crystal structure is expanding towards that of the α phase.

Figure 5.24 and Figure 5.25 show the Pareto chart, main effects plot and interaction plot where the response is lattice strain, and the inputs are pre-heating temperature, spot size, layer thickness and hatch distance. The Pareto chart indicates that pre-heating temperature, hatch distance and spot size in descending order have a statistically significant effect on the lattice strain of the as-built parts at a 0.05 significance level. Furthermore, the relationships between layer thickness and spot size, spot size and hatch distance and hatch distance and pre-heating temperature also statistically influence the lattice strain in the as-built parts.

From the main effects plot in Figure 5.25 (a), the positive strain values show that all samples analysed exhibited a positive slope from the W-H analysis indicating the lattice expanding. Furthermore, Figure 5.25 confirms that independently the layer thickness has fundamentally no effect on the lattice strain. In contrast the other three variables all demonstrate sharp slopes indicating the level of impact of each factor. Spot size and hatch distance both show negative relationships to the lattice strain whilst the pre-heating temperature has a positive relationship.

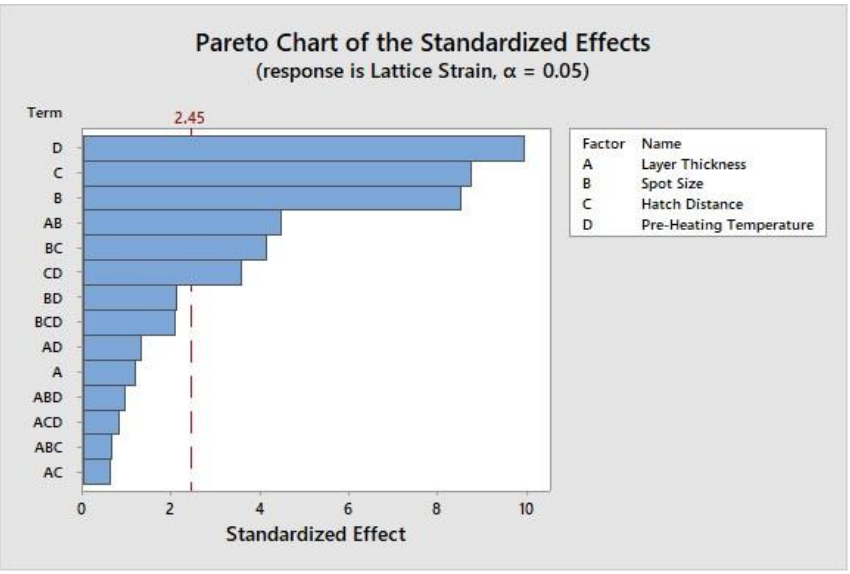

Figure 5.24: Pareto chart showing statistical significance of parameters on the lattice strain

Figure 5.26 presents the lattice strain as a function of the pre-heating temperature, the most sensitive parameter according to the Pareto chart (Figure 5.24). The positive trend is observed in each group with the samples produced using a 450 °C pre-heating temperature showing strain values 2.05 – 2.93 times greater than those processed with 150 °C for each of the groups respectively. These large lattice strains are indicative of the significant lattice expansion obtainable at higher pre-heating temperatures. Similar results have been reported in the literature where a comparable increase in lattice strain was observed during heat treatment in the same temperature window of 150 – 450 °C [161].

Examining the difference between groups in Figure 5.26 provides insight into the relationship between the spot size and layer thickness identified in the Pareto chart (Figure 5.24). For both layer thicknesses, samples processed with the lower 63 µm laser spot size led to statistically significant increases in the observed lattice strain. Though, it must be noted that the effect of the change in spot size on lattice strain is markedly greater in samples processed with a 25 µm layer thickness than for those which used 50 µm. Specifically within the group of 25 µm layer thickness, the combination of a low spot size and 450 °C pre-heating temperature produced a mean lattice strain of 0.017 microstrain which was significantly greater than any other group analysed.

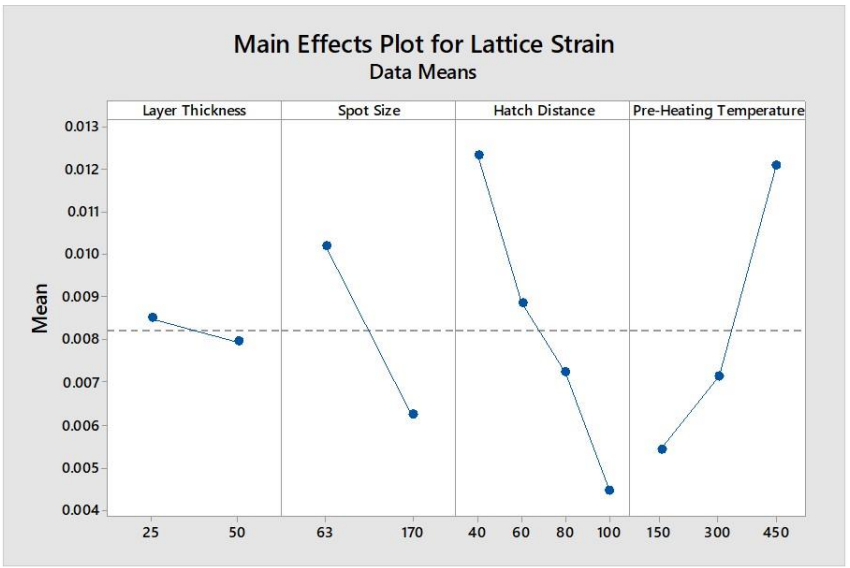

(a)

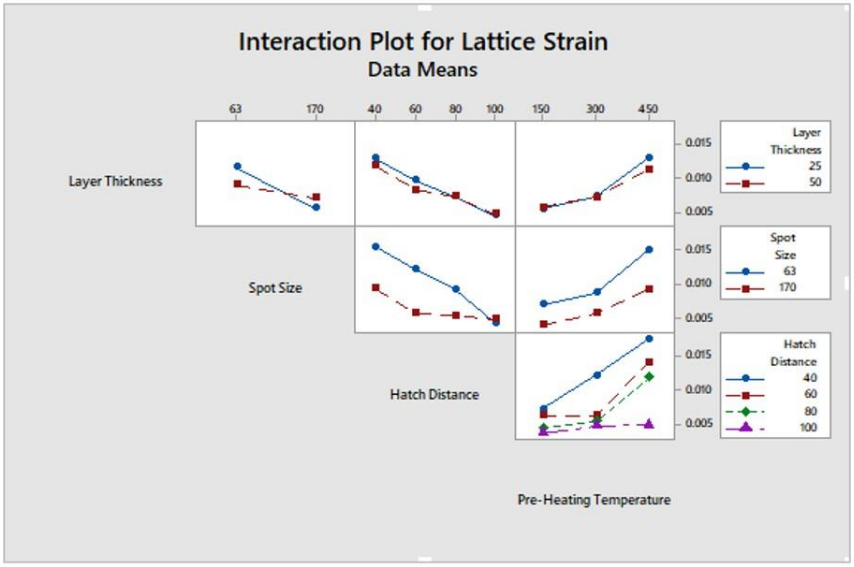

(b)

Figure 5.25: (a) Main effects and (b) interaction plots for the effect of each studied parameter on lattice strain

Figure 5.27 presents the lattice strain as a function of the hatch distance. This, along with the interaction plot (Figure 5.25 (b)) enables evaluation of the significant relationship between hatch distance and spot size as identified in the Pareto chart (Figure 5.24). Similarly to the interaction with the layer thickness, the smaller 63 µm spot size resulted in a greater lattice strain for all hatch distances, apart from the samples produced using a hatch distance of 100 µm for which both groups are approximately equal. Furthermore,

examining hatch distance independently shows that reducing the hatch distance from 100 to 40 µm led to increased lattice strain values, irrespective of the other process parameters employed. Explicitly, the hatch distance shows an almost linear relationship to lattice strain for samples processed with a 63 µm spot size. In contrast, the samples processed using the larger 170 µm spot size demonstrated no significant differences in lattice strain for samples produced with hatch distances between 60 – 100 µm. Meanwhile sharp increases in lattice strain can be observed for the 40 µm hatch distance sample groups.

The final significant relationship identified in the Pareto chart between the hatch distance and pre-heating temperature can be observed from the interaction plot in Figure 5.25 (b). This shows that samples produced with a 40 µm hatch distance show an approximate linear relationship between pre-heating temperature and lattice strain. Increasing pre-heating temperature from 150 – 450 °C led to an increase in lattice strain from 0.007 to 0.018 microstrain. In contrast the remaining hatch distance groups appear to be insensitive to increases in pre-heating temperature from 150 to 300 °C. Further increase in pre-heating temperature to 450 °C facilitated substantial increases from 0.006 to 0.013 microstrain for hatch distances of 60 and 80 µm respectively. Though a small increase can be observed, samples produced with a 100 µm hatch distance appear to be insensitive to an increase in pre-heating temperature. Further, no large lattice strain values are observed at this hatch distance irrespective of the other parameters used. This implies that lattice expansion is only possible, though to various degrees, for samples produced using hatch distances between 40 – 80 µm.

The increases in lattice strain observed for increases in pre-heating temperature or by reducing hatch distances, spot sizes and layer thicknesses can be attributed to their combined effect upon maximum temperature, residence time and cooling rates during processing. Higher pre-heating temperatures serve to increase the quasi-equilibrium temperature of the part as additional layers are scanned. This facilitates lower cooling rates following scanning but also increased temperature that the bulk part experiences in the tempering window.

The increase in ED and power density values obtained through reducing the hatch distance and laser spot size respectively appear to have a greater affect for the lower layer thickness. This can be observed from the magnitude of the lattice strains but also the

difference between the laser spot sizes. Reducing the spot size when processing with 50 µm layer thickness only has a minor impact on the lattice strain whilst the same change when using a 25 µm layer thickness serves to more than double the lattice strain observed in most cases. As previously stated, increasing the energy input serves to increase both the maximum temperature during processing but also the semi-equilibrium temperature at which the solidified part is tempered. The increase in maximum temperature serves to increase the β phase formation above the β transus temperature. Furthermore, the increase in the semi-equilibrium temperature experienced within the tempering window leads to increased residence time within the α' decomposition window. Increasing residence time at these temperatures has been proven to enhance a β → α transformation resulting in a more stable (α+β) structure.

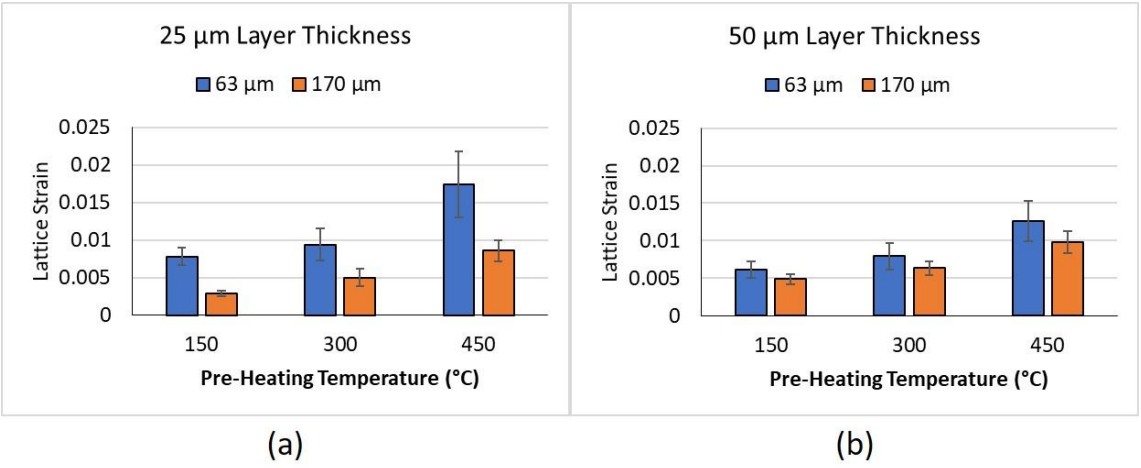

Figure 5.26: Lattice strain presented as a function of pre-heating temperature for (a) 25 µm and (b) 50 µm layer thickness respectively

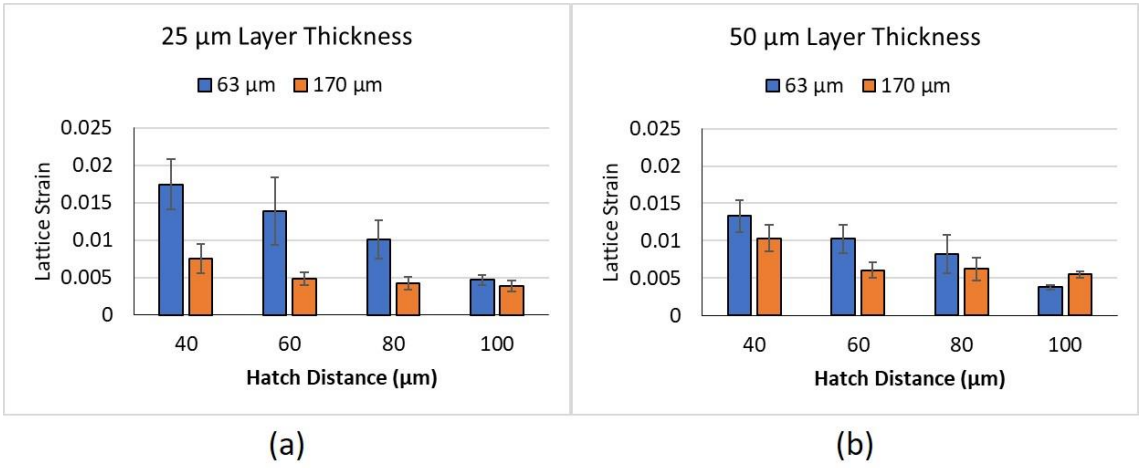

Figure 5.27: Lattice strain presented as a function of hatch distance for (a) 25 µm and (b) 50 µm layer thickness respectively

5.4.5.2 Crystal Lattice Parameters

The crystal lattice parameters were measured using Reitveld refinement as outlined in section 3.5.3. Figure 5.28 shows the Pareto chart highlighting the statistical impact of the studied parameters on the unit cell ratio c/a. Examination yields that none of the examined parameters have a statistically significant impact on the crystal lattice ratio at the 0.05 significance level.

Despite the lack of statistical significance, hatch distance has been identified as having the greatest effect on the c/a ratio out of the parameters studied. Figure 5.29 plots the c/a ratio as a function of hatch distance. A clear positive trend can be observed whereby an increase in the hatch distance from 40 – 100 µm has increased the c/a ratio from 1.595 Å to 1.5965 Å. A reduced c/a ratio at lower hatch distances correlates with stress relaxation in the crystal lattice as observed from the increased lattice strain values obtained for the same sample groups (Figure 5.27). Furthermore, the reduction in c/a ratio towards the (α+β) equilibrium value of 1.592 Å indicates decomposition of α' martensite towards an (α+β) structure [38]. This is backed up by the previously presented XRD analysis which identified the existence of BCC beta peaks and the α' → (α+β) transformation in samples with tight hatch distances. Similar results have been observed in the literature where Kaschel et al. [180] observed a reduction in the c/a ratio from 1.597 Å to 1.594 Å through heat treatment at 550 °C.

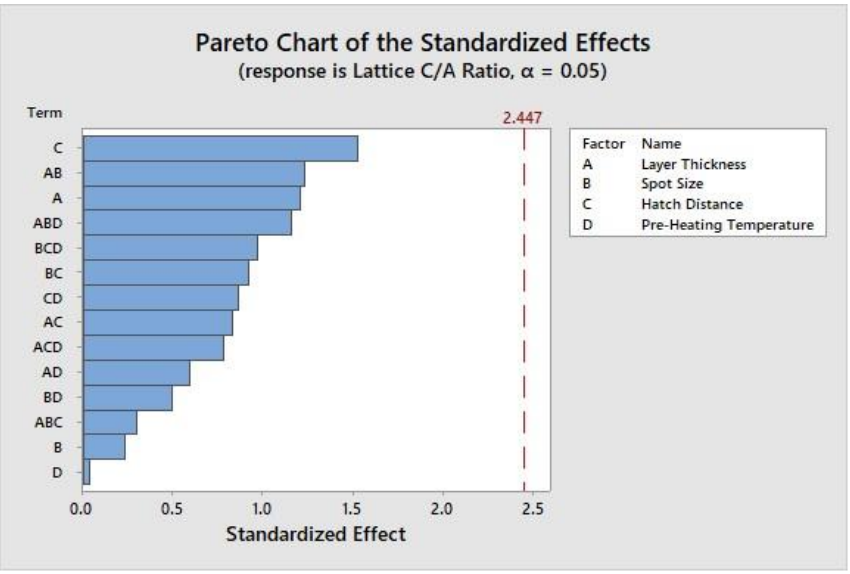

Figure 5.28: Pareto chart showing statistical significance of parameters on the crystal lattice parameter ratio

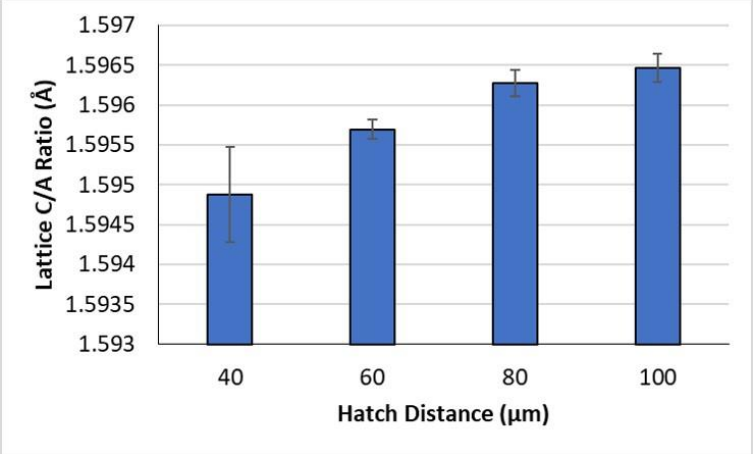

Figure 5.29: Crystal lattice parameter c/a ratio plotted as a function of hatch distance

5.4.5.3 XRD Spectra Analysis

Further evidence of α' decomposition is observed through analysis of the XRD spectra. Xu et al. [75] attributed broadening of the XRD spectra to internal residual stresses within the crystal structure. Yang et al. [116] reported that α' martensite structures presented broadening of the (101)α' and (002)α' peaks. Furthermore, they correlated the α' peaks observed shifted to greater 2θ values which is comparable to the work of Ungar [181] who demonstrated a relationship between higher 2θ values and residual stresses. Finally,

Kaschel et al. [181] observed relationships between the intensities of the (101)α/α' and (002)α/α' peaks and the growth of the β phase in heat treated Ti64 parts.

The FWHM of the XRD spectra were measured according to the process outlined in section 3.5.3. Figure 5.30 (a) and (b) show the Pareto charts for the (101)α/α' and (002)α/α' respectively. Both peaks are – at a 0.05 significance level – statistically sensitive to changes in both the hatch distance and pre-heating temperature while the (002)α/α' peak is also influenced by the laser spot size. The main effects plots presented for the same peaks in Figure 5.30 (c) and (d) demonstrate that an increase in the hatch distance from 40 – 100 µm results in peak broadening where the FWHM value increases by 43% and 52% for the (002)α/α' and (101)α/α' peaks respectively.

Conversely, increasing the pre-heating temperature from 150 – 450 °C results in a decrease in the FWHM of both peaks by 33%. A less significant impact on the (002)α/α' peak is observed when examining spot size, however decreasing the spot size from 170 to 63 µm resulted in narrowing of the peak by 20%. Similar levels of peak narrowing have been observed during in-situ high temperature XRD analysis for heat treatment temperatures of 500 °C [161]. Significant narrowing of the XRD spectra can be attributed to the relaxation of the crystal lattice as α' decomposes into an α structure. Hence, these results indicate that decomposition of α' martensite is possible at high pre-heating temperatures, small hatch distances and lower spot sizes which correlates with the increases in lattice strain as the HCP α unit cell expands from the constricted state in α' martensite structures.

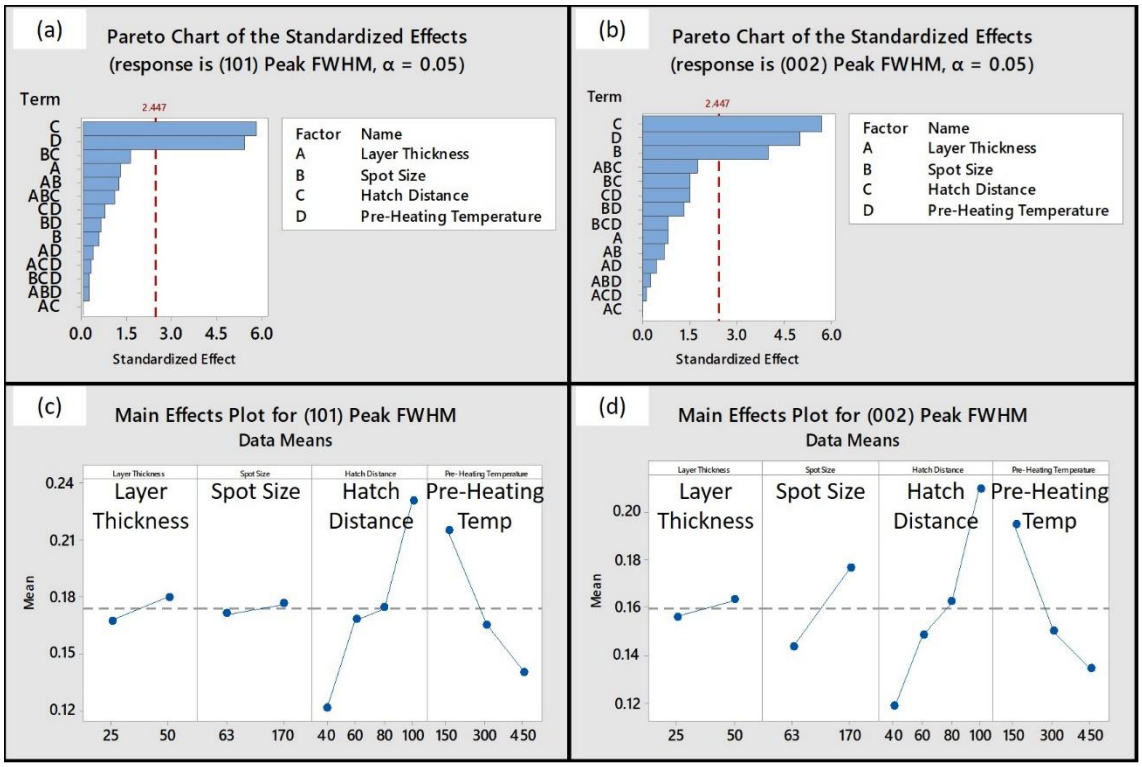

Figure 5.30: Pareto charts and main effects plots for the FWHM of (101)α/α' ((a) and (c)) and (002)α/α' ((b) and (d)) peaks respectively

The maximum intensities of the (101)α/α' and (002)α/α' peaks were obtained from the fitting of gaussian curves to the XRD spectra as outlined in section 3.5.3. Figure 5.31 (a) and (b) show the Pareto charts for the effects of the studied parameters on the peak intensity of the (101)α/α' and (002)α/α' respectively. All four studied parameters appear to exert statistical influence at the 0.05 significance level upon the intensity of the observed peaks. Figure 5.31 (c) and (d) show the main effects plots for the same α/α' peaks where a clear negative trend can be observed with respect to hatch distance. Decreasing the hatch distance from 100 – 40 µm led to a 47% increase in peak intensity of the (101)α/α' peak. Similarly, a 32% increase in peak intensity was observed for the (002)α/α' peak given the same change in hatch distance.

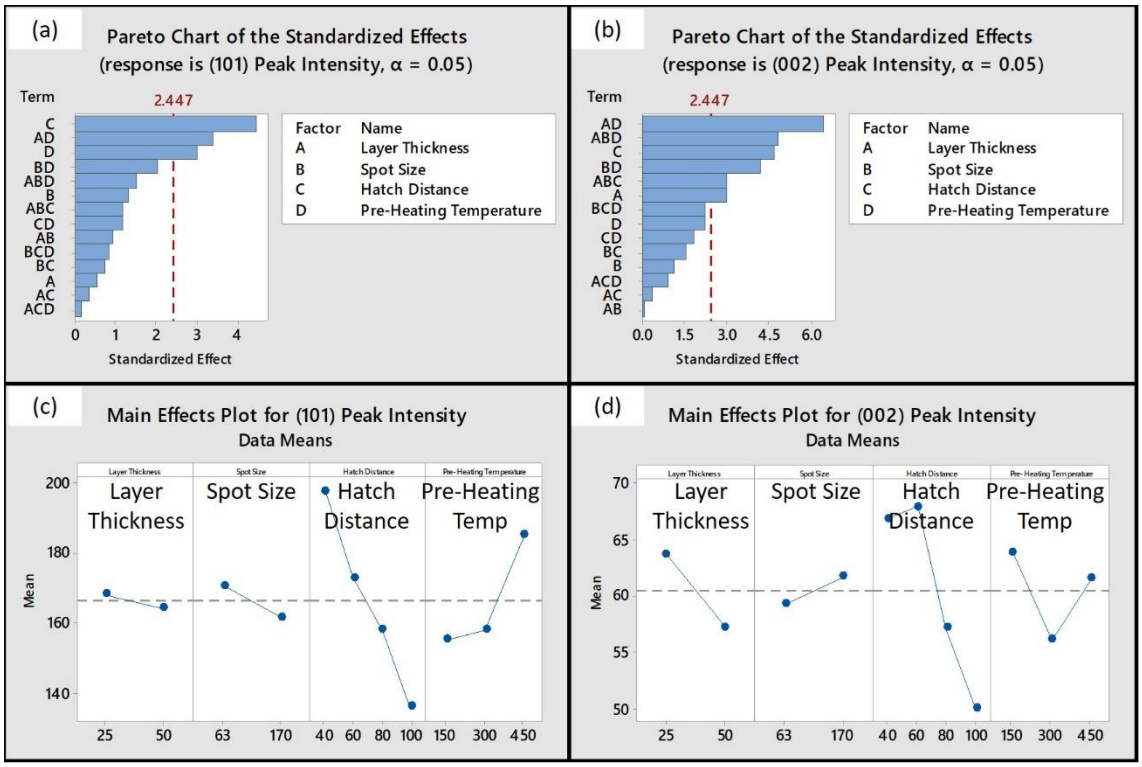

Figure 5.31: Pareto charts and main effects plots for the peak intensity of (101)α/α' ((a) and (c)) and (002)α/α' ((b) and (d)) peaks respectively

The main effects plot with regards to the effect of pre-heating provides slightly misleading results. Figure 5.32 (a) – (d) illustrates the peak intensity as a function of pre-heating temperature broken into sub-groups by layer thickness and spot size respectively. Figure 5.32 (a), (b) and (d) confirm the main effects plot in Figure 5.31 (c) where a positive relationship can be observed between pre-heating temperature and the peak intensity. In contrast Figure 5.31 (d) displays a conflicting relationship where the 150 °C pre-heating temperature appears to correlate to the highest peak intensity. Figure 5.32 (c) shows that the values obtained for the peak intensities of the (101)α/α' and (002)α/α' peaks are abnormally large.

The mean peak intensity for samples produced with a pre-heating temperature of 150 °C from the rest of the groups was 112.38 A.U. for the (101)α/α' peak and 49.15 A.U. for the (002)α/α' peak respectively. In comparison the values obtained for the (101)α/α' and (002)α/α' peaks with a pre-heating temperature of 150 °C (Figure 5.32 (c)) were 194.7 and 97.64 AU respectively. Furthermore cross referencing these samples with the OM and SEM images reveals that all samples within the 150 °C sample groups presented α'

martensite structures. Therefore these data points can be considered as outliers, most likely caused by experimental error. Excluding these samples from the analysis, Figure 5.32 (c) shows an increase in the (101)α/α' intensity and approximate stagnation of the (002)α/α' intensity for an increase in the pre-heating temperature with all other parameters unchanged.

Overall, the analysis of peak intensity across all parameter sets suggests that the pre-heating temperature has a positive relationship with the peak intensity indicating transformation from α' martensite to α phase as the pre-heating temperature is increased.

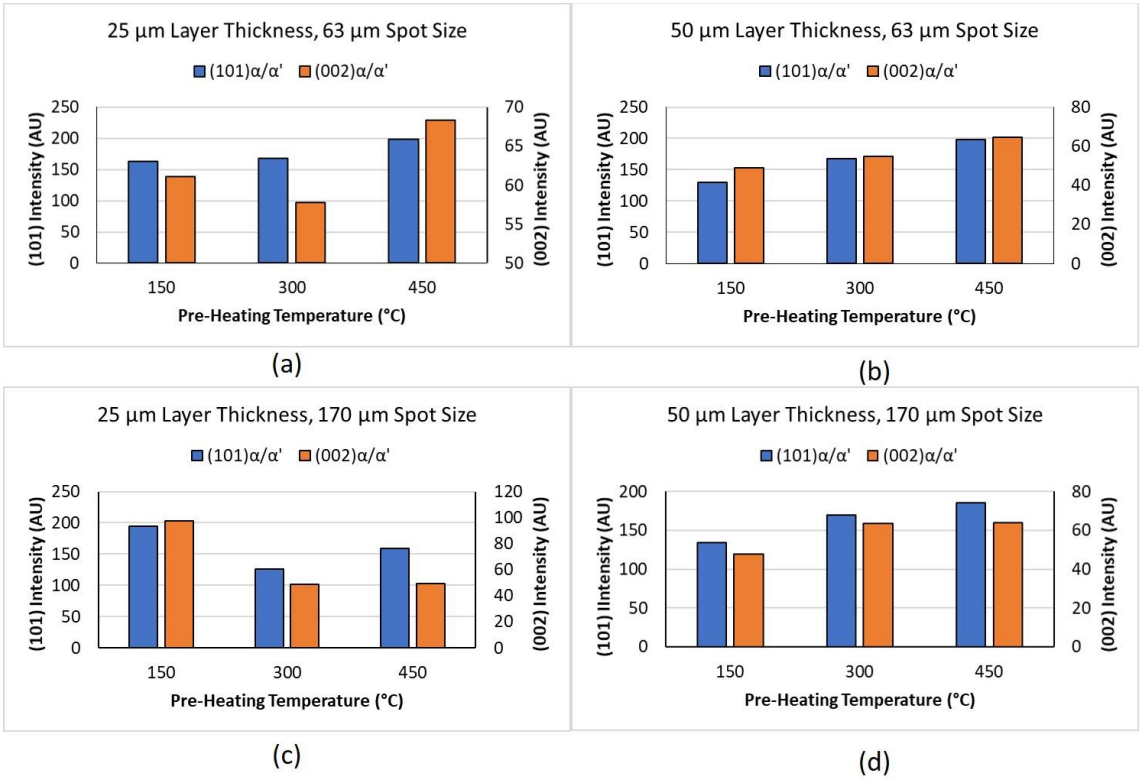

Figure 5.32: Intensity of the (101)α/α' and (002)α/α' peaks reported as a function of pre-heating temperature for each layer thickness and spot size sub-group

5.5 Conclusion

A total of forty-eight parameter sets across three pre-heating temperatures, four hatch distances, two layer thicknesses and two laser spot sizes have been examined and their influence on the resulting part's density and as-built microstructure analysed.

Statistical analysis shows that build plate pre-heating temperature has no effect on the density of as-built samples. In descending order, laser spot size, layer thickness and hatch distance all have notable contributions to the density of Ti64 specimens. Further, considering these parameters individually can provide uncertainty and hence they should be considered together. For example, processing with a 63 µm spot size led to poor density for almost all processing parameters yet utilising a 50 µm layer thickness and 100 µm hatch distance yielded specimens with a mean density above 99.5%.

In general, the smaller spot size of 63 µm led to vast over melting due to the deeper meltpool associated with the increased power density from the smaller spot size whilst increasing the spot size led to increased mean density values. The optimum density values were obtained using the larger 170 µm spot size in combination with a layer thickness of 25 µm and a hatch distance of 100 µm.

With regards to the as-built microstructure, three different structures namely, α' martensite, α' + (α+β) and Widmanstätten (α+β) were observed. From OM micrographs, the vast majority of samples observed possessed an α' martensite structure consisting entirely of α' laths contained within prior-β grains. The α' + (α+β) structure consisted of pockets of α' needles interspersed amongst larger α grains within a semi-equiaxed β grain structure and was observed for lower hatch distance and spot size values at higher pre-heating temperature. Finally, the Widmanstätten (α+β) structure consisted of larger α colonies within large quasi-equiaxed previous β grains. The Widmanstätten (α+β) structure was observed almost entirely for samples produced with a 63 µm spot size and 40 µm hatch distance at higher pre-heating temperatures irrespective of the layer thickness. Reduction in the layer thickness led to increased α' → α decomposition in the form of Widmanstätten structures appearing for higher hatch distances when 25 µm layer thicknesses were used.

SEM micrographs identified some β phase within the α' + (α+β) and Widmanstätten (α+β) structures and enabled quantification of the primary α laths. Results show that the primary α lath thickness is statistically sensitive to the pre-heating temperature where a positive relationship exists. Furthermore, hatch distance and spot size also demonstrated notable impact on the primary α lath thickness with both demonstrating a negative relationship.

Analysis of the XRD spectra led to comparable results where the (110)β and (200)β peaks were primarily observed for samples produced with the smaller 63 µm spot size, though a small number of exceptions were detected for the 170 µm spot size specimens. Furthermore, reductions in hatch distance and layer thickness along with increases in pre-heating temperature – primarily above 300 °C – correlated with observations of the β phase in the as-built samples. Quantitative analysis of the XRD spectra in the form of lattice strain, lattice c/a ratio, FWHM and peak intensity analysis was conducted. All indicate increased α' martensite decomposition towards an (α+β) structure for reduced spot size, layer thickness and hatch distance in combination with increasing pre-heating temperature.

Results presented confirm that, given the right combination of process parameters, α' martensite decomposition is possible in as-built SLM processed Ti64 specimens. Increasing the energy into the process in the form of reducing hatch distance, spot size and layer thickness served to increase α' → α transformation. However, no martensite decomposition was observed for the lowest pre-heating temperature of 150 °C and limited transformation was observed for samples produced with a 300 °C pre-heating temperature. In contrast, of the samples processed at the highest pre-heating temperature of 450 °C half presented a Widmanstätten (α+β) structure thus the most influential parameter studied is the pre-heating temperature.

Examining the effects of process parameters on both density and microstructure reveals that a trade-off exists for both spot size and hatch distance. Spot size has been identified as statistically significant for microstructure development and density level. However, in the case of density an increase in spot size resulted in an increase in density whilst increasing the spot size was detrimental to achieving in-situ α' decomposition. Similarly, hatch distance has a notable impact on both density and microstructure where increasing the hatch distance was beneficial to density but detrimental for in-situ α' decomposition. Layer thickness and pre-heating temperature demonstrate clearer relationships to density and microstructure. Processing at a 50 µm layer thickness was not conducive to achieving high density levels or in-situ decomposition. In contrast, the pre-heating temperature was statistically insignificant to density levels yet statistically significant to in-situ decomposition.

Chapter 6 Mechanical Properties

6.1 Introduction

This chapter addresses the final goal set out within section 1.3 which is to examine the effects of as-built microstructures and densities on the mechanical properties of as-built SLM processed Ti64. Elemental analysis is also presented and its effect on the mechanical properties of the as-built parts is discussed. The chapter is concluded by discussing the impact of energy input on the tensile properties of as-built components.

6.2 Experimental Method

As outlined in section 5.3, one cube and five tensile bars were built for each parameter set of pre-heating temperature, hatch distance, layer thickness and spot size. Vickers microhardness measurements were conducted on one specimen for each sample group according to ASTM E384-17 as outlined in section 3.7.1. The five tensile specimens were built in the vertical orientation according to ASTM E8/E8M figure 8 sample 4 and tested as outlined in section 3.7.2 [164]. Interstitial element analysis was conducted using inert gas fusion which is a method to quantitatively determine the content of gasses in ferrous and non-ferrous materials.

6.3 Elemental Analysis

Section 2.2 outlines how interstitial elements which include oxygen and nitrogen can be used to alter the mechanical properties of Ti64 parts [38], [43]. Specifically an increase in either of these elements serves to increase the strength of Ti64 parts at the expense of a reduced fracture strain. Literature shows that titanium has an affinity to pick up oxygen at increased pre-heating temperatures with detrimental effects to mechanical properties [135]. Hence, one sample group with the closest parameters to the optimal parameter set outlined in Chapter 4 was subjected to interstitial element analysis at three different pre-heating temperatures. Table 6.1 outlines the parameters used and the results from the interstitial elements analysis. Examination of Table 6.1 along with Figure 6.1 show a clear increase in both oxygen and nitrogen percentages given an increase in pre-heating temperature. Furthermore, all of the samples tested failed to conform to ASTM F136 [140] which gives a maximum oxygen percentage of 0.13% for Ti64 ELI.

The increase in the interstitial elements' content within the as-built parts can be attributed to the affinity of titanium to pick up oxygen at high temperatures as outlined in section 2.2. The failure to comply to the ELI standard for all samples tested indicates that even the meltpools of samples processed with low pre-heating temperatures reach sufficient temperatures to attract residual oxygen from the surrounding process chamber. Further increase in the meltpool temperature and in the quasi-equilibrium temperature of the tempering window associated with increased pre-heating temperature is well correlated

with the increasing trend in Figure 6.1. Similar results were presented by Vrancken et al. [135] who observed considerable increases in both oxygen and nitrogen content as pre-heating increased up to 400 °C.

Table 6.1: Interstitial element analysis sample parameters and results

Spot Size (µm)	Hatch Distance (µm)	Layer Thickness (µm)	Pre-Heating Temperature (°C)	Oxygen (wt. %)	Nitrogen (wt. %)
170	80	25	150	0.14	0.025
			300	0.17	0.026
			450	0.2	0.027

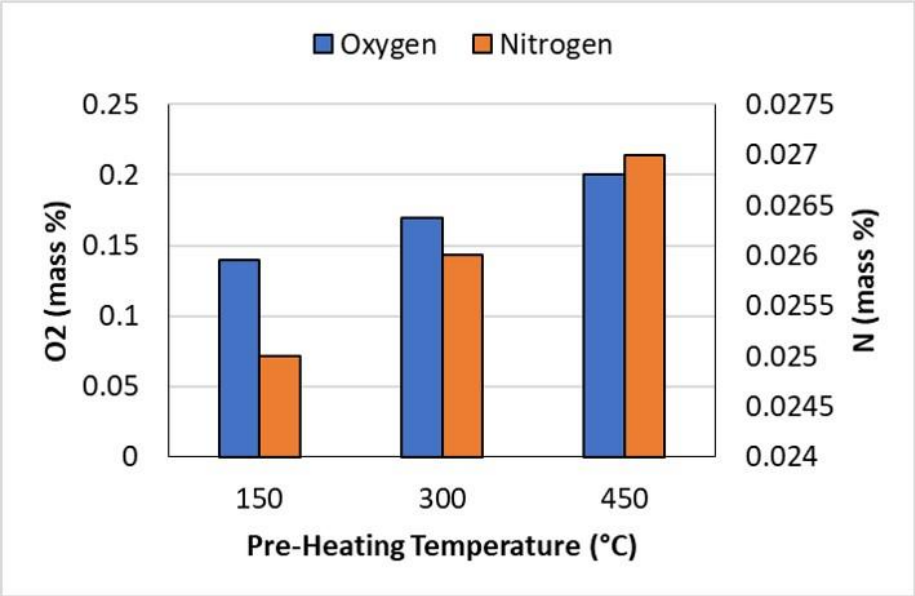

Figure 6.1: Interstitial element analysis plotted as a function of pre-heating temperature

6.4 Microhardness

Figure 6.2 shows the Pareto chart where the response is microhardness and the inputs are layer thickness, spot size, hatch distance and pre-heating temperature respectively. Analysis reveals that pre-heating temperature and the relationship between layer thickness and hatch distance are statistically significant factors at a 0.05 significance level. However, the hatch distance both independently and as part of a relationship with

both spot size and layer thickness respectively demonstrates a notable impact on the microhardness response.

Figure 6.3 shows the main effects and interaction plots where the response is microhardness. Examining the range in the main effects plot in Figure 6.3 (a) shows that all the samples sit within a relatively small window between 390 and 403 HV. These values are representative of the predominantly α'/α microstructures observed through micrographs and XRD spectra in Chapter 5 and are comparable to values reported in literature for as-built SLM processed Ti64 [182], [183].

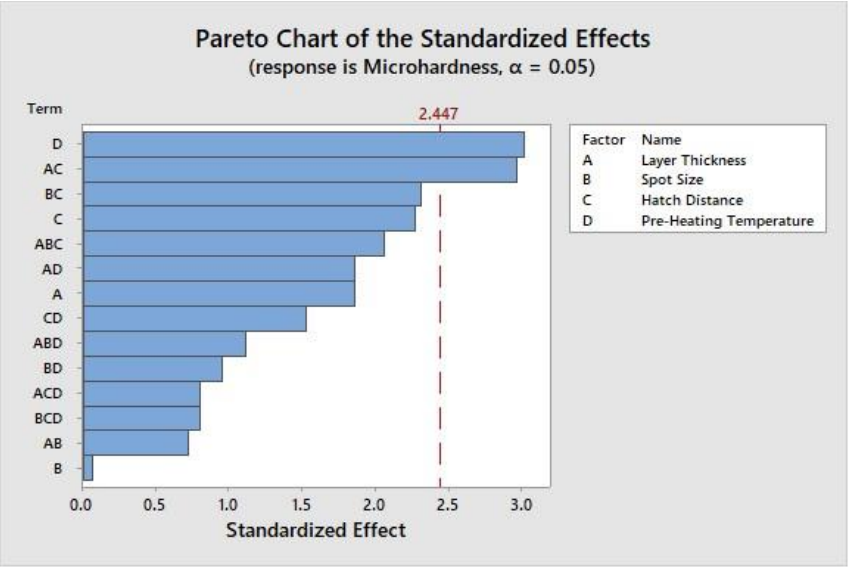

Figure 6.2: Pareto chart showing statistical influence of the studied parameters on microhardness

Further analysis of the main effects plot (Figure 6.3 (a)) shows that microhardness is insensitive to a change in spot size whilst increasing layer thickness from 25 – 50 µm leads to a small reduction of 5 HV. As indicated in the Pareto chart (Figure 6.2) pre-heating temperature and hatch distance demonstrate more considerable influence on the microhardness. Pre-heating demonstrates a positive relationship with microhardness where an increase in pre-heating from 150 – 450 °C increases the observed microhardness from 390 – 402 HV. Hatch distance shows a more complex relationship whereby a relatively sharp decline in microhardness is observed as hatch distance is increased from 40 – 60 µm but is followed by a gradual increase in the mean value as the hatch distance increases towards 100 µm.

Chapter 5 outlined the considerable affect that lowering the laser spot size and layer thickness had on the as-built microstructures with decreasing values of both parameters facilitating α' → (α+β) decomposition. Thus relatively insignificant changes observed in microhardness at the same spot size and layer thickness levels indicates that the variation in microhardness as a function of hatch distance and pre-heating temperature cannot be attributed to changes in the microstructure. Rather, the high microhardness observed for the 40 µm hatch distance sample group as well as for increased pre-heating temperatures is attributed to increases in the oxygen percentage as observed in previous literature [38], [184].

This is further confirmed through analysis of the interaction plot in Figure 6.3 (b). Examining the interaction between layer thickness and hatch distance that was identified as statistically significant demonstrates the influence of oxygen on the microhardness. The 40 µm hatch distance sample from both layer thickness groups displays an elevated microhardness value as the increase in meltpool temperature was sufficient to facilitate increased oxidation for both layer thicknesses. However, the samples built with hatch distances between 60 – 100 µm display opposite trends. The meltpool temperature of the 50 µm layer thickness group is lower than that of the 25 µm group. Hence, as the hatch distance was increased the microhardness increased due to the significant martensite observed at higher hatch distances within this group. In contrast, increasing the hatch distance within the 25 µm layer thickness group leads to a reduction in the meltpool temperature and thus a reduction in oxidation. Hence reducing the microhardness value.

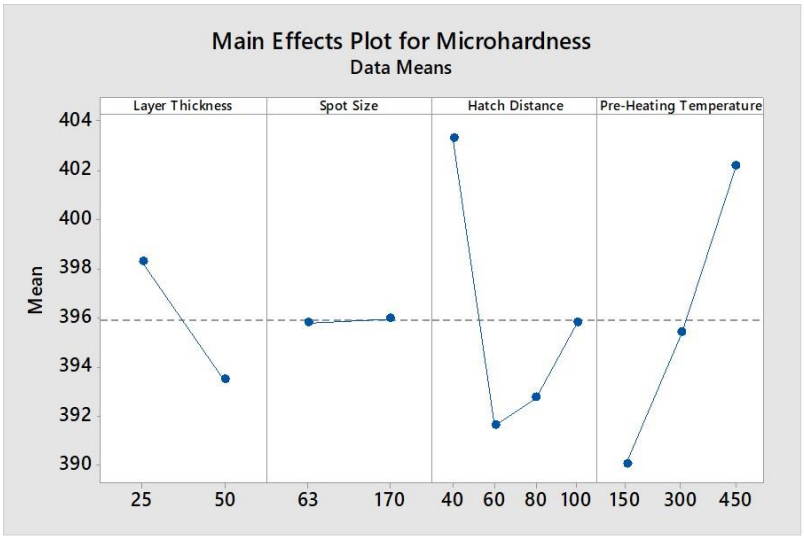

(a)

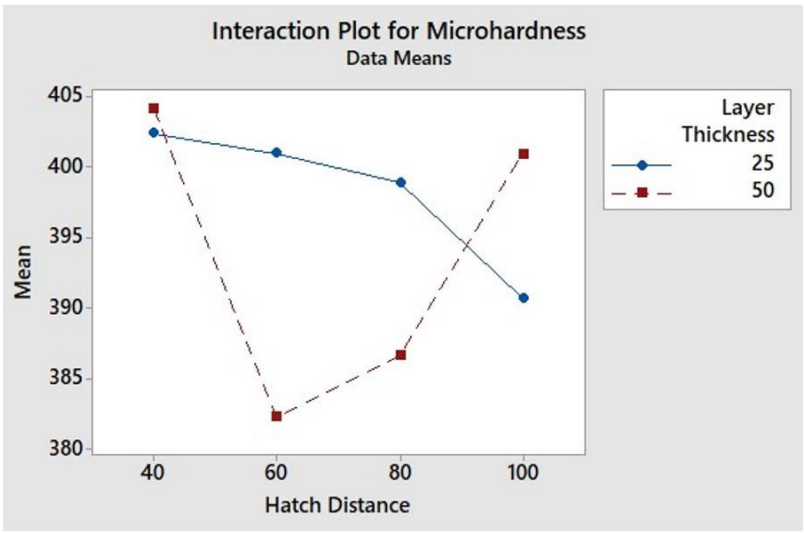

(b)

Figure 6.3: (a) Main effects plot and (b) interaction plot between layer thickness and hatch distance where the microhardness is the response

6.5 Screening Study

Before the prints from the DOE outlined in section 5.2 were conducted, a screening study was completed to determine the processing route of the tensile specimens. Given the primary goal of this thesis is to examine the capabilities of as-built parts and thus the removal of post processing from the production cycle – the goal of this screening study was to determine whether tensile bars could be printed in the net-shape. Thus the two

options were printing net shape tensile specimens or printing cylinders and machining to the desired geometry as illustrated in Figure 6.4. In each case 3 samples were built with a pre-heating temperature of 150 °C and process parameters outlined in Table 6.2. These matched the parameter set A utilised in section 4.3.2.4 which presented a mean density of 99.4% and the highest fracture strain from the heat treated specimens analysed at 13.21%.

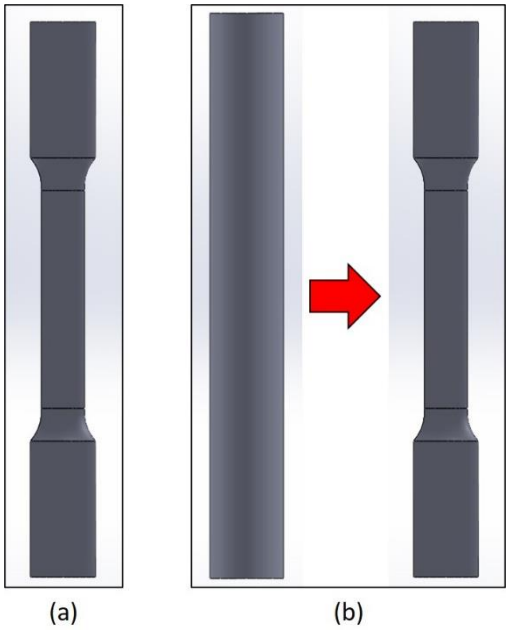

Figure 6.4: Illustrations of the two processing routes considered namely (a) net-shape and (b) machined from cylindrically printed samples

Table 6.2: Process parameters used for the tensile specimen screening study

Laser Power (W)	**Scanning Velocity (mm/sec)**	**Hatch Distance (µm)**	**Layer Thickness (µm)**	**Energy Density (J/mm^3)**
90	300	50	25	240

Figure 6.5 illustrates the tensile properties of the specimens printed in the net shape and those that were machined from a cylindrical profile. The median UTS of net shape samples was statistically superior to those measured for the machined samples with a

difference of 35 MPa in the median values reported. Furthermore, the spread in the data was significantly greater in the machined samples with a standard error of 30.26 MPa compared to 5.28 MPa observed for net shape samples. Comparison of the median yield stress values indicated no statistically significant difference between the groups though the error associated with the machined samples was five times greater than that of net shape specimens. At 6.2% and 3.74% respectively the fracture strain of the net shape samples was vastly superior to that obtained for machined specimens. These differences are attributable to increased tensile residual stresses that are imparted on specimens during machining of Ti64 as observed in literature [185]. Thus, the tensile samples built for evaluation of density and microstructure were built in the net shape.

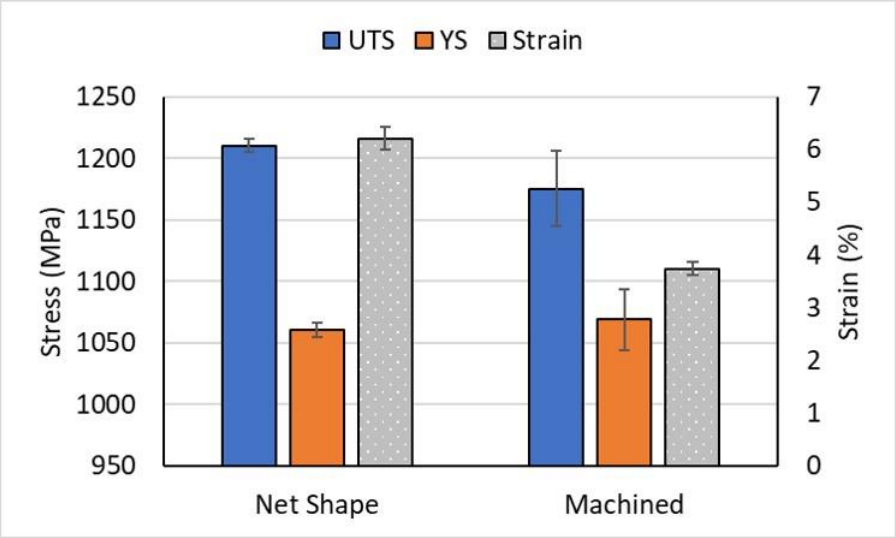

Figure 6.5: Tensile properties of net shape and machined tensile specimens respectively. Error bars represent one standard deviation

6.6 Tensile Properties

The tensile properties of SLM processed Ti64 specimens are affected by numerous variables including but not limited to, density, microstructure, and oxygen percentage. With regards to the DOE for this study presented in section 5.2, layer thickness and spot size remain fixed within any given build processed at different pre-heating temperatures whilst parts with different hatch distances can be built within each print. Hence, it is logical to consider the tensile parameters with respect to the combination of layer thickness and spot size.

6.6.1 25µm Layer Thickness, 63 µm Spot Size

This combination of layer thickness and spot size yields the highest energy input into the process from any of the parameter set groups studied as reflected through the ED and power density values in Table 5.1. Due to the high energy input into the powder bed, excessive condensate, spatter, and ejected powder was observed which caused the filter saturation level to increase beyond normal processing levels. As outlined in Chapter 4 this is not safe for processing reactive metals. Thus the number of samples per build was reduced by 50% to facilitate the safe building of tensile samples. Table 6.3 outlines the parameters used to build tensile specimens with a 25 µm layer thickness and 63 µm spot size with other process parameters remaining unchanged from Table 5.1. The two extreme hatch distance values of 40 and 100 µm were retained such that an examination of hatch distance could be conducted.

Results obtained for tensile testing are presented in Table 6.3. Cracks were observed on the surface of the grip section in samples built with a 150 and 300 °C pre-heating temperature respectively. These can be attributed to high residual stresses which form due to high energy input as observed in literature [186], [187]. The parameters chosen within this group lead to a high energy input which increases the maximum temperature of the melt pool. Accordingly rapid cooling rates occur and facilitate the formation of higher residual stresses. As a result the parts failed prematurely in the grips at the site of the cracks and tensile properties could not be recorded.

Literature shows that increasing the pre-heating temperature from 100 – 470 °C reduces the residual stress in as-built parts by up to 90% [64]. Thus the increase in pre-heating temperature to 450 °C sufficiently reduced the cooling rate and subsequent residual stress sufficiently such that no cracks were present. Results presented in Table 6.3 demonstrate a large disparity between the samples built with 40 and 100 µm hatch distances respectively. Insight on the difference between samples is obtained through examination of Figure 6.6 which displays the samples built with the 450 °C pre-heating temperature. The 40 µm samples displayed severe powder adhesion and significant oxidation due to the high meltpool temperatures associated with a large energy input. Furthermore, smaller hatch distances increase the interaction time between the material and the laser and consequently lead to a higher quasi-equilibrium temperature as discussed in section 5.4.2.

These combined effects also facilitate increased oxygen pickup from the surrounding environment. As outlined in section 2.2 oxidation of Ti samples leads to substantial embrittlement which was evident through the breaking of one sample before removal from the build plate and further confirmed with the remaining samples which had a median failure strain of just 0.53%.

Increasing the hatch distance from 40 – 100 µm decreases the ED from 300 – 120 J/mm^3 as outlined in Table 6.3. The 100 µm samples shown in Figure 6.6 demonstrate no significant powder adhesion and negligible signs of oxidation. Furthermore, samples produced with these process settings presented a mean density of 98.95% and an α' martensite structure as presented in Chapter 5. The median fracture strain of 5.91% sits broadly in line with values obtained for martensitic structures in the literature whilst a median UTS of 1094 MPa is below normal values of circa 1200 MPa for martensitic structures [91].

Table 6.3: Parameters used and tensile results for specimens processed with 25 µm layer thickness and 63 µm spot size

Pre-Heating Temperature (°C)	**Hatch Distance (µm)**	**Energy Density (J/mm^3)**	**Power Density (W/mm^2)**	**Median UTS (MPa)**	**Median Fracture Strain (%)**
150	40	300	0.029	–	–
150	100	120	0.029	–	–
300	40	300	0.029	–	–
300	100	120	0.029	–	–
450	40	300	0.029	544	0.53
450	100	120	0.029	1094	5.91

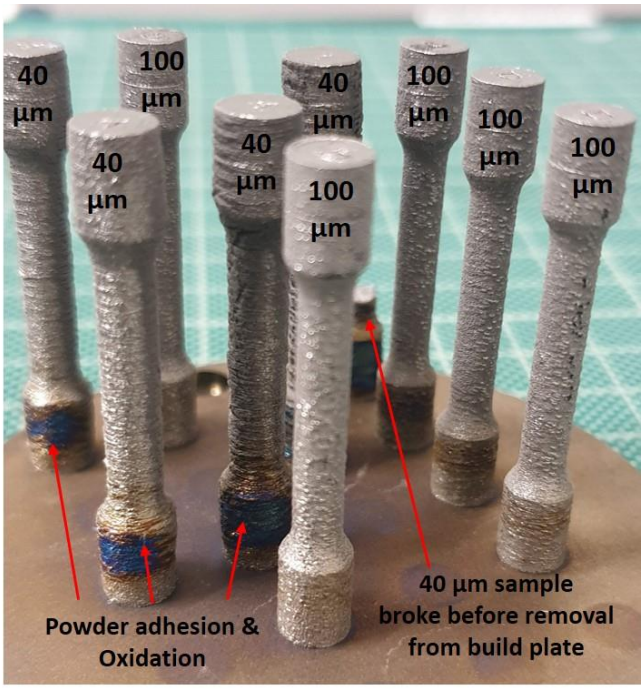

Figure 6.6: Tensile specimens printed with a 450 °C pre-heating temperature, 25 µm layer thickness and 63 µm spot size

6.6.2 50 µm Layer Thickness, 63 µm Spot Size

Two analysis of variance (ANOVA) tests were carried out to assess the difference in the means of tensile properties as a function of hatch distance and pre-heating temperature. In each case the null hypothesis is that there is no difference between the means and a confidence interval of 95% was set. Table 6.4 presents the results from both tests. With a P-value of 0.008 the relationship between hatch distance and fracture strain is the only statistically significant interaction observed. Hatch distance also presents a strong correlation to the UTS with a low P-value however, the result cannot be considered statistically significant at the 0.05 significance level.

Table 6.4: ANOVA tests carried out to assess the significance of hatch distance and pre-heating temperature on tensile properties

Response	Factor	P-Value
Fracture Strain	Hatch Distance	0.008
	Pre-Heating Temperature	0.769
UTS	Hatch Distance	0.062
	Pre-Heating Temperature	0.269

Figure 6.7 presents the tensile properties for samples built with a 50 µm layer thickness and 63 µm spot size as a function of pre-heating temperature and hatch distance. Figure 6.7 (a) shows that despite no statistically significant difference, pre-heating at or above 300 °C results in a reduction in both UTS and YS by 6%. This can be attributed to poor performance of the samples processed with a 40 µm hatch distance at the higher pre-heating temperatures of 300 and 450 °C as outlined in Table 6.5. In contrast no difference was observed in the fracture strain of samples produced across the three pre-heating temperatures examined. This correlates to the insensitivity of density to pre-heating temperature for the same sample group as indicated in section 5.4.1.2. Rather, hatch distance demonstrates a greater influence on the density of the samples which is reflected in the tensile results from Figure 6.7 (b).

Figure 6.7 (b) shows a positive relationship between the fracture strain and hatch distance where an increase in hatch distance from 40 – 100 µm led to an increase in fracture strain from 2% to 7.1%. The trend observed for the UTS is not as clear. Initially, an increase of 14% is observed as hatch distance increases from 40 – 60 µm. Then a gradual decrease in the UTS from 1183 – 1128 MPa can be observed as hatch distance increases from 60 – 100 µm. Examination of YS values presented in Table 6.5 reveals a similar trend. Section 5.4 identified increased $\alpha' \rightarrow (\alpha+\beta)$ decomposition for reduced hatch distances within this sample group, thus it would be reasonable to expect a reduction in stress values and corresponding increase in fracture strain. However, the stress and strain values outlined in Figure 6.7 (b) deviate from this expected behaviour. This can be accredited to the increase in oxygen pickup and the reduction in part density that results from printing

at lower hatch distances, as both of these characteristics will have a negative impact on the part's mechanical properties.

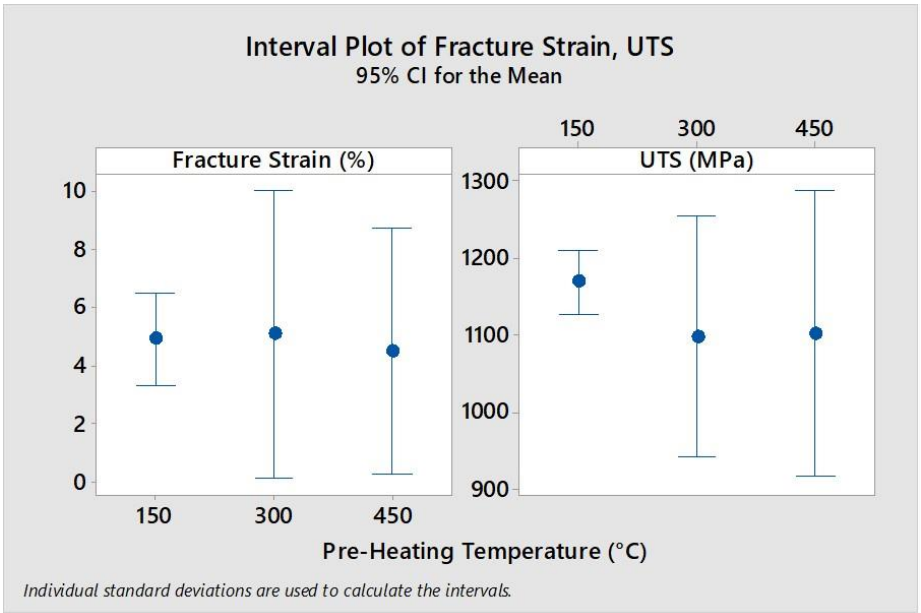

(a)

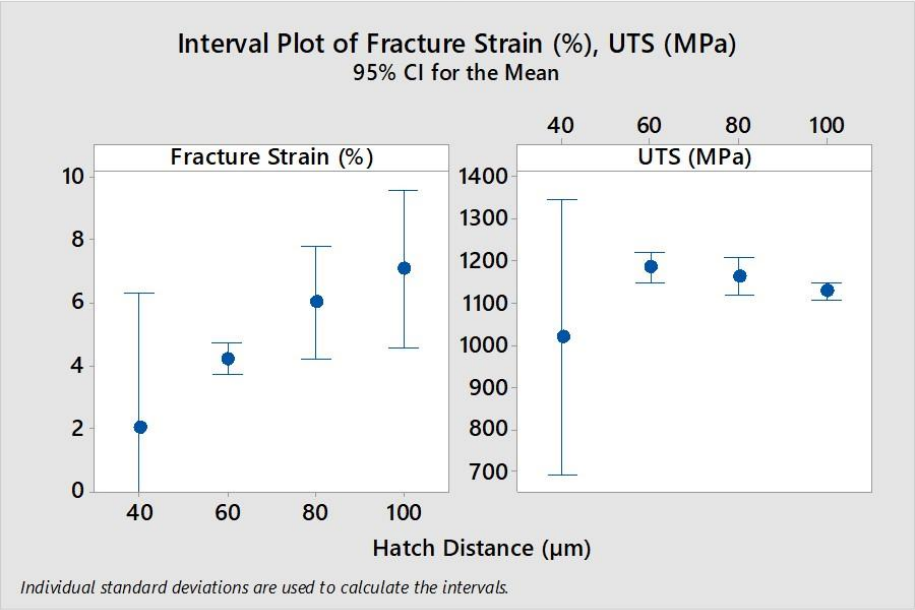

(b)

Figure 6.7: Interval plots of tensile properties for samples processed with 50 µm layer thickness and 63 µm spot size as a function of (a) pre-heating temperature and (b) hatch distance

Table 6.5: Tensile properties recorded for samples processed with 50 µm layer thickness and 63 µm spot size

Pre-Heating Temperature (°C)	Hatch Distance (µm)	Median UTS (MPa)	Median YS (MPa)	Median Fracture Strain (%)
150	40	1168.2	1081.0	3.99
	60	1189.9	1121.1	4.18
	80	1182.9	1104.8	5.27
	100	1132.4	1051.8	6.13
300	40	952.71	810.3	1.05
	60	1166.2	1097.3	4.42
	80	1153.7	1078.5	6.71
	100	1117.7	1041.6	8.13
450	40	931.3	753.0	0.94
	60	1193.9	1131.1	4.04
	80	1148.9	1091.8	5.99
	100	1132.4	1073.58	6.93

Section 5.4.1 presented an increase in the mean density from 98.7% to 99.61% as the hatch distance was increased from 40 – 100 µm for this sample group. Samples from Chapter 4 demonstrated a 47% increase in fracture strain given a similar increase in density. Hence, an increase in density facilitates an increase in the fracture strain of the as-built specimens. However, the results in Chapter 4 presented an increase in the UTS and YS values as the density increased. In contrast Figure 6.7 (b) presents a decrease in the stress values as the density of the samples increased. Furthermore, as outlined in Chapter 5 greater hatch distances which presented higher densities also correlated with less α' martensite decomposition. In such circumstances higher stress and lower strain values could be expected. Hence, the combination of an increase in the stress values with simultaneous decrease in the fracture strain for samples that presented with an $\alpha' \rightarrow (\alpha+\beta)$ transformation is indicative of increased oxidation. This is evident through analysis of the

samples processed with a 40 µm hatch distance in Table 6.5 which represent the samples with the greatest energy input into the process within this group. Figure 6.8 shows two samples from this hatch distance group at pre-heating temperatures of 300 and 450 °C. Both samples display evidence of oxidation on the surface of the specimens with the 450 °C sample exhibiting more severe oxidation than the specimen processed at 300 °C.

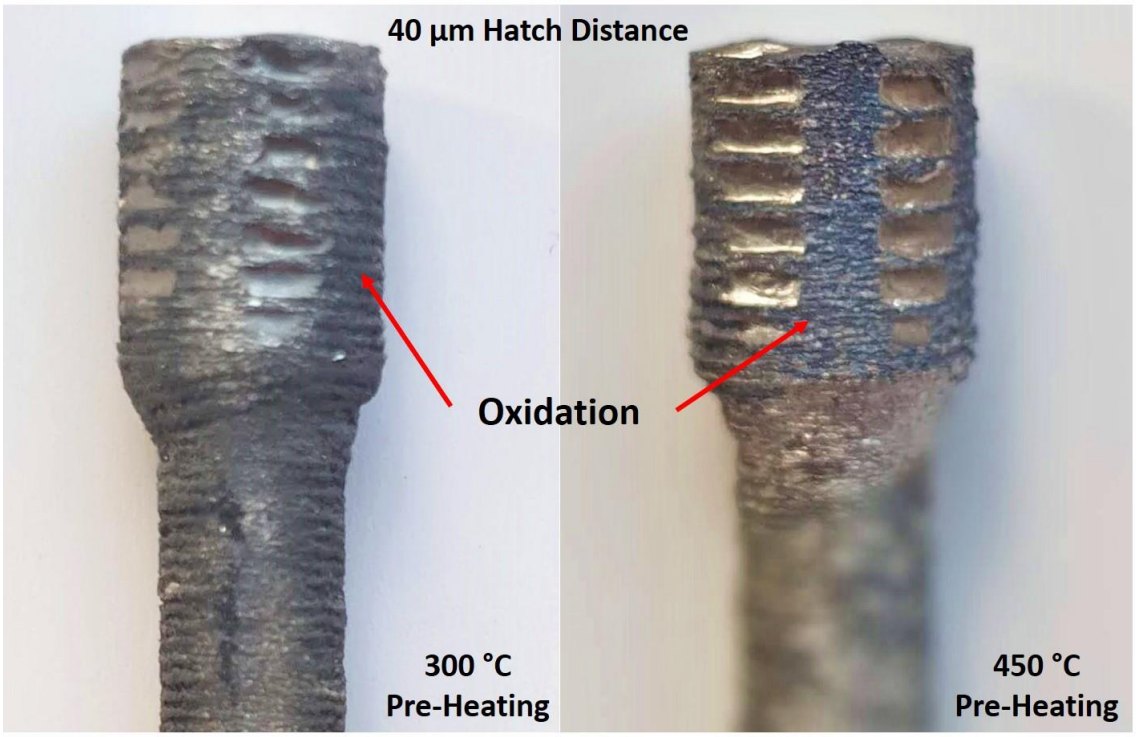

Figure 6.8: Tensile samples processed using a 40 µm hatch distance at pre-heating temperatures of 300 and 450 °C displaying signs of oxidation

Analysing the tensile properties of samples processed at 40 µm hatch distance reveals that samples built with a 150 °C pre-heating temperature demonstrated a median UTS of 1168 MPa and a median fracture strain of 3.99%. These values are typical of an α' martensitic structure and indicate that the oxygen content has not impeded the mechanical performance [91]. Section 6.3 reported a 17% increase in the oxygen content when the pre-heating temperature is increased from 150 – 300 °C. Analysing the tensile properties of the 40 µm hatch distance samples given the same increase in pre-heating temperature reveals a 73.6% reduction in fracture strain and 18% reduction in UTS. Increasing the pre-heating temperature further only serves to reduce the values. The tensile plots presented in Figure 6.9 show that the increase in oxygen content as the pre-heating

temperature increased resulted in more brittle samples that in many cases failed within the elastic region.

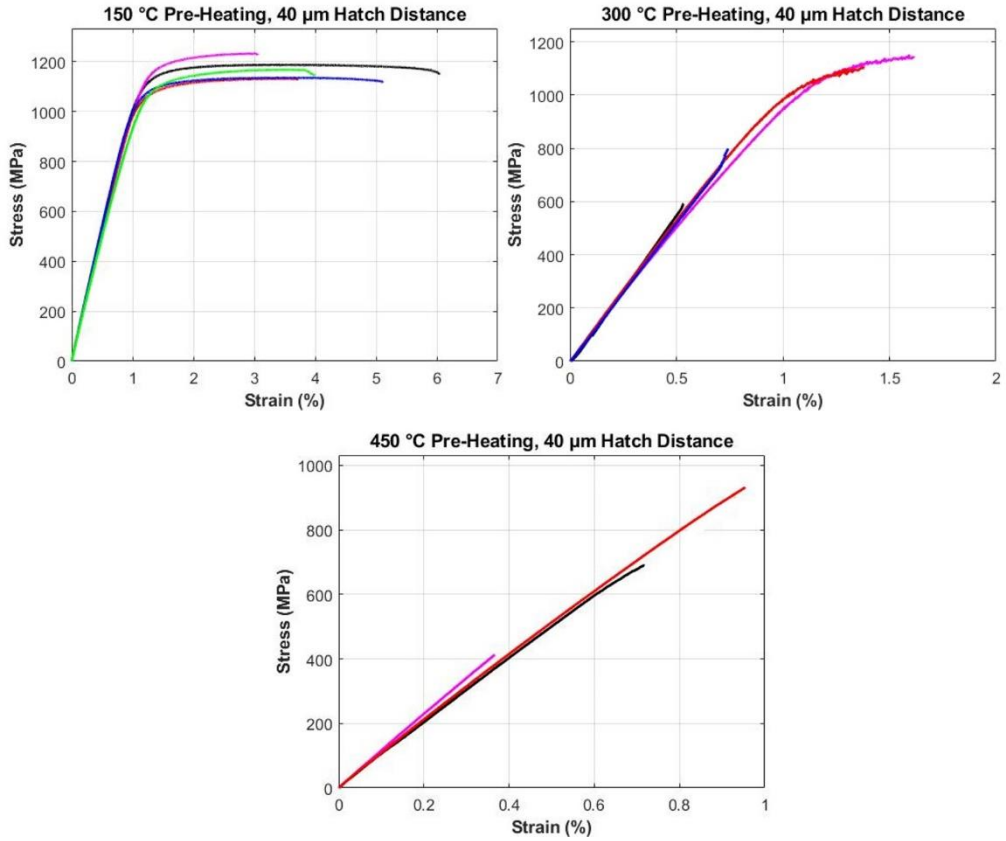

Figure 6.9: Tensile properties plotted for samples processed with 50 µm layer thickness, 63 µm spot size and 40 µm hatch distance at three pre-heating temperatures

6.6.3 25 µm Layer Thickness, 170 µm Spot Size

Table 6.6 shows the results of two ANOVA tests carried out to examine the statistical significance of changes in the hatch distance and pre-heating temperature with fixed layer thickness and spot size. The P-values indicate that neither hatch distance nor pre-heating temperature have a significant impact on the UTS of the samples. With regards to fracture strain, the hatch distance again displays no sensitivity whilst the pre-heating temperature has a statistically significant impact with a P-value of 0.017.

Table 6.6: ANOVA tests carried out to assess the significance of hatch distance and pre-heating temperature on tensile properties

Response	Factor	P-Value
Fracture Strain	Hatch Distance	0.552
	Pre-Heating Temperature	0.017
UTS	Hatch Distance	0.096
	Pre-Heating Temperature	0.083

Table 6.7 and Figure 6.10 show the tensile properties of samples built with a 25 µm layer thickness and 170 µm spot size as a function of hatch distance and pre-heating temperature. Examination reveals that increasing pre-heating temperature from 150 – 450 °C produces a statistically significant increase in the mean fracture strain from 5.68% to 9.58%. Correspondingly, the UTS and YS values decrease as the pre-heating temperature increases. However, the UTS and YS decrease by only 50 MPa and 44 MPa respectively given a 41% increase in the fracture strain value. Although no significance can be attributed to hatch distance, Figure 6.10 (b) presents a minor increase in the median fracture strain from 7.01% to 8.47% as the hatch distance is reduced from 100 – 40 µm. Similarly no statistically significant difference is observed between the stress values in the same range. Thus, pre-heating temperature has a greater effect on the as-built tensile properties within this sample group.

This sample group is the closest set of parameters to the density optimisation that was undertaken in Chapter 4 given the spot size and layer thickness match the values used during that study. Hence, as indicated in section 5.4.1 this sample group had the highest density of any other set tested with a group mean of 99.7%. Meanwhile no difference was observed for density with samples processed at different pre-heating temperatures whilst no visible oxidation was present on the samples. Furthermore, the fracture strain shows an inverse trend to the density of the samples where the density reduced from 99.83% – 99.15% as the hatch distance was reduced from 100 – 40 µm. Combined, these results indicate that the variation in tensile properties observed in Figure 6.10 can be attributed to differences in the microstructure of the samples rather than density.

With regards to the microstructures of samples from this group, Chapter 5 reported an increase in primary α lath thickness with an increase in pre-heating temperature. Similarly, β phase XRD peaks, increased lattice strain and α' → α' + (α+β) transformations were correlated to decreasing hatch distance and increased pre-heating temperatures. Finally, a Widmanstätten (α+β) structure was identified for a 40 µm hatch distance at a pre-heating temperature of 450 °C. Xu et al. [75] correlated increases in α lath thickness with increased ductility and decreased UTS and YS whilst the same trends can be expected for α → α' + (α+β) transformations due to the increase in β retention. Thus the minor decline in UTS and YS and subsequent increase in fracture strain observed in Figure 6.10 (a) can be attributed to the increase in α lath thickness and decomposition from α' → (α+β) at higher pre-heating temperatures.

Table 6.7: Tensile properties recorded for samples processed with 25 µm layer thickness and 170 µm spot size

Pre-Heating Temperature (°C)	**Hatch Distance (µm)**	**Median UTS (MPa)**	**Median YS (MPa)**	**Median Fracture Strain (%)**
150	40	1180.1	1116.82	7.07
	60	1229.88	1144.61	6.72
	80	1215.24	1106.89	5.2
	100	1164.49	1060.34	3.37
300	40	1172.2	1110.96	9.56
	60	1194.2	1116.62	7
	80	1201.6	1118.50	6.35
	100	1191.12	1082.15	7.75
450	40	1126.9	1074.75	8.77
	60	1156.86	1077.65	9.75
	80	1158.8	1060.97	9.73
	100	1167.97	1059.50	9.92

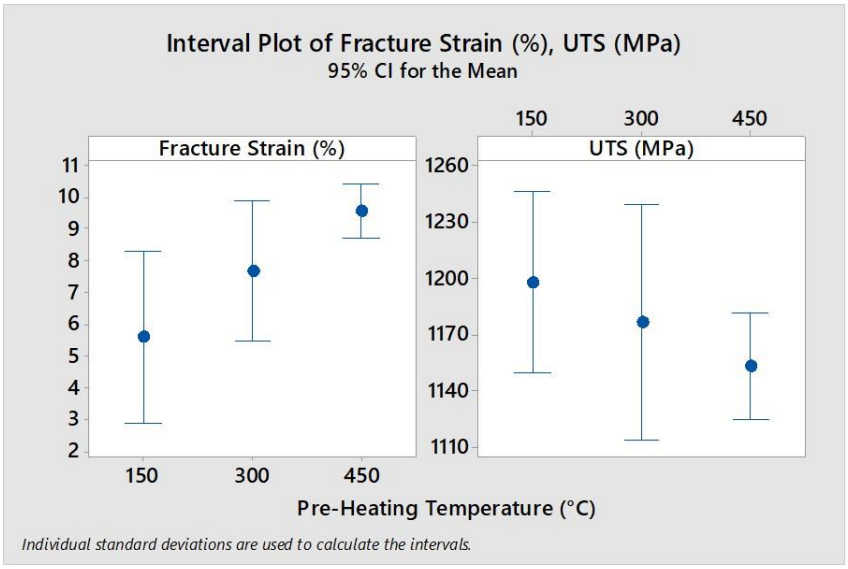

(a)

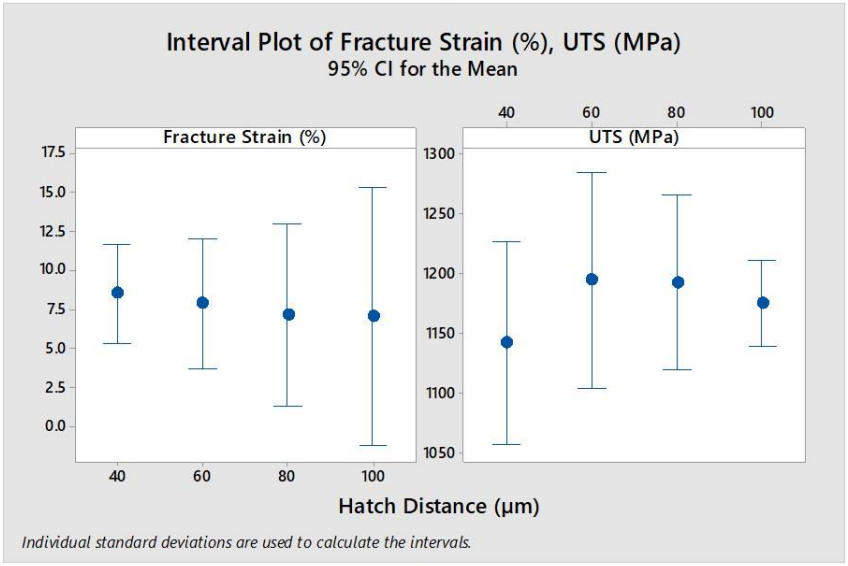

(b)

Figure 6.10: Interval plots of tensile properties for samples processed with 25 µm layer thickness and 170 µm spot size as a function of (a) pre-heating temperature and (b) hatch distance

6.6.4 50 µm Layer Thickness, 170 µm Spot Size

Table 6.8 outlines the two ANOVA tests carried out to examine the effect of hatch distance and pre-heating temperature on the tensile properties of samples with constant layer thickness and spot size. The P-values indicate that within this group which utilises

a 50 µm layer thickness and 170 µm spot size, the hatch distance and pre-heating temperature do not have any statistically significant impact on the tensile properties.

Table 6.8: ANOVA tests carried out to assess the significance of hatch distance and pre-heating temperature on tensile properties

Response	Factor	P-Value
Fracture Strain	Hatch Distance	0.471
	Pre-Heating Temperature	0.136
UTS	Hatch Distance	0.82
	Pre-Heating Temperature	0.122

Table 6.9 and Figure 6.11 present the tensile properties for the samples processed in this group as a function of hatch distance and pre-heating temperature. Overall low stress and extremely low strain values were obtained from samples produced with these settings. Confirming the ANOVA results, no clear trends can be observed between the tensile properties and pre-heating temperature in Figure 6.11 (a). Though the reduction in stress values for samples processed at a pre-heating temperature of 450 °C in comparison to the other groups is indicative of the $\alpha \rightarrow \alpha' + (\alpha+\beta)$ structures observed at higher temperatures. In contrast, Figure 6.11 (b) shows a minor increase in fracture strain and reduction in stress values as the hatch distance is decreased to 40 µm. However, the standard deviations are large which renders the trend statistically insignificant. Further, the maximum fracture strain of 2.63% observed for the 40 µm sample group is extremely poor.

The poor performance of this sample group can be attributed to a combination of the density and microstructure observed. Section 5.4.1 reports that the mean density of this sample group sits at 98.98%. While this value is not the lowest of the parameter sets exampled, the observed pores for this sample group were classified as lack of fusion defects due to under-melting. This is in contrast to the other groups which exhibited gas entrapped pores, a characteristic of over-melting. Lack of fusion defects are detrimental to mechanical properties due to the sharp crack-like morphology acting as crack initiation sites. Furthermore, the low energy input was also attributed with impeding α lath growth and $\alpha' \rightarrow (\alpha+\beta)$ decomposition meaning that fine α' martensitic structures were observed

throughout the sample group. In combination, the martensitic structure and lack of fusion defects have resulted in extremely low fracture strain values whilst all UTS values fit what would be expected for martensitic structures [91].

Table 6.9: Tensile properties recorded for samples processed with 50 µm layer thickness and 170 µm spot size

Pre-Heating Temperature (°C)	**Hatch Distance (µm)**	**UTS (MPa)**	**YS (MPa)**	**Fracture Strain (%)**
150	40	1164.02	1107.35	2.50
	60	1144.28	1089.85	1.86
	80	1126.24	1061.32	1.76
	100	1084.16	1069.86	1.38
300	40	1186.44	1138.89	4.57
	60	1189.56	1123.94	2.23
	80	1132.37	1077.68	1.66
	100	1170.70	1091.18	2.21
450	40	860.38	661.56	0.82
	60	913.72	739.66	0.93
	80	1087.15	1052.64	1.30
	100	1162.40	1111.65	1.90

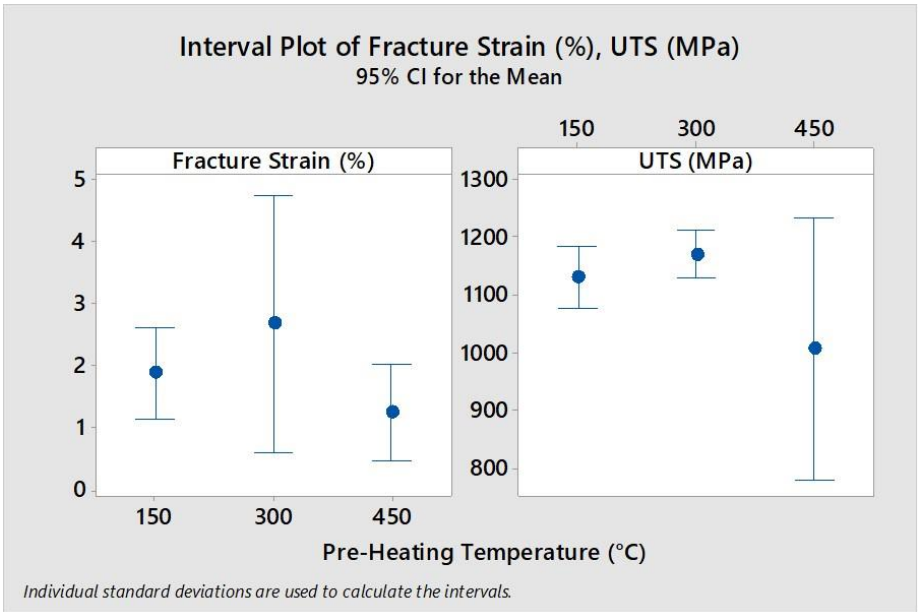

(a)

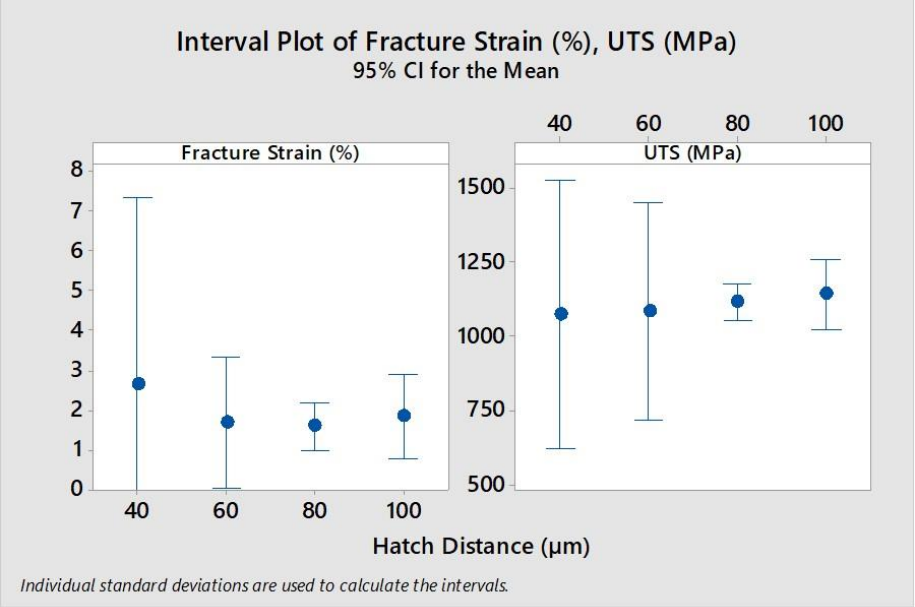

(b)

Figure 6.11: Interval plots of tensile properties for samples processed with 50 µm layer thickness and 170 µm spot size as a function of (a) pre-heating temperature and (b) hatch distance

6.7 Discussion and Conclusion

The microhardness results presented in section 6.4 yielded very little change between groups with the mean value of all of the groups tested falling within a 13 HV range which was indicative of the primarily α'/α microstructures observed. Of the parameters examined, the pre-heating temperature was the most statistically significant variable identified. However, the positive relationship observed between pre-heating temperature and microhardness was unexpected. The samples produced at higher pre-heating temperatures displayed more significant α' martensite decomposition which should lead to a reduction in hardness values. In contrast, higher oxidation was observed following pre-heating at higher temperatures as presented in section 6.3 and thus can be accredited with the increase in microhardness values.

Sections 6.6.1 – 6.6.4 outline the tensile properties observed as a function of layer thickness, spot size, pre-heating temperature and hatch distance. Three primary factors namely, part density, microstructure and oxygen content have influenced the tensile performance.

Section 6.6.1 presents the sample group with the highest energy input with ED values ranging from 120 – 300 J/mm^3 and a power density of 0.029 W/mm^2. The high energy input caused residual stresses at low pre-heating temperatures and significant oxidation at higher pre-heating temperatures. Combined these effects resulted in samples failing to produce a valid test or extremely low fracture strain results. Therefore, despite Chapter 5 reporting the most optimal microstructural conditions given high energy inputs, the associated oxidation, residual stress and indeed low density levels have a greater influence on tensile properties and yield poor results.

Section 6.6.2 presents samples with a 50 µm layer thickness and 63 µm spot size which result in intermediate energy input values in the form of ED values ranging from 60 – 150 J/mm^3 with a power density of 0.029 W/mm^2. In a similar manner to the 25 µm layer thickness samples with the same spot size, decomposition from the α' martensite structure was observed for high pre-heating temperatures and tight hatch distances of 40 – 60 µm. In such circumstances higher fracture strain and lower stress values could be expected. However, the samples that were identified as having decomposed microstructures

presented higher UTS and YS as well as lower failure strain values. Thus, despite the reduction in ED values from the 25 µm layer thickness group, the power density value of 0.029 W/mm^2 has resulted in oxidation of samples at lower hatch distances. The high power density value is indicative of a melt pool with a high maximum temperature whilst tight hatch distances increase the interaction time with the material. Combined these parameters give significant opportunity for the meltpool to pick up oxygen from the surrounding atmosphere causing significant embrittlement of the samples.

Samples processed using a 170 µm spot size with a 25 and 50 µm layer thickness are presented in sections 6.6.3 and 6.6.4 respectively. Increasing the spot size from 63 – 170 µm lowers the power density by 86.2% to 0.004 W/mm^2. Chapter 5 reported that this negatively influences α' decomposition whereby no (α+β) structures were observed when using a 50 µm layer thickness. Furthermore, the ED values of the 50 µm layer thickness group ranged from 60 – 150 J/mm^3 which in combination with the low power density resulted in a low overall energy input. As a result this was the only sample group to present with lack of fusion defects. Combined, the α' martensitic microstructure and lack of fusion defects resulted in low fracture strain and high UTS and YS values.

In contrast, at the same spot size and hence the same power density of 0.004 W/mm^2, the 25 µm layer thickness sample group resulted in increased overall energy input in the form of ED values ranging from 120 – 300 J/mm^3. Given its similarity to the process parameters developed for density optimisation in Chapter 4, this sample group facilitated the highest density of any samples observed. Furthermore, the increased energy input over the 50 µm group facilitated increased α' decomposition as hatch distance was reduced and pre-heating temperature increased. This combination of high density and microstructure tailoring led to the highest fracture strain values observed. Samples produced with a 450 °C pre-heating temperature demonstrated a mean fracture strain of 9.58% which moves in line with some heat treated samples observed in literature [188]. Further, hatch distance also has a notable influence where a fracture strain of 8.47% was observed for samples produced at 40 µm irrespective of the pre-heating temperature. Finally, despite the significant increase in fracture strain observed within this group, the UTS and YS values did not decline significantly.

From results presented in section 6.6 it is evident that the energy input into the process is crucial to the part density, microstructure and mechanical properties of as-built samples. Conflicting trends have been identified between power density, microstructure and part density in that increasing power density by reducing spot size is beneficial for α' martensite decomposition but is detrimental to part density, residual stress and oxidation. Similarly, reducing power density by increasing the spot size results in more dense components (given the correct ED values) but restricts the level of α' decomposition observed in samples. Section 6.6.3 presented mechanical properties which move close to those expected from heat treatment of SLM Ti64 due to density maximisation. Yet, the true extent to which the microstructure can impact the mechanical properties has not been uncovered due to oxidation of samples that present decomposed microstructures.

Though the energy input is crucial, the method by which the energy is developed is just as important and thus ED or power density should not be used alone to characterise the SLM process. For example the same ED value of 300 J/mm^3 has produced samples with a mean fracture strain of 0.53% and 8.95% when combined with a 63 and 170 µm spot size respectively. Similarly the same power density value of 0.004 W/mm^2 produced fracture strains of 1.58% and 7.09% given a reduction in layer thickness from 50 – 25 µm. Therefore, while these metrics are useful in determining and quantifying the energy input into the SLM process, the individual parameter levels must be considered when looking to optimise mechanical properties in the as-built state.

Chapter 7 Conclusions and Future Work

This research focused on examining the density and microstructure of as-built SLM processed Ti64 components and their effect on mechanical properties. This work is concluded by summarising the primary results and commenting on potential future research.

7.1 Conclusions

7.1.1 Produce fully dense samples using the Realizer SLM50 printer

The literature review revealed that the vast majority of density optimisation focuses on optimisation of laser parameters. Specifically the laser power and scanning velocity have been heavily studied. However, other variables such as the gas flow within the process chamber have also demonstrated the ability to affect the density of as-built parts. Hence, Chapter 4 examined the gas flow within the Realizer SLM50 through a CFD model and empirical examination to evaluate its affect on part density. Four gas flow scenarios were examined in the form of two nozzles and two flow rates. Results revealed that the gas flow configuration with the lowest velocity across the build plate resulted in the greatest meltpool width due to scattering. The scattering resulted in less energy input into the powder bed which reduced the possibility of over-melting and subsequently resulted in the highest density. Furthermore, the same configuration was the most repeatable with respect to the part density as a function of position on the build plate which was highlighted as an issue in the literature.

Following gas flow examination, a statistical examination of the laser power, scanning velocity, hatch distance and layer thickness was conducted. A number of factorial and

OFAT style experiments composed the DOE. Increasing laser power and reducing scanning velocity were determined to have the greatest impact on maximising density whilst the hatch distance was relatively insensitive in comparison. Ultimately, a combination of laser parameters capable of repeatedly producing fully dense samples was identified. The effect of density on tensile properties was then examined through processing tensile bars with four different parameter sets which resulted in three different density values. Fracture strain, UTS and YS all demonstrated a positive relationship with density. Specifically, increasing the density from 97.5% to 99.4% resulted in a 66% increase in the fracture strain.

7.1.2 Achieve in-situ decomposition of the brittle martensitic microstructure characteristic of SLM processed Ti64

Analysis of literature revealed a number of techniques for achieving in-situ decomposition of SLM processed Ti64. Namely hatch distance, layer thickness, laser spot size and pre-heating temperature all demonstrated abilities to affect the as-built microstructure. However, none of these had been examined collectively but rather individually. Thus, a DOE comprising two layer thicknesses, two spot sizes and four hatch distances at three different pre-heating temperatures was examined with regards to density and microstructure. The gas flow configuration, laser power and scanning velocity were retained from the previous section with the aim of maintaining a high density level.

Pre-heating temperature demonstrated no influence on density whilst the spot size, layer thickness and hatch distance in descending order all impact the density of as-built parts. Generally, decreasing the spot size to 63 µm from the 170 µm used during density optimisation resulted in significant over melting due to the increase in power density given the same ED values. In contrast, reducing ED values whilst maintaining the larger 170 µm spot size resulted in lack of fusion defects which are detrimental to mechanical properties.

With regards to as-built microstructure, in-situ decomposition of the α’ martensitic structure was realised. Quantitative and qualitative examination of the as-built microstructure in the form of OM, SEM and XRD analysis was performed. Three

different structures namely, α' martensitic, α' + (α+β) and Widmanstätten (α+β) were identified throughout the parameter sets studied. Increasing the pre-heating temperature, reducing the hatch distance and reducing the spot size were identified as significant with regards to decomposing the α' martensitic structure into an (α+β) structure. Of these, the pre-heating temperature was determined to have the most significant impact. No α' decomposition was observed at the lowest pre-heating temperature whilst minimal α' → α transformations were observed at a pre-heating temperature of 300 °C. In contrast, 50% of the samples produced at the highest pre-heating temperature of 450 °C demonstrated some level of α' decomposition. Finally, it is worth noting that the samples that demonstrated significant decomposition from a martensitic structure to a Widmanstätten structure correlated to low density levels due to the high energy input required for the decomposition to occur.

7.1.3 Examine the effect of density and microstructure on the mechanical properties

Mechanical properties in the form microhardness and tensile properties have been evaluated with respect to density and microstructure of as-built parts. However, two more variables in the form of residual stresses and interstitial element content also must be considered.

Analysis of the microhardness values presented reveals a small range between the lowest and highest values recorded which is indicative of the primarily α'/α microstructures which contain low β percentages identified in the previous section. However, pre-heating temperature and the relationship between layer thickness and hatch distance were determined as statistically significant factors for microhardness. Positive relationships were observed between microhardness and both pre-heating temperature and layer thickness. In contrast, the relationship with hatch distance was complex with the smallest hatch distance demonstrating high hardness values. These trends contradict what may have been expected based on literature as these samples correlated to α' decomposition which should have reduced hardness values. Examination of the oxygen content revealed that increasing the temperature during processing increases the oxygen content in parts which correlated to high hardness values. Thus, the oxygen percentage was identified as the primary contributor to the minor variations observed.

The parameters developed in the previous section to produce different microstructures were used to build tensile bars for tensile performance examination. Samples processed with a 63 µm spot size possess a power density that is 86% greater than samples processed with a 170 µm spot size. This increased power density was beneficial to α' decomposition but detrimental to density levels. Due to the high energy input, hardware restrictions limited the number of tensile samples that could be processed. Those that were built exhibited residual stresses and oxidation which led to premature failure of most samples before tensile values could be recorded. Only the largest hatch distance at the highest pre-heating temperature produced samples with relatively standard tensile properties for as-built samples. Reducing the energy input in the form of increasing the layer thickness and hatch distance with a fixed power density input reduced the effects of oxidation and removed the detrimental residual stresses. Consequently, fracture strain improved but stayed within normal values observed in the literature for α' martensitic structures.

Building samples with a 170 µm spot size reduces the power density and served to increase the part density overall. This can be attributed to the fact that the density optimisation of laser parameters took place using this spot size level. In contrast, processing at this spot size was detrimental to in-situ decomposition of α' martensite with the vast majority of samples processed at this level exhibiting α' martensitic structures irrespective of other parameters employed. However, quantitative analysis reported that the α lath size increased with increasing pre-heating temperature whilst a Widmanstätten structure was observed for a tight hatch distance when processed with a 450 °C pre-heating temperature. This combination of high density levels and microstructural tailoring led to a significant increase in fracture strain which moved in line with some heat treated samples observed in literature. Reducing the ED through increasing the layer thickness led to α' martensite retention and lack of fusion defects which resulted in extremely poor fracture strain values.

7.1.4 Concluding Remarks

The hypothesis of this research was that optimisation of density and microstructure simultaneously in as-built samples will remove the need for post process HIP/annealing treatments.

In this work, fully dense samples with nominal values of 100% have been produced. Optimisation efforts for microstructure led to the formation of a Widmanstätten (α+β) structure for which literature reports increased fracture strain values. However, bi-modal and equiaxed structures which are considered as the gold standard for microstructural composition in Ti64 were not achieved in the as-built state. Furthermore, parameters used to process fully dense samples are not conducive to achieving in-situ decomposition of α' martensite and vice-versa. However, the sample group with the best mechanical properties showed an inverse trend to density whereby the less martensitic structures resulted in increased fracture strain. Specifically, the one sample in that group that exhibited a Widmanstätten (α+β) structure presented the highest fracture strain which was in line with some heat treated samples observed in the literature. This suggests that a certain level of porosity may be acceptable for tensile performance depending on the application.

Nevertheless, based on the results presented within this work, the hypothesis must be rejected. As previously stated, the best samples possessed tensile properties that were akin to those presented in literature following some heat treatments. Yet, it is common for annealed and HIP processed samples to achieve fracture strain values in excess of 15% which was not observed in this work [117]. However, no sample set in this research possessed an (α+β) structure along with no porosity thus further research in this area may lead to as-built samples demonstrating comparable mechanical properties to those of post-processed specimens.

7.2 Future Work

Based on the results obtained during this work, the following areas of future work are suggested

7.2.1 Spot Size Development

The results presented within this research identified spot size as a statistically significant variable with regards to both part density and microstructure. The vast majority of literature does not account for spot size in optimisation attempts but rather relies on changing the ED value to achieve fully dense samples or to alter the as-built

microstructure. Analysis of the power density variable shows the value of changing the spot size. Further research regarding combined optimisation of the spot size and power density variable could achieve fully dense parts in combination with (α+β) microstructures – a combination that was not achieved in this research.

7.2.2 Microstructural Heritage

As outlined, the martensitic α' microstructure is omnipresent within as-built SLM processed Ti64 literature. Thus, research to date regarding post processing in the form of annealing and/or HIP treatments has focused on changing process variables to transform the α' structure into an equilibrium or bi-modal (α+β) structure to maximise fracture strain which comes at the expense of stress values. This work has demonstrated the ability to decompose the α' martensite during the building process which facilitated increased fracture strain values without significantly decreasing the stress values. Heat treatment of these microstructures is likely to result in different microstructural features than those observed following heat treatment of α' martensite structures. This in turn has the capability of enabling large fracture strain and stress values simultaneously.

7.2.3 Pre-Heating

As outlined throughout this thesis, pre-heating the build plate is widely accepted to decrease residual stress formation in as-built parts. However, the effect of pre-heating to high temperatures as has been done in this work, has only been reported by a small number of authors. In each case, as was observed in this work, high temperature pre-heating is beneficial to in-situ α' martensite decomposition. In combination with the right laser parameters, increased fracture strain is possible whilst maintaining high stress values. However, this study represents the first to examine multiple laser parameters at increased pre-heating temperatures. Therefore, many more combinations of parameters remain to be examined at higher pre-heating temperatures.

The drawback of increased pre-heating temperatures is that it enables significant oxidation of Ti64 samples. The subsequent embrittlement prevents analysis of the true capabilities of parts processed at high pre-heating temperatures. Thus, developing a system capable of high pre-heating temperatures without significant oxygen pickup –

perhaps through processing in a vacuum – would represent a significant leap in the field of process optimisation of as-built SLM processed Ti64.

References

[1] "ISO/ASTM 52900 Standard Terminology for Additive Manufacturing - General Principles - Terminology." .

[2] I. Campbell, O. Diegel, J. Kowen, and T. Wohlers, *Wohlers report 2018: 3D printing and additive manufacturing state of the industry: annual worldwide progress report*. Wohlers Associates, 2018.

[3] J. Kingsley, "Adding it up: The economic impact of additive manufacturing," *The Economist*. [Online]. Available: https://eiuperspectives.economist.com/technology-innovation/adding-it-economic-impact-additive-manufacturing.

[4] I. Gibson, D. Rosen, and B. Stucker, *Additive Manufacturing Technologies 3D Printing, Rapid Prototyping and Direct Digital Manufacturing*, Second. Springer Berlin Heidelberg, 2015.

[5] BS ISO/ASTM 52900:2015, "BSI Standards Publication Additive manufacturing — General principles — Terminology," 2015.

[6] M. Burns, *Automated Fabrication: Improving Productivity in Manufacturing*. Prentice-Hall, Inc., 1993.

[7] C. K. Chua, K. F. Leong, and C. S. Lim, *Rapid Prototyping: Principles and Applications2nd Edition (with Companion CD-ROM)*, vol. 1. World Scientific Publishing Co Inc, 2003.

[8] J. P. Kruth, M. C. Leu, and T. Nakagawa, "Progress in additive manufacturing and rapid prototyping," *CIRP Ann. - Manuf. Technol.*, vol. 47, no. 2, pp. 525–540, 1998.

[9] B. E. Stucker and G. D. J. Ram, "Layer-based additive manufacturing

technologies," *CRC Mater. Process. handbook. Taylor Fr. CRC Press. Boca Raton, FL*, pp. 21–26, 2007.

[10] M. E. Orme, M. Gschweitl, M. Ferrari, I. Madera, and F. Mouriaux, "Designing for additive manufacturing: Lightweighting through topology optimization enables lunar spacecraft," *J. Mech. Des. Trans. ASME*, vol. 139, no. 10, 2017.

[11] A. Alfaify, M. Saleh, F. M. Abdullah, and A. M. Al-Ahmari, "Design for additive manufacturing: A systematic review," *Sustain.*, vol. 12, no. 19, 2020.

[12] N. Hopkinson, Hague, Richard, and P. Dickens, *Rapid Manufacturing: An Industrial Revolution for the Digital Age*. 2005.

[13] D. Horst, C. Duvoisin, and R. Vieira, "Additive Manufacturing at Industry 4.0: a Review," *Int. J. Eng. Tech. Res.*, vol. 8, no. 8, pp. 3–8, 2018.

[14] A. J. Pinkerton, "[INVITED] Lasers in additive manufacturing," *Opt. Laser Technol.*, vol. 78, pp. 25–32, 2016.

[15] M. C. Sinirlioglu, "Rapid manufacturing of dental and medical parts via LASERCUSING® technology using titanium and CoCr powder materials," in *US–Turkey Workshop On Rapid Technologies, Istanbul, Turkey*, 2009, pp. 89–92.

[16] M. Ziółkowski and T. Dyl, "Possible applications of additive manufacturing technologies in shipbuilding: A review," *Machines*, vol. 8, no. 4, pp. 1–34, 2020.

[17] M. Attaran, "The rise of 3-D printing: The advantages of additive manufacturing over traditional manufacturing," *Bus. Horiz.*, vol. 60, no. 5, pp. 677–688, 2017.

[18] M. Grasso and B. M. Colosimo, "Process defects and in situ monitoring methods in metal powder bed fusion: A review," *Meas. Sci. Technol.*, vol. 28, no. 4, 2017.

[19] "Launcher," *2021*. [Online]. Available: https://launcherspace.com/.

[20] H. H. Malik *et al.*, "Three-dimensional printing in surgery: a review of current surgical applications," *J. Surg. Res.*, vol. 199, no. 2, pp. 512–522, 2015.

[21] N. Martelli *et al.*, "Advantages and disadvantages of 3-dimensional printing in surgery: A systematic review," *Surg. (United States)*, vol. 159, no. 6, pp. 1485–1500, 2016.

[22] M. D. B. S. Tam, S. D. Laycock, D. G. Bell, and A. Chojnowski, "3-D printout of a DICOM file to aid surgical planning in a 6 year old patient with a large scapular osteochondroma complicating congenital diaphyseal aclasia," *J. Radiol. Case Rep.*, vol. 6, no. 1, pp. 31–37, 2012.

[23] S. Jacobs, R. Grunert, F. W. Mohr, and V. Falk, "3D-Imaging of cardiac structures using 3D heart models for planning in heart surgery: a preliminary study," *Interact. Cardiovasc. Thorac. Surg.*, vol. 7, no. 1, pp. 6–9, Dec. 2008.

[24] M. Markert, S. Weber, and T. C. Lueth, "A beating heart model 3D printed from specific patient data," in *2007 29th Annual International Conference of the IEEE Engineering in Medicine and Biology Society*, 2007, pp. 4472–4475.

[25] S. Condino *et al.*, "How to build patient-specific synthetic abdominal anatomies. An innovative approach from physical toward hybrid surgical simulators," *Int. J. Med. Robot. Comput. Assist. Surg.*, vol. 7, no. 2, pp. 202–213, Dec. 2011.

[26] G. T. Klein, Y. Lu, and M. Y. Wang, "3D Printing and Neurosurgery—Ready for Prime Time?," *World Neurosurg.*, vol. 80, no. 3–4, pp. 233–235, 2013.

[27] Y. Liu and X. Shen, "Conclusions and Future Directions." Springer, Cham, pp. 63–65, 2014.

[28] A. F. Ayoub *et al.*, "A novel approach for planning orthognathic surgery: The integration of dental casts into three-dimensional printed mandibular models," *Int. J. Oral Maxillofac. Surg.*, vol. 43, no. 4, pp. 454–459, Dec. 2014.

[29] Z. Jaffry *et al.*, "Unicompartmental knee arthroplasties: Robot vs. patient specific instrumentation," *Knee*, vol. 21, no. 2, pp. 428–434, Dec. 2014.

[30] A. Popovich, V. Sufiiarov, I. Polozov, E. Borisov, and D. Masaylo, "Producing hip implants of titanium alloys by additive manufacturing," *Int. J. Bioprinting*, vol. 2, no. 2, pp. 78–84, 2016.

[31] D. Wang *et al.*, "Customized a Ti6Al4V Bone Plate for Complex Pelvic Fracture by Selective Laser Melting," *Materials (Basel).*, no. 1, pp. 1–14, 2016.

[32] X. Wang *et al.*, "Topological design and additive manufacturing of porous metals

for bone scaffolds and orthopaedic implants: A review," *Biomaterials*, vol. 83, pp. 127–141, 2016.

[33] L. E. Murr, S. M. Gaytan, E. Martinez, F. Medina, and R. B. Wicker, "Next generation orthopaedic implants by additive manufacturing using electron beam melting," *Int. J. Biomater.*, vol. 2012, 2012.

[34] P. Heinl, L. Müller, C. Körner, R. F. Singer, and F. A. Müller, "Cellular Ti-6Al-4V structures with interconnected macro porosity for bone implants fabricated by selective electron beam melting," *Acta Biomater.*, vol. 4, no. 5, pp. 1536–1544, 2008.

[35] C. K. Chua, C. H. Wong, and W. Y. Yeong, *Standards, Quality Control, and Measurement Sciences in 3D Printing and Additive Manufacturing*. Elsevier Science, 2017.

[36] H. Attar, M. Calin, L. C. Zhang, S. Scudino, and J. Eckert, "Manufacture by selective laser melting and mechanical behavior of commercially pure titanium," *Mater. Sci. Eng. A*, vol. 593, pp. 170–177, 2014.

[37] C. Lindemann, U. Jahnke, M. Moi, and R. Koch, "Analyzing product lifecycle costs for a better understanding of cost drivers in additive manufacturing."

[38] G. Lütjering and J. C. Williams, "Titanium : Engineering Materials and Processes," *Ed. SPRINGER*, vol. second edi, pp. 1–442, 2007.

[39] L. M. Gammon, R. D. Briggs, J. M. Packard, K. W. Batson, R. Boyer, and C. W. Domby, "Metallography and Microstructures of Titanium and its Alloys," *Mater. Park. OH ASM Int. 2004.*, vol. 9, pp. 899–917, 2004.

[40] B. Vrancken, "Study of Residual Stresses in Selective Laser Melting," no. June, 2016.

[41] D. A. Brice *et al.*, "Oxidation behavior and microstructural decomposition of Ti-6Al-4V and Ti-6Al-4V-1B sheet," *Corros. Sci.*, vol. 112, pp. 338–346, 2016.

[42] M. Yan, W. Xu, M. S. Dargusch, H. P. Tang, M. Brandt, and M. Qian, "Review of effect of oxygen on room temperature ductility of titanium and titanium alloys,"

Powder Metall., vol. 57, no. 4, pp. 251–257, 2014.

[43] J. D. M. J., "Titanium - A Technical Guide (2nd Edition)." ASM International.

[44] J. Alcisto *et al.*, "Tensile properties and microstructures of laser-formed Ti-6Al-4V," *J. Mater. Eng. Perform.*, vol. 20, no. 2, pp. 203–212, 2011.

[45] R. Boyer and G. Welsch, *Materials Properties Handbook: Titanium Alloys*. 1994.

[46] F. H. Froes, "Powder metallurgy of titanium alloys," *Advances in Powder Metallurgy*. Elsevier, pp. 202–240, 2013.

[47] P. Conradie, D. Dimitrov, G. Oosthuizen, and M. Putz, "A Cost Modelling Approach for Milling Titanium Alloys," *Procedia CIRP*, vol. 46, pp. 412–415, 2016.

[48] S. L. Sing, J. An, W. Y. Yeong, and F. E. Wiria, "Laser and electron-beam powder-bed additive manufacturing of metallic implants: A review on processes, materials and designs," *J. Orthop. Res.*, vol. 34, no. 3, pp. 369–385, 2016.

[49] M. Brandt, S. Sun, M. Leary, S. Feih, J. Elambasseril, and Q. Liu, "High-Value SLM Aerospace Components: From Design to Manufacture," *Adv. Eng. Mater. Prod. Syst. Des.*, vol. 633, pp. 135–147, 2013.

[50] J. Kruth, B. Vandenbroucke, J. Vaerenbergh, and P. Mercelis, "Benchmarking of different SLS/SLM processes as rapid manufacturing techniques," *Int. Conf. Polym. Mould. Innov. (PMI), Gent, Belgium, April 20-23, 2005*, pp. 1–7, 2005.

[51] M. K. Thompson *et al.*, "Design for Additive Manufacturing: Trends, opportunities, considerations, and constraints," *CIRP Ann. - Manuf. Technol.*, vol. 65, no. 2, pp. 737–760, 2016.

[52] M. Geetha, A. K. Singh, R. Asokamani, and A. K. Gogia, "Ti based biomaterials, the ultimate choice for orthopaedic implants - A review," *Prog. Mater. Sci.*, vol. 54, no. 3, pp. 397–425, 2009.

[53] X. Song, L. Wang, M. Niinomi, M. Nakai, and Y. Liu, "Fatigue characteristics of a biomedical β-type titanium alloy with titanium boride," *Mater. Sci. Eng. A*, vol. 640, pp. 154–164, 2015.

[54] K. Wang, “The use of titanium for medical applications in the USA,” *Mater. Sci. Eng. A*, vol. 213, no. 1–2, pp. 134–137, 1996.

[55] I. Yadroitsev, *Selective Laser Melting*. LAP LAMBERT Academic Publishing, 2009.

[56] O. Rehme, “Cellular design for laser freeform fabrication.” 2008.

[57] D. Gu *et al.*, “Densification behavior, microstructure evolution, and wear performance of selective laser melting processed commercially pure titanium,” *Acta Mater.*, vol. 60, no. 9, pp. 3849–3860, 2012.

[58] H. Attar, M. Bönisch, M. Calin, L. C. Zhang, S. Scudino, and J. Eckert, “Selective laser melting of in situ titanium-titanium boride composites: Processing, microstructure and mechanical properties,” *Acta Mater.*, vol. 76, pp. 13–22, 2014.

[59] H. Attar *et al.*, “Effect of powder particle shape on the properties of in situ Ti-TiB composite materials produced by selective laser melting,” *J. Mater. Sci. Technol.*, vol. 31, no. 10, pp. 1001–1005, 2015.

[60] H. Attar *et al.*, “Comparison of wear properties of commercially pure titanium prepared by selective laser melting and casting processes,” *Mater. Lett.*, vol. 142, pp. 38–41, 2015.

[61] T. Bormann, R. Schumacher, B. Müller, M. Mertmann, and M. Wild, “Tailoring Selective Laser Melting Process Parameters for NiTi Implants,” *J. Mater. Eng. Perform.*, vol. 21, no. December, pp. 2519–2524, 2012.

[62] S. Das, M. Wohlert, J. J. Beaman, and D. L. Bourell, “Processing of titanium net shapes by SLS/HIP,” *Mater. Des.*, vol. 20, no. 2–3, pp. 115–121, 1999.

[63] H. Meier, C. Haberland, J. Frenzel, and R. Zarnetta, “Selective Laser Melting of NiTi shape memory components,” *Innov. Dev. Des. Manuf. Adv. Res. virtual rapid Prototyp.*, pp. 233–238, 2009.

[64] H. Ali, L. Ma, H. Ghadbeigi, and K. Mumtaz, “In-situ residual stress reduction, martensitic decomposition and mechanical properties enhancement through high temperature powder bed pre-heating of Selective Laser Melted Ti6Al4V,” *Mater.*

Sci. Eng. A, vol. 695, no. April, pp. 211–220, 2017.

[65] L. Parry, I. A. Ashcroft, and R. D. Wildman, "Understanding the effect of laser scan strategy on residual stress in selective laser melting through thermo-mechanical simulation," *Addit. Manuf.*, vol. 12, pp. 1–15, 2016.

[66] L.-C. Zhang and H. Attar, "Selective Laser Melting of Titanium Alloys and Titanium Matrix Composites for Biomedical Applications: A Review," *Adv. Eng. Mater.*, vol. 18, no. 4, pp. 463–475, 2015.

[67] E. Chlebus, B. Kuźnicka, T. Kurzynowski, and B. Dybała, "Microstructure and mechanical behaviour of Ti-6Al-7Nb alloy produced by selective laser melting," *Mater. Charact.*, vol. 62, no. 5, pp. 488–495, 2011.

[68] L. C. Zhang, D. Klemm, J. Eckert, Y. L. Hao, and T. B. Sercombe, "Manufacture by selective laser melting and mechanical behavior of a biomedical Ti-24Nb-4Zr-8Sn alloy," *Scr. Mater.*, vol. 65, no. 1, pp. 21–24, 2011.

[69] L. E. Murr *et al.*, "Microstructure and mechanical behavior of Ti-6Al-4V produced by rapid-layer manufacturing, for biomedical applications," *J. Mech. Behav. Biomed. Mater.*, vol. 2, no. 1, pp. 20–32, 2009.

[70] T. Vilaro, C. Colin, and J. D. Bartout, "As-Fabricated and Heat-Treated Microstructures of the Ti-6Al-4V Alloy Processed by Selective Laser Melting."

[71] K. Puebla, L. E. Murr, S. M. Gaytan, E. Martinez, F. Medina, and R. B. Wicker, "Effect of Melt Scan Rate on Microstructure and Macrostructure for Electron Beam Melting of Ti-6Al-4V," *Mater. Sci. Appl.*, vol. 3, no. 5, pp. 259–264, 2012.

[72] H. Gong, K. Rafi, T. Starr, and B. Stucker, "The Effects of Processing Parameters on Defect Regularity in Ti-6Al-4V Parts Fabricated By Selective Laser Melting and Electron Beam Melting," 2013.

[73] L. Facchini, E. Magalini, P. Robotti, A. Molinari, S. Höges, and K. Wissenbach, "Ductility of a Ti-6Al-4V alloy produced by selective laser melting of prealloyed powders," *Rapid Prototyp. J.*, vol. 16, no. 6, pp. 450–459, 2010.

[74] W. Xu *et al.*, "Additive manufacturing of strong and ductile Ti-6Al-4V by selective

laser melting via in situ martensite decomposition," *Acta Mater.*, vol. 85, pp. 74–84, 2015.

[75] W. Xu, E. W. Lui, A. Pateras, M. Qian, and M. Brandt, "In situ tailoring microstructure in additively manufactured Ti-6Al-4V for superior mechanical performance," *Acta Mater.*, vol. 125, pp. 390–400, 2017.

[76] H. Ali, H. Ghadbeigi, and K. Mumtaz, "Effect of scanning strategies on residual stress and mechanical properties of Selective Laser Melted Ti6Al4V," *Mater. Sci. Eng. A*, vol. 712, no. November 2017, pp. 175–187, 2018.

[77] L. E. Murr *et al.*, "Microstructures and mechanical properties of electron beam-rapid manufactured Ti-6Al-4V biomedical prototypes compared to wrought Ti-6Al-4V," *Mater. Charact.*, vol. 60, no. 2, pp. 96–105, 2009.

[78] S. Leuders *et al.*, "On the mechanical behaviour of titanium alloy TiAl6V4 manufactured by selective laser melting: Fatigue resistance and crack growth performance," *Int. J. Fatigue*, vol. 48, pp. 300–307, 2013.

[79] J. P. Kruth, L. Froyen, J. Van Vaerenbergh, P. Mercelis, M. Rombouts, and B. Lauwers, "Selective laser melting of iron-based powder," *J. Mater. Process. Technol.*, vol. 149, no. 1–3, pp. 616–622, 2004.

[80] R. Morgan, C. J. Sutcliffe, and W. O'Neill, "Density analysis of direct metal laser re-melted 316L stainless steel cubic primitives," *J. Mater. Sci.*, vol. 39, no. 4, pp. 1195–1205, 2004.

[81] J. Y. H. Fuh, Y. S. Choo, A. Y. C. Nee, L. Lu, and K. C. Lee, "of the UV curing laser lithography technique process for the," *Mater. Des.*, vol. 16, no. 1, pp. 23–32, 1995.

[82] C. Qiu, C. Panwisawas, M. Ward, H. C. Basoalto, J. W. Brooks, and M. M. Attallah, "On the role of melt flow into the surface structure and porosity development during selective laser melting," *Acta Mater.*, vol. 96, pp. 72–79, 2015.

[83] M. Qian, W. Xu, M. Brandt, and H. P. Tang, "Additive manufacturing and postprocessing of Ti-6Al-4V for superior mechanical properties," *MRS Bull.*, vol.

41, no. 10, pp. 775–784, 2016.

[84] S. Pal, G. Lojen, V. Kokol, and I. Drstvensek, “Evolution of metallurgical properties of Ti-6Al-4V alloy fabricated in different energy densities in the Selective Laser Melting technique,” *J. Manuf. Process.*, vol. 35, no. September, pp. 538–546, 2018.

[85] G. Kasperovich, J. Haubrich, J. Gussone, and G. Requena, “Correlation between porosity and processing parameters in TiAl6V4 produced by selective laser melting,” *Mater. Des.*, vol. 105, pp. 160–170, 2016.

[86] H. Gong, K. Rafi, N. V. Karthik, T. Starr, and B. Stucker, “Defect morphology in Ti–6Al–4V parts fabricated by selective laser melting and electron beam melting,” in *24rd Annual International Solid Freeform Fabrication Symposium—An Additive Manufacturing Conference, Austin, TX, Aug*, 2013, pp. 12–14.

[87] S. Pang, W. Chen, and W. Wang, “A Quantitative Model of Keyhole Instability Induced Porosity in Laser Welding of Titanium Alloy,” *Metall. Mater. Trans. A Phys. Metall. Mater. Sci.*, pp. 1–11, 2014.

[88] J. Yang *et al.*, “Role of molten pool mode on formability, microstructure and mechanical properties of selective laser melted Ti-6Al-4V alloy,” *Mater. Des.*, vol. 110, pp. 558–570, 2016.

[89] M. Courtois, M. Carin, P. Le Masson, S. Gaied, and M. Balabane, “A new approach to compute multi-reflections of laser beam in a keyhole for heat transfer and fluid flow modelling in laser welding,” *J. Phys. D. Appl. Phys.*, vol. 46, no. 50, p. 505305, 2013.

[90] L. Thijs, F. Verhaeghe, T. Craeghs, J. Van Humbeeck, and J. P. Kruth, “A study of the microstructural evolution during selective laser melting of Ti-6Al-4V,” *Acta Mater.*, vol. 58, no. 9, pp. 3303–3312, 2010.

[91] C. Qiu, N. J. E. Adkins, and M. M. Attallah, “Microstructure and tensile properties of selectively laser-melted and of HIPed laser-melted Ti-6Al-4V,” *Mater. Sci. Eng. A*, vol. 578, pp. 230–239, 2013.

[92] A. A. Martin *et al.*, “Dynamics of pore formation during laser powder bed fusion

additive manufacturing," *Nat. Commun.*, vol. 10, no. 1, pp. 1–10, 2019.

[93] X. Zhao *et al.*, "Comparison of the microstructures and mechanical properties of Ti–6Al– 4V fabricated by selective laser melting and electron beam melting," *Jmade*, vol. 95, pp. 21–31, 2016.

[94] H. Gong, K. Rafi, H. Gu, G. D. J. Ram, T. Starr, and B. Stucker, "Influence of defects on mechanical properties of Ti-6Al-4V components produced by selective laser melting and electron beam melting," *Mater. Des.*, vol. 86, pp. 545–554, 2015.

[95] G. Kasperovich and J. Hausmann, "Improvement of fatigue resistance and ductility of TiAl6V4 processed by selective laser melting," *J. Mater. Process. Technol.*, vol. 220, pp. 202–214, 2015.

[96] J. Han *et al.*, "Microstructure and mechanical property of selective laser melted Ti6Al4V dependence on laser energy density," *Rapid Prototyp. J.*, vol. 23, no. 2, pp. 217–226, Dec. 2017.

[97] B. Song, S. Dong, B. Zhang, H. Liao, and C. Coddet, "Effects of processing parameters on microstructure and mechanical property of selective laser melted Ti6Al4V," *Mater. Des.*, vol. 35, pp. 120–125, 2012.

[98] R. Cunningham, S. P. Narra, C. Montgomery, J. Beuth, and A. D. Rollett, "Synchrotron-Based X-Ray Microtomography Characterization of the Effect of Processing Variables on Porosity Formation in Laser Power-Bed Additive Manufacturing of Ti-6Al-4V," *Jom*, pp. 2–7, 2016.

[99] D. Lohe and O. Vohringer, "Handbook of Residual Stress and Deformation of Steel," *Handb. Residual Stress Deform. Steel*, vol. http://www, pp. 54–69, 2002.

[100] F. Bartolomeu *et al.*, "Predictive models for physical and mechanical properties of Ti6Al4V produced by Selective Laser Melting," *Mater. Sci. Eng. A*, vol. 663, pp. 181–192, 2016.

[101] K. G. Prashanth, S. Scudino, T. Maity, J. Das, and J. Eckert, "Is the energy density a reliable parameter for materials synthesis by selective laser melting?," *Mater. Res. Lett.*, vol. 5, no. 6, pp. 386–390, 2017.

[102] U. S. Bertoli, A. J. Wolfer, M. J. Matthews, J. P. R. Delplanque, and J. M. Schoenung, "On the limitations of Volumetric Energy Density as a design parameter for Selective Laser Melting," *Mater. Des.*, vol. 113, pp. 331–340, 2017.

[103] B. Van Hooreweder, D. Moens, R. Boonen, J.-P. Kruth, and P. Sas, "Analysis of Fracture Toughness and Crack Propagation of Ti6Al4V Produced by Selective Laser Melting," *Adv. Eng. Mater.*, vol. 14, no. 1–2, pp. 92–97, 2012.

[104] I. Yadroitsava, S. Grewar, D. Hattingh, and I. Yadroitsev, "Residual Stress in SLM Ti6Al4V Alloy Specimens," *Mater. Sci. Forum*, vol. 828–829, no. August, pp. 305–310, 2015.

[105] A. Ladewig, G. Schlick, M. Fisser, V. Schulze, and U. Glatzel, "Influence of the shielding gas flow on the removal of process by-products in the selective laser melting process," *Addit. Manuf.*, vol. 10, pp. 1–9, 2016.

[106] M. Simonelli *et al.*, "Aspects of the Process and Material Relationships in the Selective Laser Melting of Aluminium Alloys," in *TMS 2015 144th Annual Meeting & Exhibition*, 2015, pp. 397–404.

[107] P. Y. Shcheglov, A. V Gumenyuk, I. B. Gornushkin, M. Rethmeier, and V. N. Petrovskiy, "Vapor–plasma plume investigation during high-power fiber laser welding," *Laser Phys.*, vol. 23, no. 1, p. 16001, 2012.

[108] J. Greses, P. A. Hilton, C. Y. Barlow, and W. M. Steen, "Plume attenuation under high power Nd: yttritium–aluminum–garnet laser welding," *J. Laser Appl.*, vol. 16, no. 1, pp. 9–15, 2004.

[109] T. Grünberger and R. Domröse, "Direct Metal Laser Sintering: Identification of process phenomena by optical in-process monitoring," *Laser Tech. J.*, vol. 12, no. 1, pp. 45–48, 2015.

[110] C. Kong, C. J. Tuck, I. A. Ashcroft, R. D. Wildman, and R. Hague, "High Density Ti6Al4V via SLM processing: Microstructure and Mechanical properties," *Solid Free. Fabr. Proc.*, pp. 475–483, 2011.

[111] B. Ferrar, L. Mullen, E. Jones, R. Stamp, and C. J. Sutcliffe, "Gas flow effects on selective laser melting (SLM) manufacturing performance," *J. Mater. Process.*

Technol., vol. 212, no. 2, pp. 355–364, 2012.

[112] M. Shunmugavel, A. Polishetty, and G. Littlefair, "Microstructure and Mechanical Properties of Wrought and Additive Manufactured Ti-6Al-4V Cylindrical Bars," *Procedia Technol.*, vol. 20, no. July, pp. 231–236, 2015.

[113] H. Attar, S. Ehtemam-Haghighi, D. Kent, X. Wu, and M. S. Dargusch, "Comparative study of commercially pure titanium produced by laser engineered net shaping, selective laser melting and casting processes," *Mater. Sci. Eng. A*, vol. 705, no. August, pp. 385–393, 2017.

[114] W. C. Huang *et al.*, "Microstructure-controllable laser additive manufacturing process for metal products," *Phys. Procedia*, vol. 56, no. C, pp. 58–63, 2014.

[115] B. Wysocki *et al.*, "Microstructure and mechanical properties investigation of CP titanium processed by selective laser melting (SLM)," *J. Mater. Process. Technol.*, vol. 241, pp. 13–23, 2017.

[116] J. Yang, H. Yu, J. Yin, M. Gao, Z. Wang, and X. Zeng, "Formation and control of martensite in Ti-6Al-4V alloy produced by selective laser melting," *Mater. Des.*, vol. 108, pp. 308–318, 2016.

[117] B. Vrancken, L. Thijs, J.-P. Kruth, and J. Van Humbeeck, "Heat treatment of Ti6Al4V produced by Selective Laser Melting: Microstructure and mechanical properties," *J. Alloys Compd.*, vol. 541, no. 0, pp. 177–185, 2012.

[118] T. Sercombe, N. Jones, R. Day, and A. Kop, "Heat treatment of Ti-6Al-7Nb components produced by selective laser melting," *Rapid Prototyp. J.*, vol. 14, no. 5, pp. 300–304, 2008.

[119] F. X. G. Mur, D. Rodríguez, and J. a. Planell, "Influence of tempering temperature and time on the α′-Ti-6Al-4V martensite," *J. Alloys Compd.*, vol. 234, no. 2, pp. 287–289, 1996.

[120] E. Sallica-Leva, R. Caram, A. L. Jardini, and J. B. Fogagnolo, "Ductility improvement due to martensite α' decomposition in porous Ti-6Al-4V parts produced by selective laser melting for orthopedic implants," *J. Mech. Behav. Biomed. Mater.*, vol. 54, pp. 149–158, 2016.

[121] A. Hussein, L. Hao, C. Yan, and R. Everson, “Finite element simulation of the temperature and stress fields in single layers built without-support in selective laser melting,” *Mater. Des.*, vol. 52, no. November 2014, pp. 638–647, 2013.

[122] P. J. Withers and H. K. D. H. Bhadeshia, “Residual stress. Part 1 – Measurement techniques,” *Mater. Sci. Technol.*, vol. 17, no. 4, pp. 355–365, 2001.

[123] C. Amon *et al.*, “Material issues in layered forming,” *Proc. Solid Free. Fabr. Sympasium*, pp. 1–10, 1993.

[124] P. Mercelis and J.-P. J. Kruth, “Residual stresses in selective laser sintering and selective laser melting,” *Rapid Prototyp. J.*, vol. 12, no. 5, pp. 254–265, 2006.

[125] H. Pohl, A. Simchi, M. Issa, and H. C. Dias, “Thermal stresses in direct metal laser sintering,” *Proc. SFF Symp.*, pp. 366–372, 2001.

[126] M. F. Zaeh and G. Branner, “Investigations on residual stresses and deformations in selective laser melting,” *Prod. Eng.*, vol. 4, no. 1, pp. 35–45, 2010.

[127] J.-P. Kruth, J. Deckers, E. Yasa, and R. Wauthle, “Assessing and comparing influencing factors of residual stresses in selective laser melting using a novel analysis method,” *Proc. Inst. Mech. Eng. Part B J. Eng. Manuf.*, vol. 226, no. 6, pp. 980–991, 2012.

[128] A. H. Nickel, D. M. Barnett, and F. B. Prinz, “Thermal stresses and deposition patterns in layered manufacturing,” *Mater. Sci. Eng. A*, vol. 317, no. 1–2, pp. 59–64, 2001.

[129] D. Buchbinder, W. Meiners, N. Pirch, K. Wissenbach, and J. Schrage, “Investigation on reducing distortion by preheating during manufacture of aluminum components using selective laser melting,” *J. Laser Appl.*, vol. 26, no. 1, p. 12004, 2014.

[130] F. Brückner, D. Lepski, and E. Beyer, “Modeling the Influence of Process Parameters and Additional Heat Sources on Residual Stresses in Laser Cladding,” *J. Therm. Spray Technol.*, vol. 16, no. 3, pp. 355–373, 2007.

[131] P. Aggarangsi, J. L. Beuth, and M. Griffith, “Melt Pool Size and Stress Control for

Laser-Based Deposition Near a Free Edge," *Proc. 14th Solid Free. Fabr. Symp.*, pp. 196–207, 2003.

[132] A. Vasinonta, J. L. Beuth, and M. Griffith, "Process Maps for Predicting Residual Stress and Melt Pool Size in the Laser-Based Fabrication of Thin-Walled Structures," *J. Manuf. Sci. Eng.*, vol. 129, no. 1, pp. 101–109, 2007.

[133] F. Abe, K. Osakada, M. Shiomi, K. Uematsu, and M. Matsumoto, "The manufacturing of hard tools from metallic powders by selective laser melting," *J. Mater. Process. Technol.*, vol. 111, no. 1–3, pp. 210–213, 2001.

[134] P. Vora, K. Mumtaz, I. Todd, and N. Hopkinson, "AlSi12 in-situ alloy formation and residual stress reduction using anchorless selective laser melting," *Addit. Manuf.*, vol. 7, pp. 12–19, 2015.

[135] B. Vrancken, S. Buls, J.-P. Kruth, and J. Van Humbeeck, "Influence of preheating and oxygen content on Selective Laser Melting of Ti6Al4V," *Proc. 16th RAPDASA Conf.*, 2015.

[136] J. Sun, Y. Yang, and D. Wang, "Parametric optimization of selective laser melting for forming Ti6Al4V samples by Taguchi method," *Opt. Laser Technol.*, vol. 49, pp. 118–124, 2013.

[137] P. Barriobero-Vila *et al.*, "Inducing stable α + β microstructures during selective laser melting of Ti-6Al-4V using intensified intrinsic heat treatments," *Materials (Basel).*, vol. 10, no. 3, pp. 1–14, 2017.

[138] G. Lütjering, "Influence of processing on microstructure and mechanical properties of (α+β) titanium alloys," *Mater. Sci. Eng. A*, vol. 243, no. 1, pp. 32–45, 1998.

[139] L. Qian, J. Mei, and X. H. Wu, "An Experimental and Modelling Study of Laser Fabricated Samples," *Mater. Sci. Forum*, vol. 539–543, pp. 3637–3642, 2007.

[140] A. International, "ASTM F136-13(2021)e1, Standard Specification for Wrought Titanium-6Aluminum-4Vanadium ELI (Extra Low Interstitial) Alloy for Surgical Implant Applications (UNS R56401)," West Conshohcken, PA, 2013.

[141] G. Theriault, “The beginner’s guide on spot size of laser beam,” 2018. [Online]. Available: https://www.gentec-eo.com/blog/spot-size-of-laser-beam. [Accessed: 06-Sep-2021].

[142] J. Ciurana, L. Hernandez, and J. Delgado, “Energy density analysis on single tracks formed by selective laser melting with CoCrMo powder material,” *Int. J. Adv. Manuf. Technol.*, vol. 68, no. 5, pp. 1103–1110, 2013.

[143] V. Gunenthiram *et al.*, “Experimental analysis of spatter generation and melt-pool behavior during the powder bed laser beam melting process,” *J. Mater. Process. Technol.*, vol. 251, 2018.

[144] M. Yakout, M. A. Elbestawi, and S. C. Veldhuis, “On the characterization of stainless steel 316L parts produced by selective laser melting,” *Int. J. Adv. Manuf. Technol.*, vol. 95, no. 5, pp. 1953–1974, 2018.

[145] M. Yakout, M. A. Elbestawi, and S. C. Veldhuis, “A study of thermal expansion coefficients and microstructure during selective laser melting of Invar 36 and stainless steel 316L,” *Addit. Manuf.*, vol. 24, pp. 405–418, 2018.

[146] X.-H. Yang, C.-M. Jiang, J.-R. Ho, P.-C. Tung, and C.-K. Lin, “Effects of Laser Spot Size on the Mechanical Properties of AISI 420 Stainless Steel Fabricated by Selective Laser Melting,” *Materials (Basel).*, vol. 14, no. 16, p. 4593, 2021.

[147] W. Shi, Y. Liu, X. Shi, Y. Hou, P. Wang, and G. Song, “Beam diameter dependence of performance in thick-layer and high-power selective laser melting of Ti-6Al-4V,” *Materials (Basel).*, vol. 11, no. 7, 2018.

[148] M. T. C. Chow, E. V Bordatchev, and G. K. Knopf, “Experimental study on the effect of varying focal offset distance on laser micropolished surfaces,” *Int. J. Adv. Manuf. Technol.*, vol. 67, no. 9–12, pp. 2607–2617, 2013.

[149] Y. Xu, D. Zhang, Y. Guo, S. Hu, X. Wu, and Y. Jiang, “Microstructural tailoring of As-Selective Laser Melted Ti6Al4V alloy for high mechanical properties,” *J. Alloys Compd.*, vol. 816, p. 152536, 2020.

[150] P. Kumar, O. Prakash, and U. Ramamurty, “Micro-and meso-structures and their influence on mechanical properties of selectively laser melted Ti-6Al-4V,” *Acta*

Mater., vol. 154, pp. 246–260, 2018.

[151] H. Ali, "Evolution of Residual Stress in Ti6Al4V components fabricated using Selective Laser Melting," *PhD Thesis Univ. Sheff.*, pp. 1–338, 2017.

[152] ASTM, "ASTM B348 Standard Specification for Titanium and Titanium Alloy Bars and Billets," *ASTM Int. Stand.*, vol. B348, p. 8, 2013.

[153] J. Schindelin *et al.*, "Fiji: an open-source platform for biological-image analysis," *Nat. Methods*, vol. 9, no. 7, pp. 676–682, 2012.

[154] I. Arganda-Carreras *et al.*, "Trainable Weka Segmentation: a machine learning tool for microscopy pixel classification," *Bioinformatics*, vol. 33, no. 15, pp. 2424–2426, 2017.

[155] J. (Hans) van Houwelingen, "The Elements of Statistical Learning, Data Mining, Inference, and Prediction. Trevor Hastie, Robert Tibshirani and Jerome Friedman, Springer, New York, 2001. No. of pages: xvi+533. ISBN 0-387-95284-5," *Stat. Med. - STAT MED*, vol. 23, pp. 528–529, Feb. 2004.

[156] MathWorks, "MATLAB and Global Optimization Toolbox," 2020. .

[157] G. K. Williamson and W. H. Hall, "X-ray line broadening from filed aluminium and wolfram," *Acta Metall.*, vol. 1, no. 1, pp. 22–31, 1953.

[158] L. Lutterotti, "Total pattern fitting for the combined size-strain-stress-texture determination in thin film diffraction," *Nucl. Instruments Methods Phys. Res. B*, vol. 268, no. 3–4, pp. 334–340, Feb. 2010.

[159] A. Belsky, M. Hellenbrandt, V. L. Karen, and P. Luksch, "New developments in the Inorganic Crystal Structure Database (ICSD): accessibility in support of materials research and design," *Acta Crystallogr. Sect. B*, vol. 58, no. 3 Part 1, pp. 364–369, Jun. 2002.

[160] L. Lutterotti, "Quantitative Rietveld Analysis in Batch Mode with Maud, and New Features in Maud 2.037," *IUCR CPD Newsl.*, vol. 32, pp. 53–55, Jan. 2005.

[161] F. R. Kaschel *et al.*, "Mechanism of stress relaxation and phase transformation in additively manufactured Ti-6Al-4V via in situ high temperature XRD and TEM

analyses," *Acta Mater.*, vol. 188, pp. 720–732, 2020.

[162] ASTM International, "Standard Test Methods for Density of Compacted or Sintered Powder Metallurgy (PM) Products Using Archimedes' Principle," *Astm B962-13*, vol. i, pp. 1–7, 2013.

[163] M. Xu, Y. Chen, T. Zhang, H. Deng, and D. Ji, "Effects of Solution Treatment on Laser Welding of Ti–6Al–4V Alloy Plate Produced through Wire Arc Additive Manufacturing," *Metals* , vol. 10, no. 10. 2020.

[164] ASTM E8, "ASTM E8/E8M standard test methods for tension testing of metallic materials 1," *Annu. B. ASTM Stand. 4*, no. C, pp. 1–27, 2010.

[165] K. Dass and S. R. Chauhan, "Machinability Study of Titanium (Grade-5) Alloy Using Design of Experiment Technique," *Engineering*, vol. 03, no. 06, pp. 609–621, 2011.

[166] L. M. Plaza, A. M. Irisarri, and A. Gil-Negrete, "Improvement of Ti-6Al-4V Fracture Toughness By Sub-Transus Heat Treatment," *Scr. Mater.*, vol. 24, no. 9, 1990.

[167] J. Metelkova, Y. Kinds, K. Kempen, C. de Formanoir, A. Witvrouw, and B. Van Hooreweder, "On the influence of laser defocusing in Selective Laser Melting of 316L," *Addit. Manuf.*, vol. 23, pp. 161–169, 2018.

[168] M. Ma, Z. Wang, M. Gao, and X. Zeng, "Layer thickness dependence of performance in high-power selective laser melting of 1Cr18Ni9Ti stainless steel," *J. Mater. Process. Technol.*, vol. 215, no. 1, pp. 142–150, 2015.

[169] H. Shipley, D. McDonnell, M. Culleton, R. Lupoi, G. O'Donnell, and D. Trimble, "Optimisation of process parameters to address fundamental challenges during selective laser melting of Ti-6Al-4V: A review," *Int. J. Mach. Tools Manuf.*, vol. 128, no. January, pp. 1–20, 2018.

[170] J. Sieniawski, W. Ziaja, K. Kubiak, and M. Motyka, "Microstructure and mechanical properties of high strength two-phase titanium alloys," *Titan. Alloy. Prop. Control*, pp. 69–80, 2013.

[171] S. S. Al-Bermani, M. L. Blackmore, W. Zhang, and I. Todd, "The origin of microstructural diversity, texture, and mechanical properties in electron beam melted Ti-6Al-4V," *Metall. Mater. Trans. A Phys. Metall. Mater. Sci.*, vol. 41, no. 13, pp. 3422–3434, 2010.

[172] A. Safdar, L.-Y. Wei, A. Snis, and Z. Lai, "Evaluation of microstructural development in electron beam melted Ti-6Al-4V," *Mater. Charact.*, vol. 65, pp. 8–15, 2012.

[173] F. J. Gil, M. P. Ginebra, J. M. Manero, and J. A. Planell, "Formation of α-Widmanstätten structure: Effects of grain size and cooling rate on the Widmanstätten morphologies and on the mechanical properties in Ti6Al4V alloy," *J. Alloys Compd.*, vol. 329, no. 1–2, pp. 142–152, 2001.

[174] Y. Fan, W. Tian, Y. Guo, Z. Sun, and J. Xu, "Relationships among the Microstructure, Mechanical Properties, and Fatigue Behavior in Thin Ti6Al4V," *Adv. Mater. Sci. Eng.*, vol. 2016, 2016.

[175] T. Ahmed and H. J. Rack, "Phase transformations during cooling in α+β titanium alloys," *Mater. Sci. Eng. A*, vol. 243, no. 1–2, pp. 206–211, 1998.

[176] X. Wu, J. Liang, J. Mei, C. Mitchell, P. S. Goodwin, and W. Voice, "Microstructures of laser-deposited Ti–6Al–4V," *Mater. Des.*, vol. 25, no. 2, pp. 137–144, 2004.

[177] X. Wu, R. Sharman, J. Mei, and W. Voice, "Microstructure and properties of a laser fabricated burn-resistant Ti alloy," *Mater. Des.*, vol. 25, no. 2, pp. 103–109, 2004.

[178] G. P. Dinda, L. Song, and J. Mazumder, "Fabrication of Ti-6Al-4V Scaffolds by Direct Metal Deposition," *Metall. Mater. Trans. A*, vol. 39, no. 12, pp. 2914–2922, 2008.

[179] V. Senthilkumar, P. Vickraman, M. Jayachandran, and C. Sanjeeviraja, "Structural and electrical studies of nano structured Sn1−xSbxO2 (x = 0.0, 1, 2.5, 4.5 and 7 at%) prepared by co-precipitation method," *J. Mater. Sci. Mater. Electron.*, vol. 21, no. 4, pp. 343–348, 2010.

[180] F. R. Kaschel, R. K. Vijayaraghavan, P. J. McNally, D. P. Dowling, and M. Celikin, "In-situ XRD study on the effects of stress relaxation and phase transformation heat treatments on mechanical and microstructural behaviour of additively manufactured Ti-6Al-4V," *Mater. Sci. Eng. A*, vol. 819, p. 141534, 2021.

[181] T. Ungár, "Microstructural parameters from X-ray diffraction peak broadening," *Scr. Mater.*, vol. 51, no. 8, pp. 777–781, 2004.

[182] C. Lancea, L. A. Chicos, S. M. Zaharia, and M. A. Pop, "Microstructure and micro-hardness analyses of titanium alloy Ti-6Al-4V parts manufactured by selective laser melting," *MATEC Web Conf.*, vol. 94, 2017.

[183] A. M. Khorasani, I. Gibson, U. S. Awan, and A. Ghaderi, "The effect of SLM process parameters on density, hardness, tensile strength and surface quality of Ti-6Al-4V," *Addit. Manuf.*, vol. 25, no. August 2018, pp. 176–186, 2019.

[184] R. Pederson, "The microstructures of Ti-6Al-4V and Ti-6Al-2Sn-4Zr-6Mo and their relationship to processing and properties," *Thesis*, p. 59, 2004.

[185] D. M. Madyira, R. F. Laubscher, N. Janse Van Rensburg, and P. F. J. Henning, "High speed machining induced residual stresses in Grade 5 titanium alloy," *Proc. Inst. Mech. Eng. Part L J. Mater. Des. Appl.*, vol. 227, no. 3, pp. 208–215, 2013.

[186] H. Ali, H. Ghadbeigi, and K. Mumtaz, "Processing Parameter Effects on Residual Stress and Mechanical Properties of Selective Laser Melted Ti6Al4V," *J. Mater. Eng. Perform.*, vol. 27, no. 8, pp. 4059–4068, 2018.

[187] V. Manvatkar, A. De, and T. DebRoy, "Spatial variation of melt pool geometry, peak temperature and solidification parameters during laser assisted additive manufacturing process," *Mater. Sci. Technol.*, vol. 31, no. 8, pp. 924–930, 2015.

[188] T. Vilaro, C. Colin, and J. D. Bartout, "As-fabricated and heat-treated microstructures of the Ti-6Al-4V alloy processed by selective laser melting," *Metall. Mater. Trans. A Phys. Metall. Mater. Sci.*, vol. 42, no. 10, pp. 3190–3199, 2011.

Appendix A: XRD Spectra

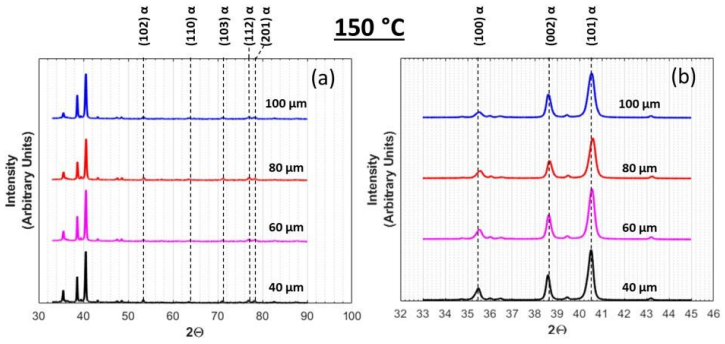

170 µm Spot Size, 25 µm Layer Thickness

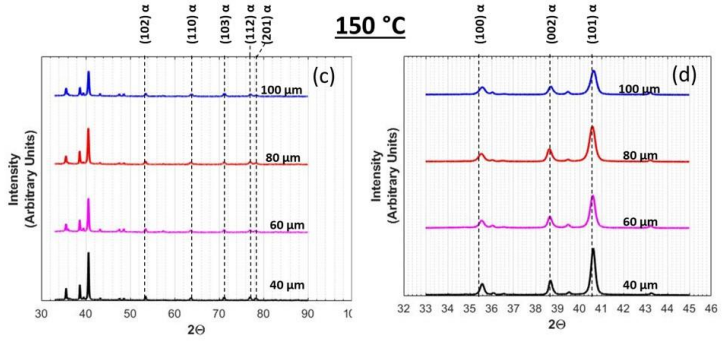

170 µm Spot Size, 50 µm Layer Thickness

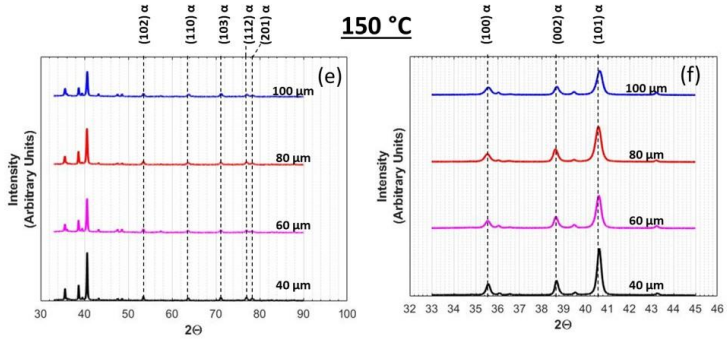

63 µm Spot Size, 25 µm Layer Thickness

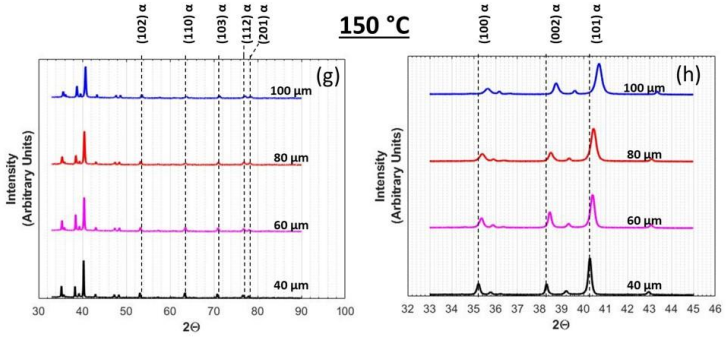

63 µm Spot Size, 50 µm Layer Thickness

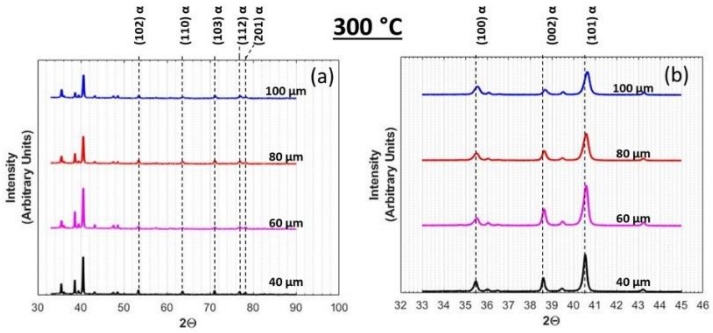

170 µm Spot Size, 25 µm Layer Thickness

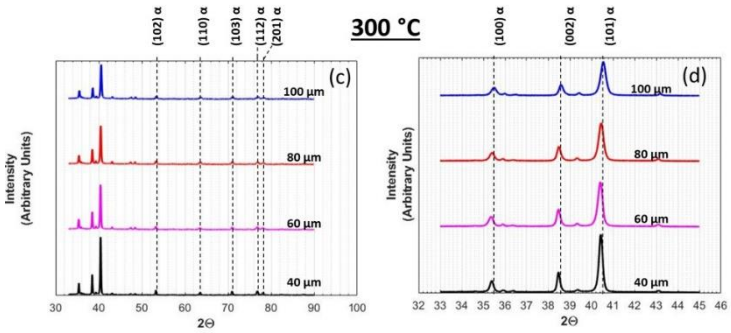

170 µm Spot Size, 50 µm Layer Thickness

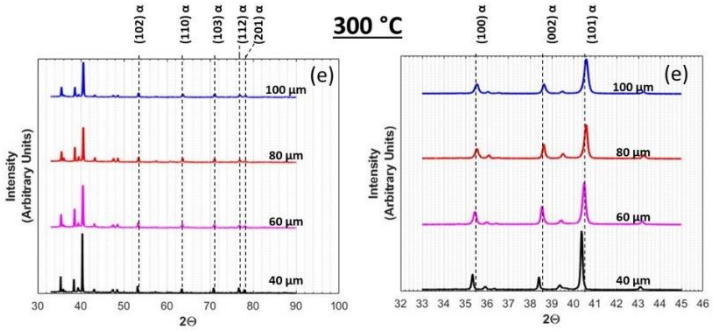

63 µm Spot Size, 25 µm Layer Thickness

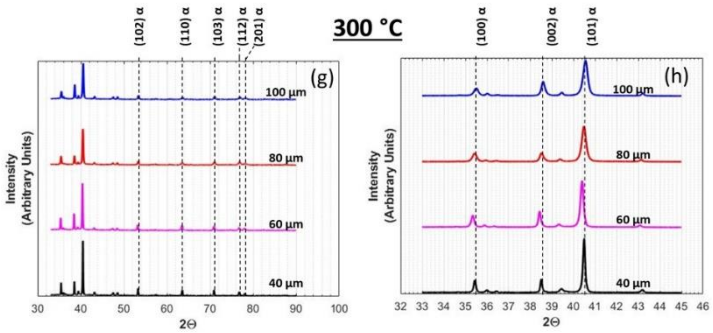

63 µm Spot Size, 50 µm Layer Thickness

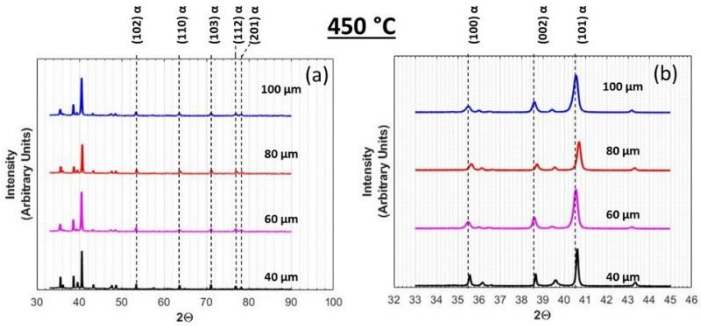

170 µm Spot Size, 25 µm Layer Thickness

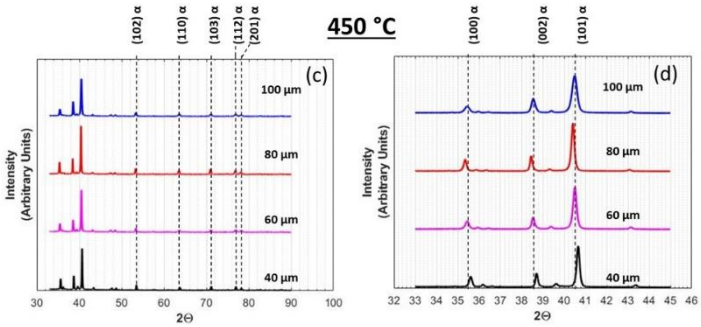

170 µm Spot Size, 50 µm Layer Thickness

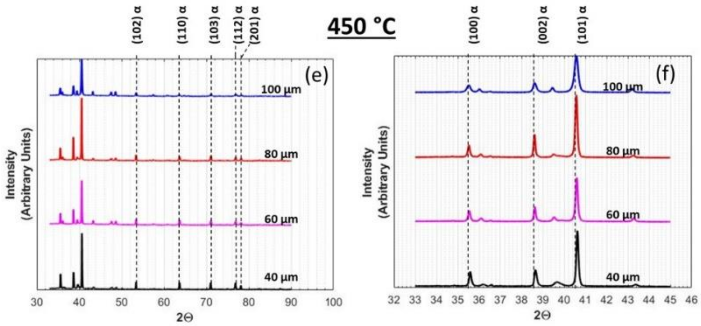

63 µm Spot Size, 25 µm Layer Thickness

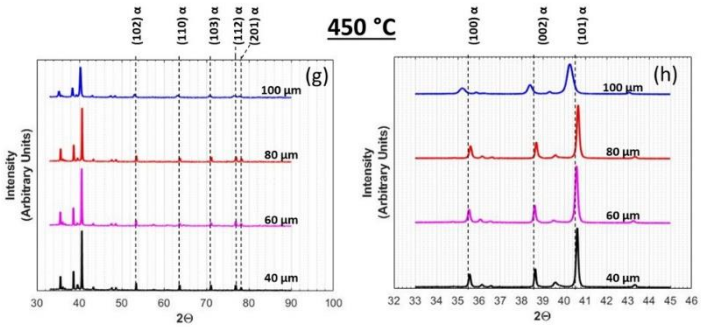

63 µm Spot Size, 50 µm Layer Thickness

XRD Profiles Observed for all parameter sets processed at 450 °C pre-heating temperature

Appendix B: Tensile Specimens

Tensile samples used for all tensile tests throughout this work. Dimensions conform to ASTM E8/E8M Figure 8 sample 4 [164].